Chapter 1

Title: **Template Directed Assembly Strategies**

Final Report

PI: Professor Chad A. Mirkin, Northwestern University

	Form Approved
# Report Documentation Page	OMB No. 0704-0188

Public reporting burden for the collection of information is estimated to average 1 hour per response, including the time for reviewing instructions, searching existing data sources, gathering and maintaining the data needed, and completing and reviewing the collection of information. Send comments regarding this burden estimate or any other aspect of this collection of information, including suggestions for reducing this burden, to Washington Headquarters Services, Directorate for Information Operations and Reports, 1215 Jefferson Davis Highway, Suite 1204, Arlington VA 22202-4302. Respondents should be aware that notwithstanding any other provision of law, no person shall be subject to a penalty for failing to comply with a collection of information if it does not display a currently valid OMB control number.

1. REPORT DATE **01 OCT 2010**	2. REPORT TYPE **FInal**	3. DATES COVERED **01-07-2009 to 01-06-2010**

4. TITLE AND SUBTITLE **US-Korea Nanotechnology, Biotechnology, and Information Technology (NBIT) Symbiosys Program - Phase I Final Report**	5a. CONTRACT NUMBER **FA23860914060**
	5b. GRANT NUMBER
	5c. PROGRAM ELEMENT NUMBER
6. AUTHOR(S) **Hongkun Park; Julie Kornfield; Moon Kim; Sungho Jin; Kang Shin**	5d. PROJECT NUMBER
	5e. TASK NUMBER
	5f. WORK UNIT NUMBER

7. PERFORMING ORGANIZATION NAME(S) AND ADDRESS(ES) **National Research Foundation of Korea (NRF), formerly Korea ,Foundation for International Cooperation of Science & Technology ,(KICOS),Trust Towwer, Flr 2, 275-7 Yangjae Dong,KR,137-739**	8. PERFORMING ORGANIZATION REPORT NUMBER **N/A**

9. SPONSORING/MONITORING AGENCY NAME(S) AND ADDRESS(ES) **AOARD, UNIT 45002, APO, AP, 96337-5002**	10. SPONSOR/MONITOR'S ACRONYM(S) **AOARD**
	11. SPONSOR/MONITOR'S REPORT NUMBER(S) **AOARD-094060**

12. DISTRIBUTION/AVAILABILITY STATEMENT
Approved for public release; distribution unlimited

13. SUPPLEMENTARY NOTES
For Author Chapter 6 to 10 This report is the final report for US-Korea NBIT Phase I (2007-2010). It contains ten final reports, each as a separate chapter. Eight reports cover full three years of research and two reports are for two years of research.

14. ABSTRACT
Chapter 6 ? SiGe Alloy Nanowire Photonics; Chapter 7 ? Self-Assembled Liquid Crystalline Gels: From Nanostructure to Function; Chapter 8 ? Extremely Low Noise CNT for Peltier and Photo-dector Device Application; Chapter 9 ? High-Res, Large-Area, Nano Imprint Lithography; Chapter 10 - Distributed Detection of Attacks/Intrusions and Prevention of Resource-Starvation Attacks in Mobile Ad Hoc Network

15. SUBJECT TERMS

16. SECURITY CLASSIFICATION OF:			17. LIMITATION OF ABSTRACT	18. NUMBER OF PAGES	19a. NAME OF RESPONSIBLE PERSON
a. REPORT **unclassified**	b. ABSTRACT **unclassified**	c. THIS PAGE **unclassified**	**Same as Report (SAR)**	**226**	

Standard Form 298 (Rev. 8-98)
Prescribed by ANSI Std Z39-18

Objectives

The goal of this research program was to develop facile routes for fabricating two-dimensional templates for the self-assembly of nanoscale structures. These patterns would enable the study of fundamental phenomena related to molecular recognition, charge transport, and optical coupling, as well as demonstrating the integration of biologically inspired motors with these nanostructures. To achieve these goals, three nanofabrication methods invented in our laboratory, Dip Pen Nanolithography (DPN)[1], Polymer Pen Lithography (PPL)[2], and On-Wire Lithography (OWL)[3], were harnessed. In order to demonstrate the utility of OWL-generated gapped nanowires (GNWs) for sensors and parallel electronic devices, the GNWs were functionalized through a variety of strategies that enabled them to act as sensitive probes for surface enhanced Raman spectroscopy (SERS) and to display a variety of molecular electronic properties. In parallel, multiplexed DPN techniques were used to generate patterned surfaces bearing chemical templates for the assembly of GNWs. The merger of these two methods will enable the future generation of large arrays of GNW based devices for a variety of applications including sensing, electronics, and molecular transport.

Status of effort

Support from this NBIT grant has contributed to the publication of 8 peer-reviewed scientific journal articles and 5 conference and meeting papers (see below, excluding outputs from the Hong laboratory). In addition, this project has allowed for the training of 1 postdoctoral fellow (A. B. Braunschweig, also supported by an NIH fellowship) and 2 graduate students (A. J. Senesi and L. R. Giam, the latter also supported by an NSF fellowship).

The developments made in this first phase of the NBIT program will now be taken forward in the second phase, where the ability to produce GNW-based sensors and DPN-printed templates will serve as the foundations to create massively parallelized two-dimensional arrays of devices. Efforts are currently underway to improve on the registry and alignment the GNWs onto the DPN-fabricated chemical templates using DNA sequences as 'addresses' to target GNWs to specific locations on the surface. This sequence specificity of DNA hybridization employed means that a GNW bearing a specific DNA sequence will attach only at the location on the surface template (generated by either PPL or DPN) which bears the complementary DNA sequence, ensuring a high degree of templating fidelity. Furthermore, the underlying chemistry associated with the synthesis of these DNA strands is highly modular and well understood, allowing the later incorporation of other chemical groups that will serve as chemical sensors or attachment points for other biomolecules such as proteins.

Abstract

This program has enabled the advancement of templated nanofabrication strategies that are the springboard to complex yet compact optoelectronic and bioelectronic devices. Additionally, the NBIT grant has also facilitated studies in fundamental molecular electronics, self-assembly, and optical coupling. In particular, we have achieved our objective of molecular patterning on surfaces with several technologically relevant and fundamentally interesting materials. We have also shown the placement of nanomaterials and GNWs within the context of larger structures on a variety surfaces with control over their position and orientation. Another objective that we have achieved was to combine DPN and PPL with OWL to create novel nanoscale device architectures that exhibit interesting electronic and photonic properties. These devices are sensitive towards chemical and physical stimuli and act as transducers, which will find applications in sensing, detection and encryption.

Personnel Supported

Andrew Senesi, Graduate Student

Wooyoung Shim, Graduate Student
Louise Giam, Graduate Student
Kyle Osberg, Graduate Student
Dan Eichelsdoerfer, Graduate Student
Wei Wei, Postdoctoral Fellow
Zijian Zheng, Postdoctoral Fellow
Yu Huang Wang, Postdoctoral Fellow

Non-Compensated contributors:
Adam Braunschweig
Lu Shin Wong

Publications

1. Chen, X.; Braunschweig, A. B.; Wiester, M. J.; Yeganeh, S.; Ratner, M. A.; Mirkin, C. A. "Spectroscopic Tracking of Molecular Transport Junctions Generated by Using Click Chemistry," *Angew. Chem. Int. Ed.* **2009**, *48*, 5178.
2. Braunschweig, A. B.; Senesi, A. J.; Mirkin, C. A. "Redox-Activating Dip-Pen Nanolithography (RA-DPN) ," *J. Am. Chem. Soc.* **2009**, *131*, 922.
3. Chen, X.; Zheng, G.; Cutler, J. I.; Jang, J.-W.; Mirkin, C. A. "In-Wire Conversion of a Metal Nanorod Segment into an Organic Semiconductor," *Small*, **2009**, *5*, 1527.
4. Chen, X.; Yeganeh, S.; Qin, L.; Li, S.; Xue, C.; Braunschweig, A. B.; Schatz, G. C.; Ratner, M. A.; Mirkin, C. A. "Chemical Fabrication of Heterometallic Nanogaps for Molecular Transport Junctions," *Nano Lett.* **2009**, 9, 3974.
5. Giam, L. R.; Wang, Y.; Mirkin, C. A. "Nanoscale Molecular Transport: The Case of Dip-Pen Nanolithography," *J. Phys. Chem A* **2009**, *113*, 3779.
6. Pedano, M. L.; Li, S.; Schatz, G. C.; Mirkin, C. A. "Periodic Electric Field Enhancement Along Gold Rods with Nanogaps," *Angew. Chem. Int. Ed.* **2010**, *49*, 78.
7. Huang, L.; Braunschweig, A. B.; Shim, W.; Qin, L.; Lim, J.-L.; Hurst, S.; Huo, F.; Xue, C.; Jang, J.-W.; Mirkin, C. A. "Matrix-Assisted Dip-Pen Nanolithography (MA-DPN) and Polymer Pen Lithography (MA-PPL)," *Small* **2010**, *in press*.
8. Lim, J. K.; Lee, B. Y.; Pedano, M. L.; Senesi, A. J.; Jang, J.-W.; Shim, W., Hong, S., Mirkin, C. A. "Alignment Strategies for the Assembly of Nanowires with Submicron Diameters," *Small*, *submitted.*

Interactions

1. AFOSR 231DX & EX Natural Materials, Systems, and Extremophiles Review, Arlington, VA; "MURI: Bioinspired Supramolecular Enzymatic Systems," and "DPN-Generated Combinatorial Libraries" (2009).
2. 2009 SPIE MOEMS – MEMS Symposium, San Jose, CA; Plenary Lecture "Massively Parallel Soft Pen Nanolithography" (2009).
3. Hybrid Materials Conference, Vinci International Convention Center, Tours, France; "Unconventional Forms of Nanofabrication" (2009).
4. Tip-Based Nanofabrication PI Review Meeting, New Orleans; "Scanning Probe Epitaxy," (2009).
5. DARPA – MEMS PI Meeting, SunRiver, OR; "Scanning Probe Epitaxy," (2009).
6. Nanyang Technological University, School of Materials Science and Engineering, Singapore; "Commercializing Advances in Nanotechnology: Challenges and Opportunities," and "DNA Rules: Materials Synthesis, Biodiagnostics, and Intracellular Gene Regulation" (2008).
7. NCI Nanotechnology Alliance Investigator Meeting, Chicago, IL; "Nanostructures in Medicine" (2008).

8. Center for Cancer Nanotechnology Excellence (CCNE) Annual Meeting, Northwestern University, Evanston, IL; "Development of Barcode Assays for the Detection of Ovarian and Prostate Cancer" (2008).
9. 23rd Annual Volwiler Science Lecture, Lake Forest College, Lake Forest, IL; "Small Things, Big Implications" (2008).
10. Biomedical Engineering Society Fall Meeting, Distinguished Achievement Award Lecture, St. Louis, MO; "Nanostructures in Medicine" (2008).
11. GoNano, Geoff Ozin's 65th Birthday Celebration, University of Toronto, Toronto, Cananda; "Polymer Pen Lithography" (2008)
12. Symposium "A Celebration of Nano and Molecular Medicine", Institute of Nano and Molecular Medicine, University of Missouri, Columbia, MO; "DNA Rules: Materials Synthesis, Biodiagnostics, and Intracellular Gene Regulation" (2008).
13. DARPA/DSRC Workshop on "Nanomanufacturing with Molecular Recognition", School of Engineering & Applied Sciences, Harvard University, Cambridge, MA; "Physical & Chemical Approaches to Nanofabrication through Molecular Recognition" (2008).
14. Department of Materials Science & Engineering, University of Michigan, Ann Arbor, MI; "Unconventional Forms of Nanofabrication" (2008).
15. CCNE Nanobiotechnology Series, Department of Radiology, School of Medicine, Stanford University, Stanford, CA; "Nanostructures in Medicine" (2008).
16. Materials Research Society Fall Meeting, Session: Nanotechnology for Biomedical Applications, Boston, MA; "Nanoparticles as Gene Regulation Materials" (2008).

Inventions
None.

Honors / Awards
2010   Elected Member of the National Academy of Sciences
2010   Herman S. Bloch Award for Scientific Excellence in Industry, University of Chicago
2010   Einstein Professorship of the Chinese Academy of Sciences (CAS)
2010   Ohio State University Edward Mack Jr. Memorial Award
2009 $500,000 Lemelson-MIT Prize
2009   Member, President's Council of Science & Technology (PCAST, Obama Administration)
2009   Elected Member of the National Academy of Engineering
2009   Havinga Medal, Leiden University, the Netherlands
2009   Thomson Reuters Most Cited Chemist in the World (#1)
2009   Gustavus John Esselen Award
2009   Pittsburgh Analytical Chemistry Award
2008   Biomedical Engineering Society's Distinguished Achievement Award
2008   National Security Science and Engineering Fellowship (NSSEFF) Award
2008   ACS Inorganic Nanoscience Award

Archival Documentation

Highly Parallelized Template Fabrication through Dip Pen Nanolithography

Understanding and Improving Ink Transport Mechanics. To create a tool that can reproducibly generate chemical templates on surfaces, the mechanism of small molecule ink transfer from a DPN probe tip to a surface was investigated. Previously it was shown that ink molecules diffuse from the tip through a water meniscus that spontaneously condenses between the tip and the surface. Mathematical treatments of this model generally assume that the tip coated with the molecular ink, typically mercaptohexadecanoic acid (MHA), which forms a self-assembled monolayer (SAM) on Au, acts as a point source with a constant concentration and diffusion flux. This constant point source model explains the observed linear increase in the diameter of the patterned MHA features as a function of the square root of the dwell time for a single tip. However, this model was unable to account for the variation in transport rates, and thus feature sizes produced by different tips within a DPN pen array and by tips inked through different methods, which is crucial to reproducibly form features of uniform size by different tips in the same array. Using a piezo-electrically driven inkjet printer, we were able to control precisely the amount of ink delivered to each tip in an array and study the relationship between the MHA deposition rate and the surface area of the tip coated by the ink (Figure 1).[4] It was found that the deposition rate is also related to the surface area of the ink dried on the tip, and that by increasing the amount of MHA deposited on the tips, the rate of transport increases. These results are the first DPN experiments that show a correlation between the amount of ink on a tip and the corresponding surface area with the transport rate. This new model enables more consistent and controllable DPN patterning and it enables the *a priori* prediction of the feature size that will be formed in the context of a DPN experiment given the tip inking and dwell time.

Molecular Patterning with Redox-Activating DPN (RA-DPN). A drawback of DPN is that the deposition of each new ink must be optimized because of differences in their solubility and transport rate. A method of circumventing this problem could include developing a universal ink that would template specific areas of a surface towards reaction with a molecule of interest, thereby avoiding the need for a time-consuming optimization process for each new ink. Thus, the combination of chemical immobilization and DPN patterning was explored to increase the scope of materials that could be patterned on a surface to create surface templates. Redox-activating DPN (RA-DPN) demonstrated that oxidizing inks could selectively generate chemical templates that would react with proteins or
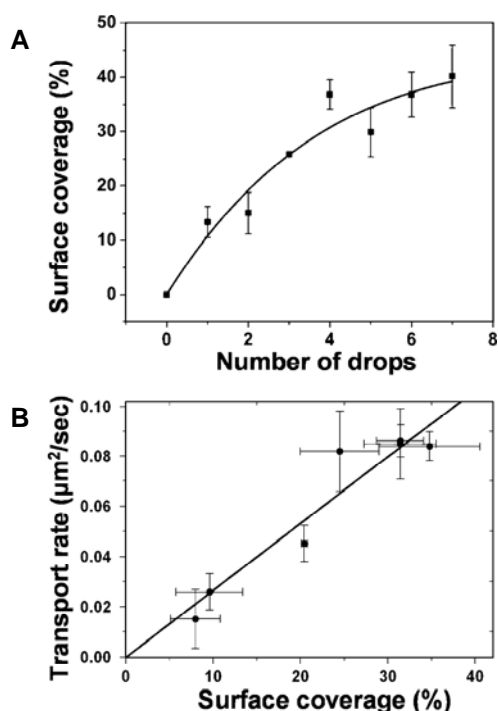
Figure 1. (A) Surface coverage dependence on the number of MHA-ethanol drops on silicon nitride DPN probes. A line was fitted using a four parameter equation with the constraint of passing through the origin of the plot. (B) MHA transport rate shows a linear dependence on the surface coverage and increases with the number of drops.

appropriately labeled DNA to form patterns of these molecules with nanoscale feature dimensions.[5] Specifically, RA-DPN relies on the delivery by DPN of the oxidant cerric

ammonium nitrate (CAN) to a hydroquinone-modified surface by DPN that reversibly switches the quinone moiety from the reduced hydroquinone to the oxidized benzoquinone forms (Scheme 1). This redox chemistry alters the reactivity of the quinone-rich surface in a highly localized manner: the benzoquinone is capable of reacting with nucleophiles via a Michael addition, while the hydroquinone remains unreactive. The patterned surface can subsequently be immersed in a solution containing a nucleophile that then reacts and is immobilized solely where the ink has been deposited and the benzoquinone persists.

Using this approach, the immobilization of both an amine-modified oligonucleotide and a protein was demonstrated (Figure 2). As expected, the size of the features formed by the deposition of CAN increased linearly with the dwell time of the probe on the surface and features as small as 165 nm were generated. Furthermore, by avoiding the need for an electrical bias to activate the quinone surfaces, RA-DPN is not limited to electrically conducting surfaces.

Matrix-Assisted Nanomaterial Patterning with Polymer Pen Lithography. A primary
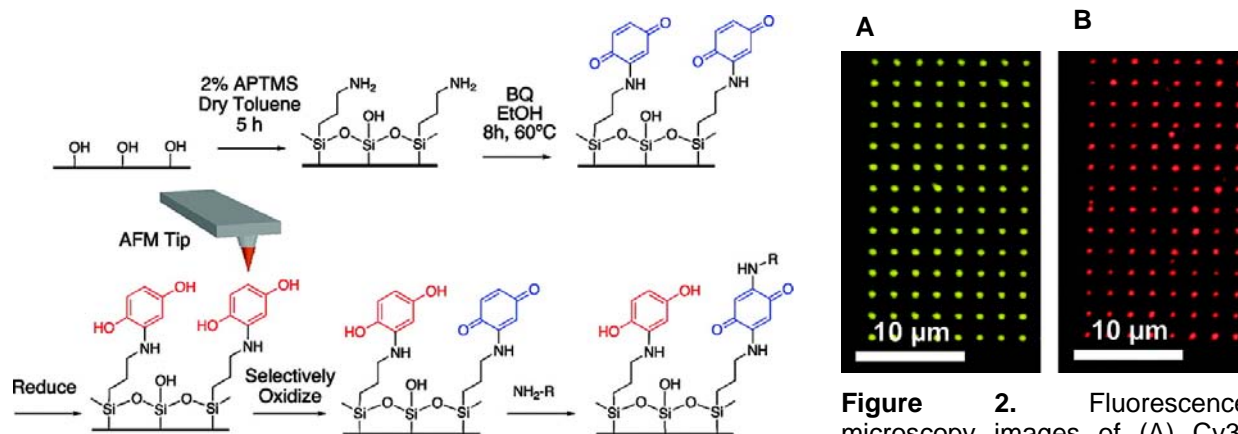
Scheme 1. The generation of hydroquinone-functionalized silicon oxide surfaces, followed by the generation benzoquinone features by the DPN deposition of CAN, followed by the immobilization of nucleophiles to the patterned areas.

Figure 2. Fluorescence microscopy images of (A) Cy3-labelled oligonucleotides and (B) AlexaFluor 549-labelled cholera toxin β subunit (right) arrays generated by RA-DPN.

objective of our NBIT program was to fabricate massively parallel arrays of nanomaterials such as carbon nanotubes and nanoparticles. As a result efforts were made towards developing a method of directly delivering nanomaterials, such as fullerenes and inorganic nanoparticles to a surface in arbitrary patterns with nanometer resolution while maintaining their interesting properties did not exist, Often, these materials could not be patterned by DPN because these relatively large and hydrophobic macromolecules were inefficiently transported across the water meniscus that formed between the probe and surface. Previous attempts to pattern such nanoparticles by conventional DPN methods thus suffered from poor reproducibility. A method for patterning these materials in the context of DPN and PPL experiments was developed that involved a novel matrix-assisted strategy where the amphiphilic polymer polyethylene glycol (PEG) was used to facilitate the transport of these nanomaterials.[6] By mixing a solution of PEG with the desired nanomaterials, it was possible to controllably and reliably generate arbitrary patterns of these materials (Figure 3). Specifically, nano- and microscale features of Au nanoparticles (AuNPs), Fe_3O_4 magnetite nanoparticles (MNPs), and C_{60} could be generated on metal, semiconducting, and insulating surfaces using this matrix-assisted DPN (MA-DPN) method.

During the course of this grant, the Mirkin laboratory developed a scanning probe lithography method, termed polymer pen lithography (PPL),[2] that uses a two dimensional

elastomeric array of pyramidal tips that can write features ranging in size from 80 nm to over 10 µm in a single writing operation. These polymer pens are robust, easy to fabricate, and amenable to the creation of massively parallel 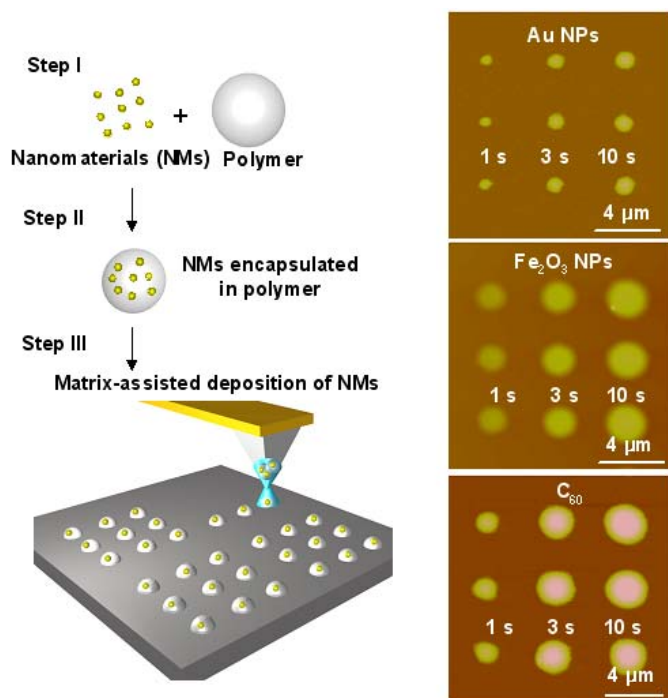arrays with as many as 11 million tips. The concept of using PEG co-deposition in combination with PPL resulted in MA-PPL.[6] Under similar deposition conditions, both the MA-DPN and MA-PPL produced nearly identical features of nanoparticles with varying sizes and solubilities. Furthermore, to demonstrate that matrix assisted patterning could be used to fabricate functioning devices in line with the objectives of NBIT, C_{60} patterns were written between electrodes to create a working photoresponsive transistor.

Figure 3. Schematic representation of the MA-DPN method (left) and AFM images of nanoparticles deposited using this method (right).

On-Wire Lithography (OWL)
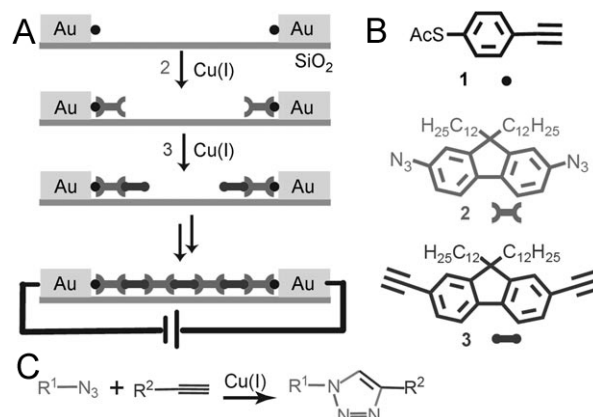**Spectroscopic tracking of Molecular Transport Junctions Generated by Using Click Chemistry.** On wire lithography (OWL) is an electrochemical-based nanofabrication method for synthesizing nanowires with positive and negative architectural features whose lengths can be controlled with sub-2 nm resolution along the long axis of the wire. Since the size of gapped features along a nanowire may be controlled with nanometer precision, these structures are well suited for the construction and study of molecular transport junctions (MTJs). Traditionally, the nanometer lengths of MTJs prohibited their interrogation with standard spectroscopic tools that could identify the chemical

Figure 4. (A) Click chemistry within the nano-gaps. (B) Molecules used in this study. (C) The alkyne–azide click reaction.

structures within the MTJs. However, given suitable composition and architecture, the gap of OWL generated nanostructures produces an enhancement of Raman signal intensity of the molecules in close proximity to the gaps by up to six orders of magnitude. Because of this Raman enhancement, OWL generated nanostructures are uniquely positioned to simultaneously examine the electronic transport properties of molecules and characterize the components of an MTJ using surface enhanced Raman spectroscopy (SERS).

As a proof of concept for simultaneous electronic and spectroscopic characterization of MTJs, we developed an *in situ* synthesis of molecular wires using click chemistry (Figure 4), where each step could be monitored by SERS, thus enabling, for the first time, a correlation between the molecular structure within an MTJ and the observed transport properties. In a typical experiment, 360 nm diameter GNW structures with 2 nm nanogaps (Figure 5A) were cast onto a substrate bearing gold microelectrodes and then connected to the electrodes by e-beam lithography and subsequent chromium and gold thermal deposition (Figure 5B). A SAM of **1** was formed on the Au GNWs and the alkyne on **1** was subsequently reacted with the azide of **2** to form a molecular bridge across the gap. The calculated S–S distance of the target bridging molecule is 2.6 nm, which is sufficient to span the 2 nm gap. The two-terminal *I–V* characteristics of the gap devices were measured at room temperature before and after click reactions (Figure 5C). The empty nanogaps and the nanogaps modified with a monolayer consisting only of **1** exhibits no conductance (< 2 pA; Figure 5C). However, following the click reaction of **1** and **2** within the gap, the *I–V* characteristics show a clear molecular response in the mA range (Figure 5C), which indicates the realization of a conjugated molecular bridge within the nanogap formed as a result of the click reaction. The yield for working devices is 41% (12 out of 29 devices with I > 0.1 nA at 1 V bias). It should be noted that the magnitude of the current measured in different MTJ devices varies from 0.1 nA to 600 mA at 1 V bias, which
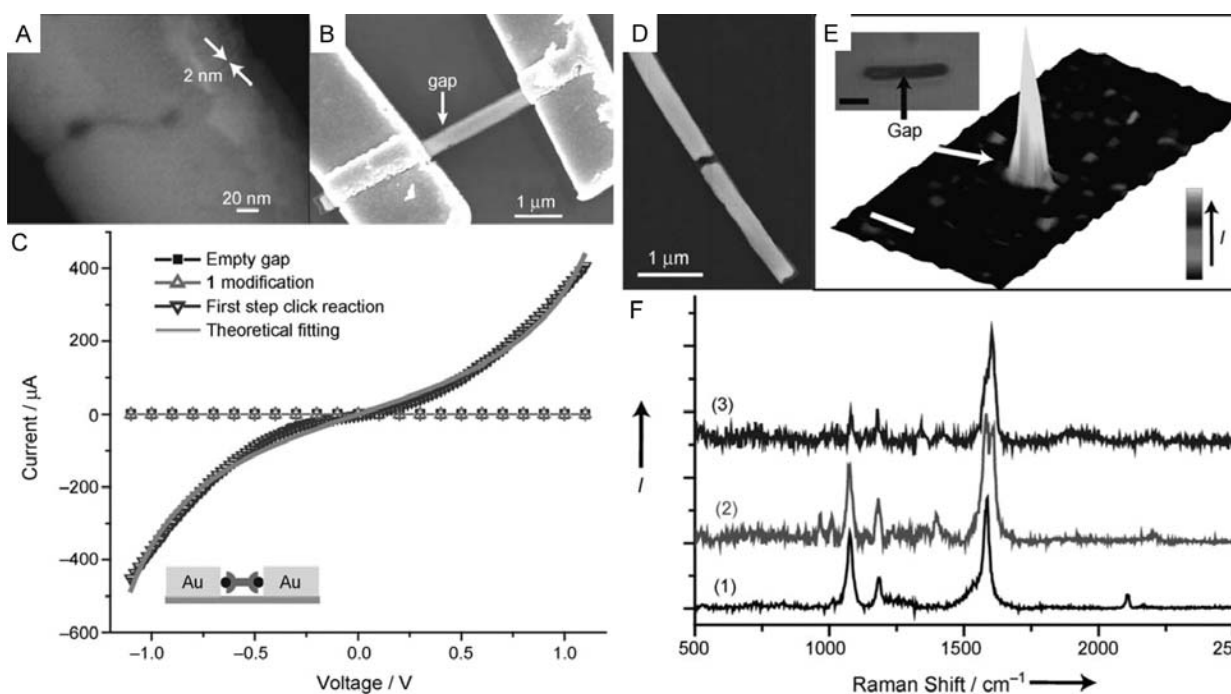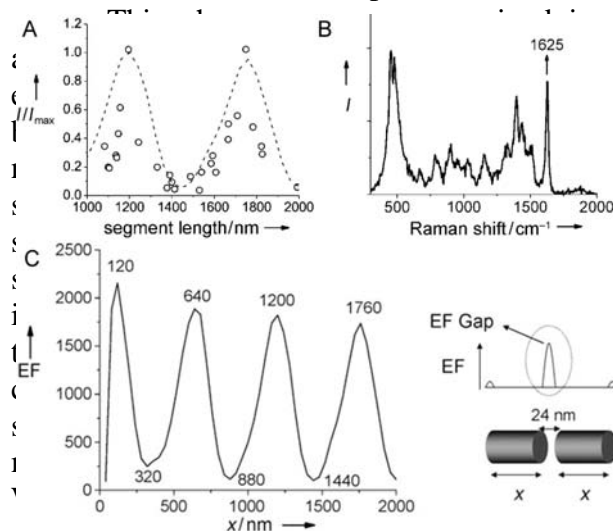

Figure 5 (A) SEM image of a 2 nm OWL-fabricated nanogap. (B) An SEM image of 2 nm nanogap–MTJ device. (C) Representative I–V response for 2 nm OWL-fabricated gaps before, after modification with 1, and the bridging click reaction of 2 with 1. The plain gray line shows the theoretical fitting of the I–V curve. (D) SEM image of an OWL-fabricated nanowire with a 100 nm nanogap. (E) 3D confocal scanning Raman images of an OWL-fabricated gap structure modified with **1**. The inset shows a simultaneously obtained optical image that shows the position of the nanogap. Scale bar: 2 mm. (F) Representative Raman spectrum taken for the different steps: 1) **1** within the gap, 2) following addition of **2**, and 3) following addition of **3**.

presumably results from the different numbers of molecules that bridge the nanogap in different experiments. It is also likely that the roughness of the electrode surface contributes to the observed variation.

SERS measurements carried out directly on the nanogaps confirm that the click reaction proceeds within these confined spaces. OWL-fabricated nanogaps less than 100 nm in width have been shown to act as Raman "hot spots" with enhancement factors as large as 10^8, therefore molecules assembled within nanogaps can be efficiently identified by SERS. To evaluate the potential of OWL-fabricated nanogaps for simultaneous assembly and spectroscopic identification, we fabricated sub-100 nm nanogap structures, with Au segments on the opposite sides of the nanogaps. In a typical experiment, the molecules were assembled by click chemistry in a nanogap (98 ± 11 nm; Figure 5A) as described above for the MTJ fabrication, and the Raman spectra and image of the gap area were measured by confocal scanning Raman microscopy. For the gap structures modified with **1**, the Raman spectrum (Figure 5F, Spectrum 1) clearly shows the presence of alkyne groups (C≡C symmetric stretch at 2108 cm^{-1}) and benzene rings (aromatic C=C stretch of **1** at 1585 cm^{-1}). In addition, when compared with the spectrum of the neat solid of **1**, the absence of thioacetyl (634 cm^{-1}) and SH (bending, 915 cm^{-1}) vibration modes indicates Au-S bonding. The confocal Raman images (Figure 5B) obtained by integrating the spectral intensity from 1520 to 1620 cm^{-1} and the bright-field optical image show that the hot spots are localized in the gap. When **2** reacts with the monolayer of **1** under the click reaction conditions, new peaks at 967 and 1010 cm^{-1} (the triazole ring stretch), 1606 cm^{-1} (aromatic C=C stretch of **2**), and 2198 cm^{-1} (asymmetric stretching of azide groups) appear, and the peak at 2108 cm^{-1} disappears (Figure 5F, Spectrum 2), which indicates that the click reaction of **1** and **2** proceeded successfully. Furthermore, when **3** reacts with **2** under click reaction conditions, the relative intensity of the peak at 1606 cm^{-1} increases (Figure 5F, Spectrum 3), which confirms the occurrence of the reaction between **3** and **2**. These SERS experiments demonstrate the direct observation of the chemical reactions within nanogaps and, as a result, confirm the chemical composition of the molecules confined within the MTJs.

Periodic Electric Field Enhancement Along Gold Rods with Nanogaps. In previous studies, it was found that small gaps (~ 2 – 25 nm) in Au OWL-generated nanostructures a few micrometers in length did not yield Raman hotspots necessary for spectroscopic characterization. Therefore two different wire architectures were necessary for electrical transport measurements and spectroscopic identification. The reasons for this were unclear, as measureable signals arise from molecules within disk pairs (~ 120 nm in length) with similar sized gaps.

This phenomenon was examined in detail through a combination of discrete dipole approximation (DDA) and experimental verification.[7] We determined that the SERS enhancement factor (EF) does not monotonically decrease with segment length, but instead oscillates as a function of the length of the wire. Au OWL-generated rods with a fixed gap of 24 nm and varying lengths of segments on either side of the gap were fabricated. The gapped Au rods were modified with an ethanolic solution of **1** and characterized by confocal Raman spectroscopy. Figure 6A shows the Raman intensity measured at the gaps of the rods; each point is based upon the integrated signal from 1520 to 1660 cm^{-1} (Figure 6B) and plotted as a function of segment length. The theoretical results are plotted on the same axes for comparison. The SEM images of corresponding SEM images of the scanned rods are shown in Figure 6A with segment lengths corresponding to the two peaks in Figure 6A were chosen as representative examples. We also carried out (DDA) calculations for the EF contribution at the gap as a function of segment length (Figure 6C). The incident wavelength, gap length, and the rod diameter were fixed at 633, 24, and 360nm, respectively. The incident polarization is taken to be parallel to the rod axis, and the wave vector is perpendicular to the axis. The EF equals $|E|^4$

/ $|E_0|^4$, where E and E_0 are the local and incident electric fields, respectively, averaged over the surfaces of the rod at the gap. The curve represents the EF variation versus segment length for a symmetric gapped rod, where the two segments are exactly the same. The segment lengths were equally varied for both sides from 40 to 2000 nm in increments of 40 nm. The EF intensity oscillates periodically with the segment length every 560 nm without significant decay. The period of the EF oscillations for segments on gapped rods (560 nm) is somewhat smaller than the period of surface plasmon polaritons (SPPs; 600 nm) that propagate along a single infinite 360 nm diameter Au rod when the wavelength of the incident light is 633 nm. Maxima occur at 120, 640, 1200, and 1760 nm. The 120 nm rod length associated with the lowest order mode is roughly one-quarter of the SPP wavelength, which is consistent with previous observations. This length arises from a 45° phase pickup in the boundary conditions, which are satisfied by SPPs that reflect at the ends of the rods. All the maxima correspond to excitation of the odd-order plasmon multipole modes of each segment. Excitation of even-order modes is symmetry-forbidden for isolated rods with this choice of polarization and wave- vector. Figure 6 shows that at least for a 24 nm gap, the SPP period correctly explains the calculated periodicity in the EF,

Figure 6. (A) Normalized SERS intensities measured at a 24 nm gap as a function of the rod segment length (both rod segments are fixed at the same length for each data point). The curves show experimental results (*) for the total integrated signal at 1625 cm^{-1} MB spectral band, where it scatters strongly, and a comparison with theoretical calculations shown in Figure 2. (B) A MB SERS spectrum on a gapped Au rod. (C) DDA simulation of the EF obtained at a 24 nm gap when varying symmetrically both segment lengths.

and the same periodicity is also observed experimentally. This fundamental study provides a basis for future research to design nanostructured materials that take advantage of the plasmonic properties of noble metals and will allow researchers to simultaneously characterize MTJs by electronic and spectroscopic techniques within in the same device.
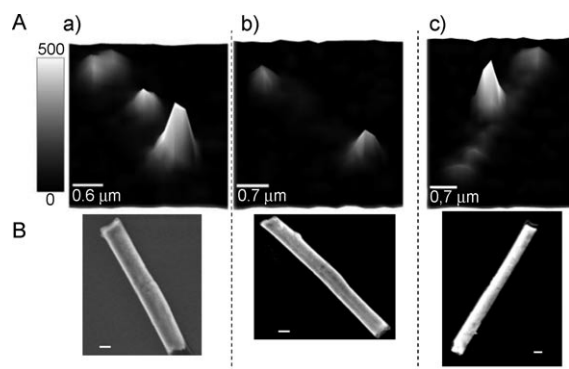

Figure 7. A) SERS scans integrating the 1625 cm^{-1} MB spectral band (scale bar: CCD counts) and B) the corresponding SEM images of the rods. The images in (A) and (B) represent rod segment lengths corresponding to a) the first maximum (x: 1200 nm; y: 520), b) middle minimum (x: 1400 nm; y: 46), and c) second maximum gap intensity (x: 1750 nm; y: 510) of the curve shown in Figure 6. Scale bar in (B): 200 nm. x = segment length, y = absolute experimental Raman intensity.

Chemical Fabrication of Heterometallic Nanogaps for Molecular Transport Junctions. In addition to varying the length and gap size of OWL-generated nanostructures, the elemental composition of each segment in a single nanowire may also be varied. Approaches for making heterometallic nanogaps, where the two electrodes are made of different metals, are interesting and useful for the field of molecular electronics from both fundamental and technological stand-points. Such structures, in principle, would allow researchers to tune the work functions of the electrode materials to better match the HOMO and LUMO of the molecules inserted in the gap. In addition, they may be extremely useful in the area of orthogonal self-assembly where adsorbate molecules can selectively assemble across such structures in a highly oriented fashion based upon different functional groups that are selective for the different metals. Existing methods for making heterometallic nanogaps that involve narrowing procedures by electrodeposition of a second metal on a pre-existing lithographically defined electrode are complicated, difficult to control, and often very low yielding. Therefore, the development of efficient and highly

parallel methods for fabricating heterometallic nanogaps with tunable dimensions would be a major step forward for the field of molecular electronics.

As a proof of concept, OWL was used to fabricate heterometallic nanogaps composed of platinum and gold.[8] In a typical experiment, 360 nm diameter multisegmented nanowires 9 μm long, Au-Ni-Pt-Au-Ni nanowires (diameter 360 nm) were synthesized by sequential electrochemical deposition of gold (3 μm), nickel (10 nm), platinum (2 μm), gold (3 μm), and nickel (1 μm). (Note: a dash denotes the physical connection between segments, while an underscore (used later) indicates a gap between the segments.) A silica backing was deposited by PECVD and the Ni segments etched in HCl, yielding the Pt_Au heterometallic nanogaps. Significantly, SEM and EDS experiments clearly show that the nickel sacrificial layers have been removed, resulting in the formation of Au_Pt heterometallic nanogaps (Figure 8). In addition, we can make Au_Pt heterometallic nanogaps with smooth rod ends (Figure 8E) by an *in situ* two-step electrochemical process. The unmodified nanogap was subsequently modified with an oligo(phenylene ethynylene) (OPE).
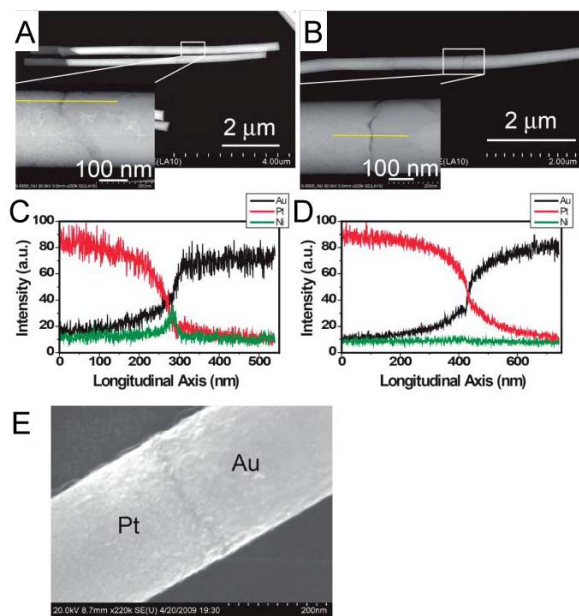
The two terminal *I-V* characteristics of the 3 nm gap devices were measured at room temperature (in the absence of light) before and after molecular assembly. The empty nanogap exhibits no conductance within the noise limit of the measurement (<2 pA). However, the nanogap devices loaded with OPE show a significant *I-V* response with rectifying behavior (black curve, Figure 9b), suggesting the assembly of the molecules across the gap with chemical connectivity to each of the metal electrodes on opposite sides of the gap. Importantly, only rods treated with the molecules have Raman spectra consistent with the OPE structure, and only these rods exhibit a rectification response. The rectifying behavior is likely a result of the different modes of contact between the ends of the molecules and the different electrode materials that span the heterometallic nanogap. One end of the molecule forms an Au-S connection while the other end forms a Pt-S connection (Figure 8c). These two different metal-molecule contacts induce different electronic coupling at the interface, different injection barriers, and unequal voltage drops. Furthermore, we deduce that hole transport from Au to Pt is enhanced leading to larger currents in the positive voltage regime than in negative bias where holes go from Pt to Au, and 30% of the OPE devices exhibited this rectification behavior. The remainder yielded no current above the noise limit of the measurement (2 pA). Indeed, they exhibited current-voltage characteristics similar to the empty nanogap structures (indicating some failure in the construction of the junction). Nevertheless, this success rate is significantly higher than that reported for other approaches.

To analyze the asymmetric MTJ, we presented a simple model based on the nonequilibrium Green's function technique. We consider the single-level system in Figure 9, whose Green's function is given by

Figure 8. SEM image of multisegmented nanowires before (A) and after (B) OWL. EDS line scan of a multisegmented nanowire before (C) and after (D) OWL. (E) SEM image of Au_Pt heterometallic nanogap with smooth rod ends.

$$Gr(E))[E-\varepsilon 0 +i(\Gamma L +\Gamma R)]^{-1} \qquad (1)$$

where ε_0 is the single-level energy, and $\Gamma L,R$ are the couplings of the molecule to the left/right electrodes. In the Landauer limit of elastic tunneling, the current (I) can be written as a function of the applied voltage (V)

$$I(V) = 2e/h \int_{-\infty}^{\infty} dE/2\pi \ [f_L(E, V) - f_R(E, V)] \ |G^r(E)|^2 \ \Gamma_L\Gamma_R \qquad (2)$$

where the Fermi functions are given by $f_k = [1 + e^{(E-\eta kV)/k_BT}]^{-1}$. The η parameters describe the voltage drop across each interface, and we make the usual assumption that these are proportional to the couplings: $\eta L = \Gamma_R/(\Gamma_L + \Gamma_R)$ and $\eta R = -\Gamma_L/(\Gamma_L + \Gamma_R)$. Thus, rectification originates from the asymmetric voltage drop across the interface due to different molecule-electrode couplings (see Figure 9 D). We use eq 2 to fit to the experimental measurement and obtain $\Gamma_{Au} = 23$ meV, $\Gamma_{Pt} = 9.4$ meV, and $\varepsilon_0 = 0.56$ meV. Thus, we find that the Au-OPE coupling is roughly 2.5 times stronger than that of Pt-OPE, leading to the observed rectification.
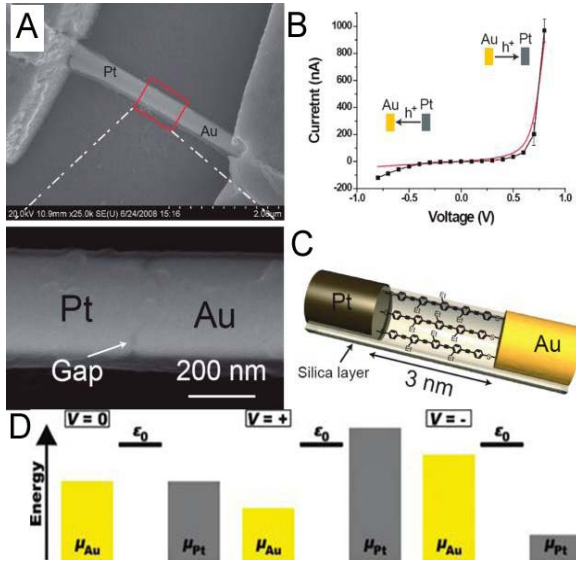
Figure 9. (A) SEM image of an OWL-fabricated device with a 3 nm Au_Pt heterometallic nanogap. (B) Representative *I-V* response for a 3 nm OWL-fabricated heterometallic nanogap device modified with OPE. Theoretical fitted *I-V* curve (red curve). (C) A sketch of the device depicting the OPE molecules spanning the 3 nm gap. (D) The single-level model used for theoretical fitting is shown. At zero bias, the chemical potentials in both electrodes are nearly equal. When voltage is applied, however, the gold level will be more strongly pinned due to the larger Au-molecule coupling. This leads to resonant transport and higher current for positive voltage (increasing Pt chemical potential) and nonresonant transport and lower current for negative voltage (increasing Au chemical potential).

We anticipate that this new method of fabricating and characterizing MTJs based on heterometallic nanogaps will be used to create a wide variety of nanoelectronic devices with diverse functions and applications that derive from the types of metals used to make the electrodes and the molecules assembled within them. Indeed, this initial work points toward the intriguing possibility of forming a bi-functional molecule capable of not only forming a MTJ within such heterometallic gap structures but also self-organizing and orienting within such structures based upon functional groups that direct the molecule ends to the corresponding electrode materials.

In-Wire Conversion of a Metal nanorod Segment into an Organic Semiconductor

In addition to molecular junctions, organic semiconductor materials have recently attracted significant interest for their potential application in the context of functional nanoscale electronic devices owing to their many unique properties such as structural and compositional diversity and physical flexibility. We have developed a new approach for creating nanowires with organic semiconductor nanojunctions, relying on the selective conversion of a single component metal segment within a multi-component nanowire using a simple chemical vapor deposition (CVD) process.[9]

As a proof-of-concept, we selected 7,7,8,8-tetracyanoquinodimethane (TCNQ) as a model system since organic charge-transfer complexes of MTCNQ (M = Ag, Cu, other metals) have been evaluated as new forms of electrical recording media. They can be reversibly switched between two stable states, which differ substantially in conductivity. We demonstrated that the resulting metal/AgTCNQ/metal nanojunctions show semiconducting behavior and can function potentially as memory devices.
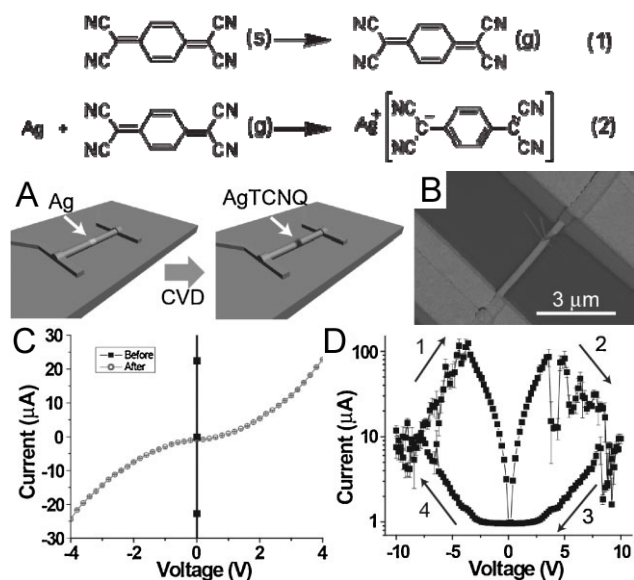

Figure 10. a) The in-wire-conversion device-fabrication method. b) SEM of Au–Ag–Au nanowire device after in-wire conversion. c) I–V response of a nanowire device before (black line) and after (grey curve) the TCNQ reaction. d) I–V characteristics of Au/AgTCNQ/Au devices showing reversible bistable switching behavior. The arrows indicate the voltage sweep directions.

In a typical experiment, 9.2-mm-long, multisegmented Au–Ag–Au nanowires (diameter 360 nm) were synthesized by sequential electrochemical deposition of gold (5 mm), silver (0.2 mm), and gold (4 mm) into AAO templates. Scanning electron microscopy (SEM) revealed that a 200-nm Ag segment is sandwiched between two Au segments. Chemical composition mapping experiments (energy-dispersive X-ray spectroscopy, EDS) confirmed the elemental identity of each segment. Ag is an excellent candidate for the metal segment precursor since, under conventional CVD conditions, TCNQ vapor will react with it at a relatively low temperature (160 ºC) to form AgTCNQ. An Au-Ag-Au segmented rod was exposed to TCNQ vapor for 2 h, during which the Ag segment was converted into needles of AgTCNQ, some of which bridged the two Au segments (Figure 10C). As expected, the volume of the resulting AgTCNQ product is substantially greater than that of the starting Ag segment; indeed each Ag^+ ion is paired with a molecule of reduced TCNQ. The needles were characterized by Raman spectroscopy, which exhibit four characteristic principal vibrational modes that are highly diagnostic of AgTCNQ, 1208 cm^{-1} (C=CH bending), 1455 cm^{-1} (C-CN wing stretching), 1603 cm (C=C ring stretching), and 2227 cm^{-1} (C≡N stretching).

To confirm further the incorporation of TCNQ into the multisegmented nanowires and to characterize the electrical properties of Au/AgTCNQ/Au junctions, devices composed of Au/Ag/Au nanowires were fabricated for electrical measurement. First, the multisegmented nanowires were cast onto a substrate and connected to microelectrodes by electron-beam lithography. The entire substrate was then placed into a vessel for reaction with TCNQ by CVD for 2 h (Figure 10A). The current was measured and plotted as a function of voltage (I–V) before and after the reaction. In a typical experiment (Figure 10B–D), prior to the in-wire growth of AgTCNQ, the resistance of the device was low (black line in Figure 10 C), which reflects the metallic nature of the Ag segment. After the reaction of the Ag with TCNQ vapor, the Ag segment was converted into AgTCNQ and electrical measurements on devices constructed from a single Au/AgTCNQ/Au rod exhibit a nonlinear I–V curve at low applied bias (<5 V) (Figure 10C), which is typical for organic semiconductor materials. This result also provides a clear indication of the conversion of the Ag segment flanked by two gold segments into AgTCNQ, through which the current transport occurs. Moreover, the I–V curves for the forward bias and

$$[Ag^+TCNQ^-]_n \underset{\text{High−impedance}}{\overset{\text{Voltage}}{\rightleftharpoons}} Ag_x + TCNQ_x + \underset{\text{Low−impedance}}{[Ag^+TCNQ^-]_{n-x}} \qquad (3)$$

reverse bias are symmetrical at low bias. Of 41 devices tested, 19 show similar semiconductive I–V responses. When a higher bias voltage (10 V) with a full cyclic sweep (-10 → 0 → 10 → 0 → -10 V) is applied to prototype devices, reversible hysteretic switching behavior is observed (Figure 10 d). As the voltage bias is swept from -10 to 10 V, the device exhibits low impedance, but when the voltage bias is swept from 10 to -10V, it exhibits high impedance. Indeed, the resistance changes by more than two orders of magnitude during the voltage sweep. The threshold voltage of the device is approximately ±5 V, at which point there is a sudden transition in current flow. One possible reason for the electrical switching is an electric field-induced reversible redox reaction at the interface, which generates neutral TCNQ and Ag species from the high-impedance AgTCNQ salt (Equation 3). This cyclical response has been observed for macroscale AgTCNQ devices, which provides further evidence for the chemical transformation in the segmented wire structure. In contrast to conventional methods for the synthesis of sandwich geometries, our method produces a gap-junction arrangement that does not require further processing of the organic layer after vapor-phase deposition of the molecular material.

Alignment Strategies for the Assembly of Nanowires with Submicron Diameters. OWL is an extremely high throughput technique, and in a typical process, billions of gapped nanostructures are synthesized. The bottleneck for device fabrication is then connecting the rods to macroscopically addressable electrodes necessary for electrical characterization. To fully take advantage of these novel nanowire structures, especially for the construction of parallel electronic devices, methods must be developed for assembling and integrating rods into addressable electronic architectures.

For ease of synthesis and mechanical stability, OWL nanowires are typically synthesized with diameters 360 nm. However, these relatively large structures are difficult to assemble and align due to the large inertial force acting upon them. Indeed, non-covalent chemical interaction approaches, which are often used for the assembly of smaller nanomaterials, provide insufficient forces to induce the alignment of heavy, large diameter nanowires from aqueous suspensions on solid substrates. To address this, we have developed two complementary methods that are simple and effective for the alignment of both individual and multiple nanowires over large areas.[10] In all experiments, Au nanowires (360 nm diameter, 5 µm long) were assembled using either capillary or mechanical forces.
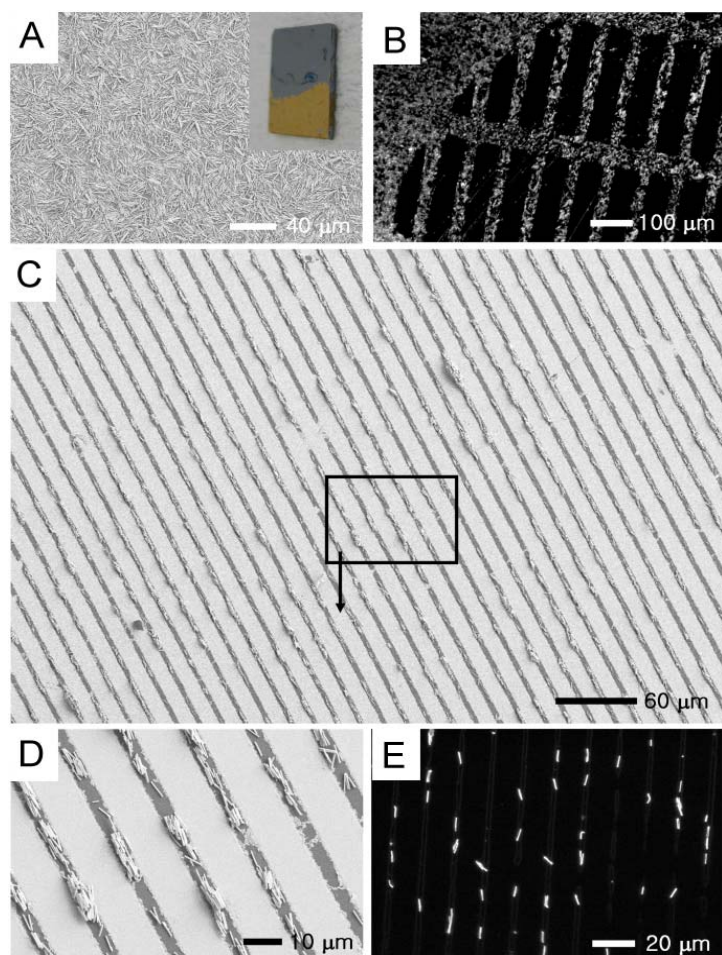
Figure 11. (A) SEM image and the photograph (inset) of Au nanorods films coated on unpatterned hydrophilic silica surfaces. (B) Dark field optical micrograph and the photograph (inset) of Au nanorods selectively assembled on the outside of hydrophobic squares (300 × 60 μm) and hydrophilic squares (300 × 300 μm). Au nanorods are aligned on the hydrophilic line stripes with 5 μm (C and D) and 1 μm (E) in width, respectively.

Existing processes for aligning nanomaterials using capillary forces typically utilize an aqueous suspension of nanomaterials, where the substrate is withdrawn through the air-water interface. For large 360 nm diameter nanowires, the resulting capillary force easily pulls them to the water phase and consequently it is necessary to decrease this capillary force to maintain nanowire-substrate contact. In the standard approximation model, the capillary force is proportional to the interfacial tension. The interfacial tension of the water-air interface is 73 mNm^{-1}, while those of the water-chloroform and chloroform-air interfaces are 28 and 27 mNm^{-1}, respectively. These observations suggests a method to efficiently and selectively assemble large diameter nanowires on a hydrophilic surface by employing the water-chloroform interface as a transfer medium with subsequent removal of the substrate through the chloroform-air interface.

Both hydrophilic silica and patterned surfaces consisting of alternating regions of hydrophilic silica and hydrophobic areas were used to examine the feasibility of this proposed strategy for assembling large-diameter Au nanowires. Here, the hydrophobic regions consist of 1-octadececanethiol self-assembled monolayer on gold. As evident from Figure 11, Au nanowires were selectively assembled at high density on the hydrophilic areas from the water-chloroform interface according to the methodology outlined above. Directional alignment was examined by assembling nanowires on patterning surfaces with alternating hydrophilic and hydrophobic lines. When the width of the hydrophilic line is comparable to or shorter than the length of the nanowire, the long axis of each nanowire is oriented along and within the line. The wires assembled over approximately 50% of the area defined by the hydrophilic lines. These aligned bundles of nanowires may be of interest to researchers to construct low-cost macroscopic devices such as nanowire network transistors.
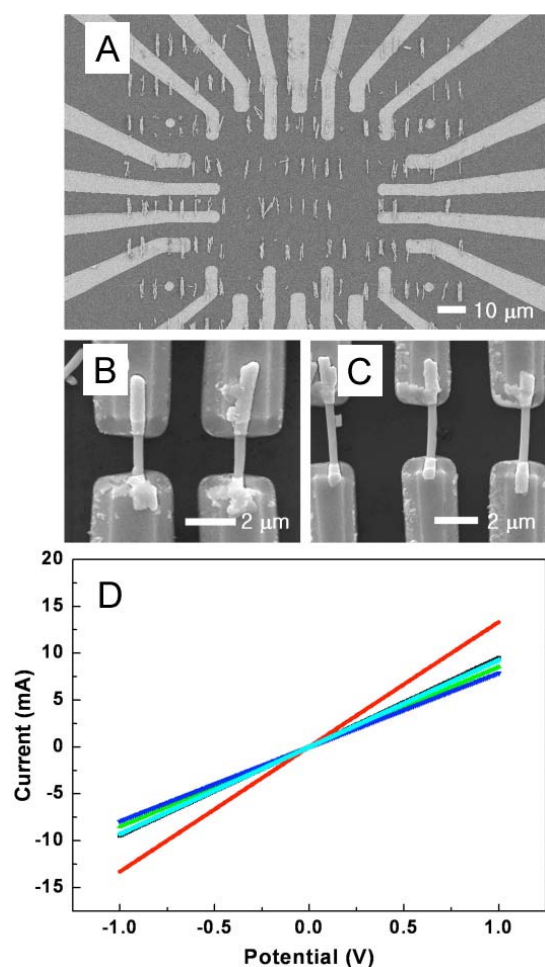
Figure 12. (a) Aligned Au nanorods on microelectrodes pattern using brushing method. SEM images of individually connected (b) two or (c) three Au nanorods and (d) their current-voltage characteristics.

To fabricate parallel MTJs, it is necessary for a single nanowire to be individually aligned at a desired position. Here, trenches were first defined in PMMA by e-beam lithography. Au nanowires were then dropcast on the substrate, and physically brushed across the trenches with pressures on the order of a few MPa, resulting in their eventual integration and alignment within each trench. Au nanowires remaining outside the trenches are subsequently removed with the e-beam resist in a lift-off process. SEM imaging confirmed the alignment of individual wires or collections of nanowires in registry with the e-beam defined lithographic patterns. Approximately 70 % of the trenches were filled, will 25% consisting of single nanowires. The individually aligned nanowires were subsequently electrically connected to microelectronic chips by e-beam lithography and electrical properties displayed the expected ohmic response with average resistivity of 6.3×10^{-4} Ωcm (Figure 12). This technique can likely be improved by automation and tighter control over the deposition conditions.

The methods outlined here are simple and effective for the alignment of large diameter nanowires over multiple length scales. These advances will enable researchers to more fully take advantage of template-grown, multisegmented and OWL-generated nanostructures for nanowire-based electronic applications.

References Cited

1. Braunschweig, A. B.; Huo, F.; Mirkin, C. A. *Nat. Chem.* **2009**, *1*, 353.
2. Huo, F.; Zheng, Z.; Zheng, G.; Giam, L. R.; Zhang, H.; Mirkin, C. A. *Science* **2008**, *321*, 1658.
3. Qin, L.; Park, S.; Huang, L.; Mirkin, C. A. *Science* **2005**, *309*, 113.
4. Giam, L. R.; Wang, Y.; Mirkin, C. A. *J. Phys. Chem. A* **2009**, *113*, 3779.
5. Braunschweig, A. B.; Senesi, A. J.; Mirkin, C. A. *J. Am. Chem. Soc.* **2009**, *131*, 922.
6. Huang, L.; Braunschweig, A. B.; Shim, W.; Qin, L.; Lim, J. K.; Hurst, S. J.; Huo, F.; Xue, C.; Jang, J.-W.; Mirkin, C. A. *Small* **2010**, *6*, 1077-1081.
7. Pedano, M. L.; Li, S.; Schatz, G. C.; Mirkin, C. A. *Angew. Chem. Int. Ed.* **2010**, *49*, 78.
8. Chen, X.; Yeganeh, S.; Qin, L.; Li, S.; Xue, C.; Braunschweig, A. B.; Schatz, G. C.; Ratner, M. A.; Mirkin, C. A. *Nano Lett.* **2009**, *9*, 3974.
9. Chen, X.; Zheng, G.; Cutler, J. I.; Jang, J.-W.; Mirkin, C. A. *Small* **2009**, *5*, 1527.
10. Lim, J. K.; Lee, B. Y.; Pedano, M. L.; Senesi, A. J.; Jang, J.-W.; Shim, W.; Hong, S.; Mirkin, C. A. *Small* **2010**, submitted.

Chapter 2

The Final Report

Title: 1-D semimetal-semiconductor homo-junction nanowires for uncooled IR detection

Principal Investigator (Korea):
Hyunjung Shin, Ph.D., Associate Professor, Kookmin University

> Telephone: +82-2-910-4897
> Facsimile: +82-2-910-4320
> E-mail: hjshin@kookmin.ac.kr

Principal Investigator (US):
Jimmy Xu, Ph.D., Professor, Brown University

> Telephone: +1-401-863-1439
> E-mail: Jimmy_Xu@brown.edu

NBIT Program 2010
Final Report

Project Title

1-D semimetal-semiconductor homo-junction nanowires for uncooled IR detection

2010-10-20

Korean Principal Investigator (KPI)		US Principal Investigator (USPI)	
Full Name	Hyunjung Shin	Full Name	Jimmy Xu
Affiliation (department)	Kookmin University (School of Advanced Materials Engineering)	Affiliation (department)	Brown University (Division of Engineering and Department of Physics)
Position	Associate Professor	Position	Charles C. Tillinghast University Professor of Engineering and Physics
Telephone	+82-2-910-4897	Telephone	+1-401-863-1439
Fax	+82-2-910-4320	Fax	+1-401-863-1439
E-mail	hjshin@kookmin.ac.kr	E-mail	Jimmy_Xu@brown.edu

Report Contents

I. Purpose of the project

The purpose of this project was to (1) develop a new class of nano-electronic 1-D structures made of a unique material system, bismuth, that can be tuned from metallic to semiconducting by controlled variation of its physical dimensions in the nano regime, (2) demonstrate the feasibility of forming a unique homo-junction between two bandgaps within the same Bi nanowire by controlled change of the wire diameter along the length, and in the optional 3rd year (3) begin the exploration of potential device applications such as un-cooled IR detection that is relevant to the AFOSR mission and nano-electronic cooling embeddable in the under-layer or over-layer of integrated circuits that are of great interest to the electronic industry in Korea and USA.

The work completed within the two-year period met the object and included both synthesis and characterization of Bismuth and Bi-alloy nanowires with a built-in homojunction and unprecedented uniformity in diameter, length, and spacing.

Fabrication Technology:

- Synthesis of self-organized AAO (Anodic aluminum oxide) templates with controlled diameter variation along the length
- Fabrication of Bi homojunction nanowires by electrochemical deposition and/or liquid phase high pressure injection into the nanopore array templates
- Fabrication of Bi-ally nanostructures

Characterization & Device Technology:

- Optical characterization of fabricated Bi nanowires to evaluate expected semi-metal to semiconductor transition with reduced diameters
- Fabrication of test devices out of Bi and Bi-alloy nanowires for the characterization of electrical and photonic properties
- Assembly of the individual Bi nanowires into test devices

Because of the project started in year 2 of the NBIT Phase I program, it only had two years, instead of three to conduct the planned three-year experiments.   But it met and exceeded the proposed goals as detailed below.

II. Progress (1): Bismuth nanowires
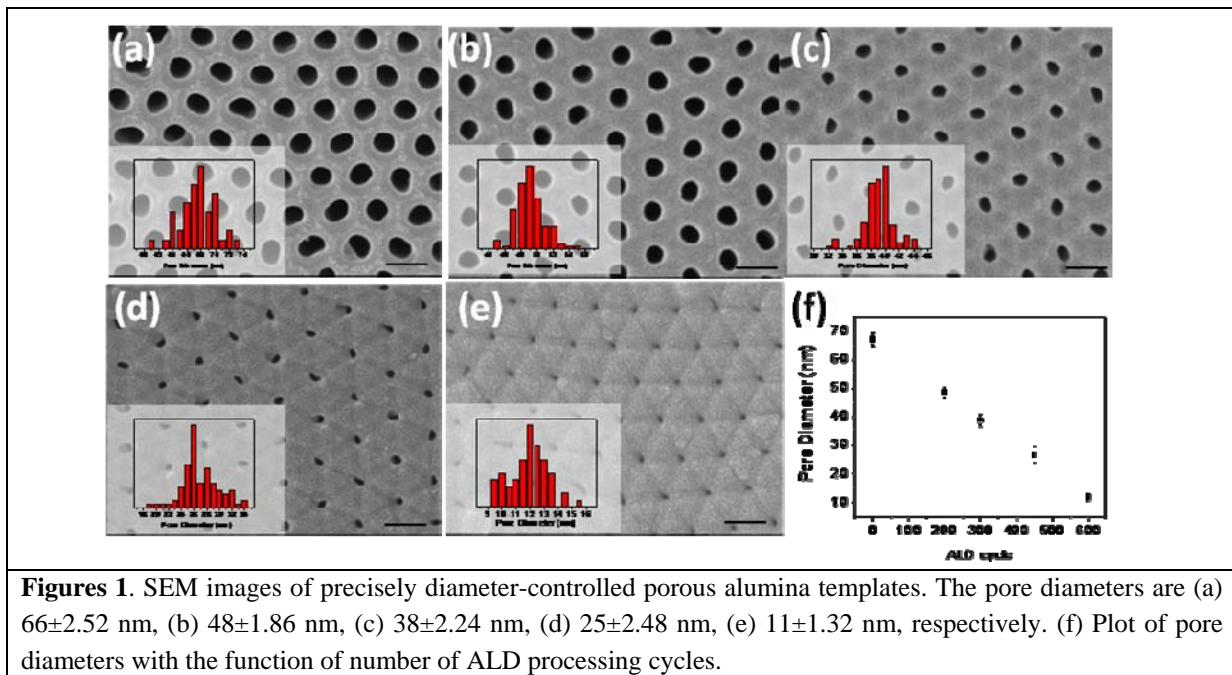
1. Introduction

Electronic transport properties of 1–D nanostructures, for example, carbon nanotubes and numerous metallic and semiconducting nanowires and tubes, are both interesting and proven useful to the creation of properties that are unavailable in bulk materials. Bismuth (Bi), in particular, is a truly interesting class of materials. Like carbon, bismuth is a most versatile elemental material in the periodic table. At low temperature, it is a superconductor (below 7 K) and at room temperature, it is a semimetal. In a most recent study of nano-patterned bismuth [1], we found that it could undergo an abrupt transition from superconducting to insulating upon imposing a nanoscale pattern in a bismuth

film. This finding of a new state, referred to in the science media as "superconducting Cooper Pairs found in insulator," was both scientifically significant and practically useful as, for example, it renders itself to such applications as high-speed single-photon detection.

At room temperature, Bismuth is a semimetal with a small band overlap (38 meV at 0 K) and has a large Fermi wavelength, a small effective electron mass (~0.001 m_e), a long carrier mean free path (~100 nm at 300 K), a low carrier concentration, and a high carrier mobility [2, 3]. Because of these unique properties of Bi, a semimetal-to-semiconductor transition and a high thermoelectric power are expected to emerge from Bi nanowires with diameters below ~ 50 nm [2, 4, 5]. By deploying the templated heterojunction growth technique first demonstrated by the Brown group, one could in principle make a semimetal (diameter > 60nm) – semiconductor (diameter < 50nm) homojunction nanowire. In this project, we studied the potential of dimensionality-induced new and/or improved properties of the Bi system, with an eye on future device applications, in particular, uncooled IR and thermoelectricity.
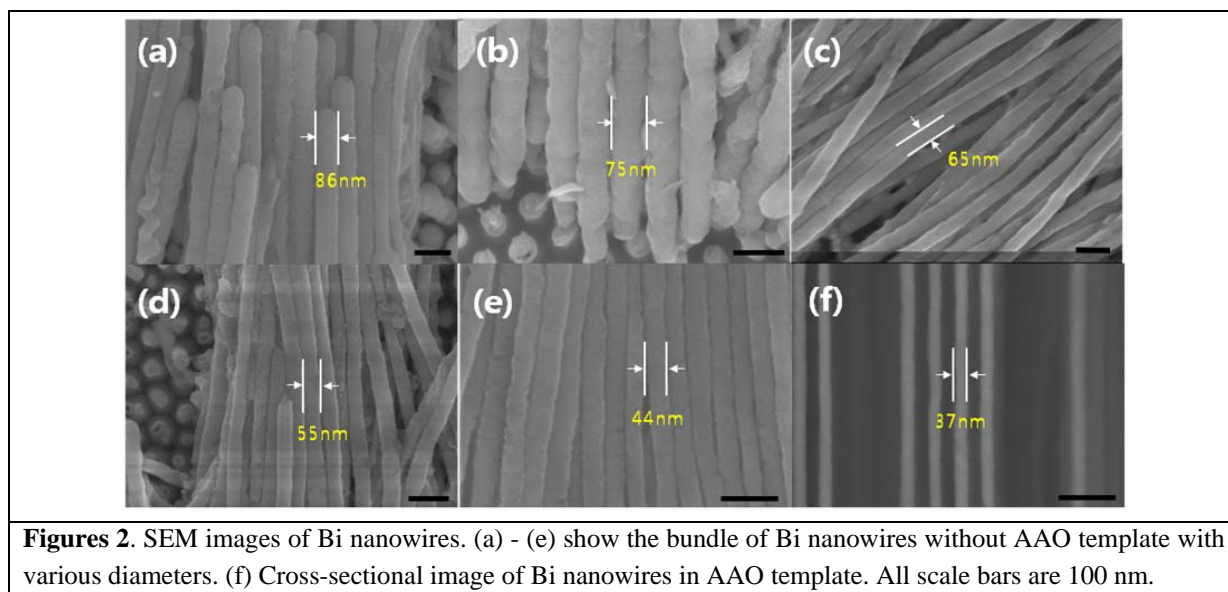
2. Synthesis of AAO templates with controlled diameter

We have fabricated bismuth nanowires arrayed in anodized aluminum oxide (AAO) templates and the diameter is precisely controlled by using atomic layer deposition (ALD) process. The AAO templates were fabricated by a well-known 2-step anodization method. The diameter of pores in AAO templates with a typical anodization process in our lab is around 70 nm. Pore diameter of the AAO templates was precisely reduced by conformal coating a thin oxide layer inside pores using ALD technique. The resulting pores with inner pore diameters and standard deviations in AAO templates are (a) 66±2.52 nm, (b) 48±1.86 nm, (c) 38±2.24 nm, (d) 25±2.48 nm, and (e) 11±1.32 nm as shown in Figure 1. The pores are well ordered with a hexagonal arrangement and its standard deviations are less than ~ 10% of their diameters. These pores are used to prepare electrochemically deposited and diameter controlled Bi nanowires. Such an idea has been validated previously in fabricating oxide nanotube with ultra-precise wall thickness and high aspect ratio (over 1:1,000) by our research group.

Figures 1. SEM images of precisely diameter-controlled porous alumina templates. The pore diameters are (a) 66±2.52 nm, (b) 48±1.86 nm, (c) 38±2.24 nm, (d) 25±2.48 nm, (e) 11±1.32 nm, respectively. (f) Plot of pore diameters with the function of number of ALD processing cycles.

3. Fabrication of Bi homojunction nanowires by electrochemical deposition

A layer of platinum (Pt) with the thickness of 200 nm which will serve as electrodes during electrochemical deposition was sputtered onto the one face of the ALD-coated AAO templates. After deposit of the Pt electrodes, the AAO templates were attached to silicon wafer as a supporter. Removing the block of Al metal in super-saturated $HgCl_2$ (Aldrich) solutions makes the AAO templates as the form of membranes. Additional etching treatment was also carried out with 1 M NaOH solutions at 30 ºC for 2 min to remove the barrier layer on the bottom side of the AAO membranes. Surface treatment on the inner pores of the membranes is of importance to make them hydrophilic. Bi nanowires were deposited in a two electrode plating cell from a hydrochloric acid solution containing 10 g/l $BiCl_3$, 50 g/l tartaric acid, 95 g/l glycerol and 50 g/l NaCl at room temperature. The pH value of the electrolyte was adjusted to 1.0 by adding appropriate amounts of 5 M aqueous ammonia. The DC deposition was carried out at different potentials (0.9 ~ 1.3 V). After electrochemical deposition of bismuth, AAO template would be removed by chemical etching. The AAO template was dissolved in 1 M NaOH aqueous solutions without disruption of Bi nanowires. Figure 2 (a)-(e) show fabricated Bi nanowires after template removing.
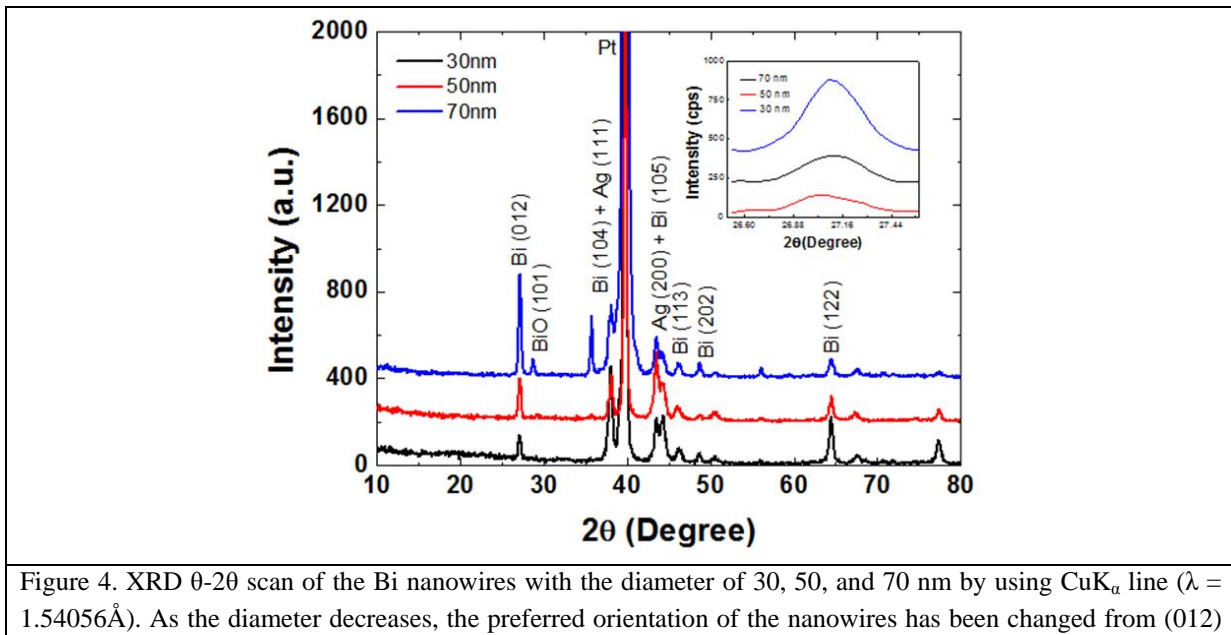

Figures 2. SEM images of Bi nanowires. (a) - (e) show the bundle of Bi nanowires without AAO template with various diameters. (f) Cross-sectional image of Bi nanowires in AAO template. All scale bars are 100 nm.

It has been experimentally established that Bismuth is a semimetal in its bulk phase (d > 60nm) and a semiconductor in its confined state (d < 50nm) [6]. This conduction mechanism change with reduced dimensionality is accompanied by yet another drastic change - the change of bandgap and density of states with diameter. This change of bandgap with diameter would produce a homo-junction in a diameter-modulated Bi nanowire and a change in the Seebeck coefficient across the junction. As a result, we could create a powerful new platform for uncooled IR sensing, leveraging on the already very large and well known thermoelectric power of Bi-based systems. Step-shaped Bi nanowires were synthesized by electrochemical deposition using AAO template with 'Y-shaped' pores. The diameter modulated 'Y-shape' pore structure was prepared through a method demonstrated by Lee et al [7]. Figure 3(a) shows the cross-sectional FESEM image of the AAO template with 'Y-shaped' pores. The corresponding step-nanowires inside the AAO template are shown in Figure 3(b). Figure 3(c) shows

clearly the shape of the step-nanowires after AAO etching. The nanowires are looked like a high neck bottle. The diameter in the broad region ~70 nm and the diameter in the neck zone is ~35 nm. The material properties of the diameter modulated Bi nanowires will be discussed in the section II-4.
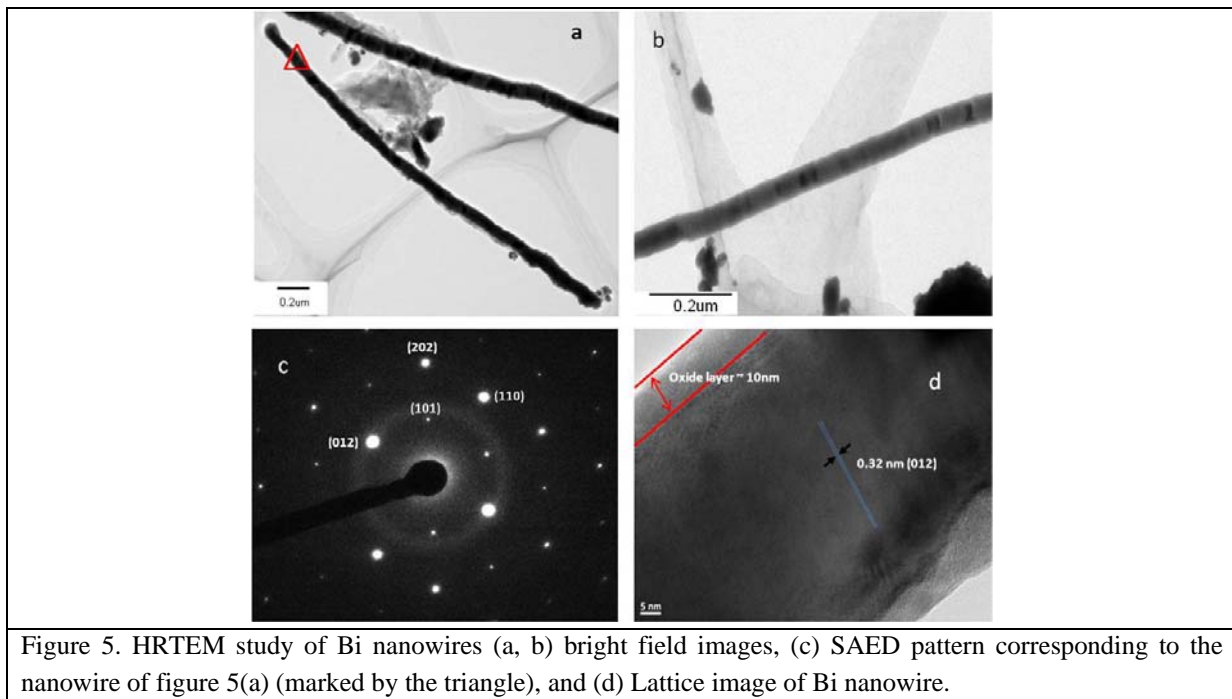

Figures 3. (a) Cross sectional FESEM image of the 'Y-shaped' AAO template (b) Cross sectional FESEM image of the step-shaped Bi nanowires inside AAO template (c) step-shaped Bi nanowires after AAO etching.
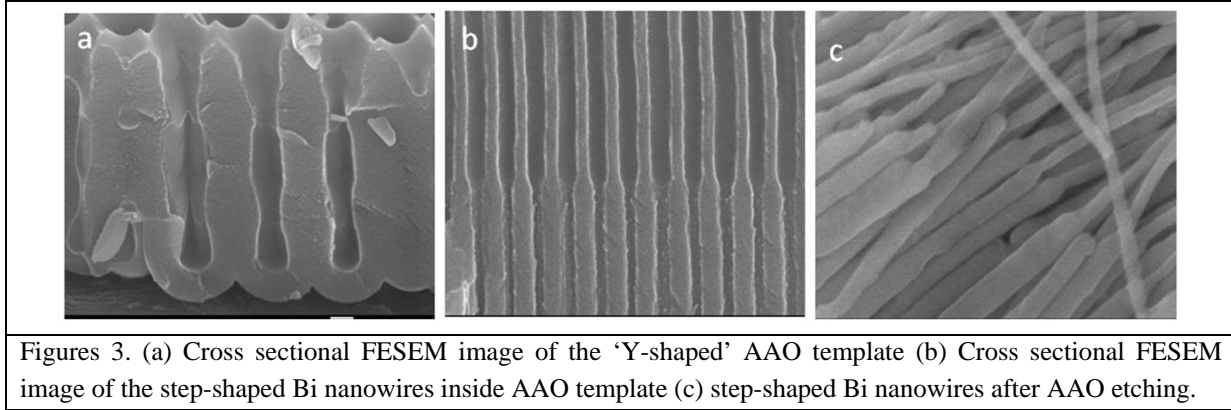
4. Material characterization of Bi nanowires

X-ray diffraction (XRD) was employed for the material phase identification and the structural analysis of the nanowires. XRD patterns of Figure 4 can be indexed to the rhombohedral structure of Bi with cell parameter of a = 4.5470Å, and c = 11.86Å (JCPDS card no. 44-1246). The sharp and intense diffraction peaks indicate that the nanowires are good crystalline. The intense peak appears ~39° is related to Pt which comes from the sputtered electrode. The appearance of the Ag peak in the diffraction pattern is mainly due to the use of silver paste during mounting of AAO with the Si substrate. The (104) peak is mostly intense in the diffraction pattern and the peak intensity increases with increase in the diameter of the nanowires (inset of Figure 4). The full width at half maxima (FWHM) of the (104) peak was also found to increase with decrease in wire diameter [8, 9]. An additional weak diffraction peak is found ~28° which is related to the cubic bismuth oxide phase (JCPDS card No.27-0054).

Figure 4. XRD θ-2θ scan of the Bi nanowires with the diameter of 30, 50, and 70 nm by using CuK$_\alpha$ line (λ = 1.54056Å). As the diameter decreases, the preferred orientation of the nanowires has been changed from (012)

to (104). Inset shows the magnified plot of (012) peak.

The Bi nanowires after AAO etching were characterized by HRTEM for further morphological and structural analysis. The bright field HRTEM images of the Bi nanowires are shown in Figure 5(a) and 5(b). The TEM study further reveals that nanowires have almost uniform diameter and they are ~10 µm long. Some planer defects were appeared in the bright field TEM image by the dark spots perpendicular to the nanowire axis. The selected area electron diffraction (SAED) pattern [Figure 5(c)] indicates that the nanowires are single crystalline rhombohedral Bi which is also consistent with the XRD pattern. The high resolution TEM image of the nanowires is shown in Figure 5(d). The inter-planar spacing (*d*) measured from the lattice fringe is ~0.32Å which is corresponding to the (012) planes. Therefore, the nanowires are preferentially directed along (012). Additionally, HRTEM image proves the presence of a thin (thickness ~10 nm) crystalline bismuth oxide (BiO) layer as a sheath of the nanowire. The presence of the crystalline (cubic) bismuth oxide phase together with Bi was also found in XRD pattern. The presence of the BiO phase indicates the oxidation of the nanowires. Bismuth oxidizes spontaneously even at room temperature in the presence of oxygen and form stable oxides. This BiO remaining at the wall, form a Bi/BiO core-shell nanowire structure which is confirmed by Figure 5(d).

Figure 5. HRTEM study of Bi nanowires (a, b) bright field images, (c) SAED pattern corresponding to the nanowire of figure 5(a) (marked by the triangle), and (d) Lattice image of Bi nanowire.

The XRD pattern of the step-nanowires is similar to the XRD pattern of the uniform nanowires [Figure 5]. The bright field HRTEM image of the step-nanowire is shown in Figure 6(a). The image reveals the diameter of the step-nanowires 70 nm in the broad region and 35 nm in the necking zone which is consistent with the FESEM study. The SAED patterns corresponding to both in the broad and neck zone [Figure 6(b) and 6(c), respectively] of the step-nanowire show similar spot pattern which are related to single crystalline rhombohedral Bi. The magnified bright field image and corresponding SAED pattern of the neck region is shown in Figure 6(d). There was no discontinuity or interface at the neck region of the step-nanowire and the SAED pattern is also similar to Figure 6(b) and 6(c). Therefore, the step-nanowires are also single crystalline like uniform nanowires. The diameter

reduction in neck region occurs merely due to the 'Y-shaped' pores in AAO template. The magnified TEM image of Figure 6(d) shows the presence of oxide sheath layer ~10 nm thick in the step-nanowires.
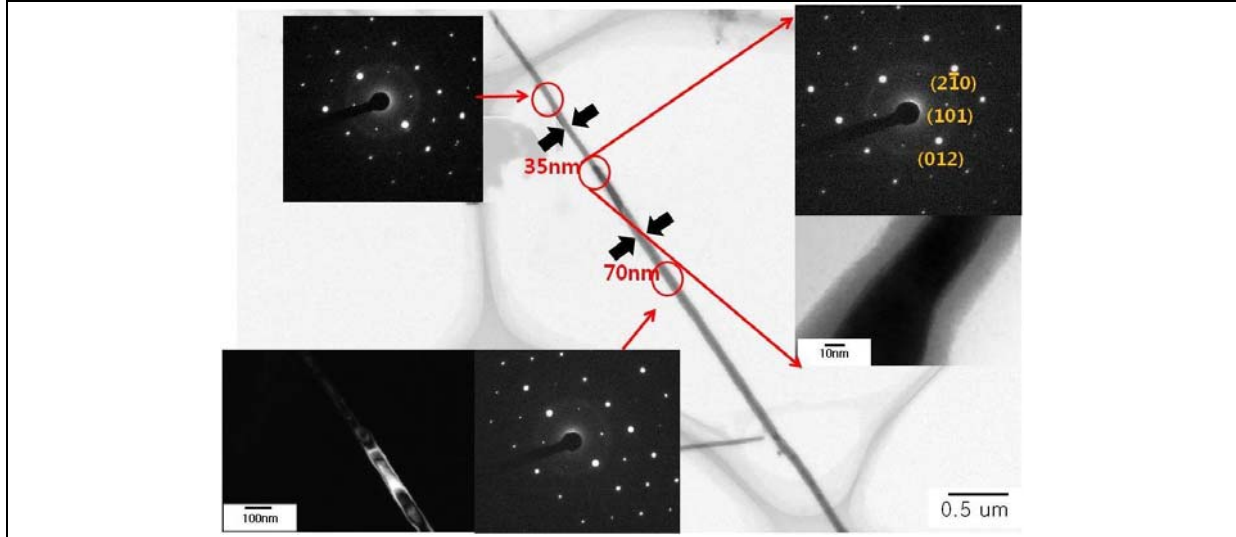

Figure 6. HRTEM study of step-shaped Bi nanowires (a) bright field images (b) SAED pattern corresponding to the neck region (c) SAED pattern corresponding to the broad region (d) SAED pattern corresponding to the step zone and magnified bright field image of the step zone.

5. Optical characterization of bismuth nanowires

To determine whether the fabricated nanowires do possess the expected size-dependent semimetal to semiconductor transition, we measured IR abortion and reflection spectra for Bi nanowire array with various diameters. The measured nanowire arrays were embedded in the AAO growth templates. FTIR was used to obtain the absorption spectra in mid-IR range (i.e., 1.25 ~ 20 μm). The dimensions of the measured samples are summarized in the table I. As a control, sample 5 was prepared to measure IR absorption by pure AAO.

TABLE 1. Dimensions of Bi nanowires in AAO pores.

Sample number	Bi nanowire diameter (nm)	AAO template height (μm)	Bi nanowire height (μm)
3	38	9.6	6
4	50	9.8	7
5	-	9.8	-
8	67	12	5

Since the Bi/AAO structures are fabricated on 200 nm-thick Pt layer and IR source cannot transmit through the substrate, reflection spectra instead were measured for investigating IR absorption. Reflectance was calibrated by reflected mid-IR intensity from an Al mirror. We have checked that the bottom Pt electrode of Bi/AAO structure can be assumed as an ideal mirror by measuring reflected signals from an AAO template with the same metal film on top.

Figure 7 shows the measured reflection spectra for the Bi/AAO samples. All measured spectra are normalized by Al mirror reference spectrum (i). Flat reflectance of backside electrode implies a

negligible effect of the bottom electrode and the substrate on IR absorption (ii). Periodic oscillation in the measured reflectance is indicative of interference within an unfilled portion of the transparent AAO template (AAO film effect) (iii). With sample 5 (iv), we obtained larger reflectance compared with (v), (vi) and (vii), which suggests IR absorption by Bi nanowires. Transition from high absorption to low absorption with decreasing diameter (v) indicates that the thinner (38 nm – diameter) Bi nanowires have turned into semiconducting and acquired a band gap. Plot vii shows high absorption over the MIR range, which indicates metallic Bi nanowire array is a good IR absorber. Decreased reflectance over 500 ~ 1800 cm^{-1} indicates lights with a wavelength of 5 ~ 20 μm are significantly absorbed by AAO (viii).

Figure 7. Reflectance spectrum of Bi nanowire arrays in AAO templates measured by FTIR spectroscopy. (i) Al mirror reference spectrum, (ii) reflectance from AAO template with backside metal on top: negligible effect of bottom electrode and substrate on IR absorption, (iii) periodicity in reflectance: interference in reflected signal (AAO film effect), (iv) AAO only: larger reflectance compared with Bi samples, (v) Bi nanowires in AAO (diameter: 50 nm), (vi) Bi nanowires in AAO (diameter: 38 nm), (vii) Bi nanowires in AAO (diameter: 67 nm), and (viii) IR spectra over 500 ~ 1800 cm^{-1}: significant absorption by AAO.

6. Summary

Bismuth nanowires with controlled diameters have been synthesized successfully by electrochemical deposition using AAO templates. The nanowires are single crystalline and are preferentially oriented along (012). The nanowires with diameters ~50 and ~38 nm are semiconducting and the nanowires having diameter ~65 nm is metallic. Step shaped Bi nanowires were also grown successfully by using AAO template with 'Y-shaped' pores. The step-size Bi nanowires can be predicted to form a metal-semiconductor self homojunction.

III. Progress (2): Bismuth sulfide nanowires

1. Introduction

The additional advances came somewhat unexpected in an experimental exploration of a new synthesis pathway for bismuth-based nanostructures. They opened up a new space in which bismuth

sulfide (Bi_2S_3) nanostructures of high uniformity and crystallinity can be made available for a variety of device applications and basic research.

Bismuth sulfide is a semiconducting material, has a direct band gap of 1.3 eV [10] and has been used in photodiode arrays or photovoltaic devices [11, 12]. It also belongs to a family of solid-state materials with applications in thermoelectric technologies based on the Peltier (cooling) effect [13] since bismuth-based materials exhibit good thermoelectric power. Like other materials, bismuth sulfides have been fabricated into 1D nanostructures in recent years. There have been several reports on the synthesis of one-dimensional nanostructured Bi_2S_3, including single-source precursor approach [12], hydrothermal/solvothermal process [14, 15], and chemical vapor deposition method [16].

Differing from these prior works, we have successfully synthesized Bi_2S_3 nanostructures with high uniformity of diameter and length using a solvothermal process. We found that their shapes can be effectively controlled by changing sulfur sources, instead of varying temperature and concentration that are more traditional but difficult to control precisely. An atomic structural study of the crystallinity confirmed that the BiS nanowires fabricated this way is single crystalline. Its electrical properties were investigated in details, by fabricating and comprehensive tests of field-effect-transistors and photodetectors.

2. Biomolecule-assisted synthesis of bismuth sulfide nanowires

In this case, the synthesis is template-free and the control of size and morphology is thermochemical. These nanostructures were prepared by biomolecule-assisted synthesis, which resulted in surprisingly high crystallinity and good uniformity, with diameters of (50 ± 10) nm and lengths of (1.9 ± 0.2) µm. To assess their electrical properties, we fabricated nanowire transistors with a back-gate structure. The as-grown nanowires are found to be n-type semiconductors and the on-off ratio of the transistors is about 10^2 with a silicon dioxide layer of 50 nm thickness as the gate insulator. More complex and functional nanowire structures are also being developed by this biomolecule-assisted synthesis, including a three-terminal nanowire structure.

Bi_2S_3 has been prepared glycerol-based aqueous solution at temperatures between 110 ℃ and 150 ℃. 2-Mercaptoethanl, glutathione-reduced (GSH-R), and glutathione-oxidized (GSH-O) were employed as sulfur source. Surfactants, poly(vinylpyrrolidone) (PVP), oleic acid and oleyl amine were tried to tune morphology of Bi_2S_3. In typical experiment, appropriate amount of $Bi(NO_3)_3$ and sulfur source molecules of micromolar range were mixed with 15 mL glycerol in glass bottle and the glass bottle was soaked into oil bath of designated temperature (molar ratio of Bi source:2-mercaptoethanol source = 1:70, 140 ℃). The SEM image of the synthesized nanowires and the histogram of the nanowire length and diameter are shown in figure 8 which reveals good uniformity, with diameters of (50 ± 10) nm and lengths of (1.9 ± 0.2) µm.

Figure 8. (a) SEM image of the synthesized Bi_2S_3 nanowires and (b) histogram of nanowire diameter (b) and length (c).
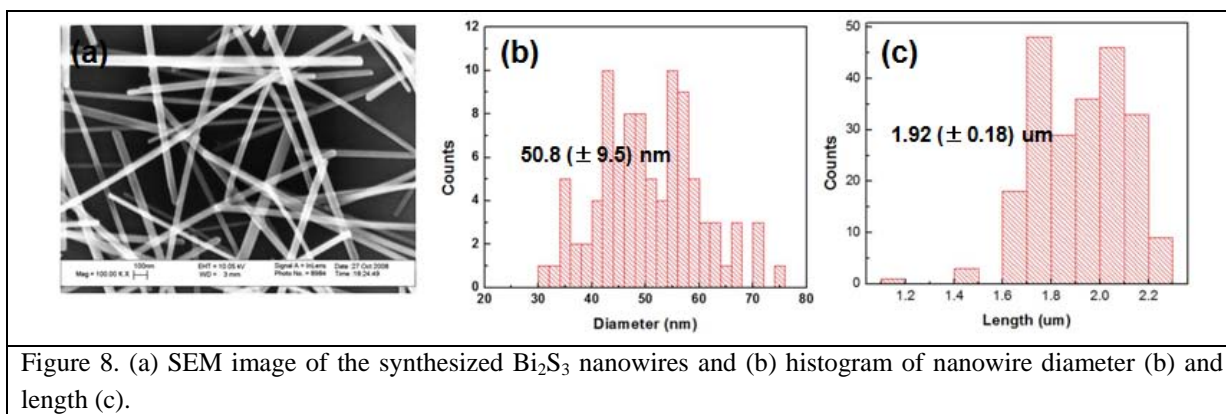
Kinetics of nanowire growth was investigated by examining SEM with growth time and it is shown in figure 9. For a given synthesizing condition, the growth rate is constant in early phase (< 100 min) then the growth saturates. Constant growth rate enables control of the diameter and length by growth time and the saturation of growth makes it possible to obtain uniform dimensions of the synthesized nanowires.
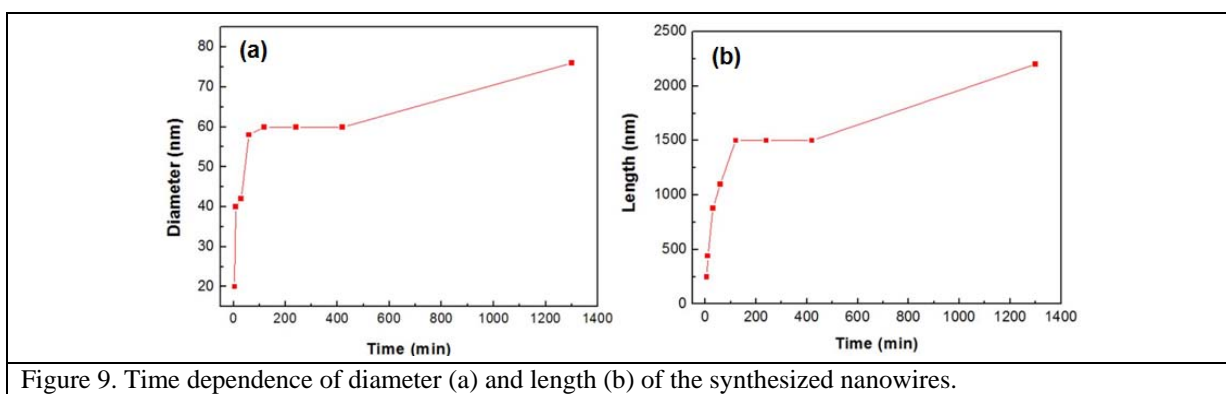
Figure 9. Time dependence of diameter (a) and length (b) of the synthesized nanowires.

The morphology of the synthesized bismuth nanostructures was tuned by sulfur source. Uniform-sized nanoparticles, nanowires, nano-sea urchin, nanorods, and nanoflowers were successfully prepared by changing sulfur sources, adding different types of surfactants into growth solution, changing growth temperature, changing concentration, and changing molar ratio between Bi ion and sulfur source molecule. Among the parameters, changing sulfur source has remarkable effect on Bi_2S_3 morphology. The SEM images of various Bi_2S_3 structures are shown in figure 10. We could get uniform-sized nanoparticles with GSH-R (a), nano-flowers of thin leaf shape with GSH-O (b), and nanowires of high aspect ratio with 2-mercaptoethanol (c). These morphology changes may result from different reactivity between bismuth ion and sulfur sources and to elucidate the mechanism one would need to do more studies on these systems.

Figure 10. SEM image of the synthesized Bi_2S_3 nanowires with different sulfur sources: (a) GSH-R, (b) GSH-O, and (c) 2-mercaptoethanol.
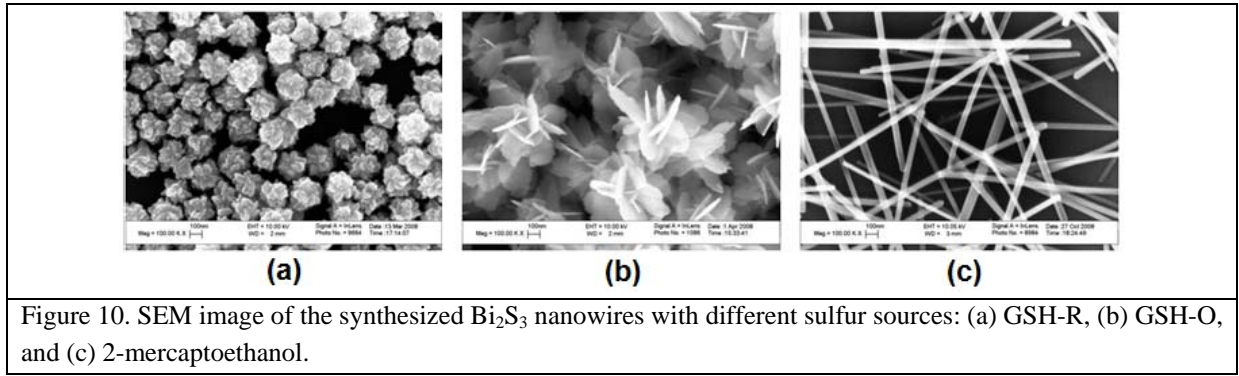
3. Characterization of bismuth sulfide nanowires

The crystallinity of the grown nanowires was confirmed by HRTEM image of a single Bi_2S_3 nanowire, which has lattice plane with spacing of 0.27 nm, corresponding to the d spacing of the (301) of orthorhombic phase [Figure 11]. The inset in the figure 11 shows corresponding SAED pattern taken along the [010] zone axis. The Bi_2S_3 nanowire was preferentially grown along the [001] crystal axis.

Figure 11. High resolution TEM image and the corresponding SAED pattern (inset).
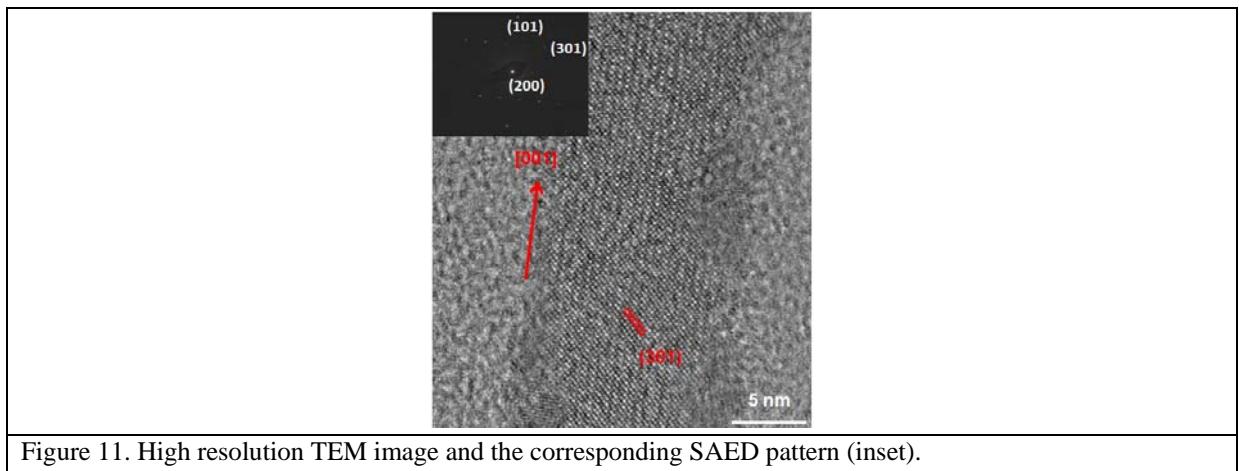
Optical absorption experiments were carried out to elucidate information on the band gap energy, which is one of the most important electronic parameters for semiconductor nanowires. Figure 12 (a) shows the spectrum of bismuth sulfide nanowire solution (in methanol). For a direct bandgap semiconductor, the bandgap energy is usually defined by the x-axis intercept of $(\alpha h\nu)^2$ versus $h\nu$, where α is absorption coefficient. [17, 18]. From figure 12 (b), we estimate the band gap is 1.55 eV.
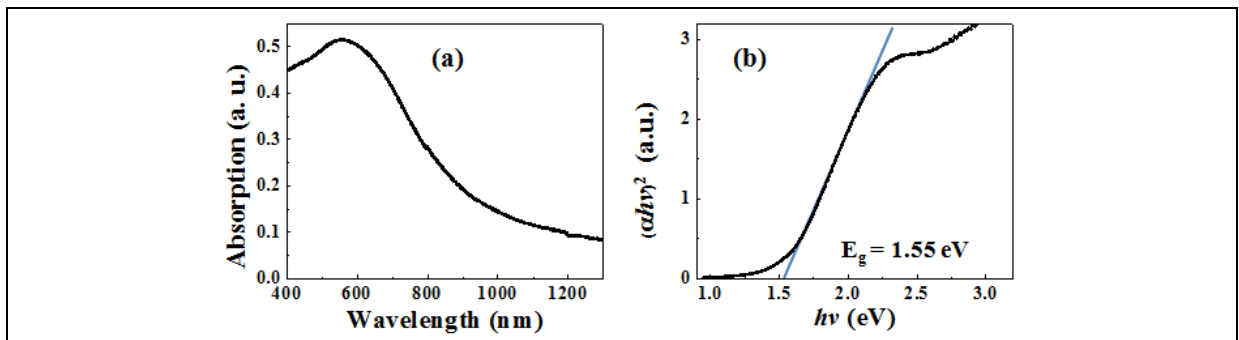
Figure 12. UV/Vis spectrum (a) absorption vs. wavelength of light source (b) $(\alpha h\nu)^2 - h\nu$ plot for band gap evaluation.

4. Bismuth sulfide field-effect-transistors and photodetectors

Electrical properties of Bi_2S_3 were measured by fabricating field-effect-transistors. The grown nanowires were dispersed onto 50 nm thick thermal oxide grown on a highly doped Si substrate. The position of source and drain electrodes was aligned to the nanowires by electron-beam lithography and 80 nm thick Pd electrodes were deposited using electron-beam evaporator. Figure 13 is an SEM image showing a Bi_2S_3 nanowire with 40 nm diameter connected with two Pd electrodes. Al is deposited on the backside highly doped Si substrate as a gate electrode.
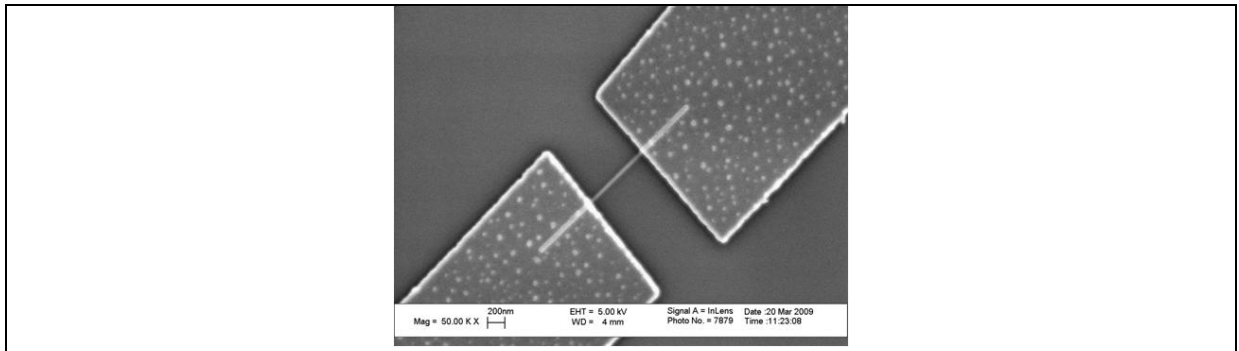
Figure 13. SEM image of Bi_2S_3 nanowire connected to Pd electrodes.

We measured electrical characteristics of the fabricated nanowire transistors using the semiconductor parameter analyzer (Agilent 4156C). Figure 14 (a) shows the $I_D - V_G$ curves measured the nanowire transistor at room temperature. The gate bias was swept from -30 to 30 V and from 30 to -30 V again. The as-grown nanowires are found to be n-type semiconductors and the on-off ratio of the transistors is about 10^2. Hysteresis in the curve is observed. We interpret this hysteresis in terms of charge injection from the nanowire into the oxide layer due to the field enhancement of the nanocurvature and the resultant change of the effective gate bias. At positive gate bias, electrons are injected from nanowires into the oxide and/or oxide – Si interface and the injected charges change the threshold voltage of the channel. With much longer integration time for the measurement, we could observe clearer hysteresis. $I_D - V_D$ curves with different gate bias is shown in the figure 14 (b). The drain voltage was swept from 0 to 4 V with the gate bias of 30, 20, 10, 0, -10, -20, and -30 V.
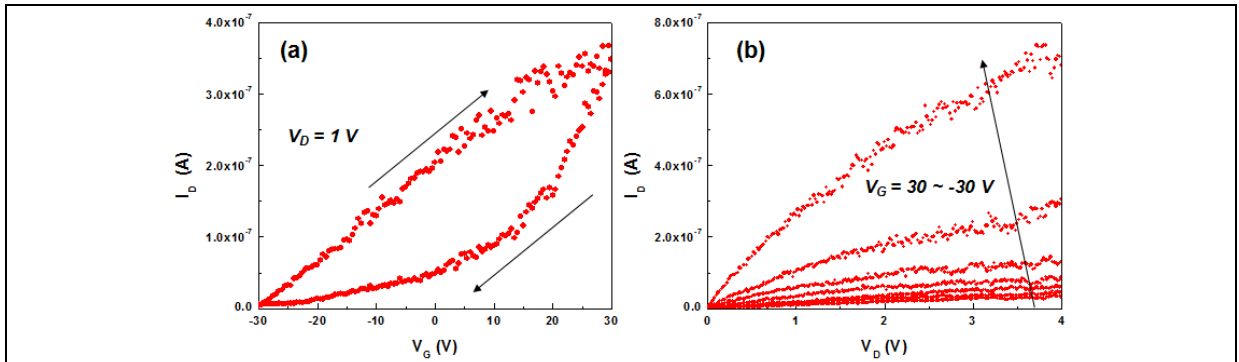
Figure 14. (a) $I_D - V_G$ plot measured from a Bi_2S_3 nanowire transistor at room temperature with 1 V drain

voltage. V_G was swept from -30 to 30 V and from 30 V to -30 V to check hysteresis. (b) I_D – V_D plot under different gate bias (30 V ~ -30 V).

We also have measured photo-response of the nanowires. Fig. 15(a) shows the typical I-V curves measured in dark and under illumination of white light. The dependence of measured photocurrent on incident optical power is shown in the Fig. 15(b). In conventional photoconductive-type photodetectors, large responsivity can be achieved by very long carrier lifetime which also results in a slow response time. However, we observed a very large responsivity ($>10^5$ A/W) with fast response time (~ ms).
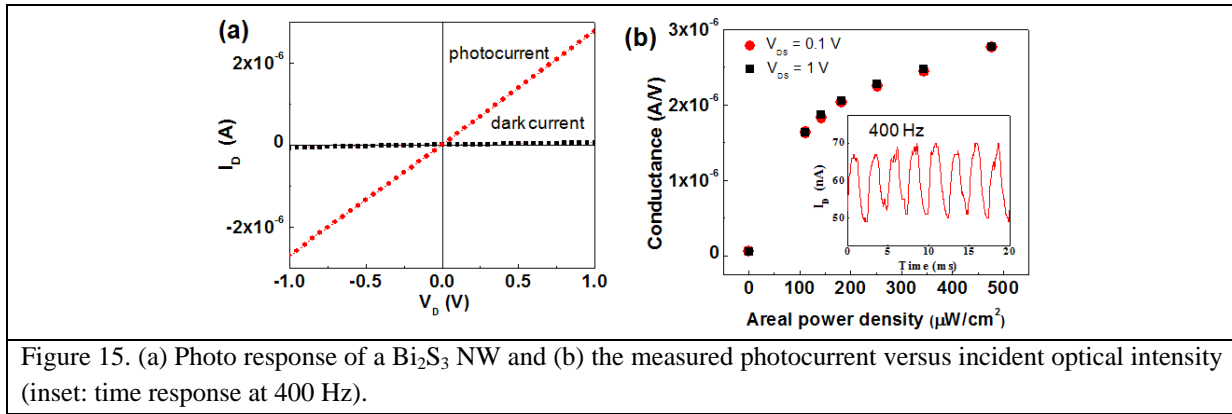
Figure 15. (a) Photo response of a Bi_2S_3 NW and (b) the measured photocurrent versus incident optical intensity (inset: time response at 400 Hz).

We attribute this sensitive and fast optical response to effective modulation of quantum tunneling at the contact by incident light. We determined the fraction of contact resistances caused by contact resistance by using four-terminal devices. Fig. 16(a) shows the SEM image of the fabricated four-terminal Bi_2S_3 nanowire photodetector and Fig. 16(b) shows the change of total, contact, and channel resistance under illumination. From the results, we verified that the high photoconductive gain is due to the optical modulation of carrier injection through contact barriers. Moreover, we conceptualized a design of high-sensitive nanowire-based photodetectors based on the mechanism of efficient modulation of the inherently high contact resistances.
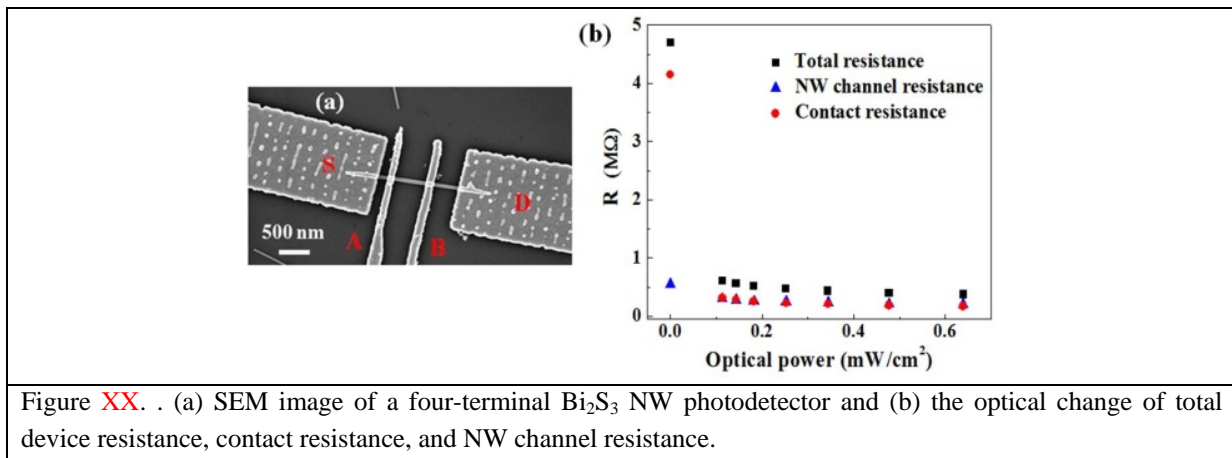
Figure XX. . (a) SEM image of a four-terminal Bi_2S_3 NW photodetector and (b) the optical change of total device resistance, contact resistance, and NW channel resistance.

4. Summary

In summary, the use of a new sulfur source molecule, 2-mercaptoethanol has been studied for the first

time in a solvothermal synthesis of bismuth sulfide nanostructures. It has yielded a rich variety of single crystalline bismuth sulfide nanostructures at relatively low temperature and atmospheric pressure. The morphology of bismuth sulfide in this synthesis process can be tuned to produce plain, tapered, cross- and T-shaped nanowires, nanoleaf-, nanowire- and nanowedge-urchin, nanoplates, nanorods, and nanoparticles, with careful addition of a biomolecule, glutathione and oleylamine and a controlled change of the ratio of Bi:ME. This result demonstrates that small biomolecules can be employed as effective agents for tuning the morphology of nanostructures in general solvothermal or hydrothermal synthesis. This represents a departure from surfactants or amphiphilic molecules which are generally used as morphology tuning agents. Measurements of atomic structures, absorption spectra, and single nanowire FET measurements of these nanostructures all confirm that they are crystalline and have a semiconductor band gap that is agreement with early works on bulk bismuth sulfide. The development of this new synthesis recipe may be beneficial to the synthesis of other metal sulfide nanostructures. The current pursuits of solar cell, IR photodetectors, thermoelectric power generation should be positively impacted by making available such a variety of morphologies.

IV. References

[1] M. D. Stewart Jr., A. Yin, J. M. Xu J, M. Valles Jr., *Science,* 318, 1273 (2007).

[2] R. T. Isaacson, G. A. Williams, *Phys. Rev.*, **185**, 682 (1969)

[3] O. Jessensky, F. Muller, and U. Gosele, *Appl. Phys. Lett.*, **72**, 1173 (1998).

[4] Y. M. Lin, X. Sun, and M. S. Dresselhaus, *Phys. Rev. B*, **62**, 4610 (2000)

[5] J. Heremans, C. M. Trush, Y. M. Lin, S. Cronin, Z. Zhang, M. S. Dresselhaus, J. F. Mansfield, *Phys. Rev. B*, **61**, 2921 (2000)

[6] Y.-M. Lin, S. B. Cronin, J. Y. Ying, M. S. Dresselhaus, and J. P. Heremans, Appl. Phys. Lett., 76, 3944 (2000)

[7] W. Lee, R. Ji, U. Gosele, K. Nielsch, Nat, Mater. 5 (2006) 741

[8] P. Scherrer, Maths. Phys K, 1 (1918) 98

[9] A. J. C. Wilson, Proc. Phys. Soc. 80 (1962) 286

[10] D. D. Miller and A. Heller, *Nature*, **262**, 280 (1976)

[11] R. Nomura, K. Kanaya, H. Matsuda, *Bull. Chem. Soc. Jpn.*, **62**, 939 (1989)

[12] B. B. Nayak, H. N. Acharya, G. B. Mitra, *Thin Solid Films*, **105**, 17 (1983)

[13] P. Boudjouk, M. P. Remington Jr., D. G. Grier, *Inorg. Chem.*, **37**, 3538 (1998)

[14] D. B. Wang, M. W. Shao, D. B. Yu, G. P. Li, Y. T. Qian, *J. Cryst. Growth*, **243**, 331 (2002)

[15] W-H Li, *Material Letters*, **62**, 243 (2008)

[16] R. S. Mane, C. D. Lokhande, *Mater. Chem. Phys*, **65**, 1 (2000)

[17] R S. A. Mahmoud, *Physica B*, **301**, 310 (2001)

[18] V. Kumar, S. K. Sharma, T. P. Sharma, V. Singh, *Opt. Mater.*, **12**, 115 (1999)

V. Acomplishments

Publications

▪ H. Park, D. Han, J. H. Kim, C.-H. Hsu, H. Shin, and J. Xu, "One Material, Multiple Faces –

Nanostructured Bismuth", *ECS Transactions*, 25 (11) 25-33 (2009)

- J. H. Kim, H. Park, C.–H. Hsu, and J. Xu, "Facile Synthesis of Bismuth Sulfide Nanostructures and Morphology Tuning by a Biomolecule," *J. Phys. Chem. C* 114, 9634 (2010)
- H. Park, H. Shin, J. H. Kim, S. Hong, and J. Xu, "Memory effect of a single-walled carbon nanotube on nitride-oxide structure under various bias conditions," *Appl. Phys. Lett.* 96, 023101 (2010)
- S. K. Panda, D. Han, H. Yoo, H. Park, J. Xu, and H. Shin, "Bismuth Nanowires with Controlled Dimensions ─ An Approach towards the Fabrication of Self-homojunction," in preparation (2010)

Invited Presentation

- H. Shin, "1-D Semimetal-Semiconductor Homo-Junction Nanowire for Uncooled IR Detection & Microelectronic Coolers (Part 1 of 2)", A joint symposium of 8th US-Korea Workshop on Nanostructured Materials & 6th Nanoelectronics, 19-20 May, 2009, Seoul, Korea
- J. Xu, "1-D Semimetal-Semiconductor Homo-Junction Nanowire for Uncooled IR Detection & Microelectronic Coolers (Part 2 of 2)", A joint symposium of 8th US-Korea Workshop on Nanostructured Materials & 6th Nanoelectronics, 19-20 May, 2009, Seoul, Korea
- H. Shin, "Confined Growth, Structures, and Energy Application of TiO2 Nanotube Arrays by Atomic Layer Deposition", MRS Fall Meeting, 2009, Nov. 30, Boston, MA

Oral Presentation

- D. Han, H. Yoo, W. Choi, C. Bae, J. Moon, H. Park, J. Xu, and H. Shin, " Fabrication of Diameter-Controlled and –Modulated Bismuth Nanowire Arrays", MRS Fall Meeting, 2009, Dec. 1, Boston MA

Electronic, Photonic and Magnetic Properties of DNA Complexed with Heavy Metal Ions

A. J. Steckl

University of Cincinnati, Nanoelectronics Laboratory

Cincinnati, OH 45221-0030 USA

Executive Summary

Program Goal: Understanding of mechanisms for charge transport, optical excitation/emission, magnetism of modified DNA.

Applications: Use modified DNA for electronic, photonic, and magnetic devices: BioLED, BioFET, BioSpinFET

Uniqueness: Aim to use unique structure of DNA double helix to develop selected devices with unique and superior characteristics.

Approaches: Collaboration between *Korea University* (KU) and the *University of Cincinnati* (UC) combines basic and applied chemistry and device engineering. We are introducing intelligent functionality in DNA materials via synthetic approaches and developing DNA thin films and novel device architectures based on the DNA materials.

Activities: Important activities have been carried out during the project -

(a) Study and optimization of biopolymer light emitting diodes (BioLEDs) incorporating DNA.

(b) Understanding the interaction of DNA polymers, surfactant molecules and luminescent dye molecules. This is a critical item for fabricating DNA-based light emitting diodes with high emission output and efficiency.

(c) Student exchange between UC (Hans Spaeth) and KU (Jung-Yuen Lee).

(d) Collaboration with AFRL-Materials Directorate (J. Grote, R. Naik) on materials properties of DNA and on applications of the BioLEDs.

1. Light Emitting Performance of DNA-based Light Emitting Devices

Deoxyribonucleic acid (DNA) polymers, the source of genetic information, are soluble only in aqueous solutions. However, after bonding with cationic surfactants, such as cetyltrimethylammonium chloride (CTMA-Cl), the DNA-surfactant complex is soluble in organic solvents. Formed into thin films, the DNA-based biopolymer material displays many useful properties, such as low optical loss, high temperature stability, tunable refractive index and low microwave insertion loss. Currently, natural DNA processed from the salmon roe and milt sacs, waste products of the fishing industry, is quite abundant and relatively inexpensive.

The unique structure of DNA has provided opportunities for novel and improved devices: photonics[1], electronics[2], spintronics[3], etc. We have demonstrated[4,5] the beneficial use of DNA nanometer thin films in OLEDs. Enhanced electroluminescent efficiency using a deoxyribonucleic acid (DNA) complex as an electron blocking (EB) material has been obtained in both green and blue emitting BioLEDs. The resulting green and blue BioLEDs showed a maximum luminous efficiency of 8.2 and 0.8 cd/A, respectively. The DNA based BioLEDs were as much as 10× more efficient and 30× brighter than their OLED counterparts. The marked improvement in photoemission of the DNA-based devices is clearly apparent in the photos of Fig. 1 which compare baseline devices (without DNA) and devices with DNA.
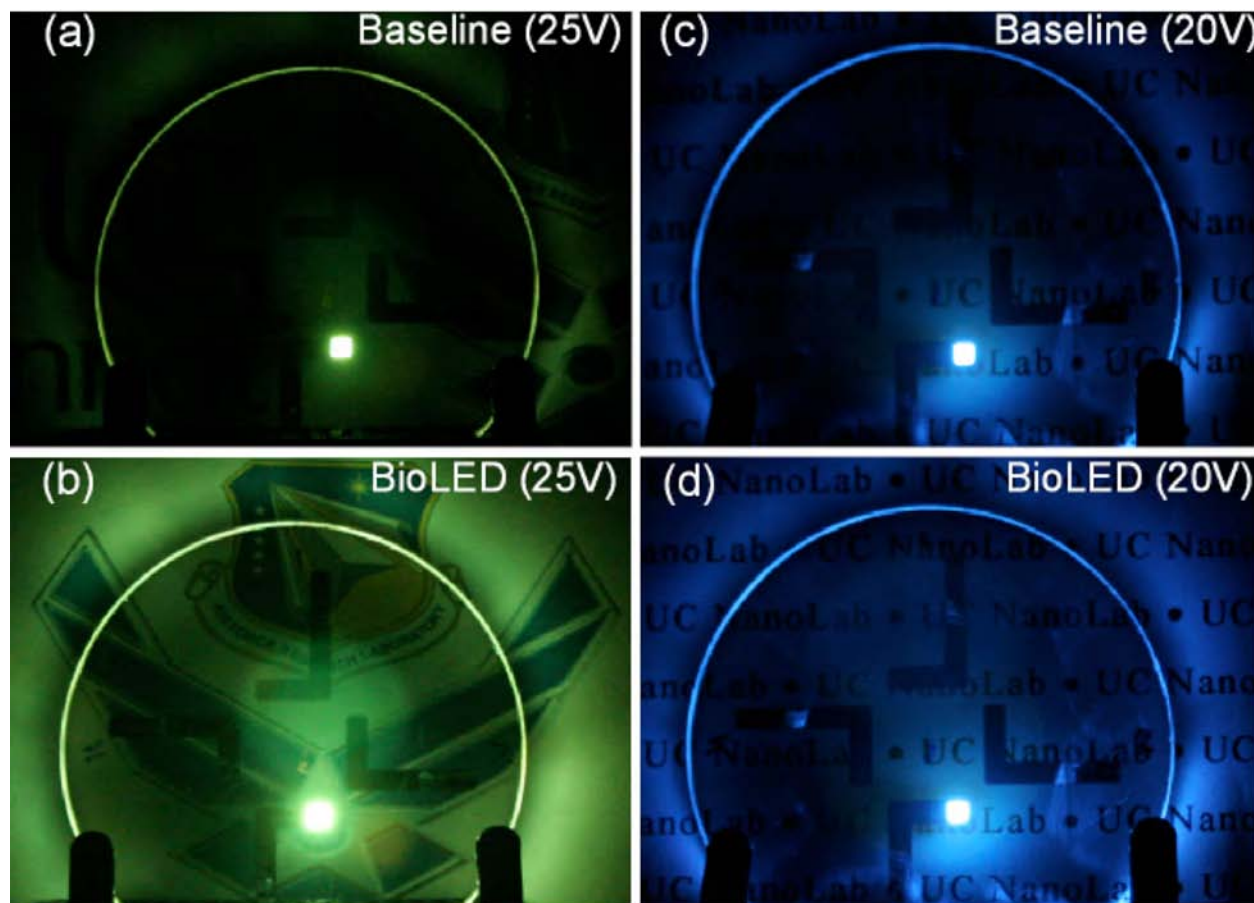
Fig. 1   Photographs of photoemission from light emitting devices: (a) green baseline OLED; (b) green DNA-based BioLED; (c) blue baseline OLED; (d) blue DNA-based BioLED.

Stimulated emission from lasing structures containing a DNA gain medium doped with organometallic dye molecule sulphorhodamine (SRh) has been successfully demonstrated[6]. The stimulated emission has shown quite a low threshold. The SRh molecule is shown in Fig. 2.

2. Interaction of DNA polymers, surfactant molecules and luminescent dyes

It is well known that many small molecules can readily interact with DNA double helix structures through three different modes: ionic, groove and intercalation binding. Many fluorescent dye molecules intercalate into the double helix of DNA, whereby the intensity of fluorescence is greatly enhanced. Amplified spontaneous and stimulated emission from structures containing a DNA-surfactant complex gain medium doped with the fluorescent dye molecules have been reported with quite a low emission threshold. One possible mechanism for the highly efficient light amplification was ascribed to the interaction between dye molecules and DNA double helix by either intercalation or groove binding. Additionally, considering the structure of DNA-surfactant complexes in the precipitation and solution form, the fluorescent dye molecules may be incorporated between surfactant molecules. Dye-surfactant interactions are of great importance in the dyeing and photographic industries, biological and medicinal photosensitization and analytical and environmental sciences. More specific to this project, a much more complete understanding of the biophysical mechanisms involved in the interaction between DNA, surfactants, and fluorophores is required in order to fully exploit the potential of combining the unique structure and properties of DNA biopolymers with various light emitting molecules in optoelectronic devices. Therefore, the relationship between the structure of selected dye molecules and their location and orientation relative to the DNA-surfactant complex was investigated in some detail.

The DNA material used in this study is derived from salmon sperm and provided by Prof. N. Ogata at Chitose Institute of Science and Technology (CIST) in Japan. After purification and protein removal, the freeze-dried DNA remains water-soluble, which impairs the possibility for thin film formation and incorporation into device structures. To change the solubility, a cationic surfactant reaction was used to convert DNA to a DNA-lipid complex. Cetyltrimethylammonium chloride (CTMA) was used to form a DNA-CTMA complex as shown in Fig. 2, which is not soluble in water but can be dissolved in organic solvents (alcohols)

Chirality of molecules is investigated by performing circular dichroism (CD) spectroscopy[7]. The sample to be considered is represented in the center of the CD spectrometer. Through this sample are passed beams of right and left circularly polarized light. In a sample that does not possess chirality (or handedness) there will be no difference in the intensity of the outgoing light. A sample with chirality will absorb, preferentially, either right or left polarized light. The difference observed between the intensity of the outgoing beams, is then correlated to the strength of the chirality of the sample and presented through a computer interface, as a CD spectrum.

Since the DNA molecule exhibits chirality, it is clear that a CD spectrum will be present in the absorption region of DNA. Far less obvious is that a CD spectrum will be observed in the absorption region of the non-chiral SRh molecule, once combined with DNA.
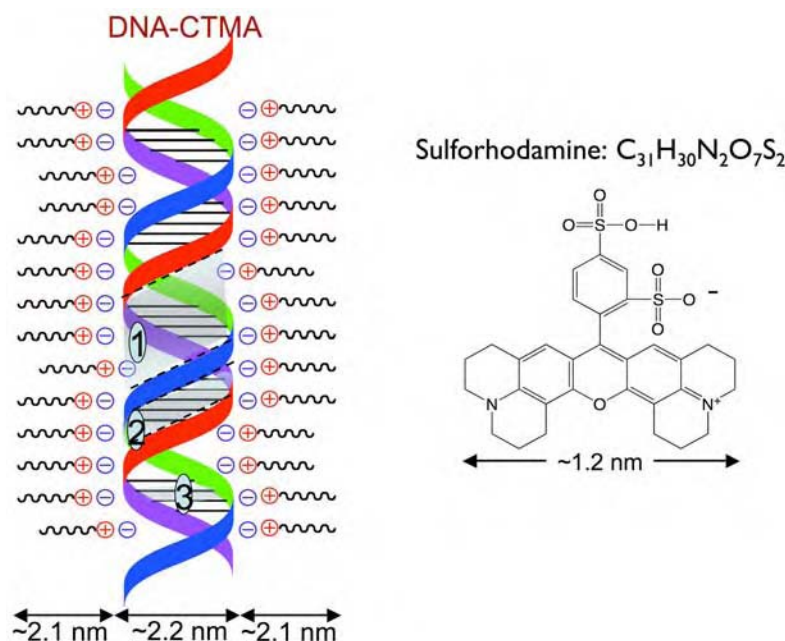
Fig. 2 The DNA-CTMA double helix polymer and the sulforhodamine molecule. The DNA double helix indicates possible locations for the binding of the SRh molecule: (1) major groove; (2) minor groove; (3) intercalation between base pairs.

2.1 Circular Dichroism Samples

CD spectroscopy experiments were performed both on liquid and thin film samples. The samples consisted of DNA:CTMA dissolved in butanol and combined with sulphorhodamine dye. The thin films were prepared from the same solutions used for the liquid samples in order to make comparisons between the two states more meaningful. Sample preparation is discussed for both, followed by an account of the CD experiments.

The liquid solutions were all 10% DNA:CTMA in butanol, by weight. This was dissolved on a rotary mixer, overnight, at room temperature. To each solution, sulphorhodamine was added in percentages of the weight of DNA:CTMA used. The solutions were each filtered through a 0.2 μm syringe-tip PTFE filter. Solutions of 0%, 2.5%, 5%, 10%, 15%, 20%, and 25% SRh to DNA:CTMA were prepared. Thin films produced via spin-coating were 1.5 μm in thickness.

CD experiments with solution samples were conducted by placing the liquid in a cylindrical cuvette with a liquid path length of 0.01mm. For DNA, the range 525-625 nm was scanned. For SRh, the range used was 220-340nm. The bandwidth was set to 15 nm and 5 nm for the DNA and SRh region, respectively. Background correction was performed, using a cuvette filled with butanol and noise was filtered from the results via the accompanying computer software.

For thin film scans, the samples used were spun on one half of the same type of cuvette as was used for the liquid samples. The CD signals observed for thin film samples were stronger than for the corresponding liquid samples in each case. This is because, despite the shorter path length of the thin films, those samples were more concentrated, due to the evaporation of the butanol.

2.2 Circular Dichroism Results

CD signal is plotted against wavelength for four samples in Fig. 3. Considered here are samples containing DNA:CTMA only and those containing DNA:CTMA with 5 wt.% SRh. In this case, the CD signal is shown in the DNA absorption region. Results for both thin film and solution samples are included. Here, there is no obvious correlation between the presence of SRh and the strength of the DNA CD signal. The strength of the signals for the thin film samples are stronger than those of the solution samples. This is typical of our samples due to the concentrated nature of the thin films, putting more material in the path of the CD spectrometer.
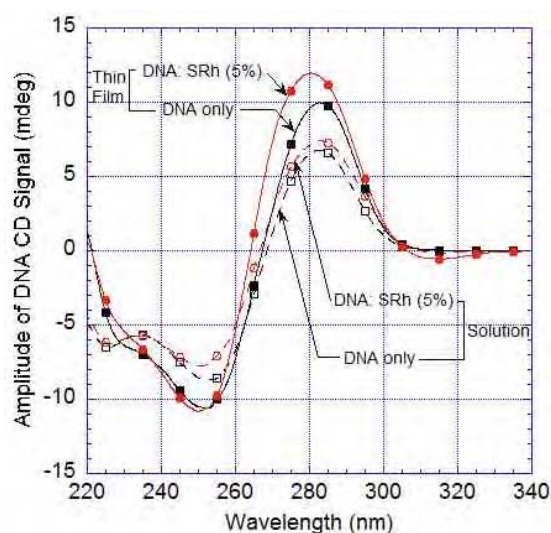
Fig. 3 CD signal (mdeg) for DNA absorption region vs wavelength (nm). DNA only and DNA:SRh 5% are included in both solution and thin film forms.

In Fig. 4, a similar plot is provided, but for the SRh absorption wavelength region. Displayed here are spectra for samples containing 2.5% and 15% SRh to DNA:CTMA by weight. Both thin film and solution spectra are provided. It is, again, observed that the thin films result in a CD spectrum of greater intensity than the solution samples. Notable, is the increase in amplitude with an increase in SRh concentration, for both thin film and solution cases.
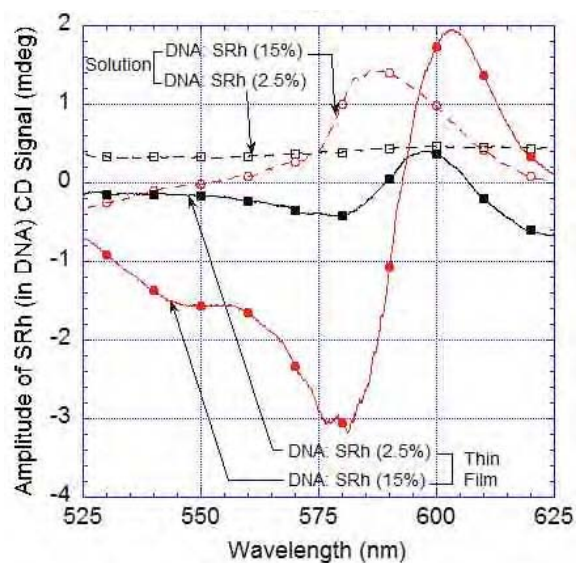
Fig. 4 CD signal (mdeg) for SRh absorption region vs wavelength (nm). DNA:SRh 2.5% and 15% are included in both solution and thin film forms.

A summary of the peak-to-peak CD amplitude (in the DNA absorption region) of the samples investigated is shown in Fig. 5. There is no obvious correlation in solution samples, between SRh concentration and *DNA* CD intensity. For thin films, the CD signal demonstrates a slight increase in intensity, in combination with SRh, with the exception of a decrease in signal at the highest concentration (25%) of SRh. It is possible that enough SRh molecules are finally attached to the DNA molecule, in the this case, to begin disturbing the chirality of the spiral.

Fig. 5 also shows peak-to-peak CD amplitude in the SRh absorption region. Here, there is a clear increase in CD signal strength, with increasing SRh concentration. This observation demonstrates that SRh takes on the chiral nature of the DNA molecules with which it has been combined. The plot flattens at higher concentrations of SRh, indicating a saturation effect, wherein the sample contains more SRh than can readily bind to the DNA.
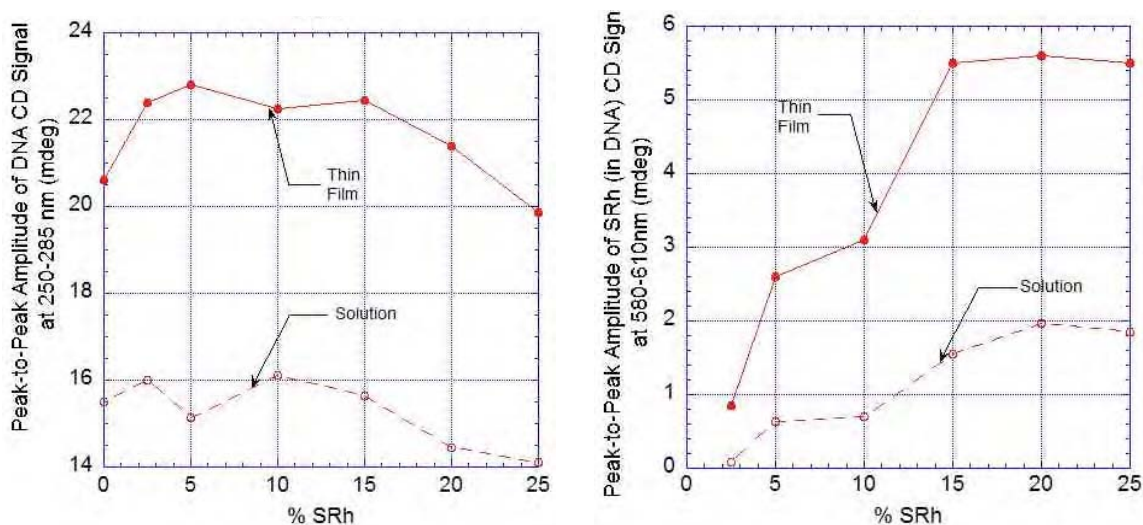
Fig. 5 Peak-to-peak CD Signal (mdeg) for DNA and SRh regions versus SRh concentration (%).

2.2 Role of Surfactant-Dye-DNA Interactions

After the CD investigation, the nature of the interaction between the DNA-Na polymer complexed with a cationic surfactant (CTMA-Cl) and sulforhodamine sodium (SRh) or rhodamine perchlorate (RhP) dye molecules (see molecule structures in Fig. 6) was further explored. A dramatic effect was observed when DNA/CTMA whitish fibrous powder was added to SRh aqueous solution which is normally pink in color. As seen in Fig. 7, the solution became clear and the DNA/CTMA powder (which does not dissolve in water) became pink. This change occurred in 20-30 minutes for a still solution and in 10-15 minutes for an agitated solution. The DNA/CTMA powder retained its pink color after repeated rinsing in clean water. A similar phenomenon was observed when RhP was substituted for SRh.
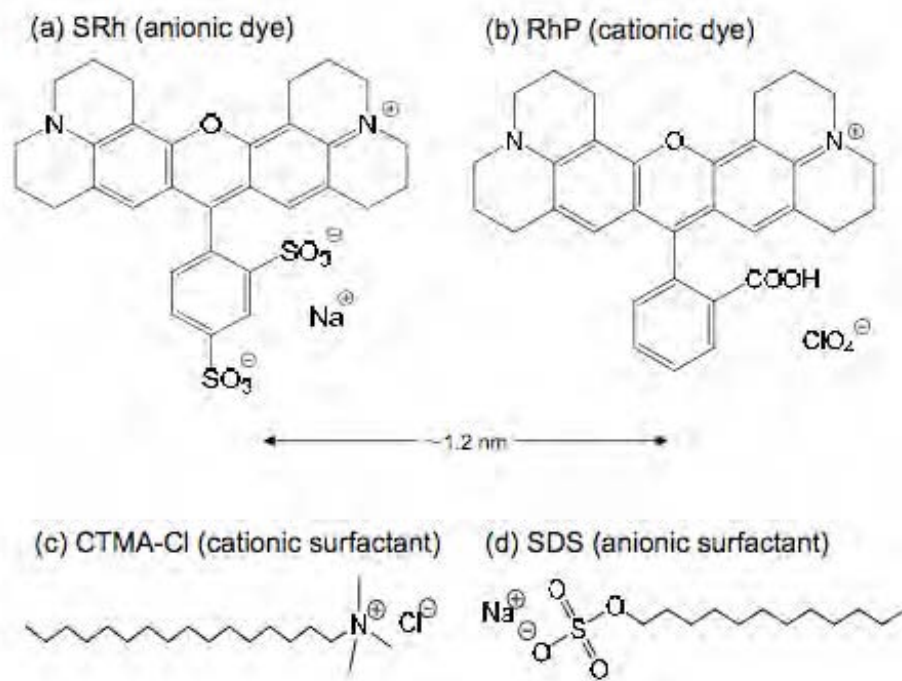
Fig. 6 Chemical structures of molecules used.
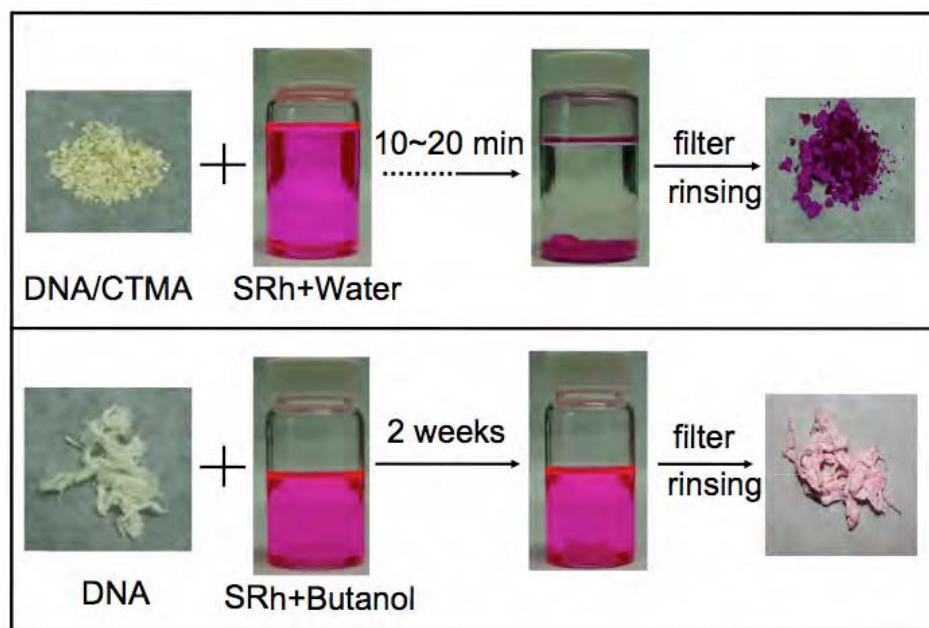
Fig. 7 Photographs illustrating the interaction between DNA/CTMA powders and DNA-Na fibers and SRh dye molecules in aqueous and butanol solutions.

Since SRh is soluble in organic solvents as well as water, a complementary experiment was carried out. DNA-Na fibers were introduced into a SRh butanol solution. After duration as long as two weeks, the solution did not change color and the DNA-Na fibers retained their white color after rinsing in clear butanol solvent (see Fig. 7).

The UV-Vis absorption and photoluminescence (PL) spectrum of the dye molecules in butanol solution are shown in Fig. 8. The rhodamine dye family is derivative of xanthene, incorporating a central group of heterocyclic fused rings. Rhodamine dyes are widely used as the gain medium in dye lasers and in fluorescence analysis. SRh is an anionic molecule in both aqueous and organic solutions, whereas the RhP molecule takes the zwitterionic form in polar protic solvents such as water and ethanol where the carboxyl group releases a proton. We found that the dye molecules did not interact directly with DNA double helix which just acted as a template for the interaction between dye molecules and CTMA in the DNA/CTMA complex. The SRh and RhP molecules yield different fluorescence characteristics with increasing DNA/CTMA amount, indicating different configurations which also been discussed inside the CTMA molecules.
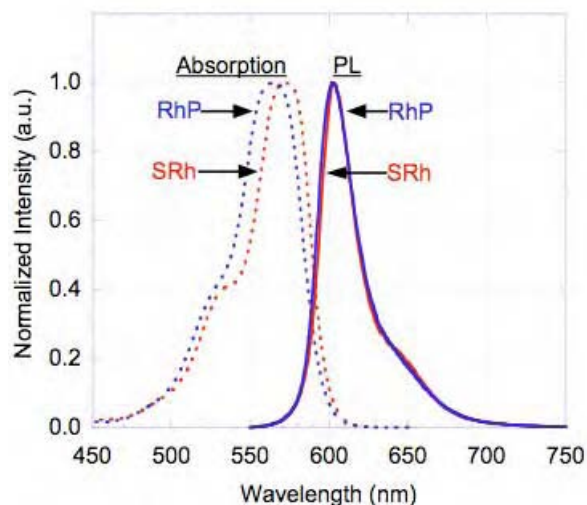
Fig. 8 Optical absorption and PL spectra (488nm excitation) of SRh and RhP in butanol.

2.2.1 Materials and sample preparation. To improve film forming characteristics, the as-received high molecular weight (MW) DNA (25~10 MDa) was sonicated, reducing the average MW to approximately 200 KDa. Next, the DNA-Na is reacted with the cationic surfactant CTMA-Cl (0.01M) in water. This forms a DNA/lipid (DNA/CTMA) complex, which precipitates out of the aqueous solution but is soluble in simple organic solvents. For the DNA/dye/CTMA solution, fluorescent dye (5 wt% to DNA/CTMA) is added into the DNA-Na aqueous solution, and then reacted with the surfactant solution, resulting in the precipitation of a pink DNA/dye/CTMA complex, which dissolves into butanol to obtain the DNA/dye/CTMA solution. For the DNA/CTMA/dye solution, the DNA/CTMA complex is formed first. Then it is reacted with the dye molecules in an organic solvent to obtain the DNA/CTMA/dye solution. Butanol was utilized as the organic solvent because of its relatively slow evaporation (due to a low vapor pressure) and moderate viscosity. All solution samples were dissolved on a rotary mixer overnight at room temperature. The DNA/CTMA/dye solutions were made with different weight ratios of DNA/CTMA to dye molecules. Optical absorption of DNA/CTMA/dye and DNA/dye/CTMA solution was performed over the near ultraviolet and visible (UV-Vis) spectrum.

For dye absorption experiments, dye molecules in aqueous (0.0025 wt %) and organic (0.0025 wt %) solutions incorporating insoluble DNA/CTMA powders and DNA-Na fibers, respectively, were used. The amount of the dye introduced into the solution was chosen with that there was 1 dye molecule for 10 DNA base pairs. UV-Vis absorption spectrum measurements were performed at 15 minutes intervals, utilizing 0.8 mL of the pure solution without undissolved DNA-Na fibers or DNA/CTMA powders, which was then return into the main mixture container after the test.

For the decomposition experiments, DNA/SRh (5 wt %) /CTMA (0.84 mmol) and DNA/CTMA (0.84 mmol) were treated with 10 mL sodium dodecylsulphate (SDS) (Aldrich) aqueous solution (0.168 M). This is equivalent to 1 SRh molecule for every 10 DNA base pairs, and 20 CTMA molecules or 20 SDS molecules, respectively. The mixtures were placed in a rotary mixer for 48 hours at room temperature and then filtered with 0.45 μm PVDF syringe filter to separate the

solution from any remaining solid. The solutions were first used for UV absorption measurements. This was followed by treatment with 1 mL diluted DNA-specific PicoGreen (Invitrogen Inc.) dye solution, and then used for the photoluminescence (PL) measurements. Solutions with same amount of DNA/CTMA and DNA/SRh/CTMA in water without SDS were also tested for comparison. The solutions without PicoGreen dye were also concentrated for the electrophoresis experiment.

2.2.2 Measurement. A Perkin-Elmer spectrometer was used to measure the UV absorption spectrum of different solutions. The PL measurements were performed with He–Cd laser excitation at 325 nm or Argon laser excitation at 488 nm. The emission spectra were analyzed by an Acton Research spectrometer equipped with a photomultiplier sensitive in the UV-Vis spectrum. High-pass filters and dichroic mirrors were utilized to block the laser pump light. The spectrometer resolution was 0.16 nm. The PicoGreen PL measurements were performed with a NanoDrop 3300 Fluorospectrometer. The electrophoresis was performed with 0.5 wt% agarose gel in TAE buffer. Ethidium bromide was used to label the DNA. All measurements were performed at 300 K.

2.2.3 Results

This relationship between the state of the DNA (Na salt vs. surfactant complex), the SRh molecules and the solvent was first quantified by measuring the optical absorption of the dye solution. Fig. 9 shows the time dependence of the normalized SRh and RhP absorption in butanol into which DNA-Na fibers were added and in aqueous solution into which DNA-CTMA powder particles were added. The SRh and RhP absorption in butanol did not change with time upon the introduction of DNA-Na fibers indicating that to a first approximation there is no direct dye-DNA reaction. On the other hand, the dye absorption in aqueous solution dramatically decreased with time with addition of DNA/CTMA powder particles. This demonstrates that the DNA/CTMA can react with dye molecules and remove them from their aqueous solution, whereas the DNA-Na is unable to perform the counterpart reaction in butanol solution. This clearly indicates there is no direct interaction between the DNA and dye molecules. Therefore, one can rule out ion exchange between the DNA and dye molecules when the dye molecules are mixed with DNA/CTMA complexes. Circular dichroism spectroscopy also supports this conclusion, as there was a strong induced CD signal for SRh in DNA/CTMA butanol solution, whereas SRh in DNA aqueous solution did not display a CD signal.

It is well known that DNA-cationic surfactant complexes can be decomposed by the addition of anionic surfactants or monovalent salts. The DNA-Na salt molecules are released from the DNA-cationic surfactant complex and surfactant aggregate structures are formed because the interaction between the oppositely charged surfactants is stronger than the one between DNA and cationic amphiphiles. This presents the opportunity to further understand the interaction between DNA, surfactant and dye molecules. The decomposition of DNA/CTMA complexes was investigated with the addition of the anionic surfactant sodium dodecylsulphate (SDS) in aqueous solution, see structure in Fig. 6d. As the DNA/CTMA powder is not soluble in water, the decomposition is not complete even after 48 hours.
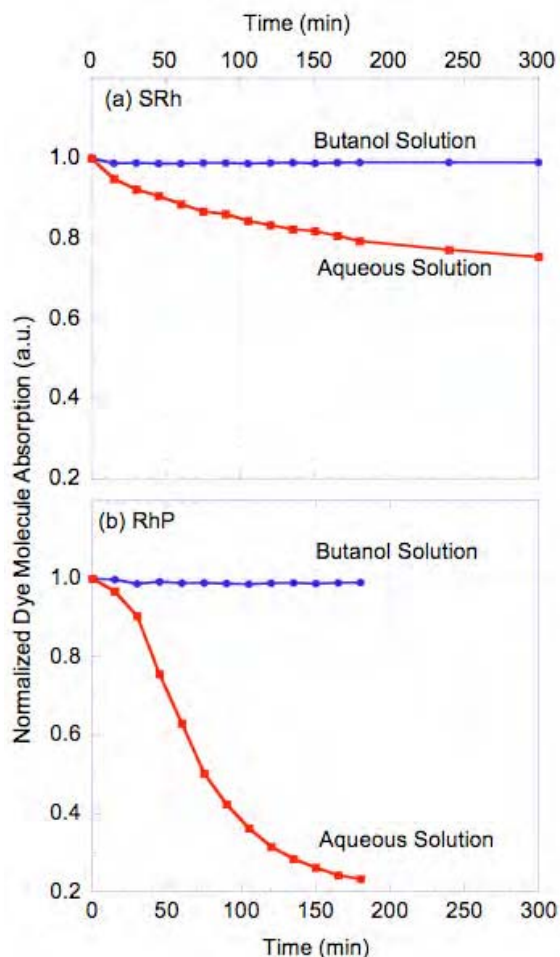
Fig. 9 Time dependence of normalized dye molecule absorption (~560-570nm) in butanol (using DNA-Na fibers) and in aqueous solution (using DNA/CTMA powder): (a) SRh; (b) RhP.

UV-Vis absorption and PL of the DNA/CTMA-SDS solution was used to characterize the decomposition degree. We investigated the influence of SRh dye molecules on the decomposition of DNA/CTMA complexes. PicoGreen was used to identify the presence of DNA double helix molecules. In Fig. 10, spectra from DNA/SRh/CTMA and DNA/CTMA aqueous and SDS solutions are compared. Since DNA/CTMA complexes do not readily dissolve in water, all solutions were filtered prior to optical measurement to remove particulates. Comparing the SDS-based solution, it is clear that the presence of the SRh molecules greatly amplified the decomposition process, leading to very strong UV (265 nm) absorption from DNA and red (590 nm) absorption from SRh. Similarly, decomposed DNA/SRh/CTMA+SDS solution exhibited strong PL signal from intercalated PicoGreen molecules (with a peak at 520 nm) and from SRh molecules (at 605 nm). On the other hand, the DNA/CTMA+SDS solution had very weak UV absorption and PicoGreen fluorescence, indicating a much less effective decomposition. As expected, the DNA/SRh/CTMA and DNA/CTMA plain aqueous solutions showed very weak absorption or fluorescence signals. When the filtered DNA/SRh/CTMA+SDS solution was concentrated and investigated with electrophoresis, the DNA and SRh molecules separated under the electric field, with DNA moving towards the anode and SRh moving towards the cathode.

All of these observations demonstrate that the dye molecules react with CTMA, and not DNA in the DNA/CTMA complex.
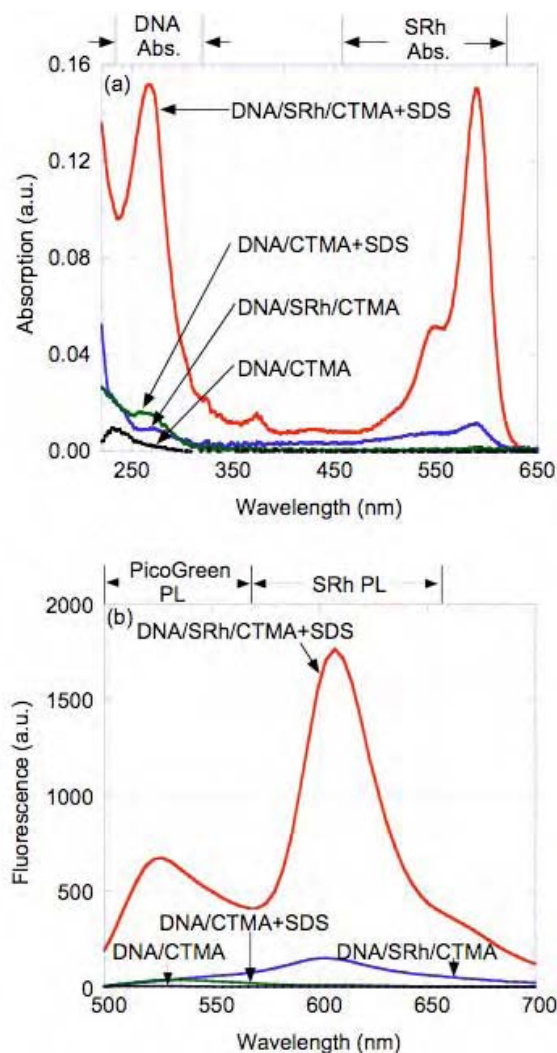

Fig. 10   Decomposition of DNA/SRh/CTMA and DNA/CTMA in SDS solutions: (a) UV-vis absorption spectra: (b) PL spectra.

The interaction between the two oppositely charged surfactant and dye molecules, SRh and CTMA-Cl (without DNA) in aqueous solution ([SRh]=40 µM, [CTMA]=0.8mM) was investigated by means of optical measurement. The results are shown in Fig. 11. For comparison, the results for DNA/SRh/CTMA butanol solution with the same SRh concentration are also presented. Interaction between SRh and CTMA-Cl molecules was indicated by the UV-Vis absorption and PL intensity decrease and slight blue shift in the peak position. The significant differences in absorption and fluorescence between the plain dye solution and the dye-surfactant aqueous solution cleanly indicate that the strong interaction between the oppositely charged molecules. A similar effect has been reported for rhodamine 6G and SDS solutions and attributed to ion pair aggregation process. The fact that the SRh and SRh/CTMA butanol solution exhibited the same absorption and fluorescence is attributed to the absence of micelles formation in organic solution (unlike the case in aqueous solution). This clearly indicates that the interaction

between the CTMA and dye molecules in DNA/CTMA complex can not be attributed to formation of the ion-pair aggregates, which would result in significant changes in the intensity and wavelength of the absorption and fluorescence.
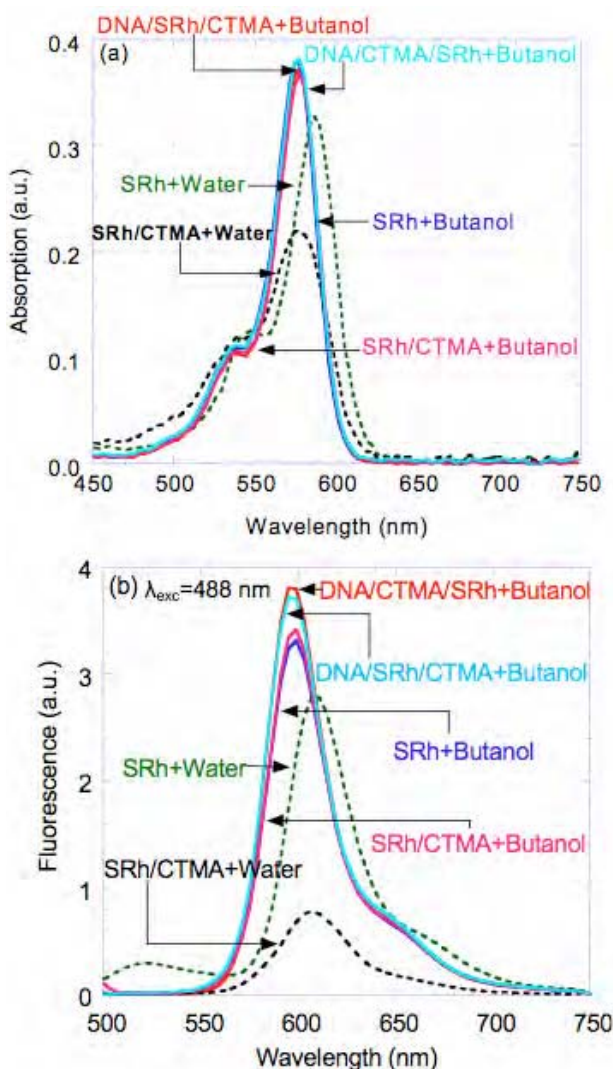

Fig. 11 UV-Vis absorption (a) and PL (b) spectra of SRh molecules in water and butanol solutions.

To more fully understand the dye molecule configuration in DNA/CTMA, the PL intensity of SRh and RhP with different weight ratio between DNA/CTMA and dye in butanol solution was measured. The results are shown in Fig. 12. It is very interesting to note that when the 325 nm laser excitation was used, the SRh PL intensity increased with increasing DNA/CTMA in the solution, whereas the RhP PL intensity decreased with DNA/CTMA concentration. When the excitation source was changed to 488 nm argon laser, the PL intensity of both SRh and RhP stayed within a common band with different DNA/CTMA concentration in the butanol solution.
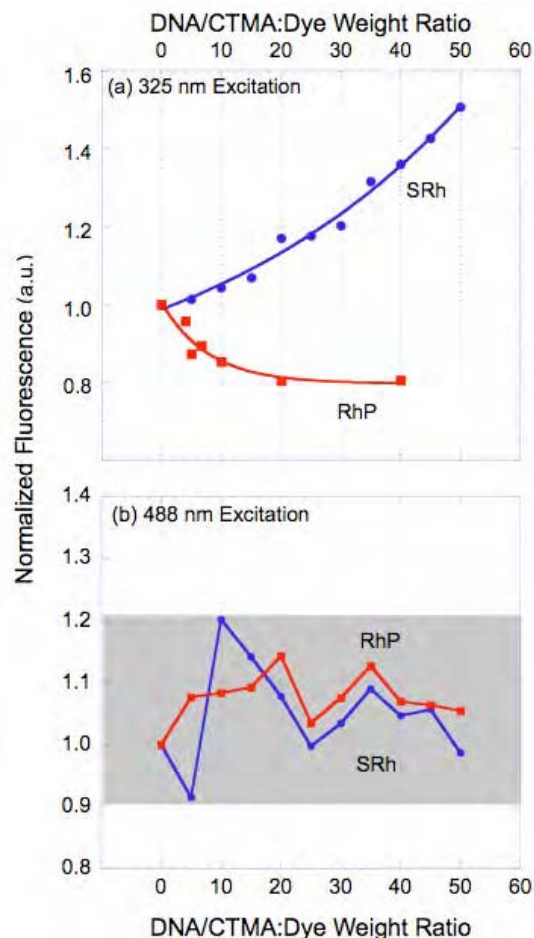
Fig. 12 Normalized PL intensity of SRh and RhP in butanol solution with the addition of different weights of DNA/CTMA with excitation at 325nm (a) and 488 nm (b).

On the other hand, as shown in Fig. 9, compared to SRh, RhP molecules are easier to remove from their aqueous solution by DNA/CTMA powders. This indicates that the SRh and RhP molecules interact with the CTMA molecules in the DNA/CTMA complex with different mechanisms. Considering the structure of these two dye molecules (Fig. 1) and DNA-surfactant complex in alcohol solution, it is reasonable to ascribe this difference to the dye molecular structures. For SRh, the steric effects due to two sulfates in the phenyl group is important as the SRh molecules incorporate into CTMA molecules in the DNA/CTMA complex. It is likely that the xanthene group incorporates first and then the phenyl group, as shown schematically in Fig. 13. By comparison, the phthalide group in RhP molecules is more easily incorporated into CTMA molecules without hindrance, resulting in the fast removal of RhP dye from their aqueous solution by DNA/CTMA powders. After incorporation, the xanthene group, which is the fluorescing group in rhodamine dyes, is located closer to the DNA base pairs for SRh compared to RhP molecules. This would lead to more efficient energy transfer between SRh molecules and DNA base pairs. Using 325 nm laser excitation, which is in the range of DNA absorption, energy is mostly absorbed by the DNA bass pairs and then transferred to SRh molecules, followed by emission from SRh excited states. As the DNA/CTMA concentration increases, more energy is absorbed by base pairs and transferred to SRh, leading to increasing PL signal from SRh

14

molecules. For RhP solutions, the greater distance between the xanthene group and the DNA base pairs prevents efficient energy transfer. Therefore, increasing DNA/CTMA concentration leads to more laser energy being absorbed by base pairs and less energy available for RhP excitation, resulting in decreasing RhP PL. When 488 nm excitation is used, which is in the range of rhodamine absorption, the energy is mainly directly absorbed by the dye molecules, and therefore, the PL signal is independent of the DNA/CTMA concentration in the solution.
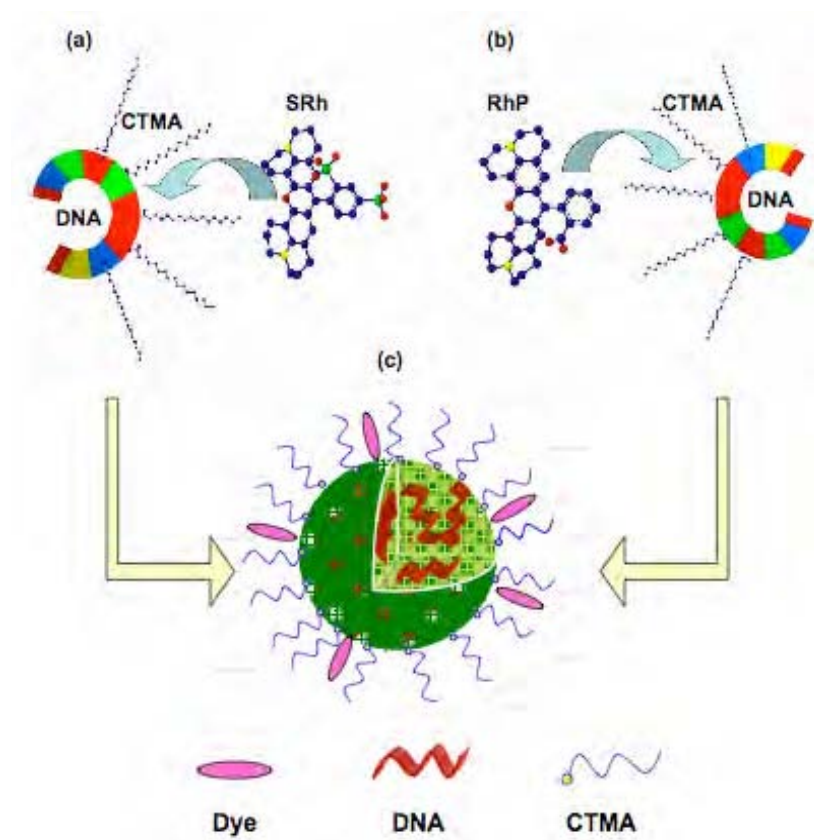
Fig. 13 Expected SRh (a) and RhP (b) molecule incorporation dynamics inside CTMA molecules in the DNA/CTMA complex.

In summary, the interaction between the rhodamine dye molecules and DNA-surfactant complexes has been investigated in this project. In contrast to the common assumption that dye molecules will interact directly with DNA double helices through either groove or intercalation binding, it appears that the DNA double helix structure simply acts as a template for the interaction between the CTMA molecules and xanthene dye molecules. Anionic SRh and zwitterionic RhP dyes incorporate into the CTMA with different structures, which yields different photoluminescence characteristics in DNA/CTMA alcohol solution. Understanding and controlling the complex interactions between DNA polymers, surfactants and dye molecules can lead to improved DNA-based OLEDs as well as other novel optoelectronic devices.

(1)   Steckl, A. J. *Nature Photonics* **2007**, *1*, 3.

(2)   Singh, B.; Sariciftci, N. S.; Grote, J.; Hopkins, F. K. *Journal of Applied Physics* **2006**, *100*, 024514.

(3)   Lee, C. H.; Do, E.-D.; Kwon, Y.-W.; Choi, D.-H.; Jin, J.-I.; Oh, D.-K.; Nishide, H.; Kurata, T. *Nonlinear Optics, Quantum Optics* **2006**, *35*, 165-174.

(4)   Hagen, J. A.; Li, W.; Steckl, A. J.; Grote, J. G. *Applied Physics Letters* **2006**, *88*, 171109.

(5)   Hagen, J. A.; Li, W. X.; Spaeth, H.; Grote, J. G.; Steckl, A. J. *Nano Lett.* **2007**, *7*, 133-137.

(6)   Yu, Z.; Li, W.; Hagen, J. A.; Zhou, Y.; Klotzkin, D.; Grote, J. G.; Steckl, A. J. *Applied Optics* **2007**, *46*, 7.

(7)   Rodger, A.; Norden, B. *Circular Dichroism & Linear Dichroism*; Oxford University Press: Oxford, 1997.

Chirality of sulforhodamine dye molecules incorporated in DNA thin films

A. J. Steckl,[1,a)] H. Spaeth,[1] K. Singh,[2] J. Grote,[2] and R. Naik[2]

[1]Nanoelectronics Laboratory, University of Cincinnati, Cincinnati, Ohio 45221-0030, USA
[2]US Air Force Research Laboratory, WPAFB, Ohio 45433-7707, USA

Thin films formed from salmon sperm DNA reacted with a cationic surfactant (CTMA-Cl) included up to 25 wt % fluorescent molecule sulforhodamine (SRh). SRh effect on DNA chirality and vice versa was investigated by circular dichroism (CD) spectroscopy. The CD signals at 250–265 nm indicate that DNA chirality was maintained or enhanced. Induced CD (iCD) signal at 580–610 nm indicates that SRh is chiral in DNA/CTMA. iCD signal from both solutions and thin films generally increases with SRh concentration. The chirality induced in SRh molecules and the absence of significant DNA reduction in chirality are clear indicators of strong binding to DNA/CTMA. © 2008 American Institute of Physics. [DOI: 10.1063/1.3027070]

The double helix structure of DNA has prompted research in novel and improved devices in several fields, including photonics,[1] electronics,[2] and spintronics.[3] Enhancement in the efficiency and brightness of organic light emitting diodes, which incorporate DNA nanometer thin films, has been previously reported.[4,5] Stimulated emission from thin film lasing structures containing a DNA gain medium doped with the fluorescent dye molecule sulforhodamine 640 (Exciton Inc., Dayton OH) (SRh) has been reported to have quite a low threshold.[6] A much more complete understanding of the biophysical mechanisms involved in the interaction between DNA, surfactants, and fluorophores is required in order to fully exploit the potential of combining the unique structure and properties of DNA (and other biopolymers) with various light emitting molecules in optoelectronic devices. Since most of the device applications utilize thin film structures, an understanding of processes and mechanisms is particularly needed as these material undergo a liquid ("wet") to solid ("dry") state transition.

In this paper we report on the nature of the interaction between DNA-Na polymer complexed with a cationic surfactant cetyltrimethylammonium chloride (CTMA-Cl) and SRh molecules. Circular dichroism (CD) spectroscopy[7] has been employed to investigate chirality in DNA/CTMA thin films and solutions containing various amounts of SRh molecules. CD is the result of differential absorption of left-and right-circularly polarized beams in molecules that have a chiral structure. A chiral structure is frequently found in biopolymers, such as nucleic acids and proteins.

The backbone of the DNA double helix consists of alternating ribose sugar and phosphate groups forming two spirals running in opposite directions. Nitrogenous bases attached at approximately right angles to the sugar/phosphate groups join the two spirals through hydrogen bonds. The four bases found in DNA, adenine (A), cytosine (C), guanine (G), and thymine (T), are uniquely paired (A-T, G-C) such that they allow a constant DNA helix diameter (~2.37 nm). In the common DNA polymorph (B-DNA), the helix has a right-handed (or clockwise) rotation. The chirality in the DNA molecule is introduced by the sugar units, with the other units (phosphate groups, bases) being intrinsically achiral. However, in the overall structure chirality is usually observed as changes in the ultraviolet (UV) absorbance of the bases in the 200–300 nm region induced by coupling to the chiral backbone. The chromophore component of the SRh molecule is a planar sequence of seven fused rings. SRh molecules incorporated in DNA/CTMA thin films have[6] main absorption and luminescence peaks at ~575 and 605 nm, respectively. Differences in the CD spectral characteristics between DNA/CTMA and DNA/CTMA:SRh samples result from an induced CD (iCD) effect,[8] caused by the interaction between the chiral DNA polymer and the achiral SRh molecules.

CD experiments were performed both on liquid and thin film samples. The samples consisted of DNA/CTMA dissolved in butanol and combined with SRh dye. The thin films were prepared from the same solutions used for the liquid samples in order to make comparisons between the two states more meaningful.

Salmon sperm DNA is extracted by an enzyme process[9] at the Chitose Institute of Science and Technology, Japan. To improve its film forming characteristics, the as-received high molecular weight (MW) DNA was sonicated[10] to reduce the average MW to approximately 200 kDa. Next, the DNA-Na is reacted with the cationic surfactant CTMA-Cl in water. This forms a DNA/lipid (DNA/CTMA) complex, which precipitates out of the aqueous solution, but is soluble in simple organic solvents. Thin film formation by spin coating is markedly easier with organic solvents versus aqueous solutions. We utilized butanol as the solvent because of its relatively slow evaporation (due to a low vapor pressure) and moderate viscosity. The butanol solutions were all 10 wt % DNA/CTMA. This was dissolved on a rotary mixer overnight at room temperature. Sulforhodamine was added to each solution as a percentage of the weight of DNA/CTMA. The solutions were each filtered through a 0.45 μm syringe-tip polytetrafluoroethylene filter. Solutions of 2.5, 5, 10, 15, 20, and 25 wt % SRh to DNA/CTMA were prepared.

Thin films produced by spin coating were typically ~1.5 μm thick. The spin-coating process started by completely flooding the substrate, followed by spreading the solution for 8 s at 300 rpm, a spin of 1 min at 400 rpm, and finally a drying spin of 10 min at 200 rpm. The film thick-

a)Author to whom correspondence should be addressed. Electronic mail: a.steckl@uc.edu.
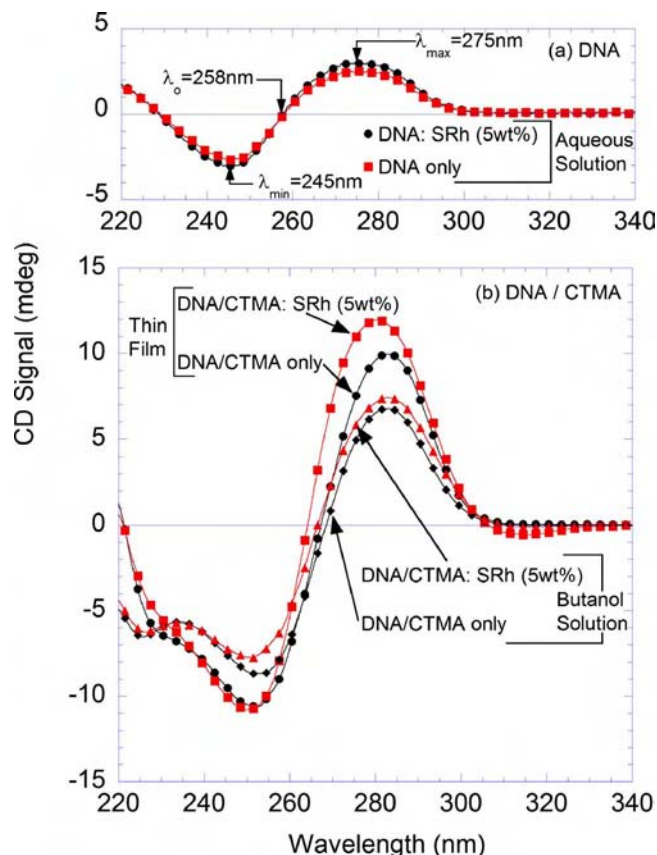
FIG. 1. (Color online) CD signal spectral response for the DNA absorption region (220–340 nm): (a) DNA and DNA/SRh (5 wt %) aqueous solutions and (b) DNA/CTMA and DNA/CTMA:SRh (5 wt %) butanol solutions and thin films.
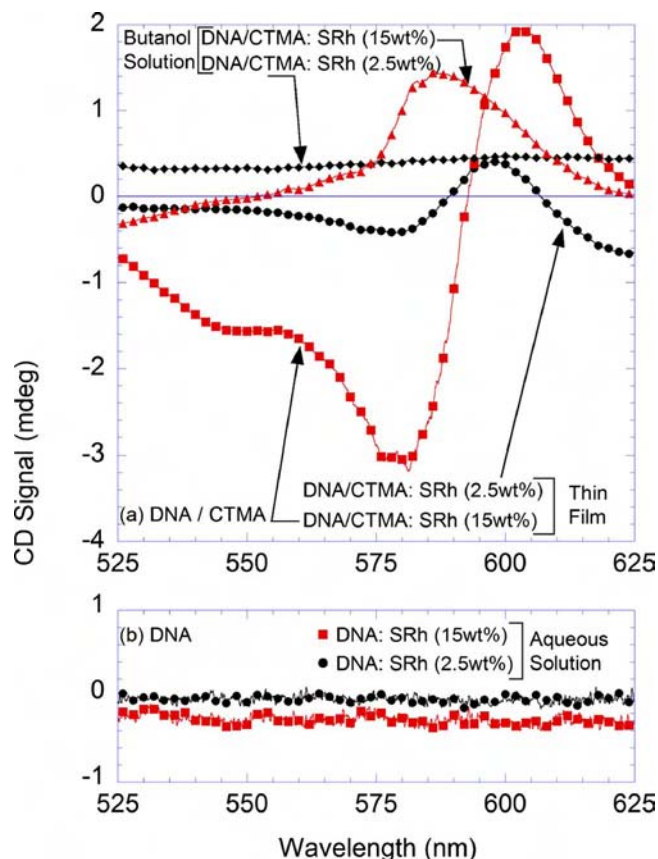

FIG. 2. (Color online) iCD signal spectral response for the SRh absorption region (525–626 nm): (a) DNA/CTMA and DNA/CTMA:SRh (2.5 and 15 wt %) butanol solutions and thin films and (b) DNA and DNA/SRh (2.5 and 15 wt %) aqueous solutions.

ness was verified with a Dektak contact profilometer.

The actual concentrations of SRh in both solution and thin film samples probably differed somewhat from the nominal values given above due to possible losses because of incomplete dissolution or the filtering process. Furthermore, in the case of the thin films it is possible that some of the SRh molecules were aggregated and not uniformly distributed. However, we have no evidence that any of these possibilities resulted in significant reductions in concentration.

CD measurements were performed with a Jasco CD spectrometer. Solution samples used a two part cylindrical cuvette (bottom with cavity and flat top) with a liquid path length of 0.01 mm (10 μm). Background correction was performed using a cuvette filled with butanol. For measurements of solid samples, thin films were spun on the top part of the cuvette. In this case, background correction was performed using a clean cuvette half. The spectrometer settings were a scan speed of 5 nm/min, response time of 1 s, and bandwidth of 15 nm. Three scans were performed and averaged for each sample. The output signal was filtered by the spectrometer software to improve the signal-to-noise ratio. We concentrated our measurements in two spectral regions: 220–340 nm for observing the DNA effects and 525–625 nm for SRh.

As a baseline reference, we measured the CD spectra of aqueous solutions of pure DNA (1 wt %) and of DNA plus SRh (5 wt % to DNA). As shown in Fig. 1(a), both aqueous DNA solutions exhibit the characteristic CD spectral features[7] of B-DNA in the near UV (220–340 nm) region: (a)

a negative band centered at 245 nm, (b) a positive band centered at 275 nm, and (c) a zero crossing at 258 nm. It is clear that the presence of a significant amount of SRh has not affected the CD signal and, hence, the conformation and structure of the DNA molecule.

Near UV CD spectra from DNA/CTMA butanol solutions and thin films were obtained as a function of SRh concentration. Shown in Fig. 1(b) are the results for liquid and solid samples containing DNA/CTMA only and those also containing 5 wt % SRh. Interestingly, the CD results for the different samples in Fig. 1(b) retain most of the spectral features of the DNA aqueous solutions, with a ~7–8 nm shift to longer wavelengths. This indicates that the helical DNA structure is not materially affected by the reaction of DNA with CTMA, by the use of organic solvents for the liquid samples, or by the absence of a liquid environment for the solid samples.

iCD spectra were obtained in the SRh absorption-luminescence wavelength region (525–625 nm). Shown in Fig. 2(a) are spectra for DNA/CTMA thin film and solution samples containing 2.5 and 15 wt % SRh. While the 2.5 wt % SRh solution sample does not show an iCD signal in this spectral window, the 15 wt % SRh solution sample displays a clear positive lobe with a peak at 585 nm. All thin film samples displayed an SRh iCD signal, always with a higher intensity than their solution counterparts due to their much higher effective volume SRh concentration. The 15 wt % SRh thin film exhibits significant negative and positive iCD lobes with maxima at 580 and 598 nm, respec-
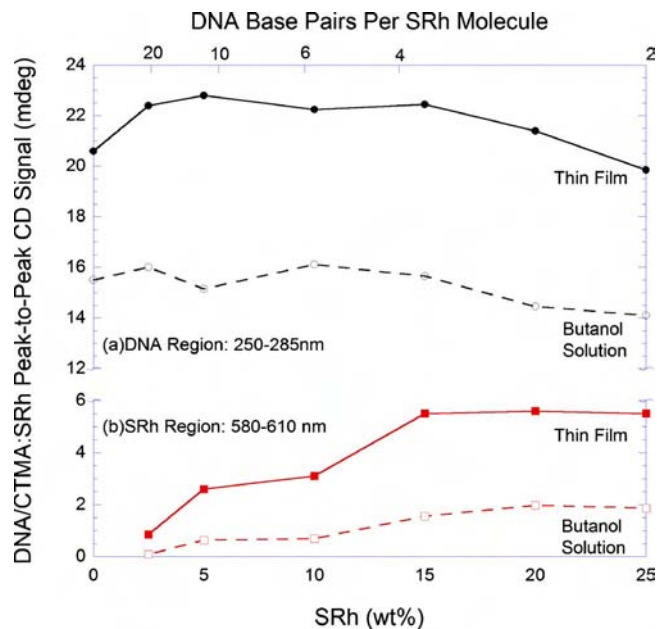
FIG. 3. (Color online) Peak-to-peak CD signal vs SRh concentration: (a) DNA absorption region and (b) SRh absorption region.

tively. Interestingly, aqueous DNA:SRh solutions did not exhibit an SRh iCD signal, as shown in Fig. 2(b). These results lead us to the conclusion that the presence of the CTMA surfactant is critical (in either a direct or indirect way) in enabling SRh to interact with the DNA double helix in order to induce SRh chirality.

The peak-to-peak (negative-to-positive lobe excursion) iCD amplitude is shown in Fig. 3 as a function of SRh concentration in both DNA/CTMA solutions and thin films. In the DNA absorption region (250–285 nm), the CD signal in thin films at first increases with SRh concentration up to ∼5 wt %, after which it is roughly constant up to a concentration of ∼15 wt %, and is followed by a reduction in signal, as shown in Fig. 3(a). It is important to point out that at 25 wt % SRh concentration, which corresponds to one SRh molecule for every two DNA base pairs, the CD signal is only slightly lower than for the film with no SRh. This is a surprisingly large amount of dye molecules being accommodated by the DNA-CTMA polymer. A similar behavior is observed for the solution samples, but at lower signal levels than for the thin film samples.

The iCD signal in the SRh absorption region is shown in Fig. 3(b) as a function of SRh concentration. A monotonic increase in iCD signal strength is observed for both thin film and solution samples with increasing SRh concentration up to ∼15 wt %. The SRh iCD signal becomes essentially satu-

rated at greater SRh concentrations. It is interesting to point out that the SRh iCD signal saturation onset occurs at the same concentration at which the DNA CD signal begins to decrease.

A reasonable explanation of the observed behavior is that the SRh molecules are strongly bound to the DNA/CTMA polymer, but probably not intercalated in the DNA double helix since the DNA/SRh aqueous solutions do not exhibit any iCD in either the DNA or SRh wavelength regions. Strong bonding would explain the presence of significantly enhanced CD for the DNA/CTMA polymer and iCD for the otherwise achiral SRh molecules. The strong, but nonintercalating, bonding would also explain the ability of DNA/CTMA to absorb a very large SRh concentration without losing its chirality.

In summary, CD spectroscopy was utilized to investigate the incorporation of SRh fluorescent dye molecules in DNA/CTMA polymers and to compare their behavior in the liquid state (solution) and the solid state (thin film). A strong iCD signal for SRh in DNA/CTMA indicates that the achiral dye molecule acquired chirality by binding to the DNA/CTMA. In contrast, SRh in DNA aqueous solution does not display an iCD signal, nor is there an enhanced CD signal on the part of the DNA. This clearly indicates the critical role of the CTMA-Cl surfactant in enabling SRh binding. Interestingly, the CD characteristics of thin films and solution samples, while different in signal intensity, followed similar overall trends. Further investigation is required to identify the nature of the SRh-DNA/CTMA binding and the mechanisms that allow such large loading without denaturing of the DNA secondary structure.

[1]A. J. Steckl, Nat. Photonics **1**, 3 (2007).

[2]B. Singh, N. S. Sariciftci, J. Grote, and F. K. Hopkins, J. Appl. Phys. **100**, 024514 (2006).

[3]C. H. Lee, E.-D. Do, Y.-W. Kwon, D.-H. Choi, J.-I. Jin, D.-K. Oh, H. Nishide, and T. Kurata, Nonlinear Opt., Quantum Opt. **35**, 165 (2006).

[4]J. A. Hagen, W. Li, A. J. Steckl, and J. G. Grote, Appl. Phys. Lett. **88**, 171109 (2006).

[5]J. A. Hagen, W. X. Li, H. Spaeth, J. G. Grote, and A. J. Steckl, Nano Lett. **7**, 133 (2007).

[6]Z. Yu, W. Li, J. A. Hagen, Y. Zhou, D. Klotzkin, J. G. Grote, and A. J. Steckl, Appl. Opt. **46**, 7 (2007).

[7]A. Rodger and B. Norden, *Circular Dichroism & Linear Dichroism* (Oxford University Press, Oxford, 1997).

[8]M. Ardhammar, B. Norden, and T. Kurucsev, in *Circular Dichroism: Principles and Applications*, 2nd ed., edited by N. Berova, K. Nakanishi, and R. W. Woody (Wiley, New York, 2000), p. 741.

[9]L. Wang, J. Yoshida, N. Ogata, S. Sasaki, and T. Kajiyama, Chem. Mater. **13**, 1273 (2001).

[10]E. M. Heckman, J. A. Hagen, P. P. Yaney, J. G. Grote, and F. K. Hopkins, Appl. Phys. Lett. **87**, 211115 (2005).

Role of Surfactants in the Interaction of Dye Molecules in Natural DNA Polymers

H. You, H. Spaeth, V. N. L. Linhard, and A. J. Steckl*

Nanoelectronics Laboratory, University of Cincinnati, Cincinnati, Ohio 45221-0030

Received May 8, 2009. Revised Manuscript Received July 10, 2009

Solutions and powders formed from salmon sperm deoxyribonucleic acid (DNA) reacted with the cationic surfactant cetyltrimethylammonium chloride (CTMA-Cl) incorporated fluorescent rhodamine molecules: anionic sulforhodamine 640 (SRh) or cationic/zwitterionic rhodamine 640 perchlorate (RhP). The role of the cationic surfactant in the interaction between rhodamine dye and DNA−surfactant molecules has been investigated in both solution and solid state using optical spectroscopy and electrophoresis. Unexpectedly, the dye molecules did not interact directly with DNA, rather the DNA double helix acted as a template for the interaction between dye molecules and CTMA in the DNA/CTMA complex. The SRh and RhP molecules yield different fluorescence characteristics with increasing DNA/CTMA amount, indicating different configurations between the CTMA ligands.

Introduction

Deoxyribonucleic acid (DNA) polymers, the source of genetic information, are soluble only in aqueous solutions. However, after bonding with cationic surfactants, such as cetyltrimethylammonium chloride (CTMA-Cl), the DNA−surfactant complex is soluble in organic solvents. Formed into thin films, the DNA-based biopolymer material displays many useful properties,[1] such as low optical loss, high temperature stability, tunable refractive index, and low microwave insertion loss. Currently, natural DNA processed from salmon roe and milt sacs, waste products of the fishing industry, is quite abundant and relatively inexpensive. To date, the DNA-based biopolymer has been reported to be a promising new material for photonics,[2] holographic information inscription,[3,4] nonlinear optics,[5,6] electronics,[7] and chemical sensors[8] applications. Significant enhancement in the efficiency and brightness of organic light-emitting diodes that incorporate DNA nanometer thin films has been previously reported.[9,10]

It is well known that many small molecules can readily interact with DNA double helix structures through three different modes: ionic, groove, and intercalation binding.[11] Many fluorescent dye molecules[12,13] intercalate into the double helix of DNA, whereby the intensity of fluorescence is greatly enhanced.[14,15] Amplified spontaneous[16] and stimulated emission[17] from structures containing a DNA−surfactant complex gain medium doped with the fluorescent dye molecules have been reported with quite a low emission threshold. One possible mechanism for the highly efficient light amplification was ascribed[16,18] to the interaction between dye molecules and DNA double helix by either intercalation or groove binding. However, a recent study[19] on circular dichroism (CD) in DNA/CTMA thin films and solutions that incorporated sulforhodamine (SRh) molecules clearly indicated the key role of the surfactant in imparting chirality to the SRh molecules. Actually, considering the structure of DNA−surfactant complexes in the precipitation[20] and solution form,[21] the fluorescent dye molecules may be incorporated between surfactant ligands. Dye−surfactant interactions are of great importance in the dyeing and photographic industries, biological and medicinal photosensitization, and analytical and environmental sciences.[22] More specific to this work, a much more complete understanding of the biophysical mechanisms involved in the interaction between DNA, surfactants, and fluorophores is required in order to fully exploit the potential of combining the unique structure and properties of DNA biopolymers with various light-emitting molecules in optoelectronic devices. Therefore, the relationship between the structure of selected dye molecules and their location and orientation relative to the DNA−surfactant complex needs to be better understood.

*Corresponding author. E-mail: a.steckl@uc.edu.

(1) Kwon, Y. W.; Lee, C. H.; Choi, D. H.; Jin, J. I. *J. Mater. Chem* **2009**, *19*, 1353–1380.

(2) Steckl, A. J. *Nat. Photonics* **2007**, *1*, 3–5.

(3) Mitus, A. C.; Pawlik, G.; Kochalska, A.; Mysliwiec, J.; Miniewicz, A.; Kajzar, F. *Proc. SPIE* **2007**, 6646.

(4) Miniewicz, A.; Kochalska, A.; Mysliwiec, J.; Samoc, A.; Samoc, M.; Grote, J. G. *Appl. Phys. Lett.* **2007**, *91*, 041118.

(5) Grote, J. G.; Hagen, J. A.; Zetts, J. S.; Nelson, R. L.; Diggs, D. E.; Stone, M. O.; Yaney, P. P.; Heckman, E.; Zhang, C.; Steier, W. H.; Jen, A. K. Y.; Dalton, L. R.; Ogata, N.; Curley, M. J.; Clarson, S. J.; Hopkins, F. K. *J. Phys. Chem. B* **2004**, *108*, 8584–8591.

(6) Krupka, O.; El-Ghayoury, A.; Rau, I.; Sahraoui, B.; Grote, J. G.; Kajzar, F. *Thin Solid Films* **2008**, *516*, 8932–8936.

(7) Stadler, P.; Oppelt, K.; Singh, T. B.; Grote, J. G.; Schwodiauer, R.; Bauer, S.; Piglmayer-Brezina, H.; Bauerle, D.; Sariciftci, N. S. *Org. Electron.* **2007**, *8*, 648–654.

(8) Yaney, P. P.; Heckman, E.; Diggs, D. E.; Hopkins, F. K.; Grote, J. G. *Proc. SPIE Int. Soc. Opt. Eng.* **2005**, *5724*, 224–233.

(9) Hagen, J. A.; Li, W.; Steckl, J.; Grote, J. G. *Appl. Phys. Lett.* **2006**, *88*, 171109.

(10) Hagen, J. A.; Li, W. X.; Spaeth, H.; Grote, J. G.; Steckl, A. J. *Nano Lett.* **2007**, *7*, 133–137.

(11) Kumar, C. V.; Asuncion, E. H. *J. Am. Chem. Soc.* **1993**, *115*, 8547–8553.

(12) Waggoner, A. *Curr. Opin. Chem. Biol.* **2006**, *10*, 62–66.

(13) Ihmels, H.; Otto, D. In *Supramolecular Dye Chemistry*; Springer-Verlag: Berlin, Germany, 2005; Vol. *258*, pp 161–204.

(14) Glazer, A. N.; Rye, H. S. *Nature* **1992**, *359*, 859–861.

(15) Larsson, A.; Carlsson, C.; Jonsson, M.; Albinsson, B. *J. Am. Chem. Soc.* **1994**, *116*, 8459–8465.

(16) Kawabe, Y.; Wang, L.; Horinouchi, S.; Ogata, N. *Adv. Mater.* **2000**, *12*, 1281–1283.

(17) Yu, Z.; Li, W.; Hagen, J. A.; Zhou, Y.; Klotzkin, D.; Grote, J. G.; Steckl, A. J. *Appl. Opt.* **2007**, *46*, 1507–1513.

(18) Lee, J. E.; Do, E. D.; Lee, U. R.; Cho, M. J.; Kim, K. H.; Jin, J. I.; Shin, D. H.; Choi, S. H.; Choi, D. H. *Polymer* **2008**, *49*, 5417–5423.

(19) Steckl, A. J.; Spaeth, H.; Singh, K.; Grote, J.; Naik, R. *Appl. Phys. Lett.* **2008**, *93*, 193903.

(20) Leal, C.; Wadso, L.; Olofsson, G.; Miguel, M.; Wennerstrom, H. *J. Phys. Chem. B* **2004**, *108*, 3044–3050.

(21) Sergeyev, V. G.; Mikhailenko, S. V.; Pyshkina, O. A.; Yaminsky, I. V.; Yoshikawa, K. *J. Am. Chem. Soc.* **1999**, *121*, 1780–1785.

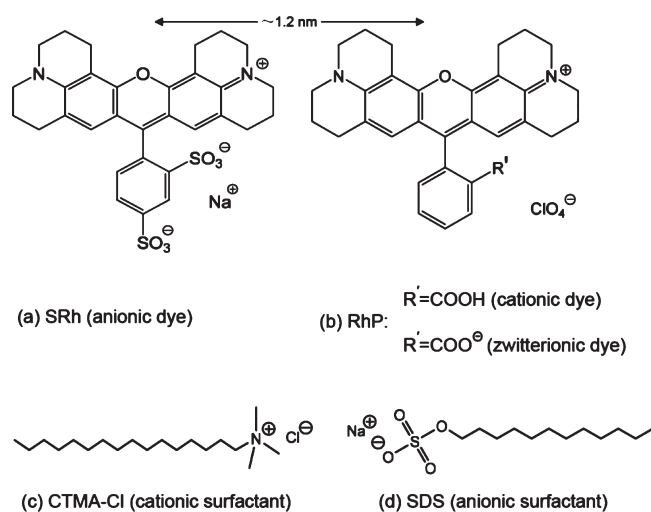(22) Micheau, J. C.; Zakharova, G. V.; Chibisov, A. K. *Phys. Chem. Chem. Phys.* **2004**, *6*, 2420–2425.

Figure 1. Chemical structure of molecules employed in this study: (a) SRh, anionic dye; (b)RhP, cationic/zwitterionic dye; (c) CTMA-Cl, cationic surfactant; (d) SDS, anionic surfactant.
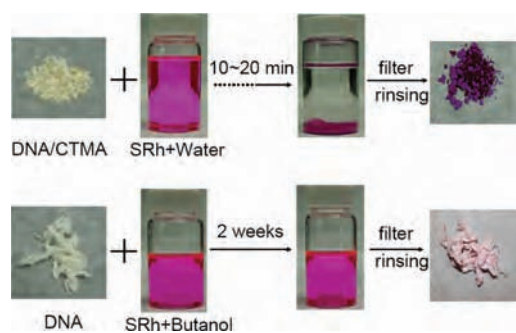

Figure 2. Photographs illustrating the interaction between DNA/CTMA powders and DNA fibers and SRh aqueous and butanol solution.

In this paper we report on the nature of the interaction between the DNA-Na polymer complexed with a cationic surfactant (CTMA-Cl) and sulforhodamine sodium (SRh) or rhodamine perchlorate (RhP) dye molecules (see molecule structures in Figure 1). The triggering event for this investigation was the dramatic effect observed when DNA/CTMA whitish fibrous powder was added to SRh aqueous solution, which was normally pink in color. As seen in Figure 2, the solution became clear, and the DNA/CTMA powder (which does not dissolve in water) became pink. This change occurred in 20−30 min for a still solution and in 10−15 min for an agitated solution. The DNA/CTMA powder retained its pink color after repeated rinsing in clean water. A similar phenomenon was observed when RhP was substituted for SRh.

Since SRh is soluble in organic solvents as well as water, a complementary experiment was carried out. DNA-Na fibers were introduced into a SRh butanol solution. After duration as long as 2 weeks, the solution did not change color and the DNA-Na fibers regained their whitish color after rinsing in clear butanol solvent (see Figure 2). Since the DNA−surfactant complex is tested in SRh aqueous solution, whereas the DNA-Na is tested in SRh butanol solution; additional DNA-Na experiments were performed with longer chain alcohols to simulate the surfactant environment. The results for DNA-Na in SRh 1-hexadecanol ($C_{16}H_{33}OH$) solution were similar to those in the case of DNA-Na into SRh butanol solution.

Therefore, we conclude that the dye molecules did not interact directly with the DNA double helix, which just acted as a template for the interaction between dye molecules and CTMA in the DNA/CTMA complex. The SRh and RhP molecules yield different fluorescence characteristics with increasing DNA/CTMA amount, indicating different configurations inside the CTMA ligands.

Experimental Methods

Materials and Sample Preparation. Salmon sperm DNA is extracted by an enzyme process at the Chitose Institute of Science and Technology, Japan.[23] To improve film forming characteristics,[24] the as-received high molecular weight (MW) DNA (25−10 MDa) was sonicated, reducing the average MW to approximately 200 KDa. Next, the DNA-Na is reacted with the cationic surfactant CTMA-Cl (0.01 M) in water. This forms a DNA/lipid (DNA/CTMA) complex, which precipitates out of the aqueous solution but is soluble in simple organic solvents. For the DNA/dye/CTMA solution, fluorescent dye (5 wt % to DNA/CTMA) is added into the DNA-Na aqueous solution, and then reacted with the surfactant solution, resulting in the precipitation of a pink DNA/dye/CTMA complex, which dissolves into butanol to obtain the DNA/dye/CTMA solution. For the DNA/CTMA/dye solution, the DNA/CTMA complex is formed first. Then it is reacted with the dye molecules in an organic solvent to obtain the DNA/CTMA/dye solution. Butanol was utilized as the organic solvent because of its relatively slow evaporation (due to a low vapor pressure) and moderate viscosity. All solution samples were dissolved on a rotary mixer overnight at room temperature. The DNA/CTMA/dye solutions were made with different weight ratios of DNA/CTMA to dye molecules. Optical absorption of DNA/CTMA/dye and DNA/dye/CTMA solution was performed over the near-ultraviolet and visible (UV−vis) spectrum.

For dye absorption experiments, dye molecules in 0.0025 wt % aqueous and organic solutions incorporating insoluble DNA/CTMA powders and DNA-Na fibers, respectively, were used. The amount of the dye introduced into the solution was chosen such that there was 1 dye molecule for 10 DNA base pairs. UV−vis absorption spectrum measurements were performed at 15 min intervals, utilizing 0.8 mL of the pure solution without undissolved DNA-Na fibers or DNA/CTMA powders, which was then returned into the main mixture container after the test.

For the decomposition experiments, equal amounts (0.84 mmol) of DNA/SRh (5 wt %) /CTMA and DNA/CTMA were treated with 10 mL of sodium dodecylsulphate (SDS) (Aldrich) aqueous solution (0.168 M). This is equivalent to 1 SRh molecule for every 10 DNA base pairs and 20 CTMA molecules and 20 SDS molecules. The mixtures were placed in a rotary mixer for 48 h at room temperature and then filtered with 0.45 μm PVDF syringe filter to separate the solution from any remaining solid. The solutions were first used for UV absorption measurements. This was followed by treatment with 1 mL of diluted DNA-specific PicoGreen (Invitrogen, Inc.) dye solution, and then used for the photoluminescence (PL) measurements. Solutions with the same amount of DNA/CTMA and DNA/SRh/CTMA in water without SDS were also tested for comparison. The solutions without PicoGreen dye were also concentrated for the electrophoresis experiment.

Measurement. A Perkin-Elmer spectrometer (Lambda 900) was used to measure the UV absorption spectrum of different solutions. The PL measurements were performed with He−Cd laser excitation (Omnichrome Series 74) at 325 nm or Argon laser excitation (Omnichrome 532−100MBS) at 488 nm. The emission spectra were analyzed by an Acton Research spectrometer

(23) Wang, L. L.; Yoshida, J.; Ogata, N.; Sasaki, S.; Kajiyama, T. *Chem. Mater.* **2001**, *13*, 1273–1281.
(24) Heckman, E. M.; Hagen, J. A.; Yaney, P. P.; Grote, J. G.; Hopkins, F. K. *Appl. Phys. Lett.* **2005**, *87*, 211115.
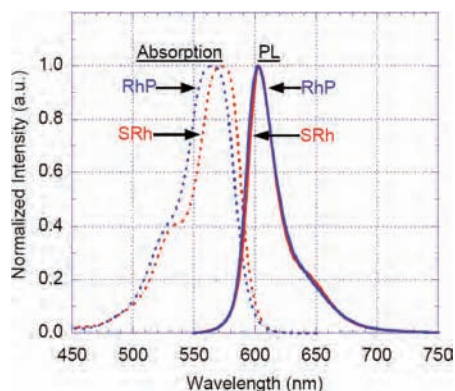
Figure 3. Optical absorption and PL spectra (488 nm excitation) of SRh and RhP in butanol solution.

(SP2550) equipped with a photomultiplier sensitive in the UV−vis spectrum. High-pass filters and dichroic mirrors were utilized to block the laser pump light. The spectrometer resolution was 0.16 nm. The PicoGreen PL measurements were performed with a NanoDrop 3300 Fluorospectrometer. The electrophoresis was performed with 0.5 wt % agarose gel in TAE buffer. Ethidium bromide was used to label the DNA. All measurements were performed at 300 K.

Results and Discussion

The rhodamine dye family is a derivative of xanthene, incorporating a central group of heterocyclic fused rings. Rhodamine dyes are widely used as the gain medium in dye lasers and in fluorescence analysis. SRh is an anionic molecule in both aqueous and organic solutions, whereas the RhP molecule can take both the cationic and zwitterionic form in solution. The relative abundance of the two forms depends on the dye concentration, solvent viscosity, and dielectric constant.[25−27] The UV−vis absorption and PL spectrum of the dye molecules in butanol solution are shown in Figure 3.

The relationship between the state of the DNA (Na salt vs surfactant complex), the SRh molecules, and the solvent was first quantified by measuring the optical absorption of the dye solutions. Figure 4 shows the time dependence of the normalized SRh and RhP absorption in butanol, into which DNA-Na fibers were added, and in aqueous solution, into which DNA-CTMA powder particles were added. The SRh and RhP absorption in butanol did not change with time upon the introduction of DNA-Na fibers, indicating that, to a first approximation, there is no direct dye−DNA reaction. On the other hand, the dye absorption in aqueous solution dramatically decreased with time with addition of DNA/CTMA powder particles. This demonstrates that the DNA/CTMA can react with dye molecules and remove them from their aqueous solution, whereas the DNA-Na is unable to perform the counterpart reaction in butanol solution. This clearly indicates there is no direct interaction between the DNA and dye molecules. Also, no evidence was observed for ion exchange between the CTMA ligands in the DNA/CTMA complex and dye molecules when the dye was mixed with DNA/CTMA in butanol solution. CD spectroscopy also supports these conclusions, as there was a strong induced CD signal for SRh in DNA/CTMA butanol solution, whereas SRh in DNA aqueous solution did not display a CD signal.[19]
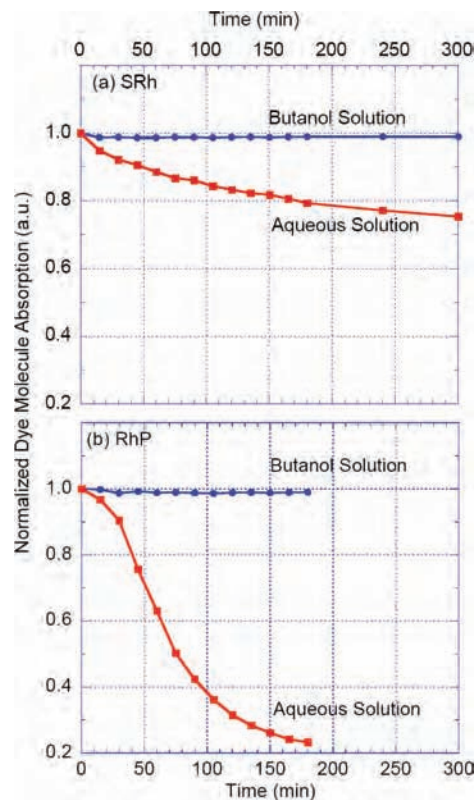

Figure 4. Time dependence of the normalized dye molecule absorption (∼560−570 nm) in butanol (with DNA-Na fiber) and in aqueous solution (with DNA/CTMA powder): (a) SRh; (b) RhP.

It is well known that DNA−cationic surfactant complexes can be decomposed by the addition of anionic surfactants[28] or monovalent salts.[29] The DNA is released from the DNA−cationic surfactant complex and surfactant aggregate structures are formed because the interaction between oppositely charged surfactants is stronger than the one between DNA and cationic amphiphiles.[30] This presents an opportunity to further understand the interaction between DNA, surfactant, and dye molecules. The decomposition of DNA/CTMA complexes was investigated with the addition of the anionic surfactant SDS in aqueous solution (see structure in Figure 1d). As the DNA/CTMA powder is not soluble in water, the decomposition is not complete even after 48 h. UV−vis absorption and PL of the DNA/CTMA−SDS solution were used to characterize the degree of decomposition. The influence of SRh dye molecules on the decomposition of DNA/CTMA complexes was investigated. PicoGreen was used to identify the presence of DNA double helix molecules. In Figure 5, spectra from DNA/SRh/CTMA and DNA/CTMA aqueous and SDS solutions are compared. Since DNA/CTMA complexes do not readily dissolve in water, all solutions were filtered prior to optical measurements to remove particulates. Comparing the SDS-based solutions in Figure 5a, it is clear that the presence of the SRh molecules greatly amplified the decomposition process, leading to very strong UV (265 nm) absorption from DNA and red (590 nm) absorption from SRh. Similarly, in Figure 5b, the decomposed DNA/SRh/CTMA+ SDS solution exhibited strong PL signal from intercalated PicoGreen

(25) Ramette, R. W.; Sandell, E. B. *J. Am. Chem. Soc.* **1956**, *78*, 4872–4878.
(26) Arbeloa Lopez, I.; Rohatgi-Mukherjee, K. K. *Chem. Phys. Lett.* **1986**, *128*, 474–479.
(27) Laughlin, R. G. *Langmuir* **1991**, *7*, 842–847.

(28) Bhattacharya, S.; Mandal, S. S. *Biochemistry* **1998**, *37*, 7764–7777.
(29) Melnikov, S. M.; Sergeyev, V. G.; Yoshikawa, K.; Takahashi, H.; Hatta, I. *J. Chem. Phys.* **1997**, *107*, 6917–6924.
(30) Dias, R.; Rosa, M.; Pais, A. C.; Miguel, M.; Lindman, B. *J. Chin. Chem. Soc.* **2004**, *51*, 447–469.
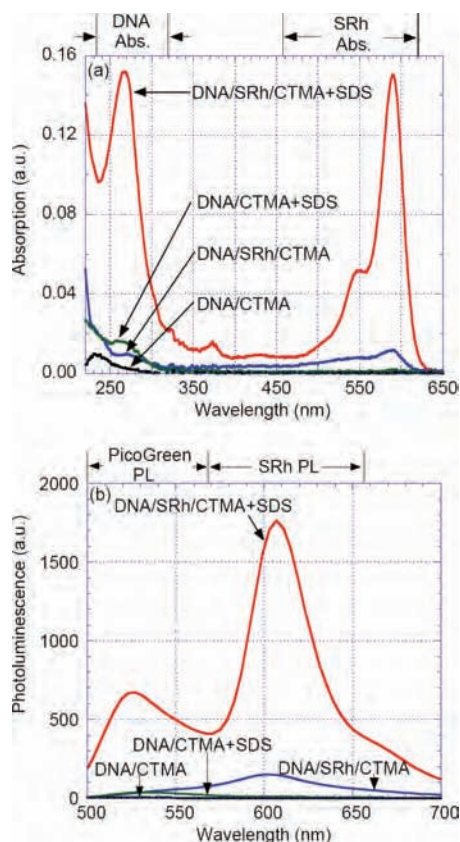
Figure 5. Decomposition of DNA/SRh/CTMA and DNA/CTMA in SDS solution: (a) UV−vis absorption spectra; (b) PL spectra. Solutions were filtered to remove solids remaining after 48 h. For comparison, spectra of DNA complexes in plain aqueous solutions are also shown.

molecules (with a peak at 520 nm) and from SRh molecules (at 605 nm). On the other hand, the DNA/CTMA+SDS solution had very weak UV absorption and PicoGreen fluorescence, indicating a much less effective decomposition. As expected, the DNA/SRh/CTMA and DNA/CTMA plain aqueous solutions showed very weak absorption or PL signals. When the filtered DNA/SRh/CTMA+SDS solution was concentrated and investigated by gel electrophoresis, the DNA and SRh molecules separated under the electric field, with DNA moving toward the anode and SRh moving toward the cathode. All of these observations demonstrate that the dye molecules react with CTMA and not directly with DNA in the DNA/CTMA complex.

The interaction between the two oppositely charged surfactant and dye molecules, SRh and CTMA-Cl (without DNA), in aqueous solution ([SRh] = 40 μM, [CTMA] = 0.8 mM) was investigated by optical measurements. The results are shown in Figure 6. For comparison, the results for DNA/SRh/CTMA butanol solution with the same SRh concentration are also presented. Interaction between SRh and CTMA-Cl molecules in aqueous solution was indicated by the UV−vis absorption and PL intensity decrease and slight blue shift in the peak position. The significant differences in absorption and PL between the plain dye solution and the dye−surfactant aqueous solution clearly indicate the strong interaction between the oppositely charged molecules. A similar effect has been reported[22] for rhodamine 6G and SDS solutions and attributed to an ion pair aggregation process. The fact that the SRh and SRh/CTMA butanol solutions exhibited nearly the same absorption and PL is attributed to the absence of micelle formation in organic solution (unlike the case
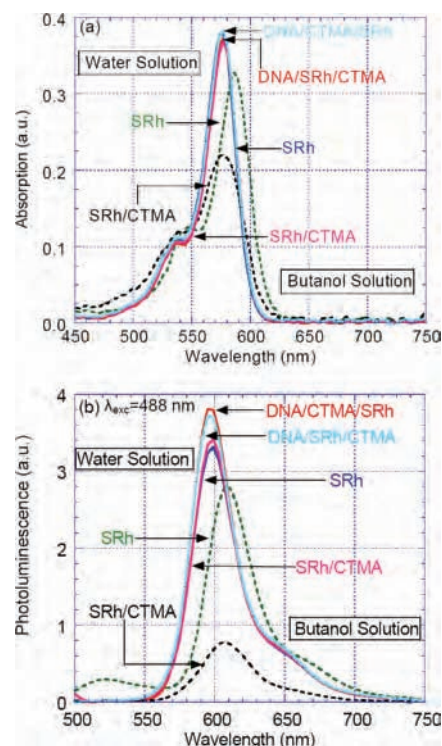

Figure 6. UV−vis absorption spectrum (a) and PL spectrum (488 nm excitation) (b) of SRh molecules with the addition of CTMA in butanol (solid line) and in aqueous solution (dash line), respectively. Data for DNA/SRh/CTMA and DNA/CTMA/SRh in butanol solutions is also shown for comparison.
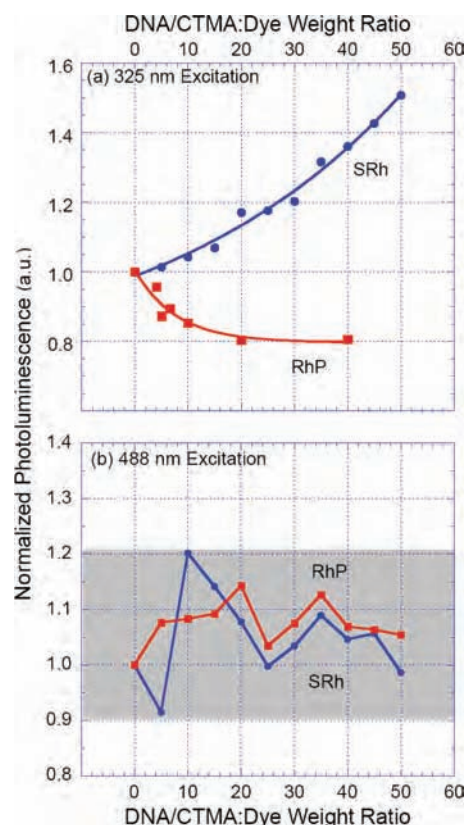

Figure 7. Normalized PL intensity of SRh (left) and RhP (right) in butanol solution with the addition of different weights of DNA/CTMA with excitation at 325 nm (up) and 488 nm (down), respectively.
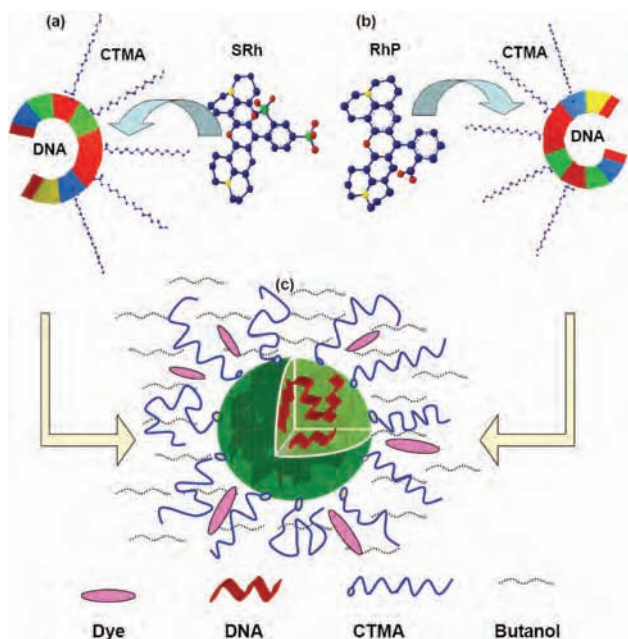
Figure 8. Expected SRh (a) and RhP (b) molecule incorporation dynamics inside the CTMA molecules in the DNA/CTMA and the final structure of the solvable DNA/dye/CTMA complex in solution (c). For simplicity, only CTMA ligands located on the surface of the globule are shown.

in aqueous solution). This indicates that the interaction between the CTMA and dye molecules in DNA/CTMA complex can not be attributed to the formation of ion-pair aggregates, which would result in significant changes in the intensity and wavelength of the absorption and PL from the dye molecules.

To more fully understand the dye molecule configuration in DNA/CTMA, the PL intensity of SRh and RhP with different weight ratios between DNA/CTMA and dye in butanol solutions was measured. The results are shown in Figure 7. It is very interesting to note that, when the 325 nm laser excitation was used, the SRh PL intensity increased with increasing DNA/CTMA in the solution, whereas the RhP PL intensity decreased with DNA/CTMA concentration. When the excitation source was changed to 488 nm argon laser, the PL intensity of both SRh and RhP stayed within a common band with different DNA/CTMA concentrations in the butanol solution. On the other hand, as shown in Figure 4, compared to SRh, RhP molecules are easier to remove from their aqueous solutions by DNA/CTMA powders. This indicates that the SRh and RhP molecules interact with the CTMA ligands in the DNA/CTMA complex with different mechanisms. Considering the structures of these two

dye molecules[25] (Figure 1) and of the DNA−surfactant complex in alcohol solution,[21] it is reasonable to ascribe this difference to the dye molecular structures. For SRh, the steric effect due to two sulfates in the phenyl group is important as the SRh molecules incorporate into CTMA ligands in the DNA/CTMA complex. It is likely that the xanthene group incorporates first and then the phenyl group, as shown schematically in Figure 8. By comparison, the phthalide group in RhP molecules is more easily incorporated into CTMA ligands without hindrance, resulting in the fast removal of RhP dye from aqueous solution by DNA/ CTMA powders. After incorporation, the xanthene group, which is the fluorescing group in rhodamine dyes, is located closer to the DNA base pairs for SRh compared to RhP molecules. This would lead to more efficient energy transfer between SRh molecules and DNA base pairs. Using 325 nm laser excitation, which is in the range of DNA absorption, energy is mostly absorbed by the DNA base pairs and then transferred to SRh molecules, followed by emission from SRh excited states. As the DNA/CTMA concentration increases, more energy is absorbed by base pairs and transferred to SRh, leading to increasing PL signal from SRh molecules. For RhP solutions, the greater distance between the xanthene group and the DNA base pairs prevents efficient energy transfer. Therefore, increasing DNA/CTMA concentration leads to more laser energy being absorbed by base pairs and less energy available for RhP excitation, resulting in decreasing RhP PL. When 488 nm excitation is used, which is in the range of rhodamine absorption (Figure 1c), the energy is mainly directly absorbed by the dye molecules, and therefore the PL signal is independent of the DNA/CTMA concentration in the solution.

In summary, the interaction between the rhodamine dye molecules and DNA−surfactant complexes has been investigated. In contrast to the common assumption that dye molecules will interact directly with DNA double helices through either groove or intercalation binding, it appears that the DNA double helix structure simply acts as a template for the interaction between the CTMA ligands and xanthene dye molecules. Anionic SRh and cationic/zwitterionic RhP dyes incorporate into the CTMA with different directions, which yields different fluorescence characteristics in DNA/CTMA alcohol solution. Understanding and controlling the complex interactions between DNA polymers, surfactants, and dye molecules can lead to novel optoelectronic devices.

Direct write electron beam patterning of DNA complex thin films

R. A. Jones, W. X. Li, H. Spaeth, and A. J. Steckl[a)]
Nanoelectronics Laboratory, University of Cincinnati, Cincinnati, Ohio 45221-0030

The authors report on the first use of direct write electron beam lithography (DW-EBL) patterning of DNA-based materials. Water insoluble and organic solvent soluble DNA:CTMA complexes were formed by reaction of DNA polymers with cationic surfactants and other molecular species. Thin films with thicknesses ranging from 85 to 300 nm were prepared by spin coating. DW-EBL was conducted using a Raith 150 system. The resulting exposed areas demonstrated either positive or negative resist properties depending on development solution. The characteristics of the DNA:CTMA material as a patternable electron sensitive resist medium are presented for different exposure conditions (10–30 kV), development conditions, structure sizes (100 nm to 20 μm), and structure complexities. Contrast values of ~2 have been obtained in both positive and negative resist modes. Both simple (20 μm diameter circle and square) and complex (Fresnel lens) patterns with nanometer scale features (<100 nm) in DNA films are possible using this method. © *2008 American Vacuum Society.* [DOI: 10.1116/1.2993258]

I. INTRODUCTION

Interest in using the unique properties of DNA has grown rapidly in the areas of bioelectronics and photonic device applications.[1–4] Several properties and processing characteristics are required in order for DNA materials to be usefully incorporated into devices. These include the formation of functional complexes and thin/thick films, ability to pattern the films, and incorporation of the patterns into device structures. The ability to form well characterized DNA complexes in solution and to form thin films with predictable properties by spin coating has been established.[5] We have previously demonstrated the use of DNA complex thin films in high performance organic light emitting diodes[6] and in optically pumped laser applications.[7] To date, several indirect techniques such as surface functionalization,[8] molecular lift-off,[9] or charge trapping[10] have been reported for obtaining DNA nano- and micro-scale features. In these patterning techniques, the DNA thin film is patterned by either the topography or the surface modification of the underlying material. Given the interest in DNA-based devices and material applications at the micro- and nano-scale (such as quantum wires, biosensors, and others) it is important to develop techniques for fine feature patterning of the DNA material. We present the first results, to our knowledge, of direct patterning of DNA thin films by electron beam lithography.

The exposure mechanism is well established for typical electron beam sensitive polymers such as poly(methyl methacrylate) for positive resist[11] and SU-8 for negative resist.[12] In positive resists, energetic secondary electrons break chemical bonds and release acid groups that in turn cut the long chain polymer into many smaller chains with lower molecular weights (MWs). This process results in development selectivity between unexposed longer chains and exposed shorter chains, with the lower MW chain polymers

being removed during development. In the case of negative resist, the absorbed secondary electron energy promotes cross-linking of the polymer chains, leading to higher MW material. The lower MW material is again selectively removed during development. Natural DNA is water soluble, which greatly limits its ability to form uniform thin films and is incompatible with standard chemical processes. Reacting DNA with cationic materials forms DNA complexes which are insoluble in water but readily soluble in organic solvents. We have utilized the reaction of DNA with $CH_3(CH_2)_{15}N(CH_3)_3$•Cl [hexadecyltrimethylammonium chloride (CTMA)] to form a DNA:CTMA (Ref. 2) complex which is soluble in butanol (and other organic solvents) and leads to the formation of uniform thin films by the spin-coating technique. Exposure to energetic electrons, shown schematically in Fig. 1, locally modifies the DNA:CTMA complex such that the exposed areas are selectively developed in aqueous solutions and the unexposed areas are selectively developed in specific organic solvents.

II. EXPERIMENT

The formation of DNA:CTMA solutions and the related material properties are discussed in previous work.[5] The film thickness is determined by the concentration of DNA:CTMA in butanol and the spin speed. In this experiment the 3 and 5 wt % DNA:CTMA in butanol solutions were used to spin coat uniform thin films ranging from 85 to 300 nm. The reproducibility of these results was verified by profilometry and ellipsometry. The thin films were then soft baked at 100 °C for 60 s. Previous work[13] suggests that the DNA:CTMA material is stable at temperatures ≤240 °C.

The electron beam patterning of the DNA:CTMA thin films was carried out using a Raith 150 direct write electron beam lithography (DW-EBL) system. All initial experiments involving development and beam conditions were conducted using two dose matrix designs consisting of arrays of 20 μm circles or squares. The exposure dose ranged from 0 to
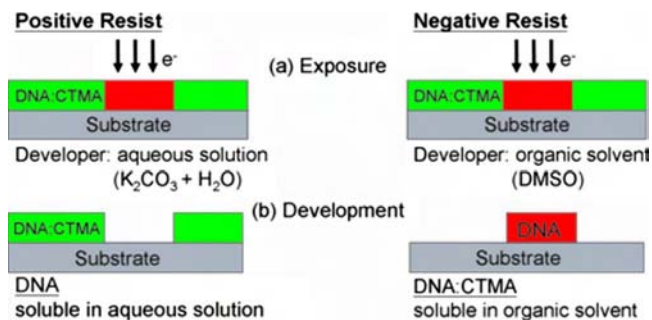
---

a)Electronic mail: a.steckl@uc.edu

FIG. 1. Electron beam lithography patterning process of DNA complex thin films: (a) exposure and (b) development.

742.5 $\mu C/cm^2$ in 7.5 $\mu C/cm^2$ increments (circles) and 15 to 600 $\mu C/cm^2$ in 15 $\mu C/cm^2$ increments (squares). Development conditions were determined using aqueous solutions and organic solvent solutions, with and without ultrasonic assistance. The effects of electron beam conditions were determined by varying the accelerating potential from 5 to 30 kV. In addition, the effect of beam current density was investigated by using two apertures (30 and 60 μm) at each accelerating potential. The beam spot size as a function of accelerating potential is constant in the selected current range but decreases with increased accelerating potential. For example, the spot size for a 20 kV accelerating potential is ~2 nm for beam currents from a few picoamperes to 100 nA. DNA:CTMA films with thicknesses from 85 to 300 nm were exposed. The results in this study used 85 and 100 nm films. Finally, the Raith "demo pattern" was exposed to determine resolution and the effect of complex geometries for the exposure/development process.

III. RESULTS

Development chemistry for the exposed dose matrix patterns was tested for a variety of aqueous solutions and organic solvents. The results summarized in Table I demonstrate that both positive and negative mode developments are possible. Using water or water with a weak salt solution removed the exposed areas. Water by itself removed the exposed areas but required a fairly long development time (~20 min) while immersed in an ultrasonic bath. The addition of small amounts of the salt potassium carbonate (K_2CO_3; 0.1–0.25 wt %) drastically reduced the development time to ~60 s and increased the resolution. K_2CO_3 is soluble in water (insoluble in alcohols), forming strongly alkaline solutions. Thus, aqueous development of DNA:CTMA acted like a positive resist developer. Several organic solvents such as butanol, propanol, and dimethylsulfoxide [$(CH_3)_2SO$; (DMSO)] were found to remove the unexposed DNA:CTMA regions. DMSO is a highly polar solvent and is usable with both water and other organic liquids. Short (<5 s) development with DMSO in an ultrasonic bath yielded the best results. Thus, development of DNA:CTMA using specific organic solvents yielded a negative resist behavior.

Resist parameters of contrast (γ) and clearing dose (D_{80}) for DNA:CTMA were measured using the square pattern dose matrix developed for 30, 60, and 90 s with H_2O +0.1 wt % K_2CO_3 solution for the positive resist process and 5 and 30 s for the DMSO negative resist process. The results for the positive process are shown in Fig. 2 for a 60 μm aperture, accelerating potentials of 10, 20, and 30 kV, and 60 s development time. The γ for these curves increased from ~1.3 to ~1.9 with increased accelerating potential, while D_{80} increased from 160 to 410 $\mu C/cm^2$. D_{80} is

TABLE I. Development conditions and results for electron beam exposed DNA:CTMA films for various positive- and negative-tone solvents.

| Developer	Time (s)	Ultrasonic (min)	Development selectivity	Resist type (+/−)
Water		20	Yes (fair)	(+)
K_2CO_3+water (0.1 wt %)	60	1	Yes (good)	(+)
K_2CO_3+water (6.25 wt %)		1	No (all material removed)	
Butanol		11	Yes (poor)	(−)
Toluene	60	5	No (all material removed)	
Dichloromethane	70	5	No (no development)	
Chlorobenzene	60	10	No (no development)	
Tetrahydrofuron	60		No (all material removed)	
DMSO		30	No (all material removed)	
DMSO		<5	Yes (good)	(−)
Amino-ethanol	60		No (all material removed)	
2-propanol	80	5	Yes (poor)	(−)
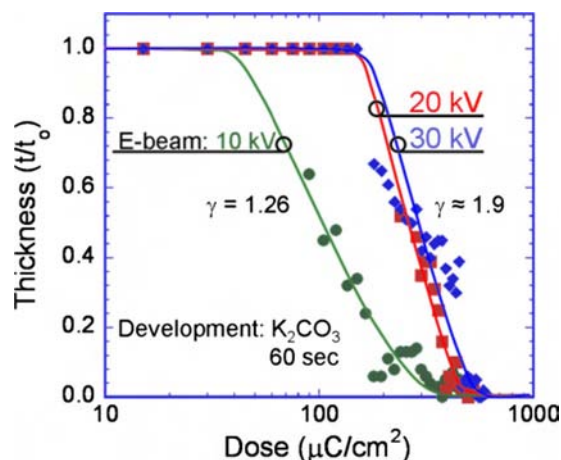
FIG. 2. Contrast curves for K_2CO_3 "positive" resist development: normalized remaining DNA:CTMA film thickness as a function of electron dose for 10, 20, and 30 kV. Contrast (γ) ranges from ~1.3 to ~2 and clearing dose (D_{80}) ranges from ~160 to 440 $\mu C/cm^2$.

defined as the dose where 80% of the material is developed. The results for the negative process are shown in Fig. 3 for a 60 μm aperture, 10 kV accelerating potential, and 5 s development time. For the negative resist development case, the γ is 2.1 and D_{80} is 400 $\mu C/cm^2$. The results for the exposures with the 30 μm aperture and different development times are similar.

Examples of DW-EBL patterning of DNA:CTMA films are shown in Fig. 4 for positive (K_2CO_3) development and in Fig. 5 for negative (DMSO) development. Atomic force microscopy (AFM) was used to scan the exposed and developed surface and create the surface and line scans. The scanned feature for both the positive and negative resist processes is part of the circular dose matrix, namely, a 20 μm diameter circle exposed at 10 kV with a dose of 240 $\mu C/cm^2$. The positive resist feature (Fig. 4) was devel-
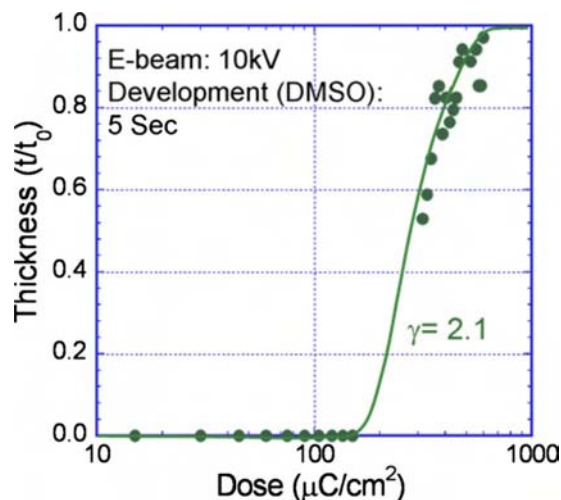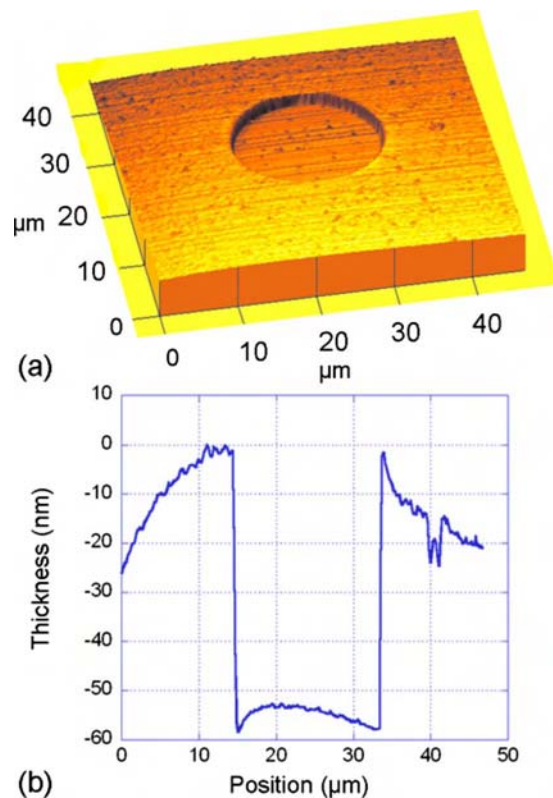

(a)

(b)

FIG. 4. AFM surface and line scan of DNA:CTMA pattern electron beam exposed at 10 kV and developed in K_2CO_3 for 60 s.

oped with 0.1 wt % K_2CO_3 solution for 60 s in an ultrasonic bath, while the negative resist process (Fig. 5) was developed with DMSO for 5 s. The original DNA:CTMA film thickness was 85 nm. The exposure dose of 240 $\mu C/cm^2$ at 10 kV is below the clearing dose for both development processes in Figs. 4 and 5. Therefore, the feature depths of ~60 and 30 nm for the positive and negative developments are less than the original 85 nm original DNA:CTMA film thickness. Both development methods produce fairly uniform features with sharp sidewall profiles. The lateral feature measurement deviates from the nominal 20 μm pattern size by <10%.

With the exposure parameters determined, several patterns involving nanoscale features and complex patterns were exposed. Feature sizes as small as 70 nm were confirmed for both the positive and negative resist processes. The AFM area and line scan in Fig. 6 of the Raith demo pattern Fresnel lens structure demonstrate both the ability to directly write complex patterns with DW-EBL in the 85 nm thin film DNA:CTMA material and resolve <100 nm features. The positive-tone pattern was obtained by electron beam exposure at 10 kV with a dose of 500 $\mu C/cm^2$ and development in 0.1 wt % K_2CO_3 solution for 60 s. The line scan shows clear features with depths of ~40–60 nm. The narrow outer ring of the lens structure has a width of ~100 nm. Features ranging from 75 nm to 1 mm have been written using the Raith 150 DW-EBL system.
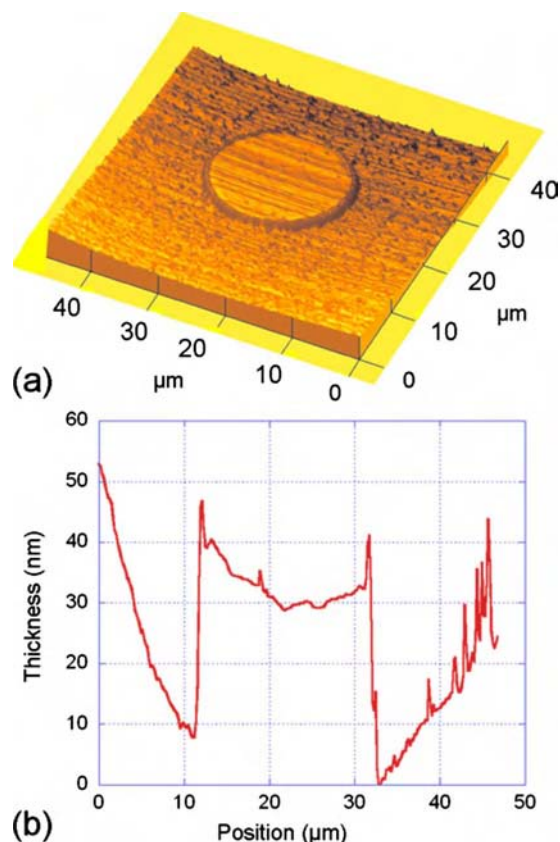

FIG. 3. Contrast curves for DMSO "negative" resist development: normalized remaining DNA:CTMA film thickness as a function of 10 kV electron dose for 5 s development. The contrast (γ) is 2.1 and the clearing dose (D_{80}) is ~400 $\mu C/cm^2$.

FIG. 5. AFM surface and line scan of DNA:CTMA pattern electron beam exposed at 10 kV and developed in DMSO for 5 s.
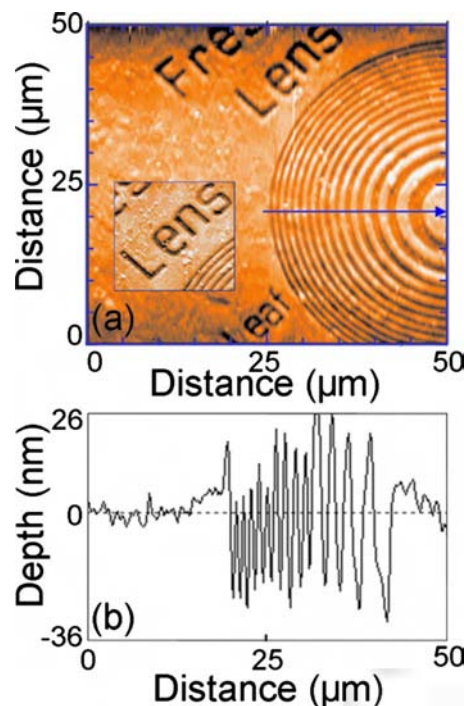

FIG. 6. AFM surface and line scan of micro/nanoscale features using the Raith demo pattern: (a) surface image of the Fresnel lens structure; (b) line scan of the Fresnel lens structure with smallest features measuring 100 nm. Positive-type pattern developed with K_2CO_3 for 60 s. Insert shows a section of the surface scan modified to improve resolution.

IV. DISCUSSION AND CONCLUSIONS

In this work we have shown that DNA:CTMA thin film material is sensitive to electron beam energies and that DW-EBL is a viable and relatively simple method for nanoscale patterning of such materials. In addition, development chemistry provides an avenue for either positive- or negative-type resist development by simply changing the development solution. Thin films of DNA:CTMA can be formed by spin coating ranging from ~50 nm to greater than 2 μm by increasing the wt % of DNA:CTMA in butanol and varying the spin speed. Contrast coefficients of 1.9–2.1 for positive and negative resist developments are comparable to commonly used positive and negative resists.[11,14] Clearing doses ranging from 160 to 450 μC/cm^2 are also comparable to these for existing resists.

We have also demonstrated features that can be exposed/developed by both positive and negative resist development processes. The larger features are shown to have a precise shape and sharp sidewalls. This process has the potential for increasing the basic knowledge of the DNA molecule and is well suited for incorporating DNA:CTMA and DNA complex materials in device applications.

The working hypothesis for the exposure/development mechanisms is still under investigation and will be published elsewhere. Possible mechanisms that need to be considered include the following: (1) electron energy breaks the ionic bond of the DNA:CTMA, resulting in the disassociation of the DNA and CTMA; (2) electrons directly charge the DNA:CTMA molecule, changing the hydrophobic character of the material; (3) electrons dissociate the alkyl tail of the CTMA molecule, reducing its hydrophobicity; (4) electrons break the double helix structure of the DNA, resulting in small double helix or single strand DNA segments, with higher solubility. All the above mechanisms can lead to the formation of water soluble DNA and CTMA or the DNA:CTMA itself becoming soluble in aqueous solution.

DNA thin films have remarkable potential for photonic applications. The discovery of direct e-beam patterning of DNA complex films creates new opportunities for incorporating DNA in novel biodevices. To fulfill these opportunities, we plan to investigate in detail the exposure/development mechanisms and their effects on the DNA material properties. We will be exploring electronic and electro-optic device applications for the DW-EBL patterning process of DNA.

[1] A. J. Steckl, Nat. Photonics **1**, 3 (2007).
[2] L. Wang, J. Yoshida, N. Ogata, S. Sasaki, and T. Kajiyama, Chem. Mater. **13**, 1273 (2001).
[3] J. G. Grote *et al.*, Proc. SPIE **5934**, 593406 (2005).
[4] M. H.-C. Jin, J. Mater. **60**, 81 (2008).

[5]E. M. Heckman, J. A. Hagen, P. P. Yaney, J. G. Grote, and F. K. Hopkins, Appl. Phys. Lett. **87**, 211115 (2005).

[6]J. Hagen, W. Li, A. J. Steckl, and J. G. Grote, Appl. Phys. Lett. **88**, 171109 (2006).

[7]Z. Yu, J. A. Hagen, Y. Zhou, D. Klotzkin, J. G. Grote, and A. J. Steckl, Appl. Opt. **46**, 1300 (2007).

[8]H. B. Yin, T. Brown, R. Greef, S. Mailis, R. W. Eason, J. S. Wilkinson, and T. Melvin, Proc. SPIE **5461**, 1 (2004).

[9]W. Hu, K. Sarveswaran, M. Lieberman, and G. H. Bernstein, IEEE Trans.

[10]P. Y. Chi, H. L. Lin, C. H. Liu, and C. D. Chen, Nanotechnology **17**, 4854 (2006).

[11]For additional information, see www.microchem.com/products/index

[12]E. A. Shields, F. Williamson, and J. R. Leger, J. Vac. Sci. Technol. B **21**, 1453 (2003).

[13]J. Hagen, W. X. Li, H. Spaeth, J. G. Grote, and A. J. Steckl, Nano Lett. **7**, 133 (2007).

[14]S. M. Sze, _VLSI Technology_ (McGraw-Hill, New York, 1988).

Nanotechnol. **4**, 312 (2005).

Final Report

Ultra-Sensitive Biological Detection
via Nanoparticle-Based Magnetically Amplified
Surface Plasmon Resonance (Mag-SPR) Techniques

KOREA-PI: Jinwoo Cheon
Professor of Chemistry
Yonsei University, Korea

US-PI: A. Paul Alivisatos
Director
Lawrence Berkeley National Laboratory, USA
Professor of Chemistry
University of California, Berkeley, UCA

I. OBJECTIVES

The ultimate goal of this project is to develop a new ultra-sensitive single molecule imaging technique, termed Mag-SPR (Magnetically-amplified Surface Plasmon Resonance), by using a magneto-plasmonic nanoparticle probe. The nanoparticle probe provides the ability to artificially control biomolecular clustering via magnetic interaction in live cells and simultaneously to visualize the clustering events at the single molecule level. To establish this new Mag-SPR technique, specifically we propose to:

(1) Construct Mag-SPR probes by rationally assembling magnetic and plasmonic components into a single nanoparticle
(2) Investigate the magnetic and plasmonic couplings of the nanoparticles and optimize their properties
(3) Visualize magnetically-activated biomolecular clustering using magnetically-amplified SPR system in single or sub-cellular level and examine its feasibility for a magnetically activated cell-signaling.

This developed technology is expected to advance current knowledge of the physical properties of nanoparticles especially in terms of the relevance between plasmonics and magnetism. Also, practical attributes of this system will be the highly-sensitive diagnostic sensing system of the biological markers specifically occurred in important biological processes such as tumorigenesis or other pathogenic prognosis.

II. STATUS OF THE EFFORT

In pursuing the goal of this project, we are in the status of being completion of the Mag-SPR technique for the biological application in single cellular level detection and diagnosis. The major progresses are summarized as the following major categories: (1) the development of a new magneto-plasmonic nanoparticle probe, a key material for "Mag-SPR" system, (2) establish an scientific understanding of the plasmonic coupling in vitro and in vivo systems, and (3) the successful application of the Mag-SPR system to actuate and monitor biomolecular clustering at the subcellular level in live cells.

III. ABSTRACT

Central biological functions in cells such as signaling and transport are systematically regulated by cooperative multiple molecular switches that are interconnected to each other. Structural analyses have provided important static information of these biomolecular switches but minimal dynamic information, while fluorescence microscopy is limited by the inherent photobleaching and blinking of organic dyes. Establishing the operating principles of molecular switches requires a probing system that allows one to control and to visualize these switches work with high spatio-temporal resolutions. In this collaborative project, our ultimate goal was to develop a probing system with such high-performance capabilities and, as a potential candidate, we proposed a new single molecule imaging technique, termed magnetically-amplified surface plasmon resonance (Mag-SPR) that uses unique magnetic and plasmonic coupling of nanoparticles. During the past research periods, an international collaborative research team, led by Prof. Cheon of the Yonsei University, Korea tackled the several issues pertaining in the development of a key nanoparticle probe and imaging platform. The US-PI, Prof. Alivisatos of

University of California, Berkeley has provided microscopic platforms and scientific backgrounds that eventually enabled the realization of Mag-SPR system.

   Significant progresses which have been made are: (1) "Plasmonic ruler" system has been made, which can detect the structural conformational change of the biological material in the single level, (2) Multi-component nanoparticle probes having dual magneto-plasmonic coupling properties were synthesized, in which several (3-5) zinc-doped manganese-ferrite nanoparticles trapped inside a silica particle provide strong magnetization and the outer-gold shell exhibits intense surface plasmon resonance light scattering at near infrared region, and (3) Magnetic manipulation system has been made which enables the spatial control of nanoparticle probe in a single cellular level.

   The Mag-SPR system has been used to study dynamic processes of biomolecular clustering in live cells, in which the entire biological processes of biomolecular recognition, cellular receptor clustering, and signaling transduction are monitored continuously. As such, work performed in the past three years is extremely valuable and provided many design insights for engineering. A core team between Korea and US is established, permitting future efforts to be conducted at a greater scale and deeper level. Overall, the research team accomplished the tasks set out in the proposal.

IV. PERSONNEL SUPPORTED

(1) Cheon Group

Mr. Jae-Hyun Lee, Graduate Student, Department of Chemistry, Yonsei University, Korea

Mr. Jung-tak Jang, Graduate Student, Department of Chemistry, Yonsei University, Korea

Ms. Mi-yun Kim, Graduate Student, Department of Chemistry, Yonsei University, Korea, She received M.S. degree.

Ms. Eun-joo Choi, Graduate Student, Department of Chemistry, Yonsei University, Korea, She received M.S. degree.

Ms. Mi Hyeon Cho, Graduate Student, Department of Chemistry, Yonsei University, Korea

Mr. Ji-wook Kim, Graduate Student, Department of Chemistry, Yonsei University, Korea

(2) Alivisatos Group

Young-wook Jun, Post Doctoral Fellow, College of Chemistry, University of California, Berkeley, USA. (Currently, assistant professor at University of California, San Francisco)

V. PUBLICATIONS

   (1) J. Kim, J. Lee, M. Cho, J. Jang, Y. Jun, A. P. Alivisatos, J. Cheon "Single molecule study of angiogenesis using magneto-plasmonic coupling of nanoparticles", in preparation

   (2) Jae-Hyun Lee, Eun Sook Kim, Mi Hyeon Cho, Mina Son, Soo-In Yeon, Jeon-Soo Shin, and Jinwoo Cheon, "Artificial Control of Cell Signaling and Growth by Magnetic Nanoparticles", *Angew. Chem. In. Ed.* **2010**, *49(33)*, 5698.

   (3) Young-wook Jun, Sassan Sheikholeslami, Daniel Hostetter, Cheryl Tajon, Charles Craik, A. Paul Alivisatos, "Continuous Imaging of Plasmon Rulers in Live Cells Reveals Early Stage Activation of Caspase-3 at the Single Molecule Level". *Proceedings of National Academy of Sciences of the Unites States of America* **2009**, *106(42)*, 17735.

(4) Young-wook Jun; Jung-wook Seo; Jinwoo Cheon, "Nanoscaling Laws of Magnetic Nanoparticles and Their Applicabilities in Biomedical Sciences", *Accounts of Chemical Research* **2008,** *41(2), 179.*

(5) Jinwoo Cheon, Jae-Hyun Lee, "Synergistically Integrated Nanoparticles as Multimodal Probes for Nanobiotechnology", *Accounts of Chemical Research* **2008,** *41(12), 1630.*

VI. INTERACTIONS
(1) Presentations
- Cheon group

- Jinwoo Cheon, "Design strategy of exceptionally strong magnetic nanoparticles and their uses as multi-modal imaging and actuation probes" *American Chemical Society*, San Francisco, USA, Mar. 21. 2010.
- Seung Ho Moon, Eun-joo Choi, Jae-Hyun Lee, Jinwoo Cheon, "Four-in-One Targeted Gene Suppression Using Magnetic Nanoparticles for simultaneous Molecular Imaging and siRNA Delivery" *Material Research Society Fall meeting*, Boston, USA, Dec. 1. 2009.
- Jung-tak Jang, Seung Ho Moon, Jinwoo Cheon, "Dopant Controlled Magnetism Tuning of Metal Oxide Nanoparticles for High Performance Magnetic Resonance Imaging and Hyperthermic Effects" *Material Research Society Fall meeting*, Boston, USA, Dec. 1. 2009.
- Jinwoo Cheon, Jae-Hyun Lee, Jinsil Choi, "New-Generation Magnetic Nanoparticles as Ultra-sensitive and Versatile Platform Materials for NanoBiotechnology" *Material Research Society Fall meeting*, Boston, USA, Dec. 1. 2009.
- Jung-tak Jang, Seung Ho Moon, Jae-Hyun Lee, Min Gyu Kim, Jinwoo Cheon, "Dopant Controlled Metal Oxide Nanoparticles for High Performance Magnetic Resonance Imaging and Hyperthermia Effects" *The University of Kyushu-Yonsei University Joint Symposium*, Seoul, Korea, Aug. 24. 2009.
- Jinwoo Cheon, "Nanoscaling Laws of Magnetic Nanoparticles and Their Biomedical Applications: New-Generation Magnetic Nanoparticles as High Performance Platform Materials for NanoBiotechnology" *A Joint Symposium of 8th US-Korea Workshop on Nanostrucured Materials and 6th US-Korea Workshop on Nanoelectronics*, Seoul, Korea, May. 20. 2009.
- Seung Ho Moon, Jae-Hyun Lee, Jinwoo Cheon, "Nanoscaling Laws of Magnetic Nanoparticles for the Utilization in Biomedicine" *The University of Tokyo - Yonsei University Joint Symposium*, Tokyo, Japan, Jan. 19. 2009.
- Jinsil Choi, Jinwoo Cheon, "Dual-modality PET-MRI probe for sentinel lymph node detection" *NanoBio-Seoul 2008*, Seoul, Korea, Oct. 31. 2008.
- Jinwoo Cheon, "Design of High Performance Nanoparticle Technology for Multi-Modal Biomedical Applications" *The 2nd Yonsei University – Chulalongkorn University Joint Symposium*, Bangkok, Thailand, Oct. 31. 2008.
- Jung-tak Jang, Hyunsoo Nah, Seung Ho Moon, Jae-Hyun Lee, Jinwoo Cheon, "Magnetism-Nanoscaling Laws and Their Biomedical Applications" *NanoBio-Seoul 2008*, Seoul, Korea, Oct. 30. 2008.
- Jinwoo Cheon, "Nano-Scaling Laws and the Design of Nanoparticles for Biomedical Studies" *Max Planck Society-Korea Joint Synposium*, Pohang, Korea, Oct. 29. 2010.

- Jae-Hyun Lee, Jung-tak Jang, Jinwoo Cheon, "Nanoscaling Laws of Nanomagnetism and Their Biomedical Application" *NCI Alliance for Nanotechnology in Cancer Investigators Meeting*, Chicago, USA, Sep. 8. 2008.
- Hyunsoo Nah, Jinsil Choi, Jinwoo Cheon, "Synergistically Integrated Multimodal Nanoparticle Probe for Biomedical Application" *NCI Alliance for Nanotechnology in Cancer Investigators Meeting*, Chicago, USA, Sep. 8. 2008.
- Mi-yun Kim, Jinwoo Cheon, "Understanding of Immunogenic Responses and Cytotoxicity caused by Engineered Nanoparticles" *Material Research Society Fall Meeting*, Boston, USA, Mar. 27. 2008.
- Jinwoo Cheon, "Design of Nanoparticles for Ultra-Sensitive Biological Studies" *The 1st Kyushu University Global COE/Yonsei Uniersity BK21 Joint Symposium on 'Future Molecular Systems'*, Seoul, Korea, Feb. 25. 2008.
- Hyunsoo Nah, Jinwoo Cheon, "Magnetism-Engineered Metal Ferrite by Controlling Size and Dopant for The Utilization in Magnetic Resonance Imaging" *The 1st Kyushu University Global COE/Yonsei Uniersity BK21 Joint Symposium on 'Future Molecular Systems'*, Seoul, Korea, Feb. 24. 2008.
- Young-wook Jun, Jae-Hyun Lee, Jinwoo Cheon, "Nano-Scale Size and Dopant Effects of Magnetism-Engineered Iron Oxide (MEIO) Nanoparticle Probes for Their Utilizations in Magnetic Resonance Imaging" *Material Research Society Fall Meeting*, Boston, USA, Nov. 28. 2007.
- Jae-Hyun Lee, Jinwoo Cheon, "Adenovirus-Magnet Hybrid Nanoparticle for Magnetic Resonance Imaging of Target Specific Gene Delivery" *Material Research Society Fall Meeting*, Boston, USA, Nov. 27. 2007.
- Jinwoo Cheon, "Magnetic Nanoparticles for Bio-Medical Applications" *Material Research Society Fall Meeting*, Boston, USA, Nov. 25. 2007.
- Jinwoo Cheon, "Design of High Performance Nanoparticle Probes for Ultra-sensitive Biological Detection" *Takeda Genome Urology*, Okinawa, Japan, Nov. 10. 2007.
- Jinwoo Cheon, "Convergence Nanoparticles for Ultra-Sensitive Molecular Imaging" *Joint Molecular Imaging Conference, Academy of Molecular Imaging (AMI) & The Society for Molecular Imaging*, Providence, USA, Sep. 8. 2007.
- Jinwoo Cheon, "Convergence Inorganic Nanocrystals" *Materials Today Asia*, Beijing, China, Sep. 3. 2007.
- Jinwoo Cheon, "Smart Nanomaterials for Biomedical Diagnosis: Convergence Nano-structures and MEIO" *Asian Chemical Congress*, Kuala Lumpur, Malaysia, Aug. 25. 2007.
- Jae-Hyun Lee, Jinwoo Cheon, "Magnetism Engineered Nanoparticles for the Ultra-Sensitive Detection of Cancer via Magnetic Resonance Imaging(MRI)" *Yonsei University - University of Tokyo Joint Symposium*, Seoul, Korea, Aug. 25. 2007.

-Alivisatos group
- A. Paul Alivisatos, "Frontiers in materials chemistry, IV," Frontiers in Materials Chemistry: A Tribute to the Dreyfus Brothers (ACS Presidential Symposium Supported by the Dreyfus Foundation), San Francisco, California, March 23, 2010.
- A. Paul Alivisatos, "The Carbon Cycle 2.0 Initiative at LBNL, Guest Speaker Hong Kong Assoc of Northern California Distinguished Speaker Luncheon Series, San Francisco, California, Nov. 16, 2009.

- A Paul Alivisatos "Nanocrystal Molecules", 44th Biennial Mtg of the German Colloid Society, Hamburg, Germany, Sept. 29 - Oct. 1, 2009. A. Paul Alivisatos, Invited Speaker, Center for Cancer Nanotechnology Excellence Symposium, Stanford University, Palo Alto, California, May 28-29, 2009. A. Paul Alivisatos, "New Nanocrystal Probes for Transient Molecular Complexes: In Vivo Single Molecule Plasmon Ruler Studies and Tetrapod Strain Gauge," Transient Molecular Complexes Workshop, San Francisco, California, August 24-26, 2009.
- A. Paul Alivisatos, Keynote Lecturer, "Artificial Molecules Built from Colloidal Nanocrystals," in the Symposium, Frontiers at the Nanoscale, (a symposium in honor of Prof. Alivisatos) and part of the 37th John Stauffer Distinguished Lecture in the Sciences series, University of Southern California, Los Angeles, California, April 7-8, 2009.
- A. Paul Alivisatos, Invited Presentor, 2009 Science Fair, Balboa Park, University of California, San Diego, California, April 1, 2009. A. Paul Alivisatos, Edgar Fahs Smith Lecture, "Nanocrystal Molecules with Application in Single Molecule biological Imaging," Pennsylvania State University, University Park, Pennsylvania, March 12, 2009. A. Paul Alivisatos, Keynote Speaker, Energy and the Environment Session, Summit on the National Academy of Engineers Grand Challenges, Duke University, Durham, North Carolina, March 2, 2009. A. Paul Alivisatos, Invited speaker, "Plasmon rulers for measuring dynamical distance changes in biological macromolecular assemblies," SPIE Conference, San Francisco, California, January 23, 2009.
- A Paul Alivisatos, Invited Speaker, Chalmers University of Technology, Gothenburg, Sweden, January 22, 2009. A. Paul Alivisatos, Invited Speaker, "Artificial Molecules Built from Colloidal Nanocrystals," the Royal Swedish Academy of Engineering Sciences, Stockholm, Sweden, January 21, 2009.
- A. Paul Alivisatos, Debye Lectures, "Nanocrystal Molecules with Application in Single Molecule Biological Imaging," and "Nanocrystals as Model Systems for Understanding Structural and Chemical Transformations in the Solid State, Cornell University, Ithaca, New York, October 1, 2008.
- A. Paul Alivisatos, Rohm and Haas Lecture, "Development of New Nanocrystal Molecules for Biological Sensing and Detecting," University of North Carolina, Chapel Hill, North Carolina, September 9, 2008.
- A. Paul Alivisatos, Invited participant in Laser Cooling Single Molecule Biophysics and Energy Symposium, Lawrence Berkeley National Laboratory, Berkeley, California, August 30, 2008.
- A. Paul Alivisatos, Invited Speaker, "Optical Properties of Plasmon Coupled Single Nanocrystal Molecules," Symposium: Single Molecule Approaches to Biology, Gordon Research Conference, New London, Connecticut, August 20, 2008.
- A. Paul Alivisatos, Invited Talk, "Nanocrystal Molecules with Application in Single Molecule Biological Imaging," Nobel Foundation Symposium on Single Molecule Spectroscopy, Stockholm, Sweden, June 2-4, 2008.
- A. Paul Alivisatos, , Invited Speaker, Nanocrystal conference, NANAX3, Lecce, Italy, May 21-23, 2008.
- A. Paul Alivisatos, Invited Speaker, "Artificial Molecules built from Colloidal Nanocrystals, IMM Symposium, the Netherlands, May 18-19, 2008.
- A. Paul Alivisatos, May 18-19, Invited Speaker, Economic Summit, Oakland Mayor Dellums, Oakland, California May 2, 2008.

- A. Paul Alivisatos, "Molecular Mechanistic Studies of the Synthesis of Colloidal II-VI Semiconductor Nanocrystals, " in the symposium, Nanostructures in Molecular Solvents; the Fred Kavli Distinguished Lectureship in Nanoscience, "Nanocrystals as Model Systems for Understanding Structural and Chemical Transportations in Solid State;" and "Chemical Transformations of Nanocrystals," in the symposium, Crystal-Shape Control and Shape-Dependent Properties--Methods, Mechanism, Theory, and Simulation, Spring 2008 MRS conference, San Francisco, California, March 25-27, 2008,.
- A. Paul Alivisatos, Invited Speaker, "Development of New Nanocrystal Molecules for Biological Sensing and Detecting," PITTCON, New Orleans, Louisiana, March 2-6, 2008.
- A. Paul Alivisatos, invited speaker in the symposium, Quantum Dot and Nanoparticle-Bioconjugates: Tools for Sensing and Biomedical Imaging, and co-chair of session on Nanoparticle-Nanoparticle and Nanoparticle-Bioreceptor Interactions, and presentor,"Plasma Rulers for Measuring Dynamical Distance Changes in Biological Macromolecular Assemblies," MRS 2007, Boston, Massachusetts.), November 26-27, 2007.
- A. Paul Alivisatos, 2007, MNSS Seminar Speaker, MIT, Cambridge, Massachusetts, November 15,.
- A. Paul Alivisatos, Nieuwland Lecture, University of Notre Dame, South Bend, Indiana, October 30-31, 2007.
- A. Paul Alivisatos, "Nanocrystals with Applications in Biological Imaging and Renewable Energy," IGERT Seminar at Levich Institute, City College of CUNY, New York, and invited talk at Yale University, New Haven, Connecticut, October 22-23, 2007.
- A. Paul Alivisatos, 2007, Chair, Session - Other One-Dimensional Systems and Thermal Properties, Keynote Speaker," Development of New Nanocrystal Molecules for
- Biological Sensing and Detecting," at the Annual Nanowire Symposium and International Conference on One-Dimensional Nanomaterials, Malmo/Lund, Sweden, September 28-30.
- A. Paul Alivisatos, Plenary Speaker, 12th Annual IUPAC International Symposium, Fukuoka, Japan, August 26-29, 2007.
- A. Paul Alivisatos, "Plasmonic Rulers for Measuring the Kinetics of Macromolecular Assembly," and "Plasmon Rulers for Measuring Dynamical Distance Changes in Biological Macromolecular Assemblies," Fall, ACS Meeting, Boston, Massachusetts August 20-22, 2008.
- A. Paul Alivisatos, Plenary Lecture in Nanotechnology at the Materials Chemistry Conference, Royal Society of Chemistry, University College London, UK, July 2-5, 2007.

VII. INVENTIONS

VIII. HONORS / AWARDS

- Cheon group
- Jinwoo Cheon, "Campus Patent Strategy Universiade Teaching Professor Award", Yonsei University, 2009
- Jinwoo Cheon, "Research Achievement Award", Yonsei University, 2008
- Jinwoo Cheon, "Best Research Award", Korean Government, 2007

- Jinwoo Cheon, "9th Songgok Science and Technology Award", Korea Institute of Science and Technology (KIST)
- Jae-Hyun Lee, "Poster Award", NCI Alliance for Nanotechnology in Cancer Investigators Meeting, 2008
- Jae-Hyun Lee, "Yonsei Graduate Student Award", Yonsei University, 2007

  - Alivisatos group
- A. Paul Alivisatos, the Linus Pauling Medal (2010)
- A. Paul Alivisatos, ACS Fellow, American Chemical Society (2009)
- A. Paul Alivisatos, R&D 100 Award, R&D Magazine (2009)
- A. Paul Alivisatos, Computation and Engineering's Nanoscience Prize, International Society for Nanoscale Science (2009)
- A. Paul Alivisatos, Fellow, Material Research Society (2009)
- A. Paul Alivisatos, Kavli Distinguished Lectureship in Nanoscience, Material Research Society (2008)
- A. Paul Alivisatos, the Ernest Orlando Lawrence Award (2007)

IX.   ARCHIVAL DOCUMENTATIONS

The proposed Mag-SPR system requires cooperative operation of two key functional components that are a plasmonic gold nanoparticle and a magnetic Zn-doped ferrite nanoparticle and. To establish Mag-SPR system successfully, it is a necessary prerequisite to validate if each component nanocrystal provide desired functional performances.

1. Gold nanocrystals offer single biomolecule imaging sensitivity for biomolecular clustering/dissociation in live cells: Plasmonic nanoparticles such as gold or silver strongly scatter light in the visible range and do not demonstrate problems associated with fluorescence dyes (photobleaching) or quantum dots (blinking), and hence can be monitored continuously and indefinitely. Additionally, they exhibit strong distance-dependent plasmon coupling properties and thus red-shifted scattering signal results from the decreased interparticle distance. These unique properties of the plasmonic nanoparticles allow them to be used as molecular rulers that measure biomolecular distances. Using this principle, we established a new plasmon probe that visualizes biomolecular clustering/dissociation processes in real-time at the single molecule level in live cells. Details were reported in our recent paper published in the Proceeding of the National Academy of Science United States America, as follow.

Continuous imaging of plasmon rulers in live cells reveals early-stage caspase-3 activation at the single-molecule level

Young-wook Jun[a], Sassan Sheikholeslami[a,1], Daniel R. Hostetter[b,1], Cheryl Tajon[b,c], Charles S. Craik[b,c], and A. Paul Alivisatos[a,2]

[a]Department of Chemistry, University of California and Materials Sciences Division, Lawrence Berkeley National Laboratory, Berkeley, CA 94720; [b]Department of Pharmaceutical Chemistry, University of California, San Francisco, CA 94158; and [c]Graduate Program in Chemistry and Chemical Biology, University of California, San Francisco, CA 94158

The use of plasmon coupling in metal nanoparticles has shown great potential for the optical characterization of many biological processes. Recently, we have demonstrated the use of "plasmon rulers" to observe conformational changes of single biomolecules in vitro. Plasmon rulers provide robust signals without photobleaching or blinking. Here, we show the first application of plasmon rulers to in vivo studies to observe very long trajectories of single biomolecules in live cells. We present a unique type of plasmon ruler comprised of peptide-linked gold nanoparticle satellites around a core particle, which was used as a probe to optically follow cell-signaling pathways in vivo at the single-molecule level. These "crown nanoparticle plasmon rulers" allowed us to continuously monitor trajectories of caspase-3 activity in live cells for over 2 h, providing sufficient time to observe early-stage caspase-3 activation, which was not possible by conventional ensemble analyses.

caspase | live cell imaging | plasmonic nanoparticles | protease sensor | single-molecule imaging

Single molecule imaging has enabled the exploration of biomolecular dynamics and has revealed processes at work that are lost by extrapolation of ensemble assays (1–17). During the past few decades, optical single-molecule techniques such as single-fluorophore tracking (4, 5) and single-molecule fluorescence resonance energy transfer (1, 6–8) have proven to be effective tools for such purposes and have provided new biological information related to enzyme activity (6); transcription (7); protein dynamics (8); identification of rare intermediates and kinetic heterogeneity during RNA folding (5, 9); and RNA-protein interactions (10). Despite recent advances, however, most studies rely on biomolecules either immobilized on substrates or confined in a matrix, and observation of single-molecule behaviors inside live cells remains challenging (11–15). The inherent limitations of molecular dyes for single-molecule imaging, including low signal intensities, complex blinking phenomena, and photobleaching, are even more pronounced in live cell studies (16). Specifically, the fast photobleaching (less than a minute) of fluorescent dyes (17) hinders the ability to continuously monitor signaling pathways that transpire on the time scale of hours. New fluorophores such as green fluorescent proteins (GFPs) and quantum dots (QDs) have led to significant improvements (18, 19). For example, GFPs can be expressed as chimeras with a protein of interest to study subcellular localization in live cells, but are still prone to photobleaching (18). QDs show less bleaching, but blinking can make the interpretation of single-molecule data obtained with QDs ambiguous (20). Recent advances suggest that blinking can be controlled, but there are still remaining issues, such as a broad photoluminescence spectrum and biocompatibility (21–23).

We recently reported an alternative imaging technique using gold nanoparticle plasmon rulers for the optical readout of in vitro single-DNA hybridization and cleavage kinetics (24, 25). Because gold nanoparticles effectively scatter visible light and do not suffer from blinking or photobleaching (26), they have great potential to provide the highly enhanced signal intensity required for single-molecule detection and greatly extend the observation time for monitoring biological processes in living cells (27). To test this hypothesis, we chose caspase-dependent apoptotic signaling as a case study because apoptosis is an important biological process for maintaining homeostasis and function of the immune system and is highly related to various autoimmune diseases and cancer (28). Previous studies with ensemble techniques have shown that the activation of caspase-3 through the apoptotic signaling pathway can take from several minutes to hours (29). The long time-scale of these signaling events has made them difficult to measure continuously at the single-molecule level with established techniques. Here, we show an in vivo application of plasmon rulers in a study of caspase-3 signaling at the single-molecule level in living cells. The signal provided by these plasmon rulers allowed continuous observation of caspase-3 activation for over 2 h, unambiguously identifying early-stage activation of caspase-3 in apoptotic cells.

Results and Discussion

Design and Synthesis of Crown Nanoparticle Plasmon Rulers. To apply the plasmon rulers to in vivo cell signaling, it is necessary to construct a nanoparticle assembly that provides a very clear signal at the single-molecule level in the highly heterogeneous and high-background scattering environment of live cells. For the design of such an assembly, it is important to recall that the polarizability, and hence the light-scattering intensity, for a pair of particles in close proximity (within one diameter) is significantly greater than that of 2 separate particles (24, 25). In fact, this applies to assemblies where the particle is surrounded by several others. Here we find, for instance, that a crown nanoparticle assembly with a core 40-nm particle surrounded by 5 others (Fig. 1 A and B) scatters light ≈44× more intensely than a single particle, along with a substantial spectral red shift ($\Delta\lambda = 75$ nm) (Fig. 1 C and D; supporting information (SI) Fig. S1). For this reason, we developed a series of crown nanoparticle plasmon rulers for this in vivo study of caspase-3 activation (Fig. 1B). These assemblies are linked together by peptides containing the
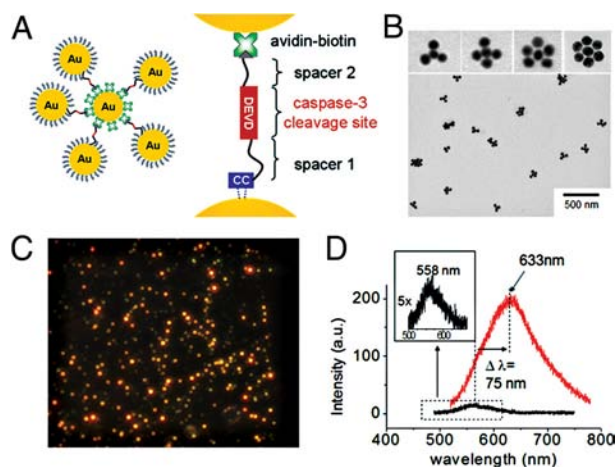
Fig. 1. Crown nanoparticle plasmon rulers. (*A*) Schematic of crown nanoparticle probes, which are composed of a NeutrAvidin-coated gold-core nanoparticle with multiple biotinylated gold satellite nanoparticles. Peptides with the caspase-3 cleavage sequence DEVD crosslink the core and satellite nanoparticles via avidin-biotin interactions. (*B*) Transmission electron microscopy (TEM) of crown nanoparticles. Approximately 3–6 satellite nanoparticles are linked to the core nanoparticle. (*C*) A representative scattering image of crown nanoparticles. Intense and bright red-colored spots correspond to a single-crown nanoparticle. (*D*) Representative scattering spectra of a single-crown nanoparticle (red) and a single gold nanoparticle (black). A single-crown nanoparticle probe exhibited a significant red shift ($\Delta\lambda = 75$ nm) and highly increased scattering intensity (≈ 44 times) compared with a single gold nanoparticle.

DEVD sequence via NeutrAvidin-biotin and Au-thiol chemistries (*SI Methods*). It is well known that caspase-3 cleaves the DEVD sequence most efficiently; therefore, caspase-3 cleavage of one of the DEVD peptides (30) in the crown nanoparticle is expected to result in an immediate reduction in light-scattering intensity. Recent reports also suggest that other caspases can exhibit some activity for DEVD (31). Although the cleavage activities of caspase-6, 8, and 10 to this substrate are negligible ($25 - 10^3$ times less active) compared with caspase-3, caspase-7 cleaves DEVD with similar efficiency. To minimize such cross-reactivity, we used a cell line in which caspase-7 is not expressed at the mRNA level. In addition, we inserted a glycine residue at the P1′ site, which is known to be optimal for caspase-3 cleavage activity. The use of a substrate containing a peptide bond avoids selectivity issues that have been observed with substrates containing activated amide bonds, such as aminocoumarin and para-nitroanilide (32, 33).

In Vitro Studies and Analyses of Enzymatic Kinetics. We first investigated the capabilities of the crown nanoparticles to detect caspase-3 activity under in vitro conditions. The NeutrAvidin-functionalized crown nanoparticles were immobilized on the biotinylated surface of a glass flow chamber (Fig. 2*A*). The scattering color and intensity were monitored under a dark-field microscope with a 100-watt tungsten lamp for illumination. Upon addition of caspase-3 (250 ng/mL), initial intense red-colored spots (Fig. 2*B*) gradually turned into yellow and then dim green spots as time elapsed (Fig. 2 *C* and *D*). Consistent with these observations, stepwise spectral blue-shifts in the scattering spectrum of a single-crown nanoparticle were detected due to sequential loss of satellite nanoparticles by caspase-3-mediated peptide cleavage (Fig. 2*E*). Single-particle trajectories of the scattering intensity recorded by electron-multiplying charge-coupled device (EMCCD; temporal frequency: 120 Hz) also show a stepwise decrease in the scattering intensity corresponding to each individual proteolytic event (Fig. 2*F* and Movie S1).
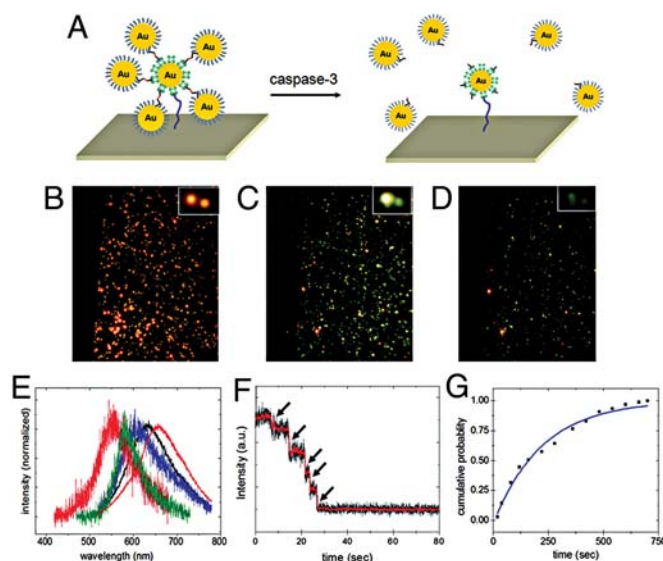

Fig. 2. In vitro caspase-3-mediated cleavage of crown nanoparticle plasmon rulers. (*A*) Schematic of experimental design. Crown nanoparticles were immobilized on a glass flow chamber via avidin-biotin chemistry. After equilibrating with buffer, caspase-3 molecules were introduced, and the color and intensity changes of crown nanoparticles were monitored under dark-field microscopy. (*B–D*) Scattering color changes upon caspase-3 treatment of crown nanoparticles. Intense red-colored spots (*B*) progressed to yellow spots (*C*) and then dim green spots (*D*). (*E*) A representative spectral shift of a single-crown nanoparticle upon caspase-3 cleavage. Initially, the crown nanoparticle exhibited a scattering peak maximum at 654 nm (red). Gradually, blue shifts were observed as time elapses, corresponding to the sequential cleavage of satellite nanoparticles. (*F*) Single-crown nanoparticle intensity trace as a function of time. The trajectory was recorded at a temporal resolution of 100 Hz by using an intensified CCD detector. Stepwise-intensity drops were observed, which correspond to the sequential satellite nanoparticle cleavages. (*G*) Determination of rate constant using crown nanoparticle rulers as a substrate. The cumulative probability of cutting is shown as a function of time. Fitting the curve yielded first-order rate constant k. Using k and literature-reported K_m, k_{cat} was calculated to be 6.17 s^{-1}.

To analyze the kinetics of cleavage by caspase-3, each proteolytic event was counted ($n = 300$) and plotted as a function of time (Fig. S2). The cumulative probability was calculated by dividing the number of cleavage events up to a given time, by the total number of cleavage events observed during the experimental time-course (Fig. 2*G*). The findings of this in vitro experiment fit well to a first-order kinetic model, with a kinetic rate constant (k) of 0.0046 s^{-1}. Using literature values for K_m and the rate constant derived from this work, the catalytic kinetic constant (k_{cat}) was calculated to 6.17 s^{-1} (34). This value falls within the range of previously reported k_{cat} values (2.4–8.2 s^{-1}) obtained in ensemble studies (34). Control experiments either in the absence of caspase-3 or with crown nanoparticle probes constructed from a peptide lacking the DEVD sequence showed only minimal cleavage (Fig. S3).

Intracellular Delivery and Distribution of Plasmon Rulers. The in vitro experiments showed that the crown nanoparticles could be used to monitor caspase-3 activity and were modified for live cell experiments. To deliver the NeutrAvidin-functionalized crown nanoparticle probes inside of cells, they were conjugated with a biotinylated form of the cell penetration peptide, TAT. Either HeLa or SW620 cells were incubated with the TAT-modified crown nanoparticle plasmon rulers for 12 h to allow sufficient time for loading into cells, and then imaged with a dark-field microscope. The background scattering from the cell details its boundary, and the bright red spots inside suggest successful
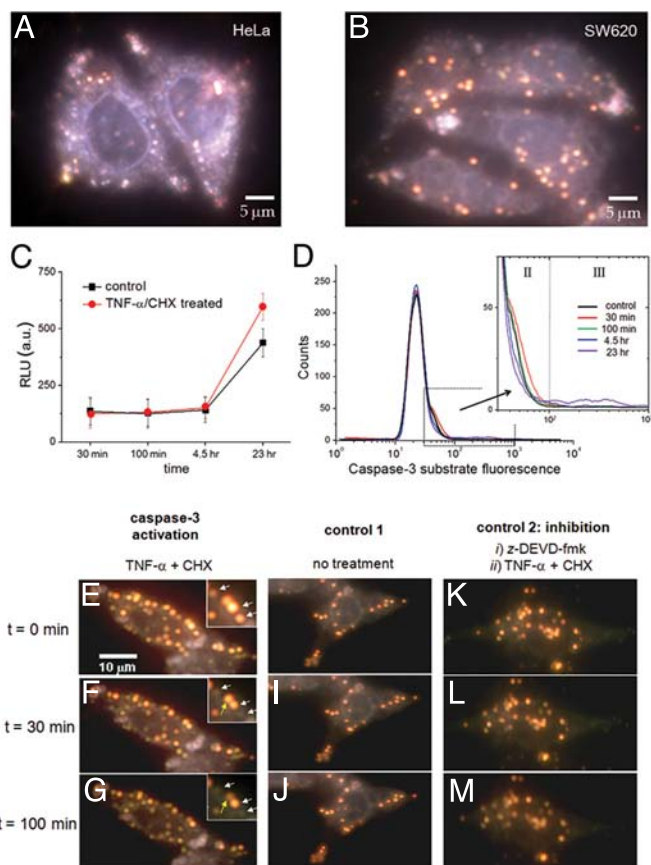
Fig. 3. Cellular delivery of crown nanoparticles in live cells and their utilization for single-molecule imaging of caspase-3 activation in apoptotic cells. (*A* and *B*) Crown nanoparticles were first conjugated with the cell penetration peptide TAT and delivered into HeLa cells and colon cancer cells SW620. Bright red-colored spots correspond to individual crown nanoparticles. (*C* and *D*) Ensemble caspase-3 activity was measured by either a luminescence assay (Caspase-Glo 3/7; Promega) or flow cytometry 30 min, 100 min, 4.5 h, and 23 h after the addition of TNF-α/CHX. (*C*) The luminescence assay shows minimal caspase-3 activation at early stages. TNF-α/CHX induced caspase-3 activation is evident only at 23 h. (*D*) Flow cytometry findings are consistent with the luminescence assay. Shoulder peaks that might be indicative of caspase-3 activity appear at early time points. (*E–G*) Caspase-3 activation was induced by the addition of the apoptotic inducers TNF-α and CHX. As time elapses, some red spots turn into either dim red or green dots. (*H–J*) Vehicle-treated cells show almost no signal change during the entire observation time. (*K–M*) Cells were pretreated with the caspase-3 inhibitor z-DEVD-*fmk*, and subsequently treated with TNF-α/CHX. There are no indications of proteolysis throughout the time course.

delivery of the plasmon rulers (Fig. 3 *A* and *B*). Without TAT modification, there was no indication of the nanoparticle delivery inside cells (Fig. S4); however, some of the nonspecifically bound plasmon rulers were seen on the culture plate at a high dose of nanoparticles (Fig. S5).

Though definitive proof of cytosolic localization of the gold nanoparticles awaits further experimentation, their subcellular distribution can be inferred from the following: TAT peptides release a wide range of cargos, such as gold nanoparticles, from endosomal compartments following endocytosis (35). SW620 cells were incubated with the TAT-conjugated crown nanoparticles for 12 h to provide time for TAT-mediated endosomal escape. The nanoparticles that remain endosomally trapped will eventually fuse with lysosomes, which are not accessible to caspase-3 (36). The apoptotic inducer used in this study has been shown to permeabilize lysosomal membranes, facilitating the

release of proapoptotic cathepsins (37). Therefore, the efficiency of our cytosolic delivery might be a function both of TAT-induced endosomal escape and lysosomal permeabilization during apoptosis. The caspase-3-mediated cleavage events described subsequently suggest that most crown nanoparticles are cytosolic.

The scattering signals from the plasmon rulers are highly intense compared with the background scattering from the cell, allowing continuous imaging at rates up to 250 Hz with an EMCCD. In addition, the scattering signal lasts more than ≈8 h under continuous illumination of visible light, with no signal decrease in healthy cells. The highly intense and stable scattering properties of crown nanoparticles should allow the detection of single-particle trajectories with high temporal resolution during caspase-3 activation.

Ensemble Assay of Caspase-3 Activity in Live Cells. Before investigating caspase-3 activity in live cells with the crown nanoparticle plasmon rulers, we first measured caspase-3 activity in cells via conventional noncontinuous fluorescence-based ensemble techniques. SW620 cells were treated with the apoptotic inducers, tumor necrosis factor-α (TNF-α), and cycloheximide (CHX). SW620 cells were chosen because caspase-7, the major competitor for the DEVD sequence, is absent in SW620 cells at the mRNA level (http://biogps.gnf.org/#goto = welcome). In addition, it is well documented that SW620 cells are resistant to death receptor-induced apoptosis and exhibit low levels of caspase-3 activity upon addition of death receptor agonists (38). We reasoned that low levels of caspase-3 activity would be an excellent test of the single-molecule sensitivity of the crown nanoparticles. To confirm the resistance of SW620 cells to death receptor-mediated apoptosis, we used ensemble analyses with peptide substrates containing the DEVD sequence. Analysis of caspase activity with a luminescent assay (Caspase-Glo 3/7; Promega) showed almost no caspase-3 activity in cell lysates 4.5 h after the addition of TNF-α/CHX. In fact, death receptor-induced caspase-3 activity was detectable only after 23 h (Fig. 3*C*). To investigate caspase-3 activity on a cell-by-cell basis, we also performed flow cytometry with a cell-permeable fluorescent DEVD substrate. Consistent with the in vitro data, only a small percentage of cells show high levels of caspase-3 activity (labeled III in Fig. 3; fluorescence intensity between 10^2 and 10^3) 23 h after addition of TNF-α/CHX (Fig. 3*D*, III, and Figs. S6 and S7). Interestingly, at early time points, an unknown shoulder peak also appears (labeled II) and then decreases gradually (Fig. 3*D*, II).

In Vivo Plasmon Rulers for Imaging of Caspase-3 Activation. Use of the crown nanoparticle plasmon rulers allows continuous observation of caspase-3 activation at the single-molecule level, and provides a clearer understanding of the origin of the shoulder peaks in the flow cytometry and the early-stage caspase-3 activation. Some crown nanoparticles exhibited sudden intensity drops after a short period (30 min and 100 min) following the addition of TNF-α/CHX (Fig. 3 *E–G* and Movie S2), which correspond to the cleavage of satellite nanoparticles by activated caspase-3. Because caspase-3 is present predominantly in the cytosol, the observed cleavage of crown nanoparticles during apoptosis is consistent with cytosolic localization. However, some nanoparticles (≈15%) do not show any signal reduction after addition of an apoptotic inducer. This is possibly due to residual endosomal trapping of a portion of the nanoparticle plasmon rulers. The peptide in our crown nanoparticle is a selective caspase-3 cleavage sequence and is unlikely to be cleaved by other endosomal proteases, such as papain-like proteases, because these proteases have been shown to be unable to degrade peptide substrates with P1 Asp (39).
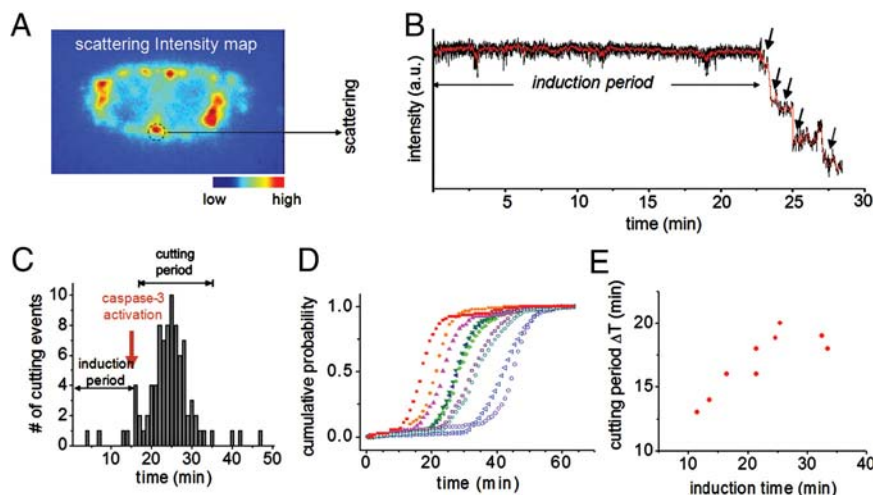
Fig. 4. Single-particle traces in live cells as a function of time. (*A*) Scattering intensity map of a single cell having internalized multiple-crown nanoparticles plasmon rulers. (*B*) Trajectory of a single-crown nanoparticle upon addition of TNF-α/CHX. Stepwise decreases in signal intensity were observed, which correspond to the sequential cleavage of satellite nanoparticles by caspase-3. (*C* and *D*) Statistical analyses of crown nanoparticle cleavages in a single cell as a function of time (*C*). Only minimal proteolysis was observed from 0 min to 16 min. Then, a rapid increase in cleavages occurs in the period from 16 to 35 min, indicative of caspase-3 activation. Caspase-3-mediated proteolysis of 10 different cells in a group (*D*). Differences in induction times across cells in the same population reflect cell-by-cell heterogeneity against caspase-3 activation. (*E*) A plot of the induction time (i.e., time from addition of apoptotic inducer until 5% of cleavages have occurred) vs. the cutting period (i.e., time following the induction period and ending when 95% of cleavages have occurred) of crown nanoparticle plasmon rulers. A slower cleavage rate was observed from cells exhibiting a longer induction time for initial cleavage.

To verify that the sudden intensity changes of the crown nanoparticle probes were due to the caspase-3 activity, a number of control experiments were performed. In the absence of TNF-α/CHX, virtually no changes in the scattering signals of the plasmon rulers were observed over the entire 2-h measurement period (Fig. 3 *H–J*). As another control, we pretreated the cells with a cell-permeable caspase-3 inhibitor, *z*-DEVD-fmk, and activated apoptotic signaling by the addition of TNF-α/CHX. No sign of cleavage was observed over the course of the experiment (Fig. 3 *K–M*). In a separate experiment, we measured the behavior of the crown plasmon nanoparticle rulers that are nonspecifically bound on the cell culture plate. The scattering signal of these rulers remained unchanged upon addition of TNF-α/CHX to cells (Fig. S5). These findings suggest that caspase-3 is activated at early time points during death receptor-induced apoptosis, and this activation is barely detectable by currently available ensemble analyses.

Interestingly, unlike small molecular probes, the movement of crown plasmon rulers is minimal during the time course. It is well known that the presence of networks of cytoskeleton filaments restricts the diffusion of large particles in cells (39, 40). Although there should be regional and cell-dependent differences, the size of void spaces (50–250 nm) is similar to that of plasmon rulers (≈100 nm) (40, 41). Their movement in the cytosol is hindered by such cytoskeletal sieving, and therefore they diffuse slowly. However, the cleaved satellite nanoparticles are smaller than the void size. Thus, upon cleavage, the freed individual particles can readily escape from the region of interest, which is defined as the diffraction limit (Fig. S8). Such limited diffusion of our plasmon rulers in the cytosol enables facile interpretation of single-particle trajectories with minimal signal perturbation by the probe movement.

Single-particle trajectories of the crown nanoparticle probes were obtained with an EMCCD enabling kinetic analysis of the enzymatic reaction in vivo and providing more details on early-stage caspase-3 activation. Fig. 4 *A* and *B* show the scattering intensity map of a whole cell labeled with crown nanoparticles and a representative time trace of a single crown nanoparticle probe upon addition of the apoptotic inducers

TNF-α/CHX, respectively (see also Figs. S9 and S10). Each cleavage event, represented by a sudden intensity drop in the time traces (Fig. 4*B*, arrows), was counted independently for each particle in all cells (Fig. 4*C*). Only minimal cleavage events were observed directly after the addition of TNF-α/CHX, but after several minutes, the number of cutting events increased dramatically (Fig. 4 *B* and *C*). The time lag (≈16 min) between the addition of the TNF-α/CHX and the majority of cleavage events is indicative of the induction time required for signaling events upstream of caspase-3 activation, such as initiator caspase-8 activation.

To further understand early-stage caspase-3 activation, we also analyzed the cleavage statistics of nanoparticles located inside 10 individual cells from the same group (Fig. S11). Interestingly, we observed significant variations in the induction times between different cells in the same population, ranging from 15 to 50 min (Fig. 4*D*). In addition, we found that differences in the induction time (labeled in Fig. 4*C*) correlate with the time required for the majority of cleavages to occur (defined as cutting period and labeled in Fig. 4*C*) (Fig. 4*E*). A longer cutting period was observed for cells exhibiting a longer induction time. Though the cutting period and induction time were correlated within a cell, variability in both measurements across cells in the same population reflect the heterogeneity in the resistance of cells to caspase-3 activation. Such findings are consistent with recent single-cell studies describing how cells in a group can exhibit different caspase-3 activation behaviors in response to the same apoptotic stimulus, and that such differences determine whether cells die or survive after a certain period (29, 42). This variability is believed to be dependent on each cell's individual resistance to death receptor-induced apoptosis (29, 42).

The crown nanoparticle plasmon ruler technique provides a new way of probing single-molecule activities in live cells. In this work, we have shown that crown nanoparticle plasmon rulers can be used for continuous observation of caspase-3 activity, establishing plasmon rulers as robust tools for single-molecule imaging in live cells. This would not be possible with conventional single-molecule imaging techniques, which are limited by much

shorter continuous observation windows or discontinuous snapshot imaging. Caspase-3 activation kinetics were successfully analyzed at the single-molecule level. Although the present study probes only enzyme activity, the design of crown nanoparticle plasmon rulers with alternate peptides of interest will allow other dynamics such as conformational changes to be studied in live cells. Furthermore, by using different types of plasmon rulers in terms of nanoparticle composition, size, shape, and number of particles, it should be possible to realize multicolor imaging of different signaling molecules in live cells. This will allow the activity of different signaling effectors to be correlated within the same cell at the single-molecule level.

Methods

Reagents. Gold nanoparticles (40 nm) were purchased from Ted Pella Inc. and were ligand exchanged with P,P'-(bis-*p*-sulfonatephenyl)-P''-phenylphosphine (BSPP) according to a literature protocol (25) and then concentrated to 5 nM. Either biotin-GSEGGSESEDEVDGGSNSGGRLCC or biotin-$CH_2CH_2(OCH_2CH_2)_6$ DEVDG-GC$H_2CH_2(OCH_2CH_2)_{12}$CC peptides were used as caspase-3 substrates and were purchased from New England Peptide Inc. HOOC$CH_2(OCH_2CH_2)_6$ S-S($OCH_2CH_2)_6$-CH_2COOH and biotin-$CH_2(OCH_2CH_2)_6$S-S($OCH_2CH_2)_6$-CH_2-biotin were purchased from PolyPure Inc. and reduced by treatment with BSPP before use.

Optical Setup. Scattering images were taken using an Axioplan 2 upright microscope (Zeiss), with a dark-field immersion oil condenser. The microscope was modified by the addition of an iXon EMCCD detector (512 × 512 pixel chip; Andor) on the imaging port of the SpectraPro 2300i spectrometer (Acton).

Synthesis of Crown Nanoparticles. Synthesis of NeutrAvidin (Ntv)-coated gold nanoparticles and peptide-conjugated gold nanoparticles are described in *SI Methods*. Fifteen microliters of Ntv-coated gold nanoparticles (1 nM) was added to 300 μL of peptide-conjugated gold nanoparticles (5 nM). After an overnight reaction at 4 °C, crown nanoparticles were separated from highly ordered aggregates and excess reactant nanoparticles via a sucrose-density gradient separation protocol with detection by UV-Vis absorption spectrometry.

In Vitro Single-Molecule Experiments. The glass flow chamber was modified with BSA-biotin (Roche) as described in the literature (23). A dilute solution of crown nanoparticle plasmon rulers was flushed into the chamber. The chamber was equilibrated with T30 buffer (10 mM Tris, 30 mM NaCl) and then flushed with 200 μL of 250 ng/mL caspase-3 in 10 mM phosphate buffer containing 50 mM NaCl. The scattering color images and intensities of the crown nanoparticle plasmon rulers in the field of view were continuously monitored by either a color camera (CoolSNAP cf; Roper Scientific) or an EMCCD. Also, we recorded the scattering spectra of individual crown nanoparticle plasmon rulers during caspase-3-mediated cleavage. For comparison, we used biotin-GSEGGSESEIETDGGSNSG-GRLCC peptide-conjugated crown nanoparticles.

Caspase-Glo 3/7 Assay. SW620 cells were maintained in DMEM, 10% FBS, 1× glutamax, and 1× penicillin/streptomycin. Four 96-well clear plates were seeded with 2 × 10^4 SW620 cells/well for a seeding density of 6.25 × 10^4 cells/cm². Cells were allowed to attach overnight. On average, cells were at 30% confluency before addition of apoptotic inducer. Before induction, media was removed and replaced with the following reagents in SW620 growth media: 1 μM staurosporine (0.1% final DMSO; Sigma, catalog no.

S6942); 0.2 μg/mL TNF-α (Invitrogen, catalog no. PHC3016) and 2 μg/mL cycloheximide (CHX) (1% final DMSO; Sigma, catalog no. C4859); or vehicle controls with matching concentrations of DMSO. A total of 12 replicates were performed. At 23 h, 4.5 h, 100 min, and 30 min after addition of apoptotic inducer, Caspase-Glo 3/7 Reagent (Promega) was added to all wells in a 1:1 ratio following manufacturer's instructions. After 10 min on a plate shaker at room temperature, 90% of the lysate volume was transferred to a 96-well solid-white plate (E&K Scientific, catalog no. EK-25075). Cell lysates were analyzed with an Analyst HT microplate reader (Molecular Devices), and data points were blank subtracted.

Flow Cytometry. A 6-well plate was seeded with 5.7 × 10^5 SW620 cells/well for a seeding density of 6 × 10^4 cells/cm². Cells were allowed to attach overnight. On average, cells were at 30% confluency before addition of apoptotic inducer. Addition of apoptotic inducers was performed as described previously. At 23 h, 4.5 h, 100 min, and 30 min after addition of apoptotic inducer, media was removed from all wells. To recover caspase-3-positive cells that might have detached during the time course, cells from the media were harvested by centrifugation at 1,000 RCF for 5 min and combined with cells recovered from the plate. The cells on the plate were detached using TrypLE Express (Gibco, catalog no. 12604–013) following manufacturer's instructions. After harvesting by centrifugation, supernatant was removed and cells were resuspended in 75 μL of PhiPhiLux G1D2 (OncoImmunin, catalog no. A304R1G). This reagent contains a peptide with the sequence DEVD-GI that is homodoubly labeled with a fluorophore (λ_{ex} = 505 nm; λ_{em} = 530 nm). Cells were incubated at 37 °C, 5% CO_2 for 1 h. Following incubation, 1 mL of flow cytometry dilution buffer (OncoImmunin) was added to each tube, and cells were harvested by centrifugation. Following supernatant removal, cell pellets were loosened by gently flicking, resuspended in 1 mL of flow cytometry dilution buffer, and transferred to 12 × 75-mm polystyrene round-bottom test tubes (BD Biosciences, catalog no. 352054). 2 × 10^4 cells were analyzed with a Beckton Dickinson FACSCalibur cytometer. Unstained cells (not loaded with substrate) were adjusted to the first decade of the FL1 channel, and data analysis was performed with FlowJo version 7.2.4. To facilitate analysis of the shoulder peaks, the major peak of each histogram (located between fluorescent intensity of 10^1 to 10^2) was overlaid and plotted in Fig. 3*D*.

Single-Molecule Imaging of Caspase-3 Catalytic Reaction in SW620 Cell Lines. Crown nanoparticles (≈0.15 pmol) were treated with 4.5 pmol of biotinylated TAT peptides for 1 h. Then, the TAT-conjugated nanoparticles were mixed with 2 mL of culture media. SW620 cells were incubated with the nanoparticle solution for 12 h. The cells were washed with 2 mL of SW620 growth media 3 times. The cells were treated with 0.2 μg/mL of TNF-α and 2 μg/mL of CHX and continuously monitored by either color camera (CoolSNAP cf; Roper Scientific) or an EMCCD (scan speed: 100 images per min) for 2 h.

1. Weiss S (1999) Fluorescence spectroscopy of single biomolecules. *Science* 283:1627–1683.
2. Giepmans BNG, Adams SR, Elissman MH, Tsien RY (2006) The fluorescent toolbox for assessing protein location and function. *Science* 312:217–224.
3. Mehta AD, Rief M, SpudichJA, Smith DA Simmons RM (1999) Single-molecule biomechanics with optical methods. *Science* 283:1689–2695.
4. Yildiz A, et al. (2003) Myosin V walks hand-over-hand: Single fluorophore imaging with 1.5-nm localization. *Science* 300:2061–2065.
5. Zhuang X, et al. (2000) A single molecule study of RNA catalysis and folding. *Science* 288:2048–2051.
6. Lu H, Xun L, Xie XS (1998) Single-molecule enzymatic dynamics. *Science* 282:1877–1882.
7. Harada Y, et al. (2001) K. Direct observation of DNA rotation during transcription by *Escherichia coli* RNA polymerase. *Nature* 409:113–115.
8. Talaga DS, et al. (2000) Dynamics and folding of single two-stranded coiled-coil peptides studied by fluorescent energy transfer confocal microscopy. *Proc Natl Acad Sci USA* 97:13021–13026.
9. Xie Z, Srividya N, Sosnick T, Pan T, Scherer NF (2004) Single-molecule studies highlight conformational heterogeneity in the early folding steps of a large ribozyme. *Proc Natl Acad Sci USA* 101:534–539.
10. Ha T, et al. (2002) Initiation and re-initiation of DNA unwinding by the *Escherichia coli* Rep helicase. *Nature* 419:638–641.
11. Sako Y, Minoguchi S, Yanagida T (2000) Single-molecule imaging of EGFR signalling on the surface of living cells. *Nat Cell Biol* 2:168–172.
12. Choi PJ, Cai L, Frieda K, Xie XS (2008) A stochastic single-molecule event triggers phenotype switching of a bacterial cell. *Science* 322:442–445.
13. Femino AM, Fay FS, Fogarty K, Singer RH (1998) Visualization of single RNA transcripts in situ. *Science* 280:585–590.
14. Teramura Y, et al. (2006) Single-molecule analysis of epidermal growth factor binding on the surface of living cells. *EMBO J* 25:4215–4222.
15. Douglass AD, Vale RD (2005) Single-molecule microscopy reveals plasma membrane microdomains created by protein-protein networks that exclude or trap signaling molecules in T cells. *Cell* 121:937–950.

CHEMISTRY

BIOPHYSICS AND COMPUTATIONAL BIOLOGY

16. Dubois A, Canva M, Brun A, Chaput F, Boilot JP (1996) Photostability of dye molecules trapped in solid matrices. *Appl Opt* 35:3193–3199.
17. Rasnik I, McKinney SA, Ha T (2006) Nonblinking and longlasting single-molecule fluorescence imaging. *Nat Methods* 3:891–893.
18. Bruchez M, Moronne M, Gin P, Weiss S, Alivisatos AP (1998) Semiconductor nanocrystals as fluorescent biological labels. *Science* 281:2013–2016.
19. Tsien RY (1998) The green fluorescent protein. *Annu Rev Biochem* 67:509–544.
20. Nirmal M, et al. (1996) Fluorescence intermittency in single cadmium selenide nanocrystals. *Nature* 383:802–804.
21. Hohng S, Ha T (2004) Near-complete suppression of quantum dot blinking in ambient conditions. *J Am Chem Soc* 126:1324–1325.
22. Fomenko V, Nesbitt DJ (2008) Solution control of radiative and nonradiative lifetimes: A novel contribution to quantum dot blinking suppression. *Nano Lett* 8:287–293.
23. Wang X, et al. (2009) Non-blinking semiconductor nanocrystals. *Nature* 459:686–689.
24. Sonnichsen C, Reinhard BM, Liphardt J, Alivisatos AP (2005) A molecular ruler based on plasmon coupling of single gold and silver nanoparticles. *Nat Biotechnol* 23:741–745.
25. Reinhard BM, Sheikoleslami S, Mastorianni A, Alivisatos AP, Liphardt J (2007) Use of plasmon coupling to reveal the dynamics of DNA bending and cleavage by single EcoRV restriction enzymes. *Proc Natl Acad Sci USA* 104:2667–2672.
26. Yguerabide J, Yguerabide EE (1998) Light-scattering submicroscopic particles as highly fluorescent analogs and their use as tracer labels in clinical and biological applications—II. Experimental characterization. *Anal Biochem* 262:157–176.
27. Huang X, El-Sayed IH, Qian W, El-Sayed MA (2006) Cancer cell imaging and photothermal therapy in the near-infrared region by using gold nanorods. *J Am Chem Soc* 128:2115–2120.
28. Igney FH, Krammer PH (2002) Death and anti-death: Tumour resistance to apoptosis. *Nat Rev Cancer* 2:277–287.
29. Albeck JG, et al. (2008) Quantitative analysis of pathways controlling extrinsic apoptosis in single cells. *Mol Cell* 30:11–25.
30. Thornberry NA, et al. (1997) A combinatorial approach defines specificities of members of the caspase family and granzyme B. *J Biol Chem* 272:17909–17911.
31. McStay GP, Salvesen GS, Green DR (2008) Overlapping cleavage motif selectivity of caspases: Implications for analysis of apoptotic pathways. *Cell Death Differ* 15:322–331.
32. Harris JL, Peterson EP, Hudig D, Thornberry NA, Craik CS (1998) Definition and redesign of the extended substrate specificity of granzyme B. *J Biol Chem* 273:27364–27373.
33. Mahrus S, Kisiel W, Craik CS (2004) Granzyme M is a regulatory protease that inactivates proteinase inhibitor 9, an endogenous inhibitor of granzyme B. *J Biol Chem* 279:54275–54282.
34. Talanian RV, et al. (1997) Substrate specificities of caspase family proteases. *J Biol Chem* 272:9677–9682.
35. Fuente JM, Berry CC (2005) TAT peptide as an efficient molecule to translocate gold nanoparticles into the cell nucleus. *Bioconjugate Chem* 16:1176–1180.
36. Werneburg NW, Guicciardi ME, Bronk SF, Kaufmann SH, Gores JG (2007) Tumor necrosis factor-related apoptosis-inducing ligand activates a lysosomal pathway of apoptosis that is regulated by Bcl-2 proteins. *J Biol Chem* 282:28960–28970.
37. Claus V, et al. (1998) Lysosomal enzyme trafficking between phagosomes, endosomes, and lysosomes in J774 macrophages. Enrichment of cathepsin H in early endosomes. *J Biol Chem* 273:9842–9851.
38. Ndozangue-Touriguine O, et al. (2008) A mitochondrial block and expression of XIAP lead to resistance to TRAIL-induced apoptosis during progression to metastasis of a colon carcinoma. *Oncogene* 27:6012–6022.
39. Rozman-Pungercar J, et al. (2003) Inhibition of papain-like cysteine proteases and legumain by caspase-specific inhibitors: When reaction mechanism is more important than specificity. *Cell Death Differ* 10:881–888.
40. Provance DW, MacDowall A, Marko M, Luby-Phelps K (1993) Cytoarchitecture of size-excluding compartments in living cells. *J Cell Sci* 106:565–578.
41. Luby-Phelps K, Castle PE, Taylor DL, Lanni F (1987) Hindered diffusion of inert tracer particles in the cytoplasm of mouse 3T3 cells. *Proc Natl Acad Sci USA* 84:4910–4913.
42. Morgan MJ, Thorburn A (2001) Measurement of caspase activity in individual cells reveals differences in the kinetics of caspase activation between cells. *Cell Death Diff* 8:38–43.

2. **Magnetic nanocrystals serve as a magnetic actuator that stimulates membrane-receptor clustering and thus activates intracellular cell signaling:** Under an external magnetic field, superparamagnetic nanoparticles are easily magnetized. When particles are brought into close proximity, the particles experience magnetic dipole-dipole attractive forces and form a particle cluster. Using this principle, we developed a new magnetic actuator, termed N-MACS (a nanoscale magneto-activated cellular signaling), by which the cell receptor mediated artificial triggering of cell growth in the pre-angiogensis stage was possible. Details were reported in our recent paper published in the Angewandte Chemie International Edition in English, as follow.

Communications

Artificial Control of Cell Signaling and Growth by Magnetic Nanoparticles**

Jae-Hyun Lee, Eun Sook Kim, Mi Hyeon Cho, Mina Son, Soo-In Yeon, Jeon-Soo Shin, and Jinwoo Cheon**

In memory of Chi Sun Hahn

Mechanical stresses on biological objects can lead to changes in a wide range of cellular properties, such as cell shape, cytoskeletal organization, and cell fate, by means of physical stimulations using dielectricity, optical trapping, and magnetic cytometry.[1–8] In particular, micrometer-sized magnetic beads have been useful since their first utilization by Crick and Hughes to draw mechanical stresses on biological objects by developing techniques such as magnetic twisting, pulling, and cell-stretching cytometry.[5–8] With the use of such magnetic stimulations, the roles of mechanical stresses for cell characteristics have been studied, which include cytoplasmic viscosity, cytoskeletal mechanotransduction, and mechanical calcium responses.[5–10]

Further scientific breakthroughs in this research field have depended on molecular-level understanding of mechanobiological processes and the induction of changes in cellular functions and/or cytoskeletal structures. The goal is to bring about single-cell or subcellular-level imaging and actuation of biological objects with high target specificity. Nanoscale probes and actuators are important because of their small sizes, which are comparable to those of many biologically meaningful molecules such as DNAs and proteins. In addition, their ability to attach multivalence func-

tional groups would be another advantage. By employing nanoparticles, difficult challenges associated with currently used micrometer-scale magnetic particles, such as probing and manipulation of a single receptor without disturbing any other rheological or cytoskeletal properties of the entire cell, can be overcome.

Recently, the groups of Ingber and Dobson have independently demonstrated that activation of ion channels is possible by using nanoscale magnetic particles.[11–13] These efforts have demonstrated that FcεRI, a cellular membrane receptor, can be magnetically agglomerated to activate the Ca^{2+} signal.[11] On the other hand, TREK-1, a membrane protein for the K^+ ion channel, is specifically activated by magnetic nanoparticles with size as small as 130 nm.[13] While these two pioneering works focused on ion-channel activations, new conceptual advances and other applications of nanoscale magneto-activated cellular signaling (N-MACS) are widely open to exploration.

Herein, we demonstrate for the first time that receptor-mediated artificial triggering of cell growth in the preangiogenesis stage is possible by the N-MACS approach. Angiogenesis is a vital process both for the growth and development of blood vessels and for tumor metastasis.[14] Conventionally, this process is initiated by several interactions that take place between specific receptors and ligands on the cell surface.[15,16] The Tie2/angiopoietin (Ang) pair, in which one Ang molecule binds to clusterize three to five Tie2 receptors, is regarded as one of the important receptor–ligand interactions.[17–19] This cluster formation is critical to activate multiple signaling steps and eventually participates in the angiogenic processes.[18–20]

Instead of using such ligands, in our study a TiMo214 monoclonal antibody (mAb)-conjugated Zn^{2+}-doped ferrite magnetic nanoparticle (Ab-Zn-MNP) is employed to target and magnetically manipulate Tie2 receptors through the steps in Figure 1a–c. To achieve this result, two permanent NdFeB magnets are positioned to exert an external magnetic field of about 0.15 T, with horizontal magnetic field lines that are oriented in the manner shown in Figure 1d. At this magnetic field strength, magnetization of Ab-Zn-MNPs can be saturated in plane (Figure 1e), which induces strong attractive forces between the dipoles of neighboring nanoparticles. This phenomenon results in the aggregation of Ab-Zn-MNPs.

For successful magnetic manipulation under mild external magnetic field conditions, we utilized a high-performance 15 nm Zn^{2+}-doped ferrite magnetic nanoparticle (Zn-MNP) instead of a conventional magnetic nanoparticle, since it exhibits a very high saturation magnetization (Figure 1e,f)

[*] J.-H. Lee,[+] M. H. Cho, Prof. J. Cheon
Department of Chemistry, Yonsei University
Seoul 120-749 (Korea)
Fax: (+82) 2-364-7050
E-mail: jcheon@yonsei.ac.kr
E. S. Kim,[+] M. Son, S.-I. Yeon, Prof. J.-S. Shin
Department of Microbiology
Institute for Immunology and Immunological Diseases
College of Medicine, Yonsei University
Seoul 120-752 (Korea)
Fax: (+82) 2-392-7088
E-mail: jsshin6203@yuhs.ac

[+] These authors contributed equally to this work.

Figure 1. a–c) Targeting and magnetic manipulation of Ab-Zn-MNPs. a,b) Ab-Zn-MNPs selectively bind to the specific cell-surface Tie2 receptors. c) In the presence of an external magnetic field, the Ab-Zn-MNPs are magnetized to form nanoparticle aggregates, which then induce the clustering of receptors to trigger intracellular signaling. d) Magnet setup and the simulated magnetic field. The inset shows magnetized nanoparticles on the cell surface. e) *M–H* curve of Zn-MNPs measured by using a superconducting quantum interference device (SQUID); *M* in emu per g magnetic atom. Zn-MNPs have a strong saturation magnetization value (ca. 160 emu per g magnetic atom) and high magnetic susceptibility ($\chi_m = 6.53 \times 10^{-2}$) which saturates at low magnetic fields below 0.1 T. f) Transmission electron microscopy (TEM) image of Zn-MNPs.

Figure 2. Magnetism-induced aggregation of Ab-Zn-MNPs on the 293-hTie2 cell surface. a) SEM images of the nanoparticles. The inset in the image on the right shows EDX spot analysis on the aggregate, which indicates a high Fe content (*γ* in atom %) of Ab-Zn-MNPs. Nanoparticles in the SEM images are false-colored as yellow for clear visibility. b) TEM images of the nanoparticles. Nanoparticles are indicated by arrows. c) Fluorescence confocal microscopy images of nanoparticles before and after application of a magnetic field. d) Tie2 receptor-bound nanoparticles before and after application of the magnetic field.

superior to that of conventional nanoparticles, such as Feridex (ca. 80 emu per g magnetic atom).[21] Also, Zn-MNP has a strong magnetic susceptibility that enables fast saturation of magnetization under a magnetic field strength of about 0.1 T (Figure 1 e). The magnitude of its tensional force is calculated to be around 10^{-17} N, which is adequate to induce only receptor clusterization, but small enough not to alter the cell shape or cytoskeletal organization.[10, 11]

The Ab-Zn-MNP conjugate (4 µg) was used to treat 4×10^6 293-hTie2 cells,[22] modified to overexpress Tie2 from the HEK293 cell line, in a petri dish at room temperature. After 30 min, unbound nanoparticles were removed by washing and the dish was placed in a magnetic field (ca. 0.15 T) for 1 h.

Most of the nanoparticles were on the cell surface at this stage. The evenly dispersed Ab-Zn-MNPs on the cell surface aggregated after application of the magnetic field, as seen by scanning electron microscopy (SEM) and TEM (Figure 2 a,b). Energy-dispersive X-ray (EDX) spot analysis of the aggregates showed that there was a high content of atomic Fe, thus confirming that the aggregates are indeed magnetic nanoparticles (Figure 2 a, inset).

Ab-Zn-MNP was also used as a fluorescence imaging probe after labeling with fluorescein. Application of the magnetic field to cells containing Ab-Zn-MNP/fluorescein resulted in a change of fluorescence distribution on the cell surface, from a weak and evenly dispersed green fluorescence to several bright, strongly fluorescent clumps (Figure 2c), which suggests that clustering of both Ab-Zn-MNPs and Tie2 receptors occurs. Clustering of Tie2 receptors can induce intracellular signaling processes that lead to angiogenesis. This takes place through several downstream signaling gateways, including phosphorylation of Tie2 and further propagation to phosphorylation of Akt, Fak, RhoA, Rac1, and ERK1/2, and the formation of endothelial nitric oxide synthase (eNOS) and reactive oxygen species (ROS) (Figure 2d, right picture).[18,20]

The formation of phosphorylated Tie2 (p-Tie2), which is the first gateway for signaling, is promoted only when cells are treated with Ab-Zn-MNPs followed by application of a magnetic field (Figure 3a–c). Western blots (Figure 3b) show that a strong band for p-Tie2 is present only in lanes 5, 7, and 9 (boxed), which corresponds to the cells that are first treated with Ab-Zn-MNPs and then subjected to a magnetic field. In contrast, other cells, which are treated with Zn-MNP (lane 2), Ab (lane 3), and Ab-Zn-MNP but are not subjected to a magnetic field (lanes 4, 6, and 8), exhibit negligibly weak bands for p-Tie2. In the presence of a magnetic field, the relative expression of p-Tie2 is dependent on the amount of Ab-Zn-MNP used to treat the cells, and increases from 3.3 to 4.1 and 4.5 as the amount of Ab-Zn-MNP increases from 2 to

4 and 8 µg. In contrast, the expression of p-Tie2 remains almost constant when a magnetic field is not applied (Figure 3c; also see lanes 4, 6, and 8 of Figure 3b). Here, the ratio of Ab to Zn-MNP is strictly controlled as 1:1, to avoid multiple binding of one nanoparticle to several receptors (see the Supporting Information, Figure S4).

Magnetic-field-induced downstream signaling associated with phosphorylation of Akt (p-Akt) is confirmed by using fluorescence confocal microscopy on immunofluorescent-stained cells (Figure 3d–f). In this procedure, Ab-Zn-MNP labeled with green-fluorescent fluorescein is used. In addition, the resulting p-Akt is labeled to emit red fluorescence by using anti-p-Akt immunoglobulin G (IgG) and its secondary antibody, Alexa 594-labeled anti-rabbit IgG. Upon application of a magnetic field, Ab-Zn-MNPs aggregate and appear as bright green fluorescing clumps (Figure 3e, 1) and the red fluorescence indicates the phosphorylation of Akt (Figure 3e, 2). The areas of green fluorescence overlaps nicely with areas exhibiting p-Akt red fluorescence, where the overlapped regions appear yellow (Figure 3e, 3). This result indicates that p-Akt is abundant in the regions where Ab-Zn-MNP aggregates are present. In contrast, when a magnetic field is not applied, the aggregation of Ab-Zn-MNPs or p-Akt is not observed (Figure 3f). In addition, the formation of ROS, another signaling product, is also observed by using fluorescence confocal microscopy only when the external magnetic field is applied (Supporting Information, Figure S5). The combined results provide strong evidence that aggregation of magnetic nanoparticles takes place when an external mag-
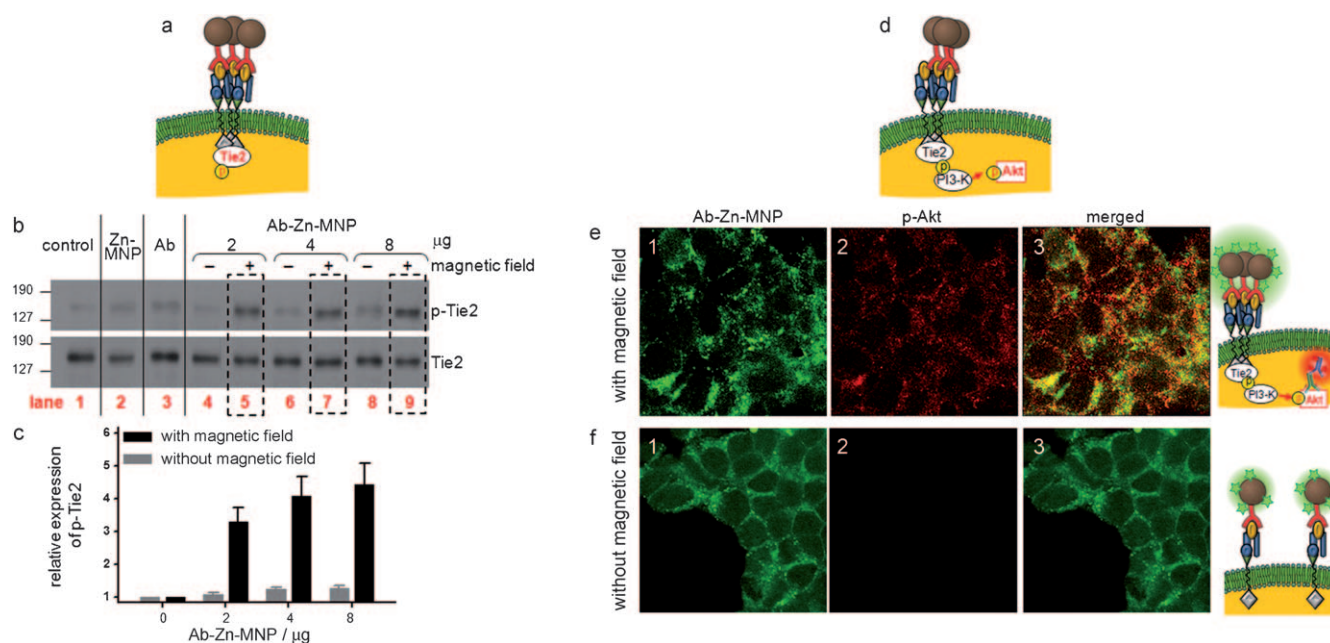
Figure 3. Intracellular signaling propagations induced by N-MACS. a) Phosphorylation of Tie2 (p-Tie2). b) Western blot analysis of 293-hTie2 cells which are stained with antibodies specific for p-Tie2 and Tie2; lane 1: control (293-hTie2 cell only), lane 2: bare Zn-MNP treated, lane 3: antibody-only treated, lanes 4–9: Ab-Zn-MNP treated without a magnetic field (−) or with a magnetic field (+). c) Relative expression of p-Tie2 versus the amount of Ab-Zn-MNP with or without application of an external magnetic field (three measurements; error bar: standard deviation). d) Phosphorylation of Akt (p-Akt). Fluorescence confocal microscopy images of cell cytoplasm after application of a magnetic field (e) and in the absence of a magnetic field (f), in which 1) Ab-Zn-MNP is labeled with fluorescein and 2) p-Akt is immunostained with anti-p-Akt IgG and anti-rabbit IgG–Alexa 594.
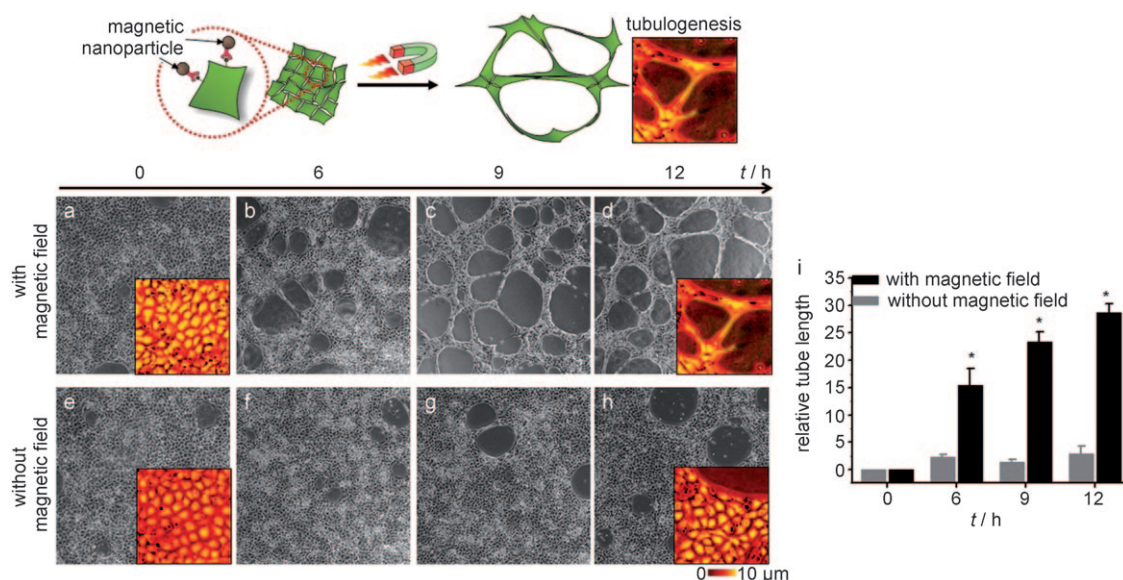
Figure 4. N-MACS on tubulogenesis of HUVECs at different time points after treatment with Ab-Zn-MNPs and application of a magnetic field (a–d) or without application of a magnetic field (e–h). Insets are magnified images of HUVECs, which are colored according to cell height from the bottom. i) Tube formation length of HUVECs with/without an external magnetic field (three measurements; error bar: standard deviation). Relative changes of tube length are shown in arbitrary units (*: $P < 0.0001$).

netic field is applied and that this process induces clustering of Tie2 receptors, which then triggers phosphorylation of Tie2 and further propagation of downstream signaling processes.

The study was extended to explore whether Tie2 receptor clusterization can initiate angiogenesis in the human umbilical vein endothelial cell (HUVEC), which is the main component comprising blood vessels that are known to possess a significant amount of Tie2 receptors.[23] The Ab-Zn-MNP (8 μg) was applied to HUVECs for 1 h at room temperature. After washing to remove unbound nanoparticles, a magnetic field of 0.15 T was applied in the same manner as in the 293-hTie2 cell experiments. The change of cellular morphology was examined by using differential interference contrast (DIC) microscopy for different times (0, 6, 9, and 12 h).

Initially, the cells have polygonal shapes and adhere to one another (Figure 4 a,e, insets). When the cells are exposed to a magnetic field for 1 h, their shapes begin to progressively change to capillary-like tubular structures, which become abundant after 9 h of magnetic field application (Figure 4 a–d). The shape transformation that takes place in HUVECs is commonly called tubulogenesis, which represents the preangiogenic stage eventually leading to blood vessel formation. In contrast, when a magnetic field is not applied, the shape change of the HUVECs is much slower (Figure 4 e–h). This observation is quantified by measuring the length of tubes where the relative length to the initial cell size changes from 0 to 15.4, 23.3, and 28.7 as time increases (Figure 4 i). These results clearly indicate that Tie2 signaling pathways in HUVECs are triggered by N-MACS and artificial angiogenesis is possible.

While some natural ligands such as angiopoietins can also induce similar effects, the N-MACS technique has unique advantages associated with the fact that it can be initiated remotely, noninvasively, and with temporal control. In addition, the methodology can be universally applied to various biological signaling processes.

[1] P. Fromherz, A. Offenhausser, T. Vetter, J. Weis, *Science* **1991**, *252*, 1290–1293.
[2] T. H. Young, C. R. Chen, *Biomaterials* **2006**, *27*, 3361–3367.
[3] J. Dai, M. P. Sheetz, *Biophys. J.* **1995**, *68*, 988–996.
[4] C. S. Chen, M. Mrksich, S. Huang, G. M. Whitesides, D. E. Ingber, *Biotechnol. Prog.* **1998**, *14*, 356–363.
[5] F. H. C. Crick, A. F. W. Hughes, *Exp. Cell Res.* **1950**, *1*, 37–80.
[6] P. A. Valberg, H. A. Feldman, *Biophys. J.* **1987**, *52*, 551–569.
[7] N. Wang, J. P. Butler, D. E. Ingber, *Science* **1993**, *260*, 1124–1177.
[8] M. Glogauer, J. Ferrier, C. A. McCulloch, *Am. J. Physiol. Cell Physiol.* **1995**, *269*, C1093–C1104.
[9] A. R. Bausch, W. Moller, E. Sackmann, *Biophys. J.* **1999**, *76*, 573–579.
[10] S. Na, O. Collin, F. Chowdhury, B. Tay, M. Ouyang, Y. Wang, N. Wang, *Proc. Natl. Acad. Sci. USA* **2008**, *105*, 6626–6631.
[11] R. J. Mannix, S. Kumar, F. Cassiola, M. Montoya-Zavala, E. Feinstein, M. Prentiss, D. E. Ingber, *Nat. Nanotechnol.* **2008**, *3*, 139–143.
[12] J. Dobson, *Nat. Nanotechnol.* **2008**, *3*, 139–143.
[13] S. Hughes, S. McBain, J. Dobson, A. J. El Haj, *J. R. Soc. Interface* **2008**, *5*, 855–863
[14] L. Coultas, K. Chawengsaksophak, J. Rossant, *Nature* **2005**, *438*, 937–945.
[15] P. Carmeliet, *Nature* **2005**, *438*, 932–936.
[16] G. D. Yancopoulos, S. Davis, N. W. Gale, J. S. Rudge, S. J. Wiegand, J. Holash, *Nature* **2000**, *407*, 242–248.

[17] P. C. Maisonpierre, C. Suri, P. F. Jones, S. Bartunkova, S. J. Wiegand, C. Radziejewski, D. Compton, J. McClain, T. H. Aldrich, N. Papadopoulos, T. J. Daly, S. Davis, T. N. Sato, G. D. Yancopoulos, *Science* **1997**, *277*, 55 – 60.

[18] L. Eklund, B. R. Olsen, *Exp. Cell Res.* **2006**, *312*, 630 – 641.

[19] W. A. Barton, D. Tzvetkova-Robev, E. P. Miranda, M. V. Kolev, K. R. Rajashankar, J. P. Himanen, D. B. Nikolov, *Nat. Struct. Mol. Biol.* **2006**, *13*, 524 – 532.

[20] R. Harfouche, N. A. Malak, R. P. Brandes, A. Karsan, K. Irani, S. N. A. Hussain, *FASEB J.* **2005**, *19*, 1728 – 1730.

[21] J.-t. Jang, H. Nah, J.-H. Lee, S. H. Moon, M. G. Kim, J. Cheon, *Angew. Chem.* **2009**, *121*, 1260 – 1264; *Angew. Chem. Int. Ed.* **2009**, *48*, 1234 – 1238.

[22] R. R. White, S. Shan, C. P. Rusconi, G. Shetty, M. W. Dewhirst, C. D. Kontos, B. A. Sullenger, *Proc. Natl. Acad. Sci. USA* **2003**, *100*, 5028 – 5033.

[23] C. William, P. Koehne, J. S. Jürgensen, M. Gräfe, K. D. Wagner, S. Bachmann, U. Frei, K.-U. Eckardt, *Circ. Res.* **2000**, *87*, 370 – 377.

Next step for the development of the proposed Mag-SPR system is to rationally design and construct a nanoparticle probe that possesses both magnetic and plasmonic components in a single particle. The nanoparticle probe should meet the following requirements in order for it to be used in Mag-SPR technology: (1) possession of a high magnetization value in order to maximize the magnetic interactions between particles under external magnetic field, (2) possession of plasmon resonance maximum at a biologically transparent window (near infrared). For this purpose, we adopted sequential nanocrystal growth strategy as described below.

3. Zn-doped manganese ferrite nanoparticles offer a maximized magnetization property: Magnetic property of nanoparticles is strongly affected by their size, shape, and composition. Previously, we reported that manganese-doped ferrite nanoparticles show enhanced magnetization value compared to other ferrite nanoparticles. We found that further enhancement of magnetization is possible through a partial replacement of tetrahedral Fe^{3+} with Zn^{2+}. Details were reported in our recent paper published in the Angewandte Chemie International Edition in English, as follow.

Nanoscaling Laws of Magnetic Nanoparticles and Their Applicabilities in Biomedical Sciences

YOUNG-WOOK JUN, JUNG-WOOK SEO, AND JINWOO CHEON*

Department of Chemistry, Yonsei University, Seoul 120-749, Korea

RECEIVED ON MAY 16, 2007

CONSPECTUS
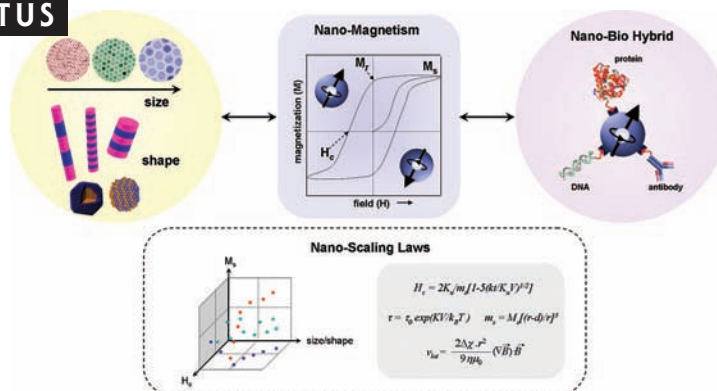
Magnetic nanoparticles, which exhibit a variety of unique magnetic phenomena that are drastically different from those of their bulk counterparts, are garnering significant interest since these properties can be advantageous for utilization in a variety of applications ranging from storage media for magnetic memory devices to probes and vectors in the biomedical sciences. In this Account, we discuss the nanoscaling laws of magnetic nanoparticles including metals, metal ferrites, and metal alloys, while focusing on their size, shape, and composition effects. Their fundamental magnetic properties such as blocking temperature (T_b), spin life time (τ), coercivity (H_c), and susceptibility (χ) are strongly influenced by the nanoscaling laws, and as a result, these scaling relationships can be leveraged to control magnetism from the ferromagnetic to the superparamagnetic regimes. At the same time, they can be used in order to tune magnetic values including H_c, χ, and remanence (M_r). For example, life time of magnetic spin is directly related to the magnetic anisotropy energy (K_uV) and also the size and volume of nanoparticles. The blocking temperature (T_b) changes from room temperature to 10 K as the size of cobalt nanoparticles is reduced from 13 to 2 nm. Similarly, H_c is highly susceptible to the anisotropy of nanoparticles, while saturation magnetization is directly related to the canting effects of the disordered surface magnetic spins and follows a linear relationship upon plotting of $m_s^{1/3}$ vs r^{-1}. Therefore, the nanoscaling laws of magnetic nanoparticles are important not only for understanding the behavior of existing materials but also for developing novel nanomaterials with superior properties.

Since magnetic nanoparticles can be easily conjugated with biologically important constituents such as DNA, peptides, and antibodies, it is possible to construct versatile nano−bio hybrid particles, which simultaneously possess magnetic and biological functions for biomedical diagnostics and therapeutics. As demonstrated in this Account, nanoscaling laws for magnetic components are found to be critical to the design of optimized magnetic characteristics of hybrid nanoparticles and their enhanced applicability in the biomedical sciences including their utilizations as contrast enhancement agents for magnetic resonance imaging (MRI), ferromagnetic components for nano−bio hybrid structures, and translational vectors for magnetophoretic sensing of biological species. In particular, systematic modulation of saturation magnetization of nanoparticle probes is important to maximize MR contrast effects and magnetic separation of biological targets.

1. Introduction

The lodestone compass, the first invention utilizing magnetic materials, was critical in aiding 12th century explorers to navigate across unexplored parts of the world. Magnetic nanoparticles, the lodestone's miniature counterpart, can act as navigators or probes to similarly guide researchers as they seek to understand the deep inside of living objects. Many migratory animals and some
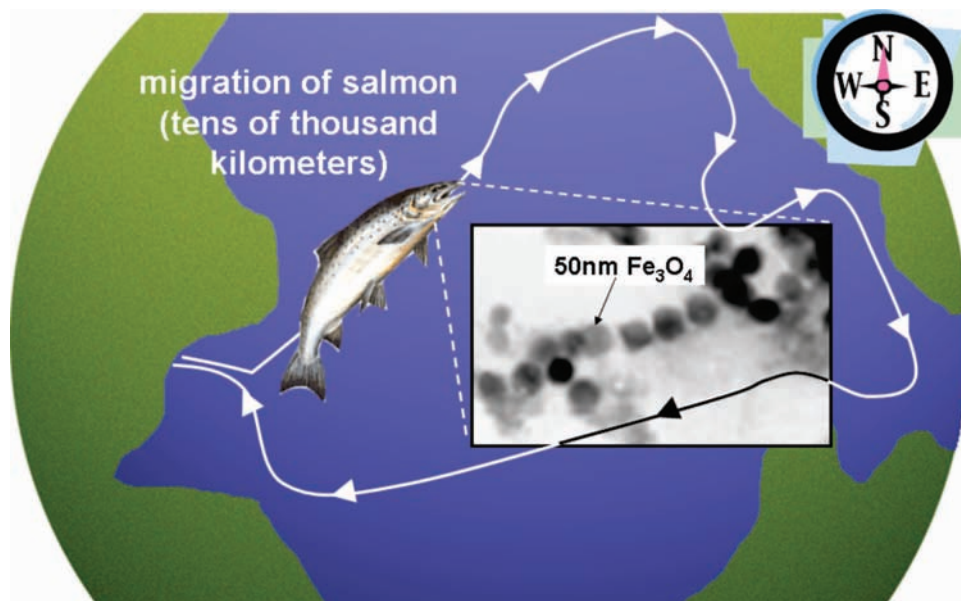
FIGURE 1. Magnetic nanoparticle-assisted natural navigation system used by salmon during migration. Reprinted with permission from *Nature* (http://www.nature.com), ref 1. Copyright 1997 Nature Publishing Group.
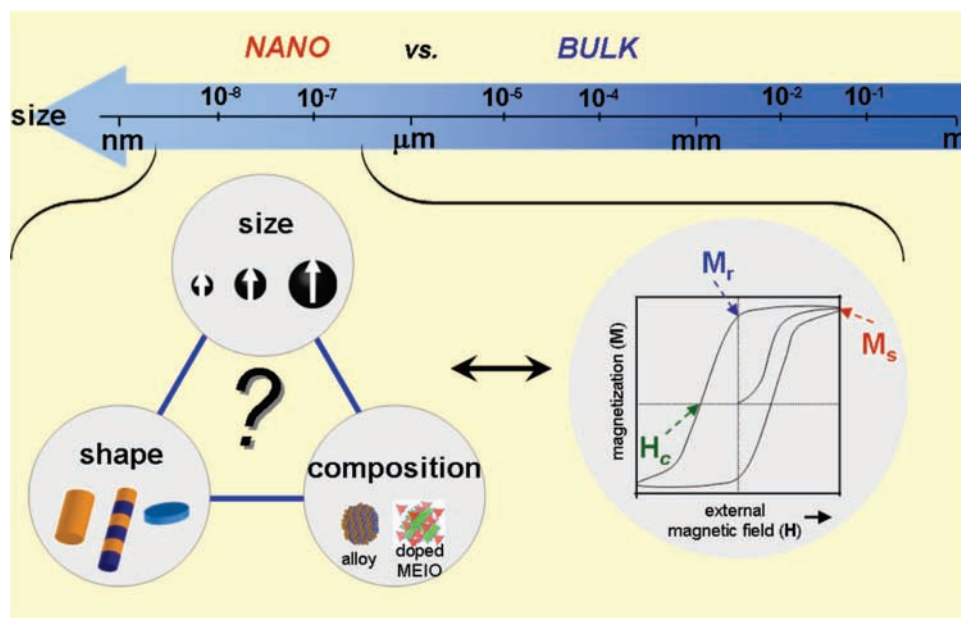
FIGURE 2. In nanometer scale, parameters such as size, shape, composition, and magnetocrystalline anisotropy strongly affect the magnetism (e.g., coercivity, mass magnetization, remanence) of nanoparticles.

microbes possess magnetic nanoparticles in their body that are utilized as a natural biomagnetic compass.[1] For example, salmon have a series of magnetic nanoparticles in the nasal capsules of their forehead, which are believed to respond to the geomagnetic field of the earth and help them reach their homes after journeys that can last tens of thousands of kilometers for three to four years (Figure 1).[1]

Scientists have developed artificial magnetic nanoparticles through chemical synthetic routes. In particular, recent progress in this field has yielded new types of magnetic nanoparticles with precisely tuned size, shape, and composition.[2–10] Many new interesting phenomena have been observed in these magnetic nanoparticles that are unique from their bulk counterparts. In addition to developing synthetic methods for these nanoparticles, understanding of their nanoscaling laws is also of great importance. The fundamental magnetic properties such as coercivity (H_c) and susceptibility (χ) are no longer permanent material characteristics and are susceptible to variations in their size, shape, and composition.[2,7,11–18] As a
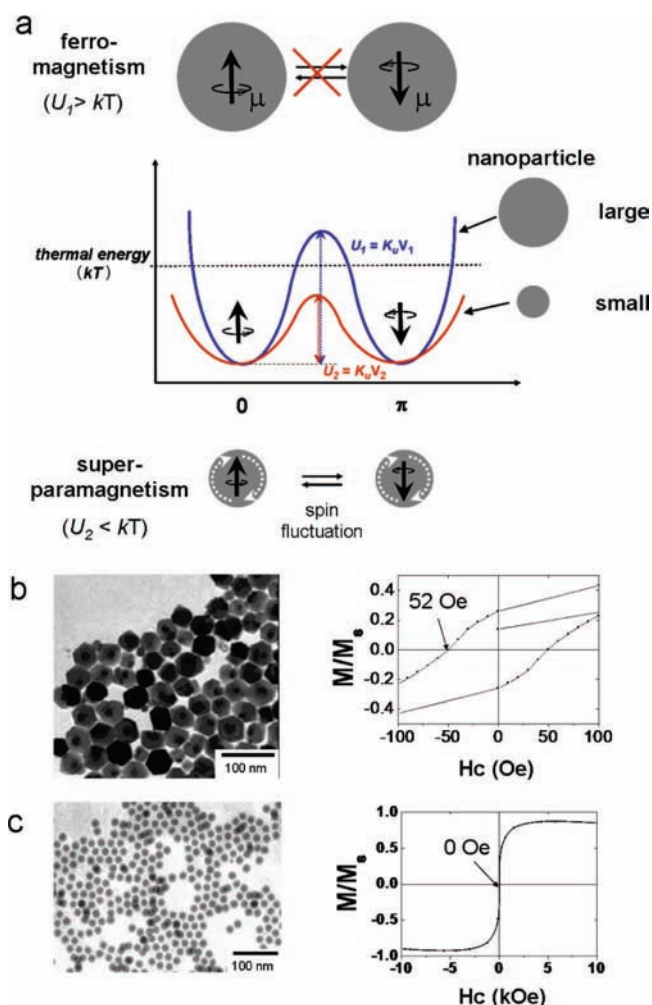
FIGURE 3. Nanoscale transition of magnetic nanoparticles from ferromagnetism to superparamagnetism: (a) energy diagram of magnetic nanoparticles with different magnetic spin alignment, showing ferromagnetism in a large particle (top) and superparamagentism in a small nanoparticle (bottom); (b, c) size-dependent transition of iron oxide nanoparticles from superparamagnetism to ferromagnetism showing TEM images and hysteresis loops of (b) 55 nm and (c) 12 nm sized iron oxide nanoparticles. Reproduced with permission from ref 9. Copyright 2004 American Chemical Society.

result, these scaling relationships can be used accordingly to tune magnetism from the ferromagnetic regime (unusually high magnetic energy product, $\mathbf{B}H_{max}$) to the superparamagnetic regime (zero coercivity in nanoscale regime).[15-18] Therefore, the nanoscaling laws of engineered magnetic nanoparticles are important not only to understand the behavior of existing materials but also to develop novel materials with superior properties.

Biomedical applications of such artificially engineered magnetic nanoparticles are promising since they can be useful as next-generation probes and vectors, which can significantly advance the current clinical diagnostic and therapeutic

methods.[7,19-32] Upon conjugation with target-specific biomolecules, these magnetic nanoparticles can travel in human bodies via blood or lymphatic vessels and recognize desired biological targets and report their positions. Alternatively, by focusing an external magnetic field to the target region, magnetic nanoparticles can direct therapeutic agents to a localized target.

With such issues in mind, here we discuss the nanoscaling laws that determine the magnetic characteristics of artificially engineered nanoparticles. We will also address newly observed properties associated with these materials and describe their utilization as versatile and high performance probes for biomedical sciences.

2. Nanomagnetism Scaling Laws of Engineered Nanoparticles

In bulk materials, the key parameters for determining magnetic properties such as coercivity (H_c) and susceptibility (χ) are composition, crystallographic structure, magnetic anisotropic energy, and vacancies and defects.[33-36] However, when their size is decreased to the nanoscale regime, at least two more important parameters are strongly involved: size and shape (Figure 2).

2.1. Size Effects. One of the interesting size-dependent phenomena of nanoparticles is superparamagnetism. The magnetic anisotropic energy barrier from a spin-up state to spin-down state of the magnet is proportional to the product of the magnetic anisotropic constant (K_u) and the volume (V) of the magnet.[36] While bulk materials have magnetic anisotropic energies that are much larger than the thermal energy (kT) (Figure 3a (blue line)), the thermal energy of the nanoparticle is sufficient to readily invert the magnetic spin direction, although it is insufficient to overcome the spin–spin exchange coupling energy (Figure 3a (red line)). Such magnetic fluctuation leads to a net magnetization of zero, and this behavior is called superparamagnetism. The transition temperature from ferromagnetism to superparamagnetism is referred to as the blocking temperature (T_b) and is defined by the relationship $T_b = K_uV/25k$.[36] Such size-dependent magnetism changes can be observed in $\gamma\text{-}Fe_2O_3$ and cobalt nanoparticles.[9,12] $\gamma\text{-}Fe_2O_3$ nanoparticles of 55 nm exhibit ferrimagnetic behavior with a coercivity of 52 Oe at 300 K, but smaller 12 nm sized $\gamma\text{-}Fe_2O_3$ nanoparticles show superparamagnetism with no hysteresis behavior (Figure 3b,c). For cobalt nanoparticles, ferromagnetic to superparamagnetic transitions occur at much lower temperatures (T_b) of 10, 20, 100, 180, and 370 K for nanopar-
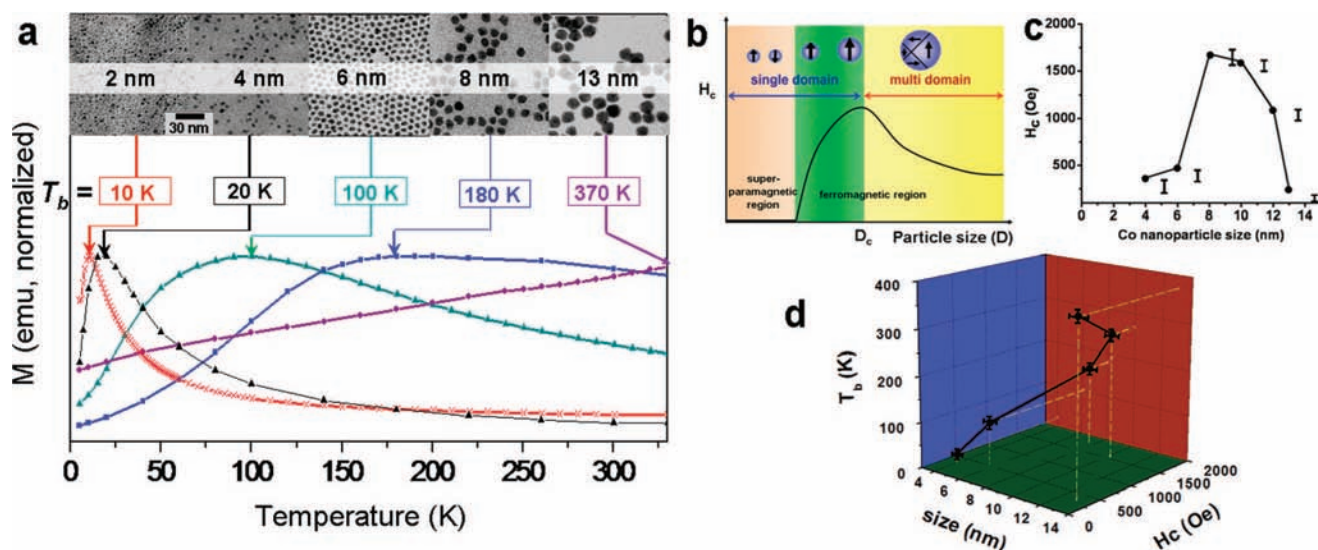
FIGURE 4. (a) Zero-field cooling curves and TEM images of Co nanoparticles with sizes of 2, 4, 6, 8, and 13 nm, (b) size-dependent magnetic domain structures from superparamagnetism to single domain and multidomain ferromagnetism, (c) size-dependent coercivity of Co nanoparticles, and (d) plot of H_c and T_b vs size of Co nanoparticles. Reproduced with permission from ref 7 (Figure 4a) and ref 12 (Figure 4b–4d). Copyright 2007 Royal Society for Chemistry and Copyright 2002 Wiley-VCH.

ticles with sizes of 2, 4, 6, 8, and 13 nm, respectively, in comparison to 1394 K for bulk cobalt (Figure 4a).

Nanoparticle size effects can also be observed in changes in magnetic coercivity (H_c). In contrast to the bulk magnet, which possesses multiple magnetic domain structures, nanoparticles possess single magnetic domain structures below a certain critical size (D_c) where all magnetic spins in the nanoparticle align unidirectionally (Figure 4b). In this single-domain regime, the magnetic coercivity increases as the size of the nanoparticle increases with the relationship $H_c = 2K_u/m_s[1 - 5(kT/K_uV)^{1/2}]$ where m_s is the saturation magnetization.[36] Above the critical size ($D > D_c$), multidomain magnetism begins in which a smaller reversal magnetic field is required to make the net magnetization zero. In the case of Co nanoparticles, the magnetic coercivity increases from 370 to 1680 Oe in a single-domain regime as the size of the Co nanoparticles increases from 4 to 8 nm (Figure 4c).[12] However, the magnetic coercivity decreases to 1600, 1100, and 250 Oe as the size of the Co nanoparticles further increases to 10, 12, and 13 nm by forming multimagnetic domains (Figure 4c). Therefore, the critical single-domain size of Co nanoparticles is expected to be around 8–10 nm. From such size-dependent properties of cobalt nanoparticles, a graph of scaling laws of cobalt nanoparticles on coercivity and blocking temperature is shown in Figure 4d.

Saturation magnetization of nanoparticles is also strongly dependent on their size. Intrinsically, magnetic materials possess magnetically disordered spin glass like layers near the surface due to the reduced spin–spin exchange coupling energy at

the surface.[37,38] In bulk cases, since the disordered surface layer is minimal compared with the total volume of the magnet, such surface spin canting effects are negligible. Upon reduction of the size of magnetic materials to nanoscale regime, however, the surface canting effects are dramatically pronounced in the saturation magnetization value (m_s), described as

$$m_s = M_s[(r - d)/r]^3 \qquad (1)$$

where r is the size, M_s is the saturation magnetization of bulk materials, and d is the thickness of disordered surface layer.[37] For very small nanoparticles less than ~5 nm, such size effect on m_s is more noticeable, since internal spins of the nanoparticle also start to be canted as well as the surface spins due to increased interactions between the surface and internal spins.[37]

Such size effects on magnetization have been well demonstrated in the case of magnetism-engineered iron oxide (MEIO), Fe_3O_4, nanoparticles.[13] As the size of MEIO nanoparticles increases from 4 to 6, 9, and 12 nm, the mass magnetization values change from 25 to 43, 80, and 101 emu/(g Fe), respectively (Figure 5a). This result shows a linear relationship upon the plotting of $m_s^{1/3}$ vs r^{-1} (Figure 5b) as predicted in eq 1. Such size-dependent mass magnetization values directly affect their magnetic resonance (MR) signal enhancement capabilities for molecular imaging of biological targets (*vide infra*).

2.2. Shape and Composition Effects on Nanomagnetism. The anisotropic constant (K_u) is known to be strongly correlated with various anisotropies such as shape, magne-
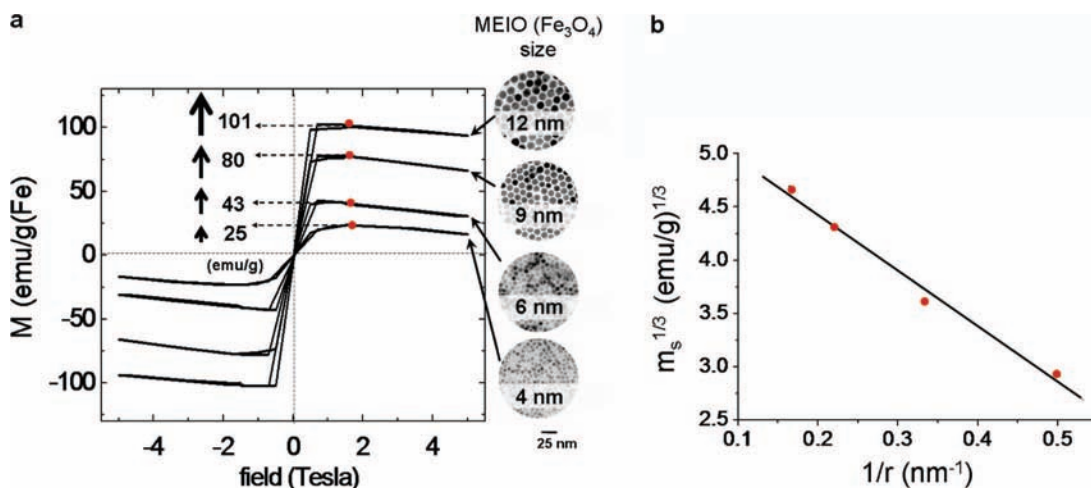
FIGURE 5. Size dependent mass magnetization values of 4, 6, 9, and 12 nm magnetism-engineered iron oxide (MEIO) nanoparticles: (a) hysteresis loops, mass magnetization values at 1.5 T, and TEM images; (b) plot of $m_s^{1/3}$ vs r^{-1}. Reproduced with permission from ref 13. Copyright 2005 American Chemical Society.

tocrystalline, and exchange.[33−36] For example, shape anisotropy of particles is expressed as

$$K_u = [H_a + (N_2 − N_1)M_s]M_s/2 \qquad (2)$$

where H_a is the anisotropy field and N_2 and N_1 are the demagnetization factors parallel and perpendicular to the easy axis of the magnetic particle.[36] Such effects can be observed in CoPt barcode-structured nanowires with various aspect ratios.[39] The aspect ratios ($\gamma = b/a$) of Co bar fragments are tuned by controlling their length (b) with a fixed diameter (a) of 65 nm (Figure 6a−d). For Co nanowires with a high aspect ratio ($\gamma = 45$), the coercivity of the nanowire magnetized along the b direction ($H_{c(b)}$) is 668 Oe (Figure 6e (red line)). As γ is decreased to 3.5, 1, and 0.25, the coercivity of the sample decreases to 667, 164, and 76 Oe, respectively (Figure 6f−h (red lines),i (red squares)), indicating that higher γ (i.e., larger shape anisotropy) of the Co bar fragments leads to the larger magnetic coercivity. Such shape anisotropy effects can be also observed upon changes in the direction of the external magnetic field. For nanowires with rod-shaped Co bar fragments ($\gamma = 45$ or 3.5), larger magnetic coercivities are obtained from nanowires magnetized along the b direction ($H_{c(b)}$) than from nanowires magnetized along the a direction ($H_{c(a)}$) (Figure 6e,f,i). In contrast, nanowires with disk-shaped Co bar fragments (i.e., $\gamma = 1$ or 0.25) have higher $H_{c(a)}$ than $H_{c(b)}$ (Figure 6g−i). Such results indicate that the magnetically easy axis of the nanowires changes from b direction to a direction due to shape anisotropy effects as the shape of the Co bar fragments varies from rods to discs.

The magnetocrystalline phase of the nanoparticle is significant in determining the magnetic coercivity of the nanoparticle.[15−18] This can be observed in magnetic nanoalloys with anisotropic crystalline structures. Co@Pt core−shell nanoparticles composed of an isotropically structured face-centered cubic (fcc) Co core and a nonmagnetic Pt shell exhibit superparamagnetic behavior with zero coercivity at room temperature (Figure 7a,b,d).[15−17] However, after thermal treatment, they transform to anisotropically structured face-centered tetragonal (fct) CoPt nanoalloys (Figure 7a,c), which now exhibit room-temperature ferromagnetic behavior with a coercivity value of 5300 Oe due to large magnetocrystalline anisotropy (Figure 7e).[16]

Compositional modification of nanoparticles by the adoption of magnetic dopants can significantly change the magnetism of nanoparticles.[14] For example, magnetism-engineered iron oxide (MEIO), Fe_3O_4, nanoparticles have a ferrimagnetic spin structure where Fe^{2+} and Fe^{3+} occupying O_h sites align parallel to the external magnetic field and Fe^{3+} in the T_d sites of fcc-packed oxygen lattices align antiparallel to the field (Figure 8a). Since Fe^{3+} possesses a d^5 electron configuration with a high spin state and Fe^{2+} has a d^6 configuration with a high spin state, the total magnetic moment per unit $(Fe^{3+})_{T_d}(Fe^{2+}Fe^{3+})_{O_h}O_4$ is approximately $4\mu_B$. Incorporation of a magnetic dopant M^{2+} (M = Mn, Co, Ni) with electron configurations of d^5, d^4, and d^3, respectively, to replace O_h Fe^{2+} leads to change in the net magnetization (Figure 8b). The magnetic moment per unit $MnFe_2O_4$ (Mn-MEIO), $CoFe_2O_4$ (Co-MEIO), and $NiFe_2O_4$ (Ni-MEIO) is now estimated as $5\mu_B$, $3\mu_B$, and $2\mu_B$, respectively. Due to such compositional effects, the experimentally observed mass magnetization value at 1.5 T gradually decreases from 110 emu to 101, 99, and 85
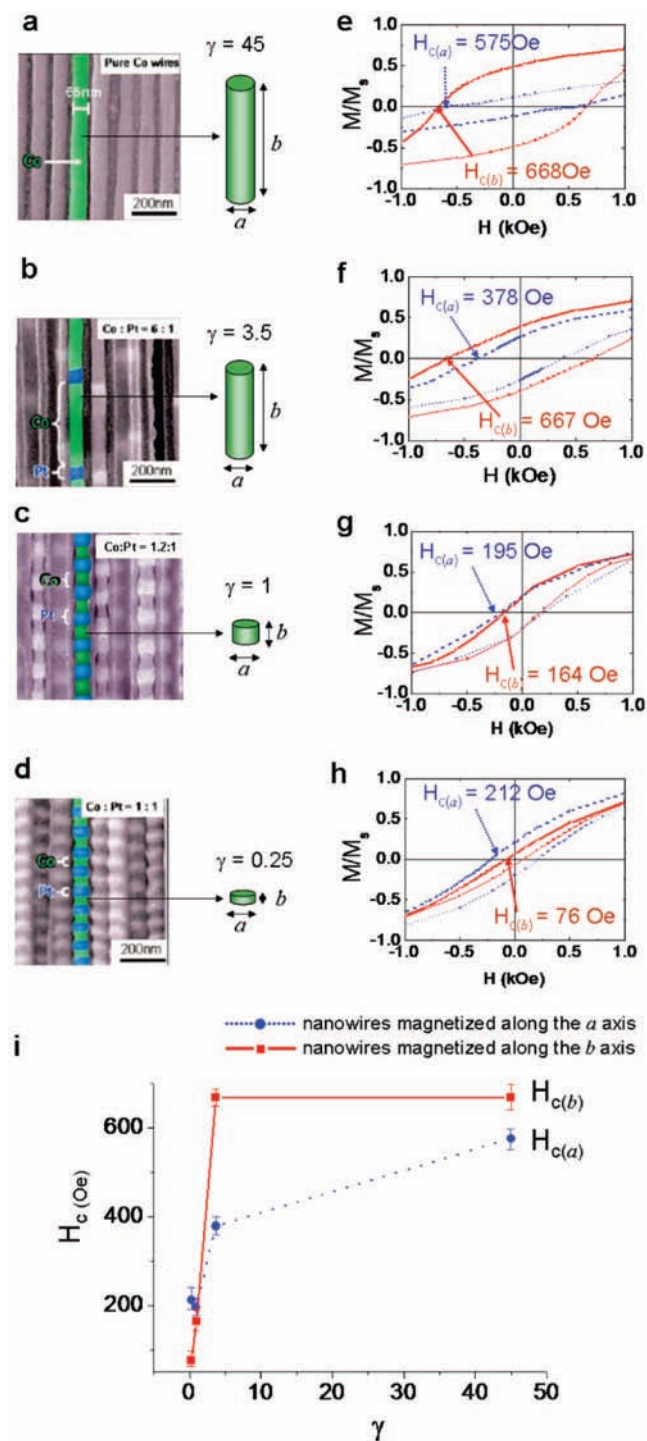
FIGURE 6. Scanning electron microscopic (SEM, a−d) images of CoPt barcodes with various aspect ratio (γ) of Co bars and their shape-dependent magnetism (e−h) under parallel (i.e., b axis) and perpendicular (i.e., a axis) magnetic fields with respect to the nanowire direction and (i) plot of coercivity ($H_{c(a)}$, $H_{c(b)}$) vs γ. Reproduced with permission from ref 39. Copyright 2005 American Chemical Society.

emu per mass of magnetic atoms (emu/g(M+Fe)) for Mn-MEIO, MEIO, Co-MEIO, and Ni-MEIO, respectively (Figure 8c).[14]
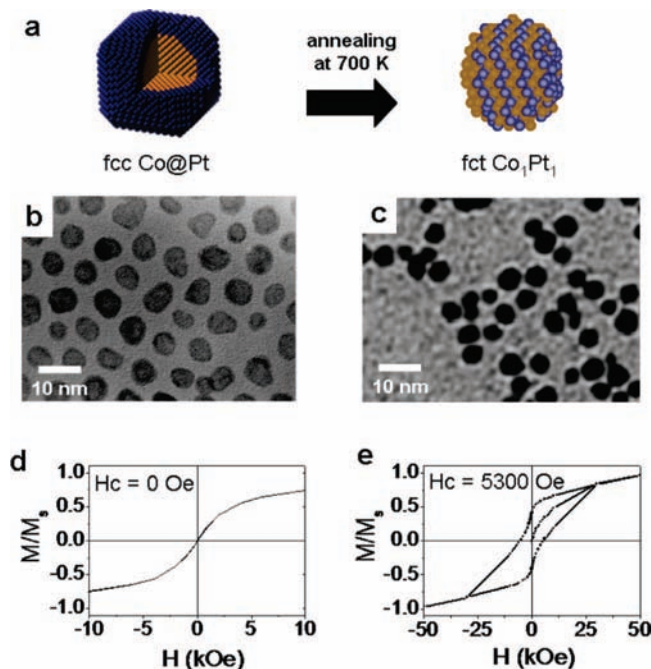
FIGURE 7. Magnetocrystalline phase effects on magnetism: (a) schematic of ferromagnetic phase transition of fcc Co@Pt core–shell nanoparticles to fct CoPt nanoalloys; TEM images and hysteresis loops of (b, d) fcc Co@Pt core–shell nanoparticles and (c, e) fct CoPt nanoalloys. Reproduced with permission from ref 16. Copyright 2004 American Chemical Society.

3. Magnetism-Engineered Nanoparticles for Biomedical Applications

Attaining the specific targeting ability of magnetic nanoparticles is important for their biomedical applications. This can be achievable by tailoring nanoparticle surface with appropriate ligands, which can endow high colloidal and biostability, low nonspecific binding affinity, and facile bioconjugation with target-specific chemical and biological molecules.

3.1. Magnetic Resonance Imaging of Biological Targets.

Magnetic nanoparticles provide strong contrast effects on surrounding tissues under MRI scans and therefore have served as important probes for MR imaging. MR contrast effects of magnetic nanoparticles can be simply understood in terms of their effect on the spin–spin relaxation time of surrounding water protons. Conventional iron oxide based contrast agents such as superparamagnetic iron oxide (SPIO) and related nanoparticle probes (e.g., cross-linked iron oxide (CLIO)) have limited uses for advanced MR imaging due to their relatively poor magnetic contrast effects (i.e., low magnetic moment and also low r_2 coefficient).[25,40,41] Therefore, a new type of magnetic nanoparticles such as MEIO with high and tunable mass magnetization values are needed to enhance the relaxation process of the proton nuclear spins.[42]
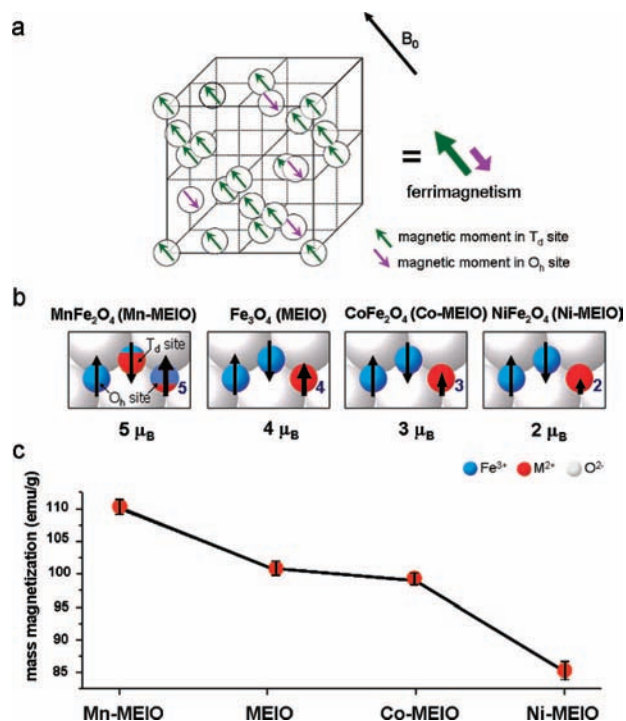
FIGURE 8. (a) Ferrimagnetic spin structure of inverse spinel ferrites and (b) schematic spin moments and (c) mass magnetization values of various metal-doped MEIO nanoparticles (MFe_2O_4, M = Mn, Fe, Co, Ni). Reprinted with permission from *Nature Medicine* (www.nature.com), ref 14. Copyright 2007 Nature Publishing Group.
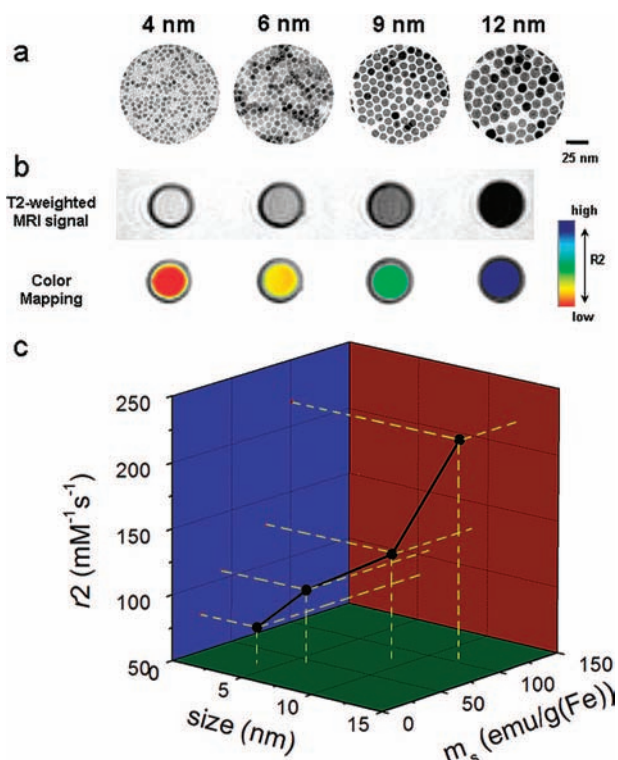
FIGURE 9. Nanoscale size effects of MEIO nanoparticles on MR contrast effects: (a) TEM images; (b) MR images and their color maps; (c) plot of m_s and r_2 values vs size of 4, 6, 9, and 12 nm MEIO. Reproduced with permission from ref 13. Copyright 2005 American Chemical Society.
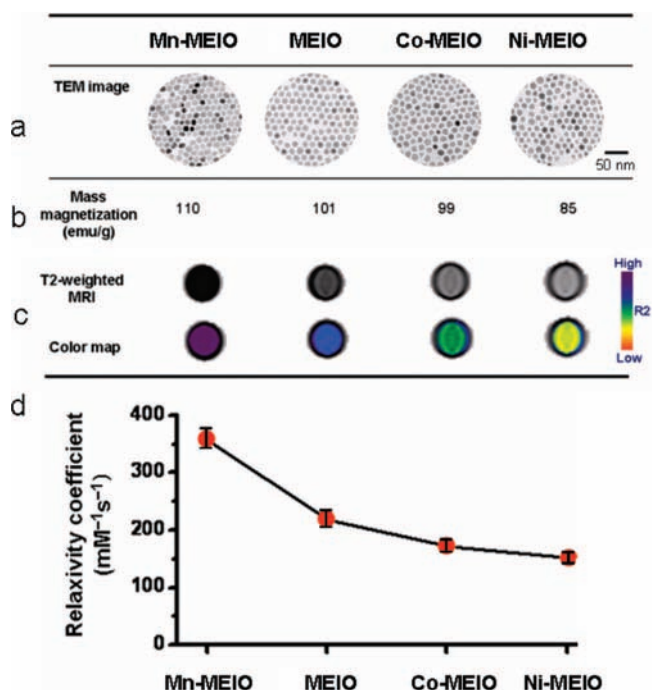
FIGURE 10. Composition effects of metal-doped MEIO nanoparticles: (a) TEM images; (b) mass magnetization values; (c) MR images and their color maps; (d) relaxivity coefficient (r_2) values of Mn-MEIO, MEIO, Co-MEIO, and Ni-MEIO. Reprinted with permission from *Nature Medicine* (www.nature.com), ref 14. Copyright 2007 Nature Publishing Group.

In particular, significant shortening of the spin–spin relaxation time (T_2) of the proton is possible by using a new type of magnetic nanoparticles.

As described in section 2.1, larger MEIO nanoparticles possess higher magnetization values and exhibit stronger MR contrast effects, which are observed as darker MR contrast and blue in color MRI maps (Figure 9a,b).[13] The relaxivity coefficient (r_2), which is a direct indication of contrast enhancement effects, is 78 mM^{-1} s^{-1} for 4 nm MEIO and gradually increases to 106, 130, and to 218 mM^{-1} s^{-1} for 6, 9, and 12 nm size MEIO nanoparticles (Figure 9c).

In addition to the size effects, magnetic dopant effects of MEIO nanoparticles are also significant. For example, Mn-MEIO nanoparticles with the highest magnetization values of 110 emu/g(Mn+Fe) exhibit the best MR signal enhancement effects with an r_2 of 358 mM^{-1} s^{-1} (Figure 10).[14] Other metal-doped MEIO nanoparticles including MEIO, Co-MEIO, and Ni-MEIO with diminished mass magnetization values of 101 emu/g(Fe), 99 emu/g(Co+Fe), and 85 emu/g(Ni+Fe), respectively, show less MR contrast effects with r_2 of 218, 172, and 152 mM^{-1} s^{-1}, respectively, which is consistent with the trend of mass magnetization of nanoparticles (Figure 10). It is noteworthy that the r_2 of 12 nm Mn-MEIO nanoparticles is ~5.8 times higher than that of conventional molecular MR imaging contrast agents such as cross-linked iron oxide (CLIO) nanoparticles.
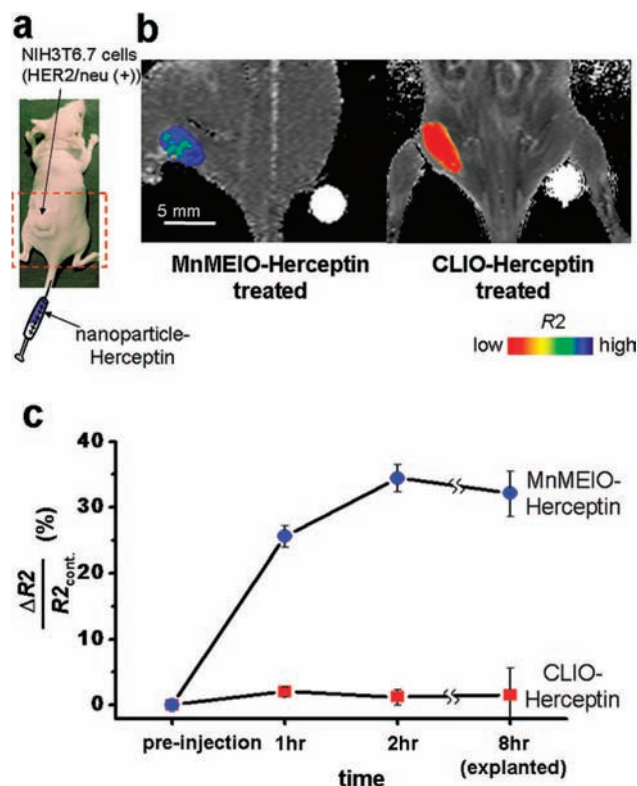
FIGURE 11. Ultrasensitive *in vivo* cancer detection through the utilization of Mn-MEIO−Herceptin nanoparticle probes: (a) tail vein injection of the Mn-MEIO−Herceptin probes into a mouse with a small (∼50 mg) HER2/neu positive cancer in its proximal femur region; (b) color-mapped MR images of the mouse treated with Mn-MEIO−Herceptin conjugates; (c) time-dependent R_2 changes at the tumor site after injection of Mn-MEIO−Herceptin probes (blue circle) and CLIO−Herceptin probes (red square). Reprinted with permission from *Nature Medicine* (www.nature.com), ref 14. Copyright 2007 Nature Publishing Group.

Such MR signal enhancement effects of Mn-MEIO nanoparticles enable successful ultrasensitive *in vivo* detection of biological targets.[14] When these molecules are conjugated with a cancer-targeting antibody, Herceptin, and intravenously injected into a mouse with a small HER2/neu positive cancer (∼50 mg), they selectively detect small cancer with strong MR signals shown as blue color, which represents high MR relaxivity ($R_2 = 1/T_2$)) (Figure 11a,b). In contrast, there is no noticeable MR signal change ($\Delta R_2/R_{2,\text{control}}$) at the cancer region from the mouse treated with conventional CLIO−Herceptin conjugates (Figure 11b,c).

3.2. Ferromagnetic Magnet−DNA Network Structures. Self-assembly of biomolecules to form highly ordered and programmed three-dimensional structures through specific molecular recognition and biological interactions such as protein–protein interaction, DNA hybridization, hydrogen bonding, and van der Waals forces has been observed.[43,44] In particular, DNA is a naturally occurring biopolymer with sequence-specific self-
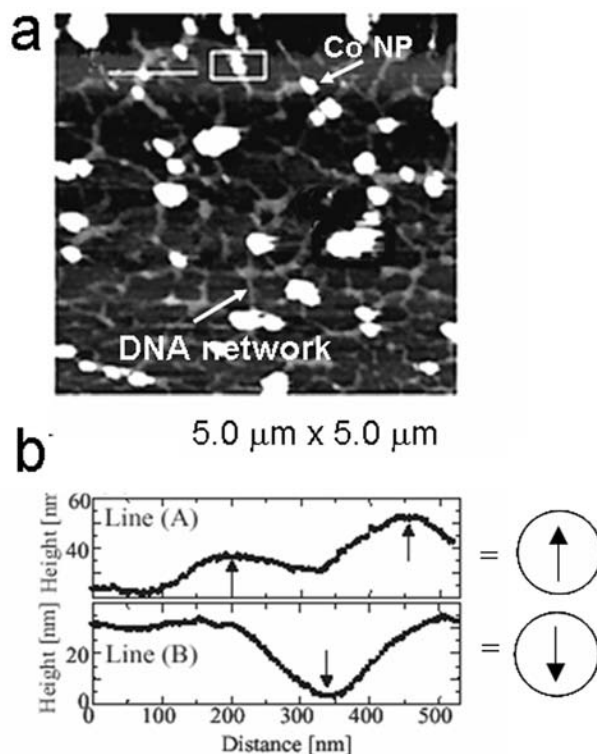
FIGURE 12. (a) Atomic force microscopic images of a DNA−Co nanoparticle hybrid network structure and (b) magnetic force microscopic scanning of a single Co nanoparticle with either parallel (top) or reversal (bottom) spin directions located in different regions. Reproduced from ref 45 with permission. Copyright 2002 American Scientific Publishers.

assembly capabilities. By engineering DNA sequences, it is possible to form various DNA nanoarchitectures such as multimers, wires, and networks. Therefore, DNA molecules can serve as templates for making magnetic nanoparticle assemblies. For example, hybridization of ferromagnetic Co nanoparticles with DNA induces the formation of magnetic nanoparticle network structures.[45] Based on the nanoscaling laws described in section 2.1, Co nanoparticles show single-domain ferromagnetic behaviors around 10 nm. When ferromagnetic 12 nm Co nanoparticles coated with 2-mercaptoethylamine hydrochloride are mixed with poly(C)·poly(G) single-stranded DNA (ssDNA), Co nanoparticles on double-stranded DNA (dsDNA) network structures are formed due to the electrostatic interaction between positively charged nanoparticles and negatively charged dsDNA networks (Figure 12a). Magnetic force microscopic (MFM) images of these magnet−DNA network structures show that the nanoparticles have both up-spin and down-spin states like "bits" in magnetic data storage (Figure 12b). Furthermore, such a ferromagnetic−bio hybrid system can be potentially useful for the detection of biological events such as DNA hybridization and cleavage via MFM or superconducting quantum interference device (SQUID) sensors.
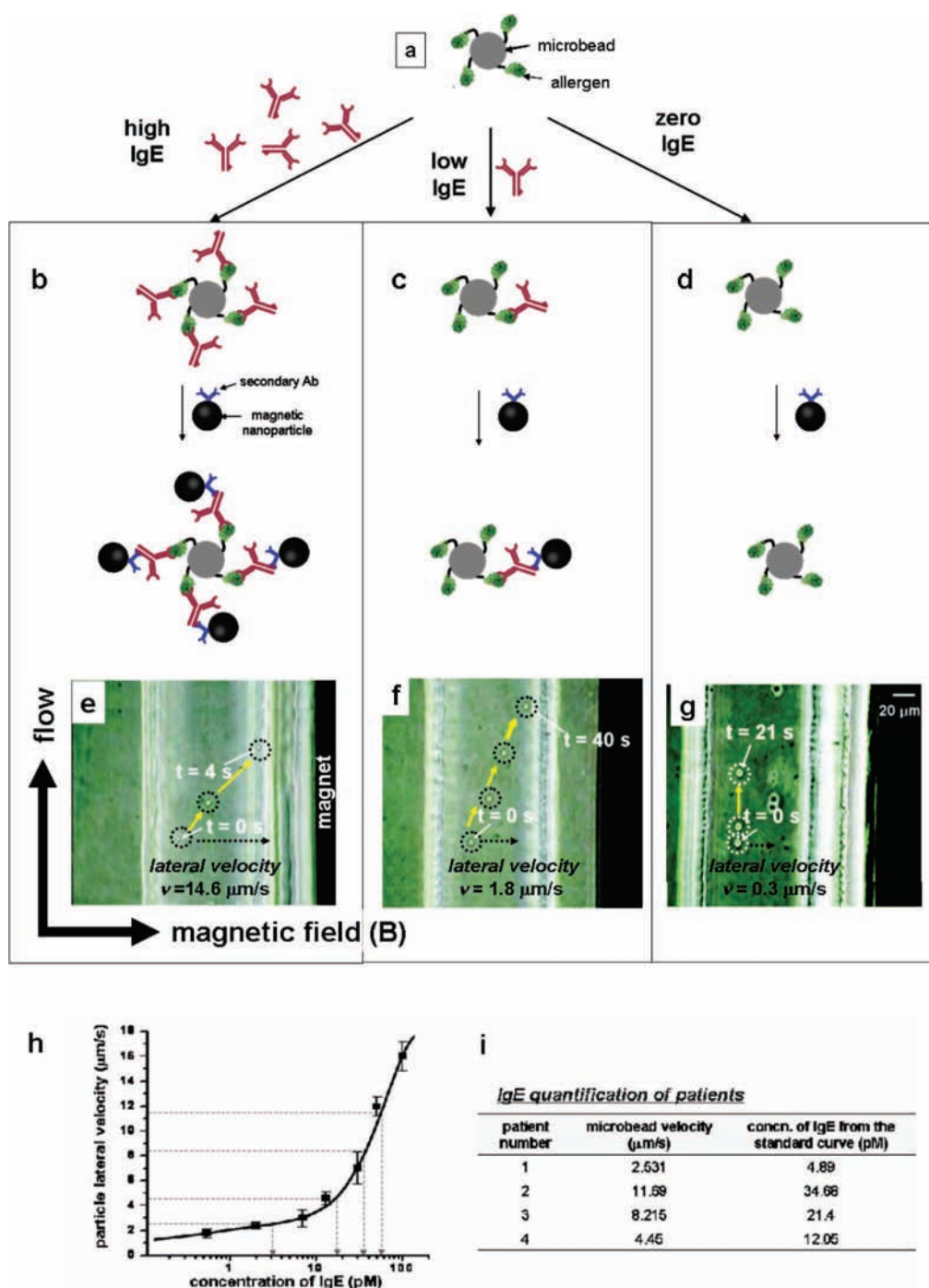
FIGURE 13. Magnetophoretic sensing of allergen-specific IgE: (a) microbeads coated with allergen; detection scheme at (b) high, (c) low, and (d) zero concentration of the target IgE; (e–g) magnetophoretic movements of the samples shown in panels b–d; (h) standard calibration curve of particle lateral velocity vs IgE concentration; (i) quantification of target IgE in sera of patients calculated by the standard curve in panel h. Reproduced with permission from ref 49. Copyright 2007 American Chemical Society.

3.3. Magnetophoretic Biosensing and Separation.

Magnetophoretic sensing and separation of biological targets can also be accomplished by using magnetic particles. When an external magnetic field is applied perpendicular to the flow direction of a microfluidic channel, magnetic particles experience a magnetic force (*F*), which drives their magnetophoretic lateral movement with a velocity of v_{lat}.

$$v_{lat} = \frac{2\Delta\chi r^2}{9\eta\mu_0}(\nabla\vec{B}) \cdot \vec{B} \tag{3}$$

where $\Delta\chi$ is magnetic susceptibility of the particle, r is the particle radius, μ_0 is the vacuum permeability, and B is the external magnetic field.[46]

Jun et al.

Magnetic beads have been widely used for such magnetic sensing and separation purposes, but these still have problems including low magnetic susceptibility and magnetic inhomogeniety.[46−48] By use of nanoparticles with well-defined size and magnetism, however, ultrasensitive and reliable allergen-specific IgE detection is possible.[49] Magnetic susceptibility of nanoparticles plays an important role in the velocity control and subsequent biological target separations as predicted by eq 3. Allergies are caused by a hypersensitive reaction between allergens and allergen-specific IgE antibodies. Allergen-specific IgE can be found in the serum of the allergy patient, but its concentration is very low, and therefore highly sensitive detection of IgE is important.[50] Microbeads coated with mite allergen from *Dermatophagoides farinae* (Figure 13a) are first mixed with the target IgE with varying concentrations. Then anti-human IgE-coated MEIO nanoparticles with the capability to bind to the Fc region of the target IgE are further added, and the resulting solution is injected into the microfluidic channel. At a high concentration of the target IgE, significant lateral movement of microbeads with a velocity (v_{lat}) of ∼15 μm/s is observed (Figure 13b,e), while reduced ($v_{lat} = $ ∼2 μm/s) and negligible lateral movements are seen at lower concentrations of IgE or no IgE, respectively (Figure 13c,d,f,g). Such observations are reasonable since the higher IgE concentrations induce more binding of MEIO nanoparticles onto the microbeads. Quantitative detection of the target IgE in sera is also possible up to sub-picomolar IgE levels (∼500 fM) by using a target IgE concentration vs lateral velocity standard calibration curve (Figure 13h,i).

4. Concluding Remarks

In this Account, we have discussed the nanoscaling laws of magnetic nanoparticles and reviewed selected case studies on metal, metal ferrite, and metal alloy nanoparticles. In the size range of 1−50 nm, parameters including size, shape, and composition have a tremendous influence on magnetic characteristics such as coercivity and magnetization values. Such scaling laws of magnetic nanoparticles can make them programmable for their ultimate performance for specific biomedical applications, as demonstrated in their utilization as superior MR contrast agents and magnetic separation vectors. Although the current understanding of nanoscaling laws of magnetism is still limited, more studies and experimental exploration into this area of nanomagnetism can lead to significant advances in various fields of next-generation biomedical sciences such as drug delivery, hyperthermia, MRI, magnetic separation and biosensors, and nanobiofunctional magnetic materials.

This research is supported by the Korea Research Council of Fundamental Science & Technology, the National Research Laboratory (Grant M1060000255), Nano-Bio Science & Technology Program (Grant M1050300218-05M0300-21810), NCRC (Grant R15-2004-024-02002-0), NCI Center for Cancer Nanotechnology Excellence (CCNE), NBIT (Grant K20716000001-07A0400-00110), and 2nd stage BK21 for Chemistry.

BIOGRAPHICAL INFORMATION

Young-wook Jun received his B.S. degree from Yonsei University and Ph.D. degree from the Korea Advanced Institute of Science and Technology in 2005, where he studied the synthetic and mechanistic aspects of nanocrystals. After a postdoctoral training on nanoparticle-assisted MRI at Yonsei University with Professor Cheon, he is currently working on the nanoparticle-assisted single molecule spectroscopy of biological phenomena with Professor Alivisatos at the University of California, Berkeley.

Jung-wook Seo received his B.S. and M.S. degrees from Seoul National University and his Ph.D. degree from Yonsei University in 2007. His thesis was focused on the development of metal oxide and metal chalcogenide nanocrystals. He is a senior scientist at Samsung-Electromechanics where he works in the field of surface metalization and nanoparticle researches for electronic devices.

Jinwoo Cheon is the director of Convergence Nanomaterials National Research Laboratory of Korea. He graduated from Yonsei University with B.S. and received his Ph.D. from University of Illinois, Urbana−Champaign in 1993. After postdoctoral training at U.C. Berkeley and also at UCLA, he joined the KAIST where he was an assistant and then associate professor. In 2002, he moved to Yonsei University. His research interests include the development of functional inorganic nanoparticles and their biomedical and energy related applications.

FOOTNOTES

*To whom correspondence should be addressed. E-mail: jcheon@yonsei.ac.kr.

REFERENCES

1   Walker, M.; Diebel, C.; Haugh, C.; Pankhurst, P.; Montgomery, J.; Green, C. Structure and function of the vertebrate magnetic sense. *Nature* **1997**, *390*, 371–376.

2   Murray, C. B.; Sun, S. H.; Doyle, H.; Betley, T. Monodisperse 3d transition-metal (Co, Ni, Fe) nanoparticles and their assembly into nanoparticle superlattices. *MRS Bull.* **2001**, *26*, 985–991.

3   Sun, S. H.; Zeng, H.; Robinson, D. B.; Raoux, S.; Rice, P. M.; Wang, S. X.; Li, G. X. Monodisperse MFe$_2$O$_4$ (M = Fe, Co, Mn) nanoparticles. *J. Am. Chem. Soc.* **2004**, *126*, 273–279.

4   Sun, S. H. Recent advances in chemical synthesis, self-assembly, and applications of FePt nanoparticles. *Adv. Mater.* **2006**, *18*, 393–403.

5   Hyeon, T. Chemical synthesis of magnetic nanoparticles. *Chem. Commun.* **2003**, 927–934.

6   Jana, N. R.; Chen, Y.; Peng, X. Size- and shape-controlled magnetic (Cr, Mn, Fe, Co, Ni) oxide nanocrystals via a simple and general approach. *Chem. Mater.* **2004**, *16*, 3931–3935.

188 ■ ACCOUNTS OF CHEMICAL RESEARCH ■ 179-189 ■ February 2008 ■ Vol. 41, No. 2

7 Jun, Y.; Choi, J.; Cheon, J. Heterostructured magnetic nanoparticles: Their versatility and high performance capabilities. *Chem. Commun.* **2007**, 1203–1214.

8 Park, J.; An, K. J.; Hwang, Y. S.; Park, J. G.; Noh, H. J.; Kim, J. Y.; Park, J. H.; Hwang, N. M.; Hyeon, T. Ultra-large scale synthesis of monodispersed nanocrystals. *Nat. Mater.* **2004**, *3*, 891–895.

9 Cheon, J.; Kang, N.-J.; Lee, S.-M.; Yoon, J.-H.; Oh, S. J. Shape evolution of single-crystalline iron oxide nanocrystals. *J. Am. Chem. Soc.* **2004**, *126*, 1950–1951.

10 Shevchenko, E. V.; Talapin, D. V.; Rogach, A. L.; Kornowski, A.; Haase, M.; Weller, H. Colloidal synthesis and self-assembly of CoPt$_3$ nanocrystals. *J. Am. Chem. Soc.* **2002**, *124*, 11480–11485.

11 Leslie-Pelecky, D. L.; Rieke, R. D. Magnetic properties of nanostructured materials. *Chem. Mater.* **1996**, *8*, 1770–1783.

12 Park, J.-I.; Kang, N.-J.; Jun, Y.; Oh, S. J.; Ri, H. C.; Cheon, J. Superlattice and magnetism directed by the size and shape of nanocrystals. *ChemPhysChem* **2002**, *3*, 543–547.

13 Jun, Y.; Huh, Y.-M.; Choi, J.-s.; Lee, J.-H.; Song, H.-T.; Kim, S. J.; Yoon, S.; Kim, K.-S.; Shin, J.-S.; Suh, J.-S.; Cheon, J. Nanoscale size effect of magnetic nanocrystals and their utilization for cancer diagnosis via magnetic resonance imaging. *J. Am. Chem. Soc.* **2005**, *127*, 5732–5733.

14 Lee, J.-H.; Huh, Y.-M.; Jun, Y.; Seo, J.-w.; Jang, J.-t.; Song, H.-T.; Kim, S. J.; Cho, E.-J.; Yoon, H.-G.; Suh, J.-S.; Cheon, J. Artificially engineered magnetic nanoparticles for ultra-sensitive molecular imaging. *Nat. Med.* **2007**, *13*, 95–99.

15 Park, J.-I.; Cheon, J. Synthesis of "solid solution" and "core—shell" type cobalt—platinum magnetic nanoparticles via transmetalation reactions. *J. Am. Chem. Soc.* **2001**, *123*, 5743–5746.

16 Park, J.-I.; Kim, M. G.; Jun, Y.; Lee, J. S.; Lee, W.-r.; Cheon, J. Characterization of superparamagnetic "core-shell" nanoparticles and monitoring their anisotropic phase transition to ferromagnetic "solid solution" nanoalloys. *J. Am. Chem. Soc.* **2004**, *126*, 9072–9078.

17 Lee, W.; Kim, M. G.; Choi, J.; Park, J. I.; Ko, S. J.; Oh, S. J.; Cheon, J. Redox-transmetalation process as a generalized synthetic strategy for core-shell magnetic nanoparticles. *J. Am. Chem. Soc.* **2005**, *127*, 16090–16097.

18 Sun, S.; Murray, C. B.; Weller, D.; Folks, L.; Moser, A. Monodisperse FePt nanoparticles and ferromagnetic FePt nanocrystal superlattices. *Science* **2000**, *287*, 1989–1992.

19 Mirkin, C. A.; Niemeyer, C. M. *Nanobiotechnology II: More Concept and Applications*; Wiley-VCH: Weinheim, Germany, 2007.

20 Huh, Y.-M.; Jun, Y.; Song, H.-T.; Kim, S. J.; Choi, J.-s.; Lee, J.-H.; Yoon, S.; Kim, K.-S.; Shin, J.-S.; Suh, J.-S.; Cheon, J. In vivo magnetic resonance detection of cancer by using multifunctional magnetic nanocrystals. *J. Am. Chem. Soc.* **2005**, *127*, 12387–12391.

21 Xu, C.; Xu, K.; Gu, H.; Zheng, R.; Liu, H.; Zhang, X.; Guo, Z.; Xu, B. Dopamine as a robust anchor to immobilize functional molecules on the iron oxide shell of magnetic nanoparticles. *J. Am. Chem. Soc.* **2004**, *126*, 9938–9939.

22 Son, S. J.; Reichel, J.; He, B.; Schuchman, M.; Lee, S. B. Magnetic nanotubes for magnetic-field-assisted bioseparation, biointeraction, and drug delivery. *J. Am. Chem. Soc.* **2005**, *127*, 7316–7317.

23 Weissleder, R.; Moore, A.; Mahmood, U.; Bhorade, R.; Benveniste, H.; Chiocca, E. A.; Basilion, J. P. In vivo magnetic resonance imaging of transgene expression. *Nat. Med.* **2000**, *6*, 351–355.

24 Lewin, M.; Carlesso, N.; Tung, C. H.; Tang, X. W.; Cory, D.; Scadden, D. T.; Weissleder, R. Tat peptide-derivatized magnetic nanoparticles allow in vivo tracking and recovery of progenitor cells. *Nat. Biotechnol.* **2000**, *18*, 410–414.

25 Pankhurst, Q. A.; Connolly, J.; Jones, S. K.; Dobson, J. Applications of magnetic nanoparticles in biomedicine. *J. Phys. D* **2003**, *36*, R167–R181.

26 Jordan, A.; Scholz, R.; Wust, P.; Fahling, H.; Felix, R. Magnetic fluid hyperthermia (MFH): Cancer treatment with AC magnetic field induced excitation of biocompatible superparamagnetic nanoparticles. *J. Magn. Magn. Mater.* **1999**, *201*, 413–419.

27 Bulte, J. W. M.; Kraitchman, D. L. Iron oxide MR contrast agents for molecular and cellular imaging. *NMR Biomed.* **2004**, *17*, 484–499.

28 Ferrari, M. Cancer nanotechnology. Opportunities and challenges. *Nat. Rev. Cancer* **2005**, *5*, 161–171.

29 Kim, J.; Park, S.; Lee, J. E.; Jin, S. M.; Lee, J. H.; Lee, I. S.; Yang, I.; Kim, J. S.; Kim, S. K.; Cho, M. H.; Hyeon, T. Designed fabrication of multifunctional magnetic gold nanoshells and their application to magnetic resonance imaging and photothermal therapy. *Angew. Chem., Int. Ed.* **2006**, *45*, 7754–7758.

30 Rosi, N.; Mirkin, C. Nanostructures in biodiagnostics. *Chem. Rev.* **2005**, *105*, 1547–1562.

31 Stoeva, S. I.; Huo, F. W.; Lee, J. S.; Mirkin, C. A. Three-layer composite magnetic nanoparticle probes for DNA. *J. Am. Chem. Soc.* **2005**, *127*, 15362–15363.

32 Harisinghani, M. G.; Barentsz, J.; Hahn, P. F.; Deserno, W. M.; Tabatabaei, S.; van de Kaa, C. H.; de la Rosette, J.; Weissleder, R. Noninvasive detection of clinically occult lymph-node metastases in prostate cancer. *N. Eng. J. Med.* **2003**, *348*, 2491–2505.

33 Cullity, B. D. *Introduction to Magnetic Materials*; Addison-Wesley Publishing: Reading, MA, 1972.

34 McCurrie, R. A. *Ferromagnetic Materials: Structure and Properties*; Academic Press, San Diego, CA, 1994.

35 Cornell, R. M.; Schwertmann, U. *The Iron Oxides*; Wiley-VCH: Weinheim, Germany, 2003.

36 Jales, D. *Introduction to Magnetism and Magetnic Materials*; CRC Press, Boca Raton, FL, 1998.

37 Morales, M. P.; Veintemillas-Verdaguer, S.; Montero, M. I.; Serna, C. J. Surface and internal spin canting in γ-Fe$_2$O$_3$ nanoparticles. *Chem. Mater.* **1999**, *11*, 3058–3064.

38 Morales, M. P.; Serna, C. J.; Bødker, F.; Mørup, S. Spin canting due to structural disorder in maghemite. *J. Phys.: Condens. Matter* **1997**, *9*, 5461–5467.

39 Choi, J.; Oh, S. J.; Ju, H.; Cheon, J. Massive fabrication of free-standing one-dimensional Co/Pt nanostructures and modulation of ferromagnetism via a programmable barcode layer effect. *Nano Lett.* **2005**, *5*, 2179–2183.

40 Weissleder, R.; Lee, A. S.; Fischman, A. J.; Reimer, P.; Shen, T.; Wilkinson, R.; Callahan, R. J.; Brady, T. J. *Radiology* **1991**, *181*, 245–249.

41 Tanimoto, A.; Kuribayashi, S. *Eur. J. Radiol.* **2006**, *58*, 200–216.

42 Koenig, S. H.; Keller, K. E. Theory of 1/T1 and 1/T2 NMRD profiles of solutions of magnetic nanoparticles. *Magn. Reson. Med.* **1995**, *34*, 227–233.

43 Wille, H.; Drewes, G.; Biernat, J.; Mandelkow, E.; Mandelkow, E. M. Alzheimer-like paired helical filaments and antiparallel dimers formed from microtubule-associated protein tau in vitro. *J. Cell Biol.* **1992**, *118*, 573–584.

44 Winfree, E.; Liu, F. R.; Wenzler, L. A.; Seeman, N. C. Design and self-assembly of two-dimensional DNA crystals. *Nature* **1998**, *394*, 539–544.

45 Lee, H. Y.; Sacho, Y.; Kanki, T.; Tanaka, H.; Shirakawa, H.; Cheon, J.; Yoon, J.-H.; Kang, N.-J.; Park, J.-I.; Kawai, T. DNA-directed magnetic network formation with ferromagnetic nanoparticles. *J. Nanosci. Nanotechnol.* **2002**, *2*, 613–615.

46 Hayes, M. A.; Polson, N. A.; Phayre, A. N.; Garcia, A. A. Flow-based microimmunoassay. *Anal. Chem.* **2001**, *73*, 5896–5902.

47 Pamme, N.; Manz, A. On-chip free-flow magnetophoresis: Continuous flow separation of magnetic particles and agglomerates. *Anal. Chem.* **2004**, *76*, 7250.

48 Fan, Z. H.; Mangru, S.; Granzow, R.; Heaney, P.; Ho, W.; Dong, Q.; Kumar, R. Dynamic DNA hybridization on a chip using paramagnetic beads. *Anal. Chem.* **1999**, *71*, 4851–4859.

49 Hahn, Y. K.; Jin, Z.; Kang, H.; Oh, E.; Han, M.-K.; Kim, H.-S.; Jang, J.-t.; Lee, J.-H.; Cheon, J.; Kim, S.-H.; Park, H. S.; Park, J.-K. Magnetophoretic immunoassay of allergen-specific IgE in an enhanced magnetic field gradient. *Anal. Chem.* **2007**, *79*, 2214.

50 Tizard, I. R. *Immunology*, 4th ed.; Saunders College Publishing: Orlando, FL, 1995.

Communications

Critical Enhancements of MRI Contrast and Hyperthermic Effects by Dopant-Controlled Magnetic Nanoparticles**

*Jung-tak Jang, Hyunsoo Nah, Jae-Hyun Lee, Seung Ho Moon, Min Gyu Kim, and Jinwoo Cheon**

Magnetic characteristics are crucial for the successful performances of magnetic nanoparticles in biomedical applications such as magnetic resonance imaging (MRI), drug delivery, cellular signaling, and hyperthermia.[1–4] Therefore, the development of new types of nanoparticles is particularly important. In this regard, a metal dopant substitution strategy of metal ferrite nanoparticles has been pursued to achieve high and tunable nanomagnetism.[5] In the case of Zn^{2+} doping, however, the use of nonequilibrium reactions has typically resulted in nonstoichiometric or metastable states in which Zn^{2+} ions are disordered between T_d and O_h sites.[6–8] A recent report of successful Zn^{2+} doping includes the use of diethyl zinc (Et_2Zn) as a new Zn^{2+} ion source;[9] however, because of the highly unstable and pyrophoric nature of the precursor, such a synthetic protocol for nanoparticles is still far from ideal for the achievement of large-scale reproducibility and precise dopant controls. In this study, we have overcome a number of previous challenges; not only is size monodispersity with a large-scale (ca. 10 g) synthesis achieved, the proper positioning of Zn^{2+} dopants in T_d sites in metal ferrite nanoparticles is also demonstrated, which ultimately leads to successful magnetism tuning. Our obtained nanoparticles exhibit an extremely high magnetization value (175 emu g^{-1}) and provide the largest MRI contrast effects ($r2 = 860$ mм$^{-1}$s^{-1}) among the contrast agents reported to date. They have an eight- to fourteenfold increase in MRI contrast and a fourfold enhancement in hyperthermic effects compared to conventional iron oxide nanoparticles.

For decades, iron oxide (Fe_3O_4) nanoparticles have served as the model material in the biomedical research field associated with magnetism.[10] However, considering that the effects of magnetic nanoparticles for biomedical applications are strongly dependent on their magnetic characteristics, it is important to devise nanoparticles with high and tunable magnetism, especially saturation magnetization (M_s) values, while maintaining high size monodispersity. For example, nanoparticles with tunable magnetism, such as manganese-doped metal ferrite and FeCo nanoparticles, have enhanced MRI contrast effects that are significantly superior to that of conventional iron oxide nanoparticles.[5a, 11] This enhancement is significant for clinical purposes as the nanoparticle probe dosage level can be progressively lowered when using probes that have improved contrast enhancement effects. In the first part of this study, we present a large-scale, simple, and reliable synthetic protocol to achieve Zn^{2+} doping controlled metal ferrite nanoparticles. A one-pot thermal decomposition method was used, which involved a metal chloride (MCl_2, $M = Zn^{2+}$, Mn^{2+}, and Fe^{2+}) and iron tris-2,4-pentadionate ($[Fe(acac)_3]$) in the presence of oleic acid, oleylamine, and octyl ether.[12] The Zn^{2+} doping level, a key parameter, was carefully controlled by varying the initial molar ratio of the metal chloride precursors. As shown in Figure 1a–c, a series of 15 nm sized Zn^{2+} doped nanoparticles of $(Zn_xMn_{1-x})Fe_2O_4$ and $(Zn_xFe_{1-x})Fe_2O_4$ ($x = 0$, 0.1, 0.2, 0.3, 0.4, and 0.8) with single crystallinity and size monodispersity ($\sigma < 5\%$) were

[*] J.-t. Jang, H. Nah, J.-H. Lee, S. H. Moon, Prof. J. Cheon
Department of Chemistry, Yonsei University
Seoul 120-749 (Korea)
Fax: (+82) 2-364-7050
E-mail: jcheon@yonsei.ac.kr
Dr. M. G. Kim
Pohang Accelerator Laboratory (PAL)
Pohang 790-784 (Korea)

Supporting information for this article is available on the WWW under http://dx.doi.org/10.1002/anie.200805149.
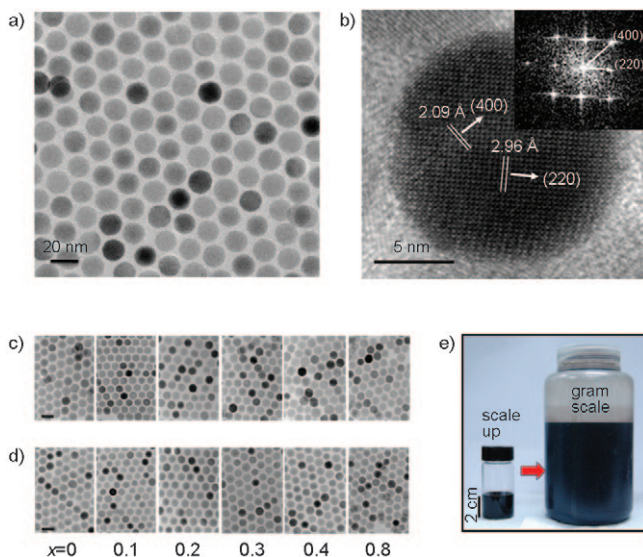
Figure 1. a) TEM image of 15 nm $(Zn_{0.4}Fe_{0.6})Fe_2O_4$ nanoparticles. b) High-resolution TEM image of 15 nm $(Zn_{0.4}Fe_{0.6})Fe_2O_4$ nanoparticles. The inset shows the FFT pattern. c,d) TEM images of 15 nm $(Zn_xMn_{1-x})Fe_2O_4$ (c) and $(Zn_xFe_{1-x})Fe_2O_4$ (d) nanoparticles (scale bar: 20 nm). e) Photograph showing that the synthesis of 15 nm $(Zn_{0.4}Fe_{0.6})Fe_2O_4$ nanoparticles can be scaled up to ca. 10 g.

successfully obtained. High-resolution transmission electron microscopy (TEM) analysis, its associated fast Fourier transformation (FFT) pattern (Figure 1 d), and X-ray diffraction (XRD; see Figure S1 in the Supporting Information) indicate that the nanoparticles have high-quality crystallinity. Although typical syntheses were carried out to produce tens of milligrams of nanoparticles, the reaction was easily scaled up to the gram scale (ca. 10 g) in a one-pot reaction without sacrificing the quality of the nanoparticles (Figure 1 e). The Zn^{2+} doping level was estimated by using energy dispersive X-ray spectroscopy (EDS) and inductively coupled plasma atomic emission spectroscopy (ICP-AES; see Figure S2 in the Supporting Information).

Additionally, it is important to confirm that the dopant Zn^{2+} ions mainly occupy T_d sites of the spinel matrix by using extended X-ray absorption fine structure (EXAFS) analysis to examine the Zn and Fe K-edges (Figure 2 a). Fourier-transformed (FT) Fe K-edge k^3-weighted EXAFS spectra of $(Zn_xFe_{1-x})Fe_2O_4$ nanoparticles exhibit the characteristic FT peak features of a spinel structure. For the partially substituted Zn^{2+} ions, the FT peak at 3.1 Å in the Zn K-edge EXAFS spectra originates from central Zn^{2+} ions in T_d holes. The FT peak intensity gradually increases as the Zn^{2+} doping level of $(Zn_xFe_{1-x})Fe_2O_4$ nanoparticles increases from $x = 0.1$ to 0.2, 0.3, and 0.4 (Figure 2 a, red solid line). In contrast, the peak at 2.6 Å, which is due to the Zn^{2+} ions in O_h sites, is almost negligible (Figure 2 a, black dotted line). Therefore, we conclude that the Zn^{2+} ions mainly reside in T_d sites rather than O_h sites.[13] Similarly, for $(Zn_xMn_{1-x})Fe_2O_4$ nanoparticles, the Zn^{2+} ion occupation in T_d sites is also confirmed by EXAFS analysis (see Figure S3 in the Supporting Information).

The magnetism of the Zn^{2+} doped metal ferrite nanoparticles was measured using a superconducting quantum interference device (SQUID) at 300 K (Figure 2 e). The M_s value gradually increases as the Zn^{2+} doping level of $(Zn_xMn_{1-x})Fe_2O_4$ nanoparticle increased from $x = 0$ to 0.1, 0.2, 0.3, and 0.4, with M_s values of 125, 140, 154, 166, and 175 emu g^{-1} (Zn + Mn + Fe), respectively. The M_s value reaches its maximum at $x = 0.4$ but diminishes to 137 emu g^{-1} at $x = 0.8$ (Figure 2 e, red line). In a similar fashion to $(Zn_xFe_{1-x})Fe_2O_4$ nanoparticles, the M_s value changes from 114 to 126, 140, 152, 161, and 115 emu g^{-1} (Zn + Fe) for $x = 0$ to 0.1, 0.2, 0.3, 0.4, and 0.8, respectively (Figure 2 e, black line). In both cases, the M_s value reaches its maximum of 175 emu g^{-1} (Zn + Mn + Fe) and 161 emu g^{-1} (Zn + Fe) at $x = 0.4$, which far exceeds the value of 127 emu g^{-1} (Fe) observed for undoped bulk iron oxide (Fe_3O_4), and are the highest values observed among the various metal ferrite nanoparticles reported to date.[14]

The magnetism tuning of nanoparticles is successful since the change of antiferromagnetic coupling interactions between T_d and O_h sites can be modulated by using Zn^{2+} dopants.[15] For instance, when Zn^{2+} ions are added to the unit cell of a spinel structure ($x < 0.4$), they occupy T_d sites (Figure 2 c). This phenomenon induces the partial removal of antiferromagnetic coupling interactions between Fe^{3+} ions in the T_d and O_h sites.[16] Incremental changes in the M_s value are therefore clearly observed (Figure 2 b–d). However, at very
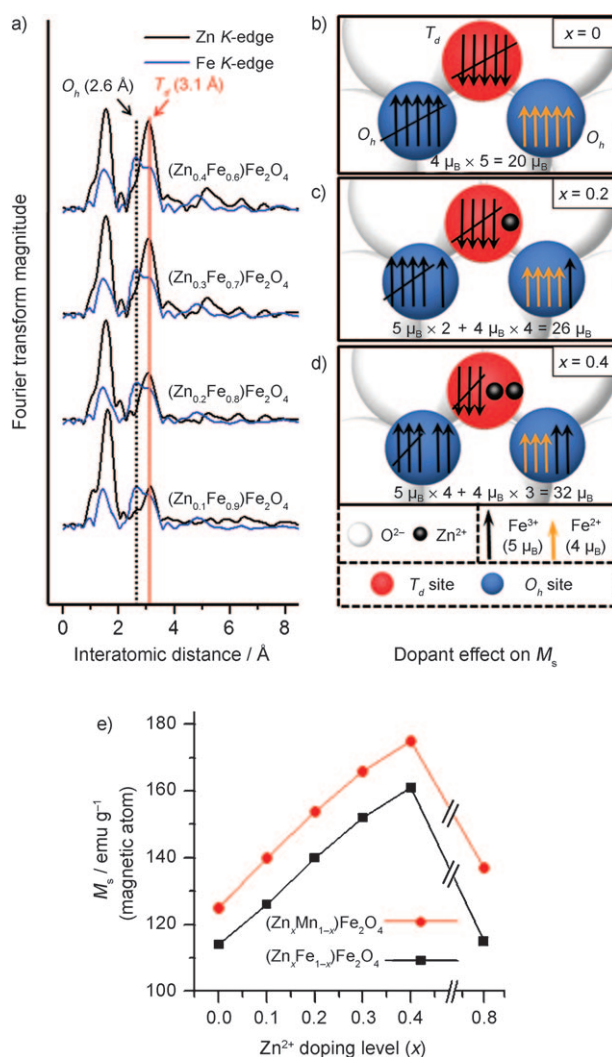
Figure 2. a) Zn K edge EXAFS spectra of $(Zn_xFe_{1-x})Fe_2O_4$ nanoparticles ($x = 0.1$, 0.2, 0.3, and 0.4). The intensity of the peak at 3.1 Å (red line) gradually becomes stronger as the Zn^{2+} doping level is increased, which indicates that the amounts of Zn^{2+} ions in T_d sites progressively increase. b) Undoped, c) Zn^{2+} doped ($x = 0.2$), and d) Zn^{2+} doped ($x = 0.4$) magnetic spin alignment diagrams in spinel-structured $(Zn_xFe_{1-x})Fe_2O_4$ nanoparticles under an applied magnetic field. e) Graphs of M_s versus Zn^{2+} doping level $(Zn_xM_{1-x})Fe_2O_4$ (M = Mn^{2+}, Fe^{2+}) nanoparticles (red line: $(Zn_xMn_{1-x})Fe_2O_4$, black line: $(Zn_xFe_{1-x})Fe_2O_4$).

high Zn^{2+} ion levels, antiferromagnetic coupling interactions between Fe^{3+} ions in each O_h site are dominant and the net magnetization moment decreases. In fact, the theoretical magnetization value of pure $ZnFe_2O_4$ ($x = 1$) is calculated to be zero.[17]

In MRI, the contrast enhancement effects are directly related to the M_s value of the nanoparticles. Specifically, spin–spin relaxivity ($R2 = 1/T2$) represents the degree of $T2$-weighted MRI contrast effect where the $R2$ value is roughly proportional to the square of the M_s value.[18] The Zn^{2+} dopant effects of metal ferrite nanoparticles on the MRI contrast enhancements were measured at 4.5 T and compared with the effects of conventional iron oxide nanoparticles (Feridex and cross-linked iron oxide (CLIO)) with the same

concentration and MRI sequence (Figure 3a–c). The relaxivity coefficient ($r2$), which is obtained as the gradient of the plot of $R2$ versus the molarity of magnetic atoms, increases as the Zn^{2+} doping level of $(Zn_xMn_{1-x})Fe_2O_4$ nanoparticles
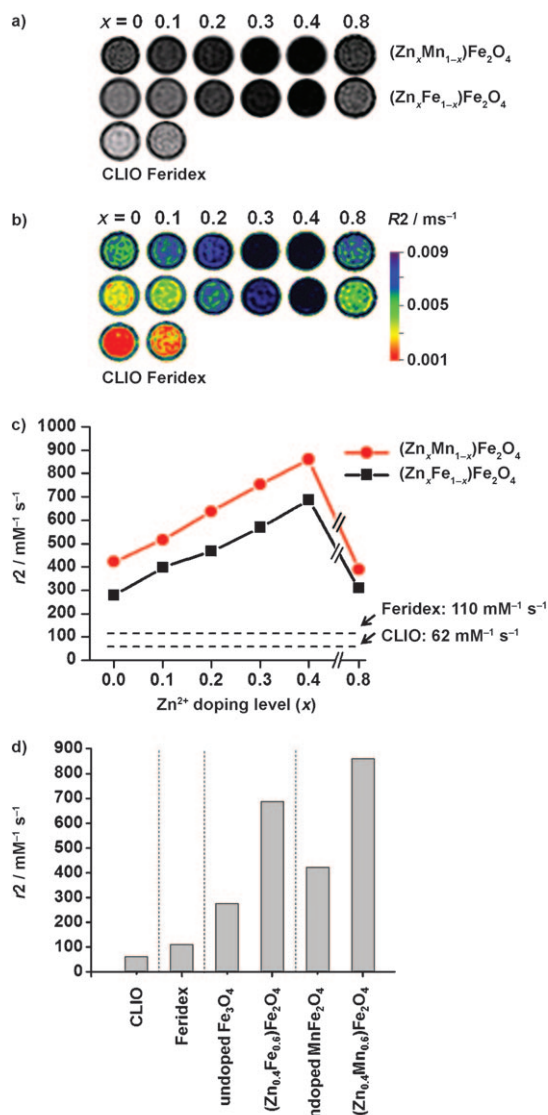
Figure 3. MR contrast effects of $(Zn_xM_{1-x})Fe_2O_4$ ($M = Mn^{2+}$, Fe^{2+}) nanoparticles upon changes in the Zn^{2+} doping level. a) $T2$-weighted MR images of $(Zn_xM_{1-x})Fe_2O_4$ ($M = Mn^{2+}$, Fe^{2+}) nanoparticles, Feridex, and CLIO and b) their color-coded images, where red indicates low $R2$ and violet indicates high $R2$ values. c) Graphs of $r2$ versus Zn^{2+} doped $(Zn_xM_{1-x})Fe_2O_4$ ($M = Mn^{2+}$, Fe^{2+}) nanoparticles at 4.5 T. d) Comparison of $r2$ values of nanoparticles, showing that Zn^{2+} doped nanoparticles have significantly enhanced MRI contrast effects compared to conventional iron oxide nanoparticles.

increases from $x = 0$ to 0.1, 0.2, 0.3, and 0.4 with values of 422, 516, 637, 754, and 860 $mM^{-1}s^{-1}$, respectively. The $r2$ value reaches its maximum at $x = 0.4$ but decreases to 388 $mM^{-1}s^{-1}$ at $x = 0.8$ (Figure 3c, red line). Similarly, for $(Zn_xFe_{1-x})Fe_2O_4$ nanoparticles, the $r2$ value changes from 276 to 397, 466, 568, 687, and 307 $mM^{-1}s^{-1}$ for $x = 0$ to 0.1, 0.2, 0.3, 0.4, and 0.8, respectively (Figure 3c, black line). The $r2$ value of CLIO is

62 $mM^{-1}s^{-1}$ and Feridex is 110 $mM^{-1}s^{-1}$ (Figure 3c, dashed lines). Based on the $r2$ values, the 15 nm sized $(Zn_{0.4}Mn_{0.6})Fe_2O_4$ nanoparticles have MRI contrast effects of 860 $mM^{-1}s^{-1}$ that are 13.8 and 7.8 times larger than those of CLIO and Feridex, respectively. Also, these $(Zn_{0.4}Fe_{0.6})Fe_2O_4$ and $(Zn_{0.4}Mn_{0.6})Fe_2O_4$ nanoparticles have superior MRI contrast effects that are 2.5 and 2 times larger than those of undoped Fe_3O_4 (276 $mM^{-1}s^{-1}$) and $MnFe_2O_4$ (422 $mM^{-1}s^{-1}$) nanoparticles, respectively (Figure 3d).

The high M_s value of the nanoparticles can also be used to achieve magnetically induced heat generation for the thermal treatment of cancer and other diseases.[19] Enhancement of SLP (specific loss power), the standard criterion for hyperthermia effects (defined as the thermal power dissipation divided by the mass of the magnetic material and the heat capacity of solution), is important in order to obtain high efficacy with smaller dose levels in biomedical applications.[20] The SLP values are highly dependent on magnetic relaxation processes and are roughly proportional to the M_s value and the magnetocrystalline anisotropy constant (K), and are inversely proportional to the size distribution of the nanoparticles (σ).[21] Our 15 nm sized $(Zn_{0.4}Mn_{0.6})Fe_2O_4$ nanoparticles with a high M_s value of 175 emu g^{-1} ($Zn + Mn + Fe$), monodispersity ($\sigma < 5\%$), and increased anisotropy are therefore ideal candidates for hyperthermic studies. The SLP value of $(Zn_{0.4}Mn_{0.6})Fe_2O_4$ nanoparticles is 432 $W g^{-1}$, which is four times larger than that of Feridex (115 $W g^{-1}$) when measured under identical conditions (Figure 4a). Further in vitro hyperthermic cancer cell treatment tests were performed. As shown in Figure 4b, most (84.4%) HeLa cells treated with $(Zn_{0.4}Mn_{0.6})Fe_2O_4$ nanoparticles died after 10 minutes of alternating current (AC) magnetic field appli-
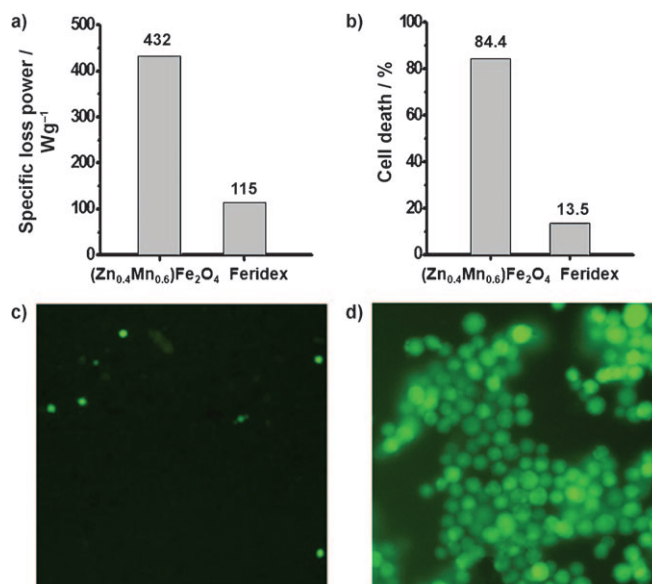
Figure 4. a) SLP values for $(Zn_{0.4}Mn_{0.6})Fe_2O_4$ and Feridex in a 500 kHz AC magnetic field with an amplitude of 3.7 kA m^{-1}. b) Percentage of HeLa cells killed after treatment with $(Zn_{0.4}Mn_{0.6})Fe_2O_4$ nanoparticles or Feridex and the subsequent application of an AC magnetic field for 10 min. Fluorescence microscopy images of AC magnetic field applied HeLa cells treated with c) $(Zn_{0.4}Mn_{0.6})Fe_2O_4$ nanoparticles and d) Feridex, stained with calcein indicating live cells as green fluorescence.

cation, whereas only 13.5% of cells died when treated with Feridex. After AC magnetic field application, fluorescence microscope images in which live cells were stained with calcein, which emits green fluorescence, show very weak fluorescence for the cells treated with $(Zn_{0.4}Mn_{0.6})Fe_2O_4$ nanoparticles, whereas intense green fluorescence is observed for those treated with Feridex (Figure 4 c,d). Additionally, our preliminary in vitro study indicates that these Zn^{2+} doped nanoparticles are nontoxic to healthy cells (see Figure S7 in the Supporting Information).

We have successfully demonstrated that the high magnetism of metal ferrite nanoparticles can be very effectively modulated and achieved by Zn^{2+} dopant control. The nanoparticles act as MR contrast and hyperthermia agents, which have *r*2 values that are eight to fourteen times greater for MRI and SLP values that are four times greater for hyperthermia cancer cell treatments than conventional nanoparticle agents. In addition, these nanoparticles are nontoxic. Such high-performance magnetic nanoparticles fabricated by using this magnetism engineering concept could play a significant role in the improvement of current diagnostics, therapeutics, and other biomedical studies such as cell actuation.

Experimental Section

Materials and instruments: All chemicals were purchased from Aldrich. Zinc(II) chloride, manganese(II) chloride, iron(II) chloride, and iron(III) tri-2,4-pentadionate were used as received. Oleic acid and oleylamine were purified by distillation under an argon atmosphere. Feridex was obtained from TAEJOON Pharmaceutical Co. Transmission electron microscopy (TEM) and high-resolution TEM analyses were performed on JEOL-2100 and JEM-ARM 1300S instruments. Elemental analysis was carried out by using inductively coupled plasma atomic emission spectroscopy (OPTIMA 4300DV, PerkinElmer, USA) and energy dispersive X-ray spectroscopy (EDS; INCA, Oxford Instruments). X-ray powder diffraction studies were conducted using a Rigaku D/MAX-RB diffractometer equipped with a graphite-monochromated $Cu_{K\alpha}$ radiation source (40 kV, 120 mA). Magnetic properties were measured with a superconducting quantum interference device (SQUID) magnetometer (Quantum Design MPMS-7).

15 nm $(Zn_xMn_{1-x})Fe_2O_4$ and $(Zn_xFe_{1-x})Fe_2O_4$ ($x = 0$, 0.1, 0.2, 0.3, 0.4, and 0.8) nanoparticles were prepared following a slightly modified procedure.[5a,11] A typical small-scale synthesis to produce $(Zn_{0.4}Mn_{0.6})Fe_2O_4$ nanoparticles is as follows: $ZnCl_2$ (0.03 g), $MnCl_2$ (0.04 g), and $[Fe(acac)_3]$ (0.353 g) were placed in a 50 mL three-neck round-bottom flask in the presence of surfactants (oleic acid and oleylamine) in octyl ether. The reaction mixture was heated at 300°C for 1 h and, after removing the heating source, the reaction products were cooled to room temperature. Upon addition of ethanol, a black powder precipitated and was isolated by centrifugation. The isolated nanoparticles were dispersed in a solvent such as toluene. The typical yield of nanoparticles was 40 mg. For large-scale synthesis, the same procedures were utilized in which the amounts of reagents used were $ZnCl_2$ (3.6 g), $MnCl_2$ (4.8 g), and $[Fe(acac)_3]$ (42.4 g) and the yield of obtained nanoparticles was 9.8 g. $(Zn_{0.4}Fe_{0.6})Fe_2O_4$ nanoparticles were obtained by using $FeCl_2$ instead of $MnCl_2$ under identical conditions. In order to control the Zn^{2+} doping level, different amounts of Zn^{2+}/Mn^{2+} or Zn^{2+}/Fe^{2+} metal chloride precursors were used under identical conditions. $(Zn_{0.1}Mn_{0.9})Fe_2O_4$: $ZnCl_2$ (0.01 g) and $MnCl_2$ (0.06 g); $(Zn_{0.2}Mn_{0.8})Fe_2O_4$: $ZnCl_2$ (0.015 g) and $MnCl_2$ (0.05 g); $(Zn_{0.3}Mn_{0.7})Fe_2O_4$: $ZnCl_2$ (0.02 g) and $MnCl_2$ (0.045 g); $(Zn_{0.8}Mn_{0.2})Fe_2O_4$: $ZnCl_2$ (0.06 g) and $MnCl_2$(0.015 g). In the case of $(Zn_xFe_{1-x})Fe_2O_4$ nanoparticles, an equivalent amount of $FeCl_2$ was

used instead of $MnCl_2$. The organic surfactants on the nanoparticle surface were removed and exchanged with 2,3-dimercaptosuccinic acid (DMSA) to make the nanoparticles completely dispersed in the aqueous medium.[22] Then these water-soluble nanoparticles were used for MR measurements and hyperthermic experiments.

SLP measurements and in vitro hyperthermia experimental methods: The sample of nanoparticles (($Zn_{0.4}Mn_{0.6})Fe_2O_4$ or Feridex, 5 mgmL^{-1}) was placed inside a water-cooled copper coil which produced an alternating magnetic field in the frequency range of 500 kHz with an amplitude of up to 3.7 kAm^{-1}. The temperature was measured with a thermometer (TES-1307) placed in the center of the sample. In order to compare cell extinction effects, HeLa cells (1 × 106 cells), which were treated with $(Zn_{0.4}Mn_{0.6})Fe_2O_4$ nanoparticles and Feridex (0.5 mgmL^{-1}), respectively, were heated for 10 min.

MRI contrast effect measurement of Zn^{2+} doped metal ferrite nanoparticles: All MRI experiments were performed with a 4.7 T animal MRI instrument (Bruker, Germany) with a 72 mm volume coil at the Korea Basic Science Institute in Ochang. We measured the relaxivity coefficients (*r*2, mM^{-1}s^{-1}) of various $(Zn_xM_{1-x})Fe_2O_4$ nanoparticles ($x = 0$, 0.1, 0.2, 0.3, 0.4, and 0.8, M = Mn^{2+}, Fe^{2+}) by using the Carr–Purcell–Meiboom–Gill (CPMG) sequence at room temperature: TR(repetition time) = 5 s, 128 echoes with 7 ms even echo space, 2 acquisitions, in-plane pixel size = 547 μm × 547 μm, section thickness = 2 mm.

XAS measurements: Zn, Fe, and Mn *K*-edge X-ray absorption spectra were recorded on the BL7C1 beam line of the Pohang light source with a ring current of 130–190 mA at 2.5 GeV. A Si(111) double-crystal monochromator was employed to monochromatize the X-ray photon energy. The incident X-ray photon flux was monitored by N_2 gas-filled ionization. The EXAFS data from samples were collected in fluorescence mode. Higher-order harmonic contaminations were eliminated by detuning to reduce the incident X-ray intensity by approximately 30%. Energy calibration was simultaneously carried out for each measurement with Zn, Fe, and Mn metallic films placed in front of the third ion chamber.

[1] a) E. Roduner, *Nanoscopic Materials: Size-Dependent Phenomena*, RSC, London, **2006**; b) S. Sun, *Adv. Mater.* **2006**, *18*, 393–403; c) Y.-w. Jun, J.-w. Seo, J. Cheon, *Acc. Chem. Res.* **2008**, *41*, 179–189; d) A.-H. Lu, E. L. Salabas, F. Schüth, *Angew. Chem.* **2007**, *119*, 1242–1266; *Angew. Chem. Int. Ed.* **2007**, *46*, 1222–1240; e) U. Jeong, X. Teng, Y. Wang, H. Yang, Y. Xia, *Adv. Mater.* **2007**, *19*, 33–60.

[2] a) J. W. M. Bulte, D. L. Kraitchman, *NMR Biomed.* **2004**, *17*, 484–499; b) D. L. J. Thorek, A. K. Chen, J. Czupryna, A. Tsourkas, *Ann. Biomed. Eng.* **2006**, *34*, 23–38; c) Y.-w. Jun, J.-H. Lee, J. Cheon, *Angew. Chem.* **2008**, *120*, 5200–5213; *Angew. Chem. Int. Ed.* **2008**, *47*, 5122–5135.

[3] a) J. Gao, L. Li, P.-L. Ho, G. C. Mak, H. Gu, B. Xu, *Adv. Mater.* **2006**, *18*, 3145–3148; b) T. Leakakos, C. Ji, G. Lawson, C. Peterson, S. Goodwin, *Cancer Chemother. Pharmacol.* **2003**, *51*, 445–450; c) P. Moroz, S. K. Jones, B. N. Gray, *Int. J. Hyperthermia* **2002**, *18*, 267–284.

[4] a) R. J. Mannix, S. Kumar, F. Cassiola, M. Montoya-Zavala, E. Feinstein, M. Prentiss, D. E. Ingber, *Nat. Nanotechnol.* **2008**, *3*, 36–40; b) J. Dobson, *Nat. Nanotechnol.* **2008**, *3*, 139–143.

[5] a) J.-H. Lee, Y.-M. Huh, Y.-w. Jun, J.-w. Seo, J.-t. Jang, H.-T. Song, S.-j. Kim, E.-J. Cho, H.-G. Yoon, J.-S. Suh, J. Cheon, *Nat. Med.* **2007**, *13*, 95–99; b) C. Liu, B. Zou, A. J. Rondinone, Z. J. Zhang, *J. Am. Chem. Soc.* **2000**, *122*, 6263–6267; c) R. A.

McCurrie, *Ferromagnetic Materials: Structure and Properties*, Academic Press, New York, **1994**; d) J. E. Thompson, *The Magnetic Properties of Materials*, Stonebridge Press, Bristol, **1968**.

[6] a) J. F. Hochepied, P. Bonville, M. P. Pileni, *J. Phys. Chem. B* **2000**, *104*, 905–912; b) J. F. Hochepied, M. P. Pileni, *J. Appl. Phys.* **2000**, *87*, 2472–2478; c) R. Arulmurugan, B. Jeyadevan, G. Vaidyanathan, S. Sendhilnathan, *J. Magn. Magn. Mater.* **2005**, *288*, 470–477.

[7] a) G. F. Goya, H. R. Rechenberg, M. Chen, W. B. Yelon, *J. Appl. Phys.* **2000**, *87*, 8005–8007; b) C. Rath, N. C. Mishra, S. Anand, R. P. Das, K. K. Sahu, C. Upadhyay, H. C. Verma, *Appl. Phys. Lett.* **2000**, *76*, 475–477; c) S. A. Oliver, V. G. Harris, H. H. Hamdeh, J. C. Ho, *Appl. Phys. Lett.* **2000**, *76*, 2761–2763.

[8] a) S. Nakashima, K. Fujita, K. Tanaka, K. Hirao, *J. Phys. Condens. Matter* **2005**, *17*, 137–149; b) K. Tanaka, S. Nakashima, K. Fujita, K. Hirao, *J. Appl. Phys.* **2006**, *99*, 106103.

[9] C. Bárcena, A. K. Sra, G. S. Chaubey, C. Khemtong, J. P. Liu, J. Gao, *Chem. Commun.* **2008**, 2224–2226.

[10] a) M. Kettering, J. Winter, M. Zeisberger, S. B. Streck, H. Oehring, C. Bergemann, C. Alexxiou, R. Hergt, K. J. Halbhuber, W. A. Kaiser, I. Hilger, *Nanotechnology* **2007**, *18*, 175101; b) R. Hergt, R. Hiergeist, M. Zeisberger, G. Glockl, W. Weitschies, L. P. Ramirez, I. Hilger, W. A. Kaiser, *J. Magn. Magn. Mater.* **2004**, *280*, 358–368; c) R. Weissleder, A. Moore, U. Mahmood. E. Bhorade, H. Benveniste, E. A. Chiocca, J. P. Basilion, *Nat. Med.* **2000**, *6*, 351–354.

[11] a) W. S. Seo, J. H. Lee, X. Sun, Y. Suzuki, D. Mann, Z. Liu, M. Terashima, P. C. Yang, M. V. Mcconnell, D. G. Nishimura, H. Dai, *Nat. Mater.* **2006**, *5*, 971–976; b) G. S. Chaubey, C. Barcena, N. Poudyal, C. Rong, J. Gao, S. Sun, J. P. Liu, *J. Am. Chem. Soc.* **2007**, *129*, 7214–7215.

[12] a) S. Sun, C. B. Murray, D. Weller, L. Folks, A. Moser, *Science* **2000**, *287*, 1989–1992; b) S. Sun, H. Zeng, D. B. Robinson, S. Raoux, P. M. Rice, S. X. Wang, G. Li, *J. Am. Chem. Soc.* **2004**, *126*, 273–279; c) J. Park, K. An, Y. Hwang, J.-G. Park, H.-J. Noh, J.-Y. Kim, J.-H. Park, N.-H. Hwang, T. Hyeon, *Nat. Mater.* **2004**, *3*, 891–895; d) N. R. Jana, Y. Chen, X. Peng, *Chem. Mater.* **2004**, *16*, 3931–3935.

[13] a) S. Nakashima, K. Fujita, K. Tanaka, K. Hirao, T. Yamamoto, I. Tanaka, *Phys. Rev. B* **2007**, *75*, 174443; b) S. J. Stewart, S. J. Figueroa, J. M. R. Lopez, S. G. Marchetti, J. F. Bengoa, R. J. Prado, F. G. Requejo, *Phys. Rev. B* **2007**, *75*, 073408.

[14] R. M. Cornel, U. Schwertmann, *The Iron Oxides*, Wiley-VCH, Weinheim, **2000**.

[15] B. D. Cullity, *Introduction to Magnetic Materials*, Addison-Wesley, London, **1972**.

[16] P. G. Bercoff, H. R. Bertorello, *J. Magn. Magn. Mater.* **1997**, *169*, 314–322.

[17] A. Martin, M. K. Krause, I. Halevy, J. Gal, W. Schafer, G. Will, M. Hillberg, R. Wappling, *Phys. Rev. B* **1996**, *53*, 9143–9152.

[18] S. H. Koenig, K. E. Keller, *Magn. Reson. Med.* **1995**, *34*, 227–233.

[19] S. Mornet, S. Vesseur, F. Grasset, E. Duguet, *J. Mater. Chem.* **2004**, *14*, 2161–2175.

[20] J.-P. Fortin, C. Wilhelm, J. Servais, C. Menager, J.-C. Bacri, F. Gazeau, *J. Am. Chem. Soc.* **2007**, *129*, 2628–2635.

[21] R. E. Rosensweig, *J. Magn. Magn. Mater.* **2002**, *252*, 370–374.

[22] Y.-w. Jun, Y.-M. Huh, J.-s. Choi, J.-H. Lee, H.-T. Song, S. Kim, S. Kim, S. Yoon, K.-S. Kim, J.-S. Shin, J.-S. Suh, J. Cheon, *J. Am. Chem. Soc.* **2005**, *127*, 5732–5733.

4. Sequential assembly of multiple nanoparticle components to silica matrix efficiently forms dual-functional Mag-SPR probes: In order to synthesize Mag-SPR probes, we adopted sequential assembly strategy of component nanocrystals to a host silica particle (Figure 1). First, we assembled single or multiple Zn-doped manganese ferrite nanoparticles into a silica nanoparticle through the inverse micelle strategy in which silica nanoparticles grow inside a pre-formed inverse amphiphilic polymer (Igepal-580, Sigma) micelle containing magnetic nanoparticles. Obtained $Zn_{0.4}Mn_{0.6}Fe_3O_4@SiO_2$ nanoparticles are over-coated by a gold nanoshell through a slight modification of known method. By adjusting experimental parameters such as magnetic nanoparticle concentration and gold precursor concentration, the number of particles inside a silica particle and the gold shell thickness were controlled (Fig. 1c,d). We chose a multi-cored (3-4 magnetic nanoparticles) nanoshell having surface plasmon maximum at 600 nm as a Mag-SPR probe, in order to maximize magnetic properties while minimizing the optical perturbation by biological autofluorescence.
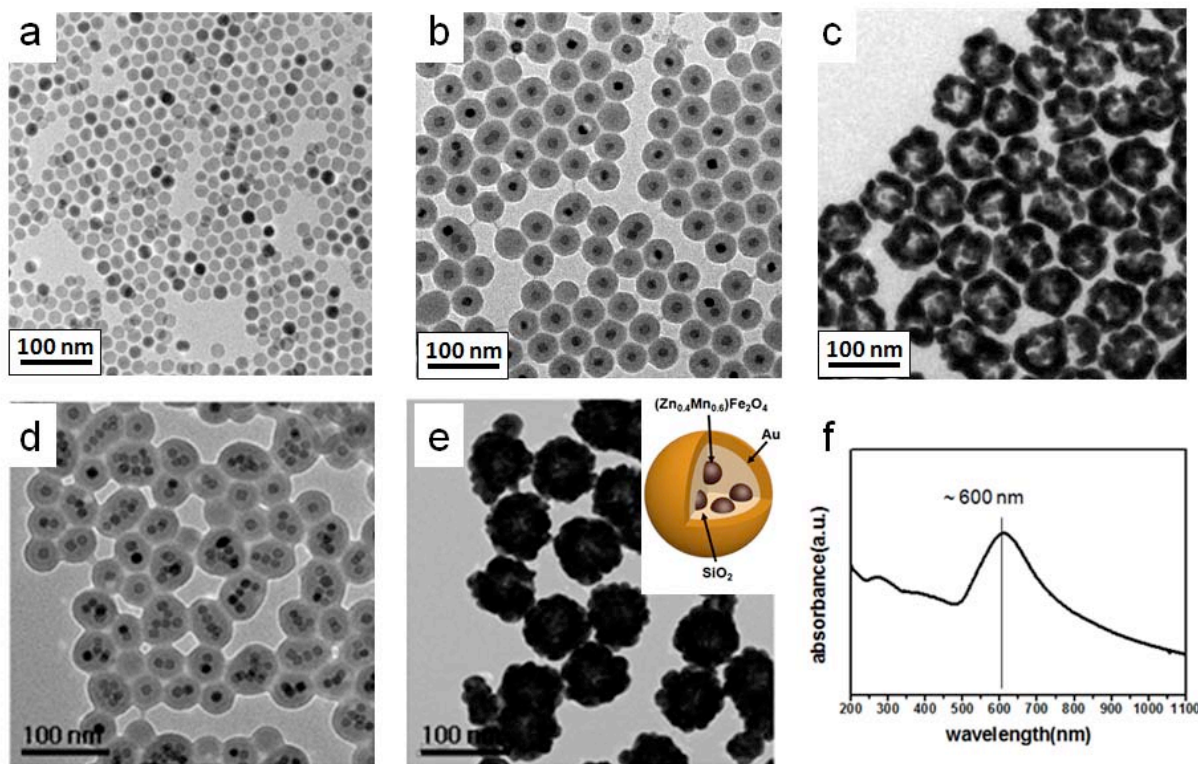
<Figure 1> (a-c) Single magnetic-cored Mag-SPR probe. TEM images of (a) as-synthesized 15 nm sized $MnFe_2O_4$ nanoparticle used as magnetic core, (b) silica coated particle, and (c) gold coated particle upon the silica layer. (d-e) Multi magnetic-cored Mag-SPR probe. (d) TEM image of multi-cored particle where the silica is coated over the $Zn_{0.4}Mn_{0.6}Fe_2O_4$ nanoparticles and (e) the subsequent gold coated Mag-SPR probe. (f) Schematic drawing of multi-core Mag-SPR probe. ~8 magnetic nanoparticles are encapsulated by the silica layer which is coated by the gold shell. (d) UV-Vis absorption spectrum of the synthesized Mag-SPR probe which shows strong absorption peak at 600 nm.

5. Magnetic tweezer can generate a focused magnetic field that exerts about pN forces to a single Mag-SPR probe:

In order to manipulate the developed Mag-SPR prove on the cell surface, the development of manipulator which exerts magnetic forces enough to control the movement of particle is essential. For this purpose, we set up a magnetic tweezer system that is mounted to a dark field microscope. Figure 2 shows the image of a tapered magnetic tweezer having a tip size of 3 μm. When considering the average size of cells is ~20 μm, this magnetic tip is small enough to generate a focused magnetic field to induce Mag-SPR probe clustering in a single cell.
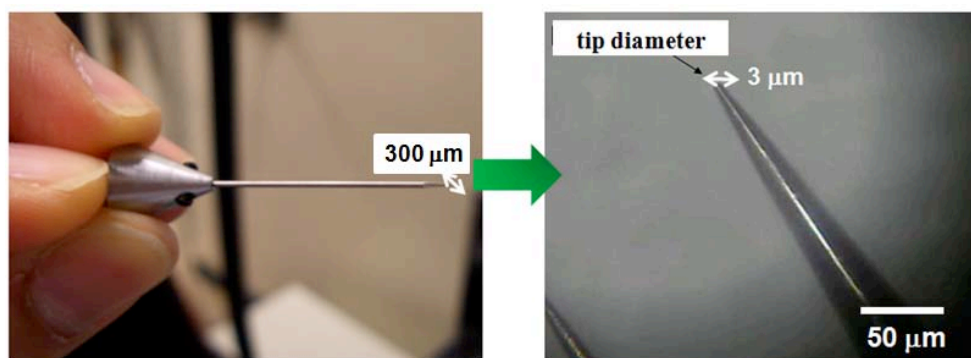
<Figure 2> Magnetic steep tip for the micro-manipulation of the Mag-SPR probe. The end of the tip diameter is 3 μm.

In order to determine distance-dependent magnetic forces exerted from the tweezer to the Mag-SPR probe, we generated a force calibration curve by using the Stokes' law (Figure 3). Per our observation, a Mag-SPR particle about 5 um apart from the tweezer experiences about 0.6 pN that significantly exceeds the activation barrier for the free protein movement (~100 fN, Marago *et al. NanoScience and Technology* **2010**, *Part 1*, 23).
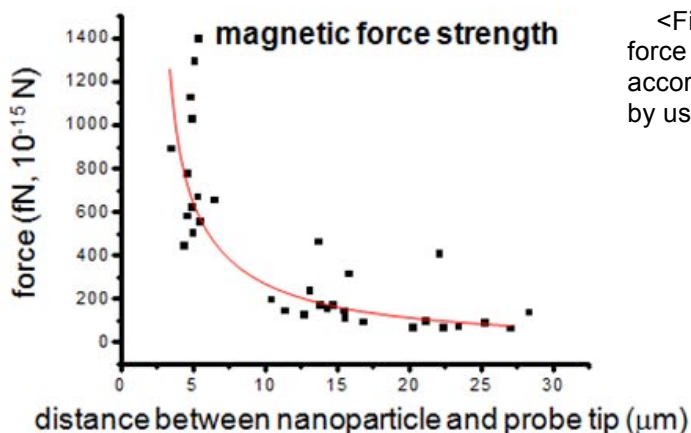
<Figure 13> The strength of magnetic force exerted on the end of the probe tip according to the distance, which is measured by using Stokes's law.

6. Mag-SPR probes enabled magnetically actuated biomolecular clustering and its simultaneous visualization at the single molecule level.

As a case study to demonstrate the Mag-SPR technique for biomolecular clustering in live cells, we chose ErbB-2 membrane receptor clustering in live cells. We conjugated Mag-SPR probes with a Herceptin, a well-known antibody to ErbB-2 receptors and treated them with cancer cells (SK-BR-3) overexpressing ErbB-2 receptors. Red dots corresponding to the individual Mag-SPR probe scattering were clearly observed, which indicate successful single molecule detection of ErbB-2 receptors. Additionally, since the Mag-SPR probe do not photobleach or blink, we could continuously monitor progressive binding of MagSPR-Herceptin conjugates onto ErbB-2 receptors (Fig. 5).
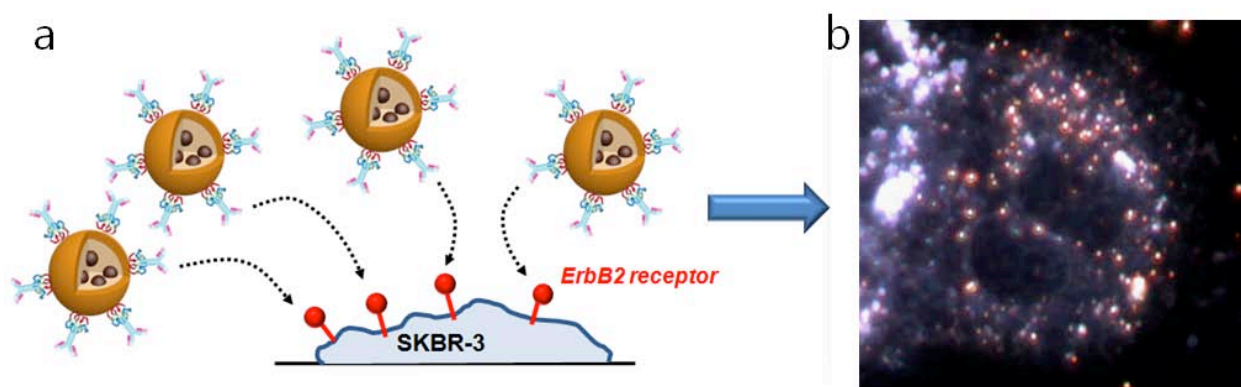
<Figure 4> (a) Schematic drawing of Mag-SPR probe binding on the breast cancer cell (SK-BR-3) and (b) the actual dark field image of nanoprobe binding on the cell surface.
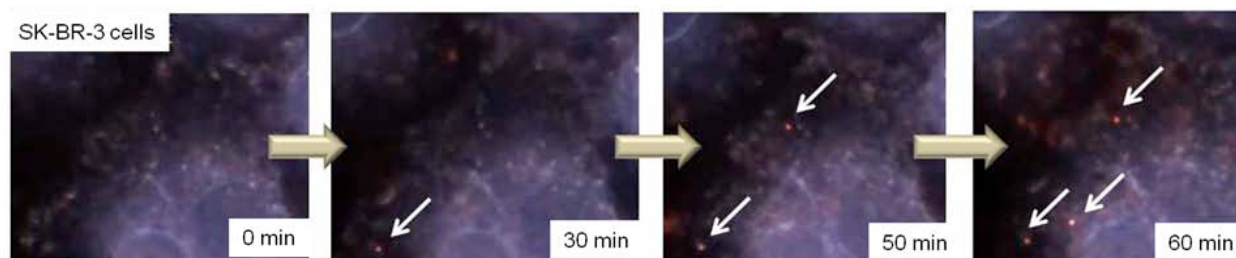
<Figure 5> Dark field image of in situ binding of Mag-SPR probe on the cancer cell surface. White arrows indicate the Mag-SPR probes bound on the cell surface. 1 pico mole of nanoprobes is treated to the cell and three of nanoprobes are bound in one cell in one hour.

13
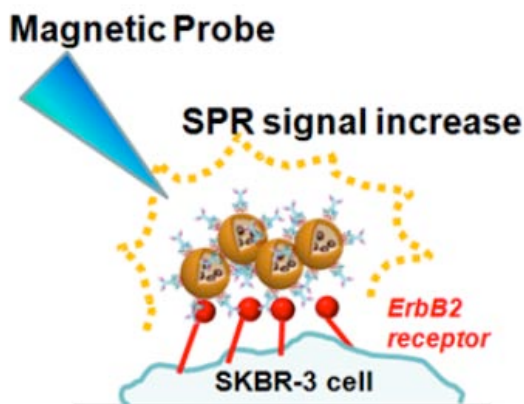
We applied a focused magnetic field with a magnetic tweezer to a single cell to induce ErbB-2 clustering through magnetic dipole-dipole interaction (Figure 6). Figure 7 shows the progressive clustering of Mag-SPR probes at different temporal points of 0 min, to 10, 20, 30, 40, 50, and 120 min (see the white arrows in Figure 7). This result implies that the magnetically-actuated clustering of biomolecules was possible through our Mag-SPR technique with high spatial resolution.
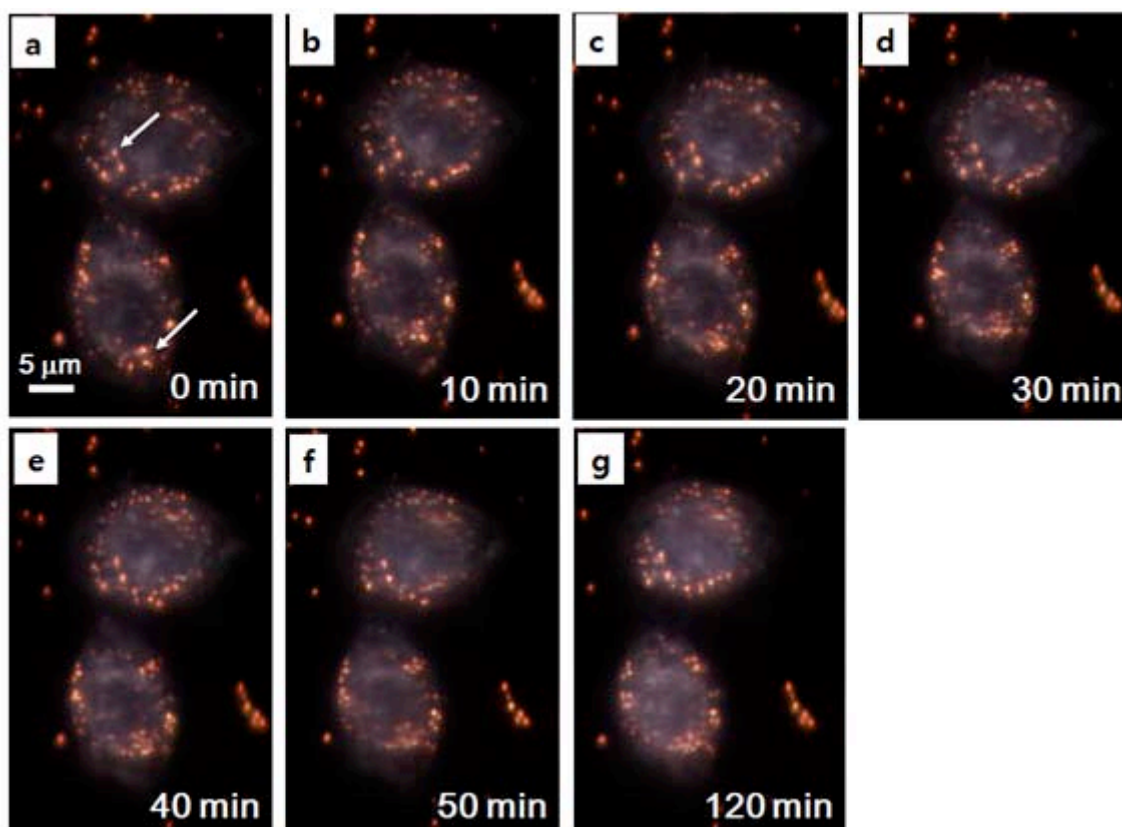
<Figure 7> (a-g) Dark field image of cancer cell treated with Mag-SPR probe which is magnetically manipulated for ~ 2 hours. White arrow indicates the representative nanoprobe at initial stage. This location of this nanoprobe gradually changes after two hour application of magnetic field.

X. SOFTWARE AND/OR HARWARE

None

Final Report

Processing and Characterization of Hierarchical Carbon Fiber Composites

USPI : H. Thomas Hahn, Ph.D. (UCLA)
KPI : Kun-Hong Lee, Ph.D. (POSTECH)
Co-KPI : Sang-gi Lee, Ph.D. (Ehwa Women's University)

Final Report

Research Title: Processing and Characterization of Hierarchical Carbon Fiber Composites

Research Institute: Mechanical and Aerospace Engineering Department, University of California, Los Angeles, USA

Principal Investigator: Professor H. Thomas Hahn

Co-Investigator: Hansang Kim, Eliah Novin

1.1. Objective

The aim of Task III is to develop processing methods for hierarchical carbon fiber composites and investigate their mechanical and electrical properties to ascertain the benefits of the hierarchical reinforcement concept. The results are fed back to the Korean co-investigators to refine the entire development process.

1.2. Status of Effort

A variety of hierarchical carbon fiber composites were prepared by two different processes: vacuum assisted resin transfer molding (VARTM) and wet lay-up. Both of them were followed by autoclave cure. As expected, carbon nanotubes grown on carbon fibers were found to increase the out-of plane electrical conductivity of the composite substantially but not the in-plane conductivity. Fracture toughness results and the associated fractographic examinations indicate that the adhesion between carbon nanotubes (CNTs) and carbon fibers is critical to improving the fracture toughness of the composite.

1.3 Research accomplishments

1.3.1. Processing hierarchical carbon fiber composites

Hierarchical carbon fiber composites were fabricated by using vacuum assisted resin transfer

molding (VARTM) and wet lay-up, followed by autoclave cure. In both cases, Epon 862 epoxy resin with Epikure W curing agent (100:26.5 mix ratio by weight) were used as the matrix system. Carbon nanotubes (CNTs) were perpendicularly grown on AS4 (Hexcel Co.) plain weave fabric (12 cm x 2 cm) at Postech. Figure 1 shows a schematic of different types of composites prepared for various tests. For fracture toughness (mode 1) tests, a piece of Teflon film was inserted in the middle during lay-up to make a pre-crack.
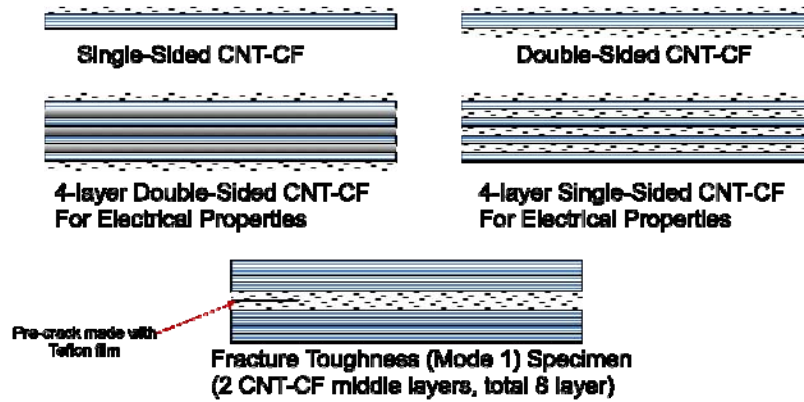
Figure 1. Schematic of hierarchical composites for various tests

For wet lay-up, strips of AS4 fabric with CNTs were immersed in epoxy for 4 hours in a vacuum oven at 60 $^{\circ}$C to promote good wetting of CNT forest with epoxy. Figure 2 shows a schematic of VARTM process used in this study. The outer vacuum bag was used to give better compaction during cure. Even for the wet lay-up process, vacuum and pressure were applied the same way as in the VARTM process.

For both types of processes, curing was done in an autoclave at temperature ? and pressure ? for how many hours ?.
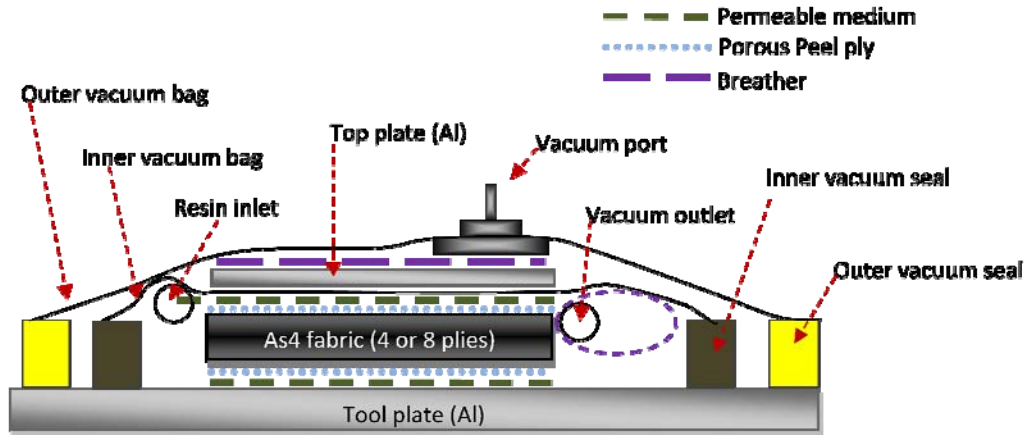
Figure 2. Vacuum assisted resin transfer molding (VARTM) set-up.

1.3.2. Fracture toughness test

The mode-I fracture toughness tests were conducted in accordance with ASTM D5528, Figure 3. Unless the CNT-CF adhesion was good, the composites with CNTs did not show any improvement in fracture toughness even though the CNTs were perpendicularly grown on the carbon fibers, which had been expected to blunt the crack propagation, Figure 4 and Table 1.

Table 1 shows the effect of composite preparation on fracture toughness.   The VARTM process was not so good as the wet lay-up process because there was not enough time for the resin to penetrate into the CNT forests.   When the wetting is good as in the wet-lay-up process, the fracture toughness is sensitive mainly to the adhesion between CNTs and CFs. If the CNT-CF adhesion is not strong, CNTs can be easily detached from the CF surfaces without improving the fracture toughness.   During the growth of CNTs, attempts were made to enhance the bonding between the CNTs and CFs.   The composite with improved CNT-CF adhesion indeed shows a

larger toughness than those without the adhesion enhancement.
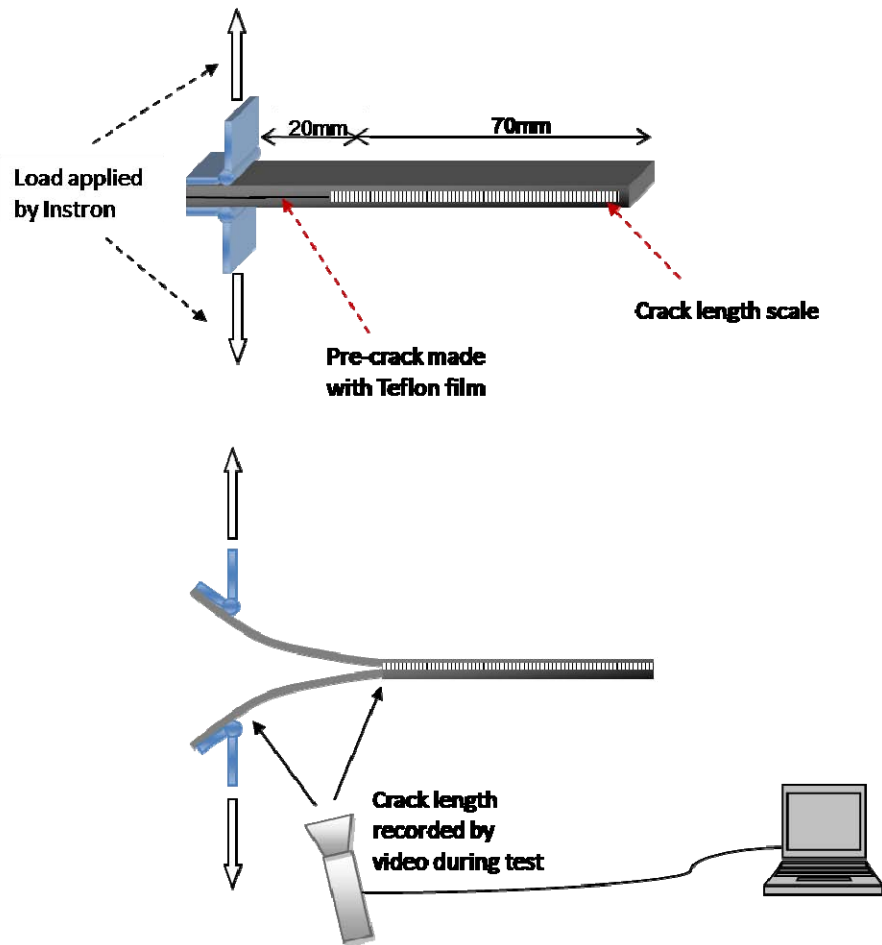
Figure 3. Fracture toughness (mode I) test set-up
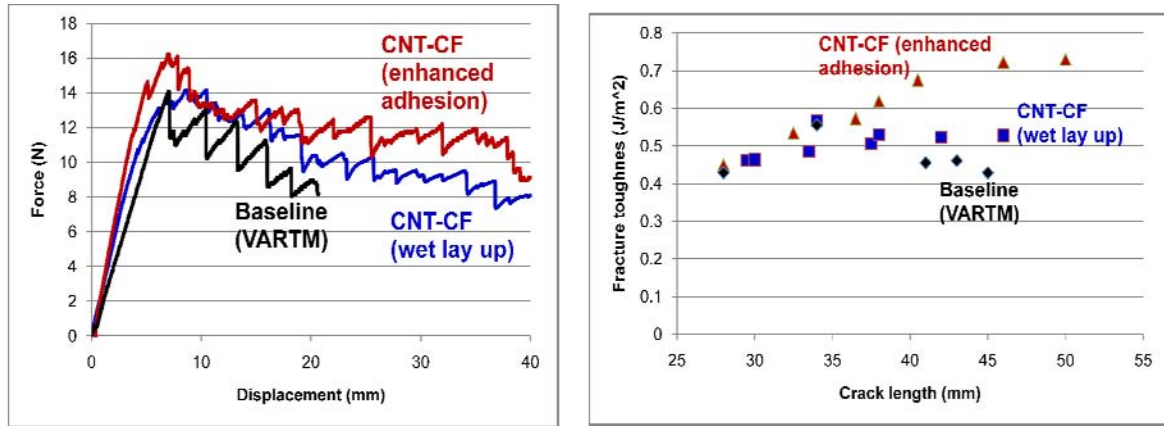
Figure 4. (a) Typical force-displacement curves; (b) fracture toughness vs. crack length.

Table 1. Fracture toughness results

Material	Processing	Mode I Fracture toughness (J/m^2), Average (STDEV)
Carbon fiber (AS4)	VARTM	430 (57.5)
Short (<10 micron) MWNT-CF		363 (14.8)
Long (>14 micron) MWNT-CF		381 (14.2)
Long MWNT-CF	Wet lay-up (no vacuum treatment)	432 (4.9)
Carbon fiber (AS4)	Wet lay-up	469 (9.2)
Long MWNT-CF	Wet lay-up	509 (72.1)
Very Long (~300 μm) MWNT-CF (adhesion enhanced)	Wet lay-up	690 (92.7)

Figure 5 shows the fracture surfaces of composites with CF-matrix interface failure. The

smooth fracture surface implies not much resistance to the crack propagation and the bare fiber

surfaces are seen on both the baseline composite without CNTs and the one with CNTs. However, the fracture surface of the adhesion-enhanced composite is quite different: most CNTs appear to emanate from the carbon fiber surfaces, Figure 6.
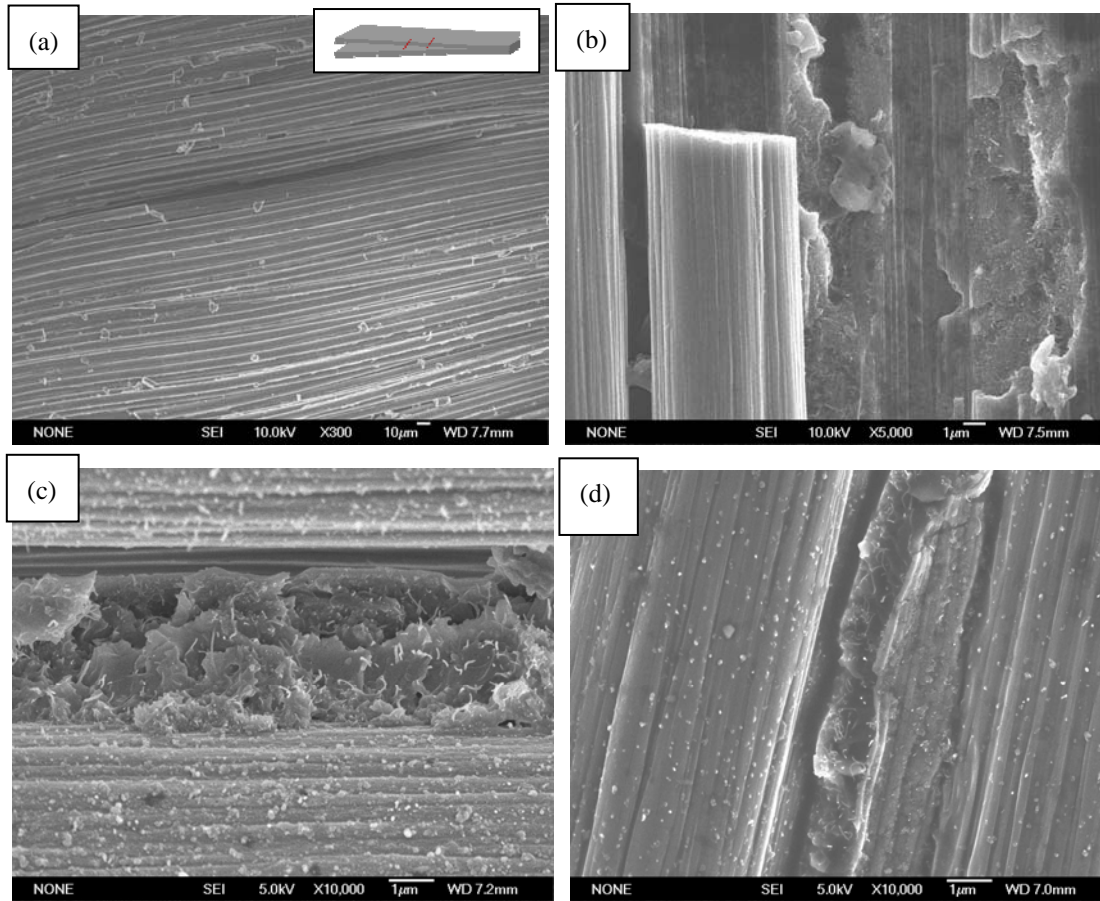
Figure 5. (a) Fracture surface of a baseline (no CNTs) composite; (b) smooth fiber surface of a CNT-CF composite showing bare fiber surfaces; (c) and (d) CNTs found only in the resin but not on the fibers.
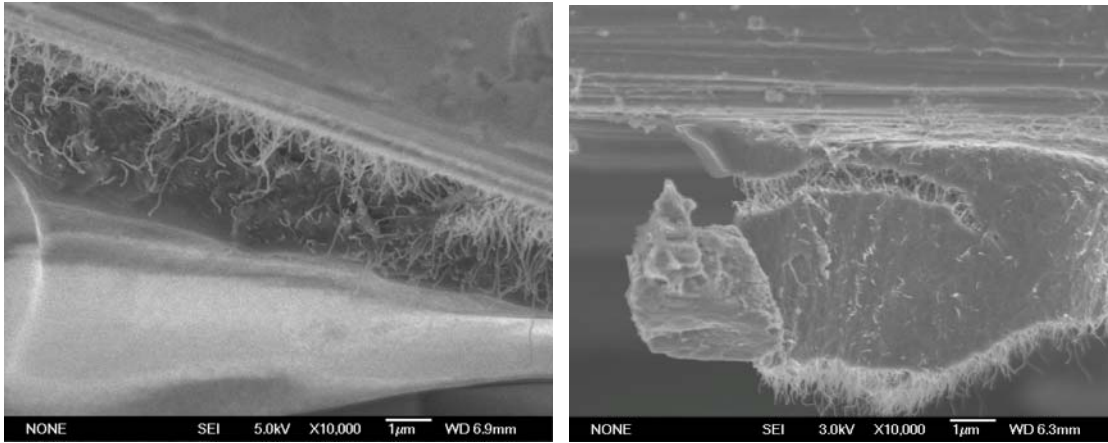
Figure 6. Composite with good CNT-CF adhesion: (a) CNTs adhering to carbon fiber surfaces; (b) fracture through the middle of resin.

1.3.3 Electrical conductivities

The out-of-plane electrical conductivity, the in-plane conductivity, and the sheet resistance were measured on both the 4-layer hierarchical composites and the baseline composite. As expected, the out-of-plane conductivity and the sheet conductance improved substantially in the presence of CNTs, Figure 7.   However, the in-plane conductivity did not change much.

The out-of-plane electrical conductivity is quite sensitive to the fiber volume fraction: it increases with the fiber volume fraction. Therefore, the composites with lower thickness but with the same number of plies show higher out-of-plane electrical conductivity. The fiber volume fraction of each composite was measured using a matrix digestion method to rule out the fiber volume fraction effect on the electrical conductivity as much as possible.   For example, panel #1 with no CNTs and panel # 3 with CNTs in Figure 7 show similar fiber volume fractions. Hence, we can claim the higher out-of-plane electrical conductivity is really attributed to the CNT effect, not to the fiber volume fraction effect.
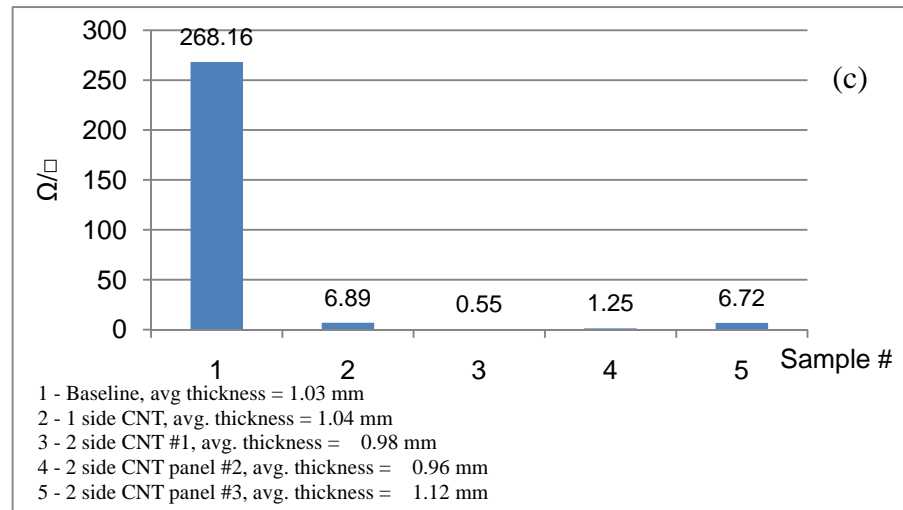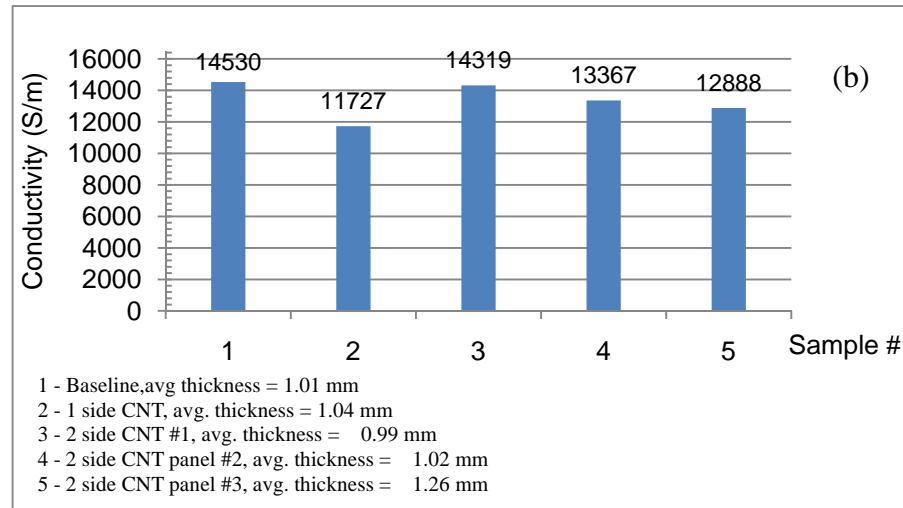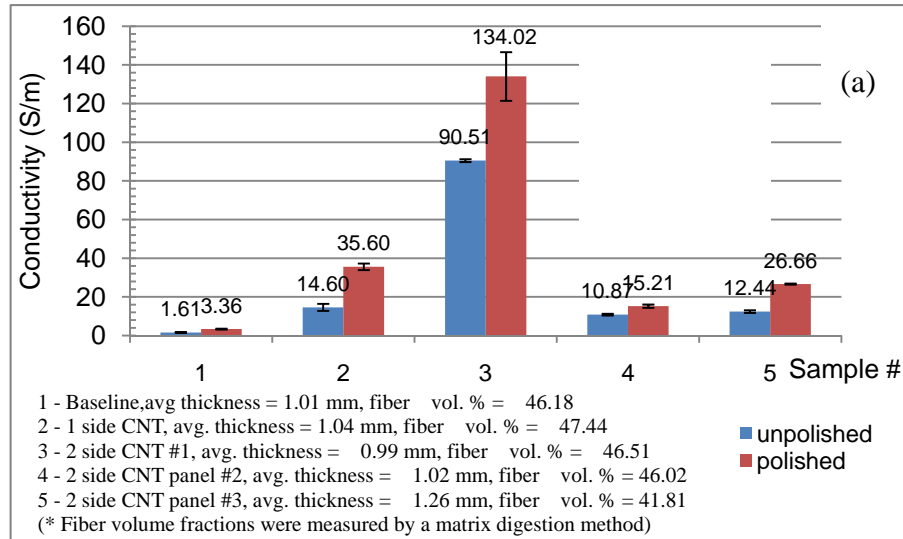
Figure 7. (a) Out-of-plane electrical conductivity; (b) In-plane electrical conductivity; (c) sheet resistance

1.3.4 Resistance change measurement during mode-1 fracture toughness tests

Figure 8 shows a schematic of composite lay-ups used to study the effect of CNTs on the resistance change during fracture toughness test. Figure 9 shows the expected current path and dimensions of a typical sample.
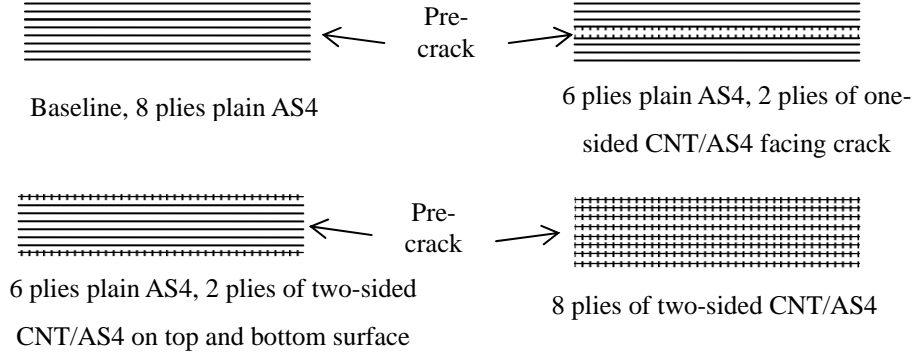
Figure 8. Summary of composite lay-ups for fracture toughness tests.
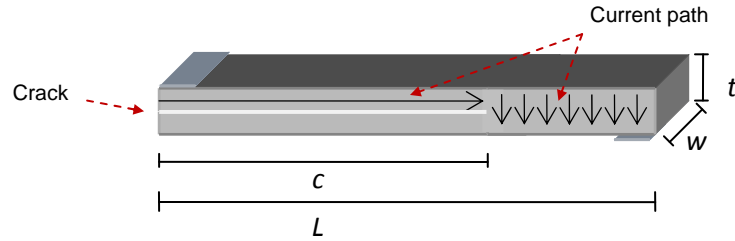
Figure 9. Sample dimensions and current path

A simple model for the effect of the crack on the measured resistance may be given as

$R = \rho_{in} \frac{c}{w \times t/2} + \rho_{out} \frac{t}{w \times (L-c)}$, where ρ_{in} and ρ_{out} are the in-plane and out-of-plane resistivity,

respectively, t is the thickness of the sample, w is the width, L is the length between electrodes, and

c is the crack length. It is further assumed that the in-plane resistivity is very low since the current

flow is mainly in the direction of the highly conducting carbon fibers. Therefore, the top surface of

the sample is assumed to be at the same potential, and so the out-of-plane current through the thickness of the sample to the bottom electrode will dominate the response. In the limit of the crack reaching the entire length of the sample, the first term goes to zero as there is no longer a conducting path between the two electrodes and the second term goes to infinity. Taking this approach, the resistance change would follow an exponential increase up to the infinite resistance when the crack length equals the length of the sample.

Figure 10 is a plot of the suggested function defining the resistance change versus crack length for the baseline composite. The sample dimensions are taken as $t = 1.75$mm, $w = 15$mm. The through-the-thickness ρ_{out} is about 0.3 $\Omega \cdot$m and the contact resistance 1.2 Ω. Figure 10 shows the calculated resistance, the calculated resistance plus the contact resistance, and the normalized resistance change over the course of the crack propagating from 0 to 60 mm.
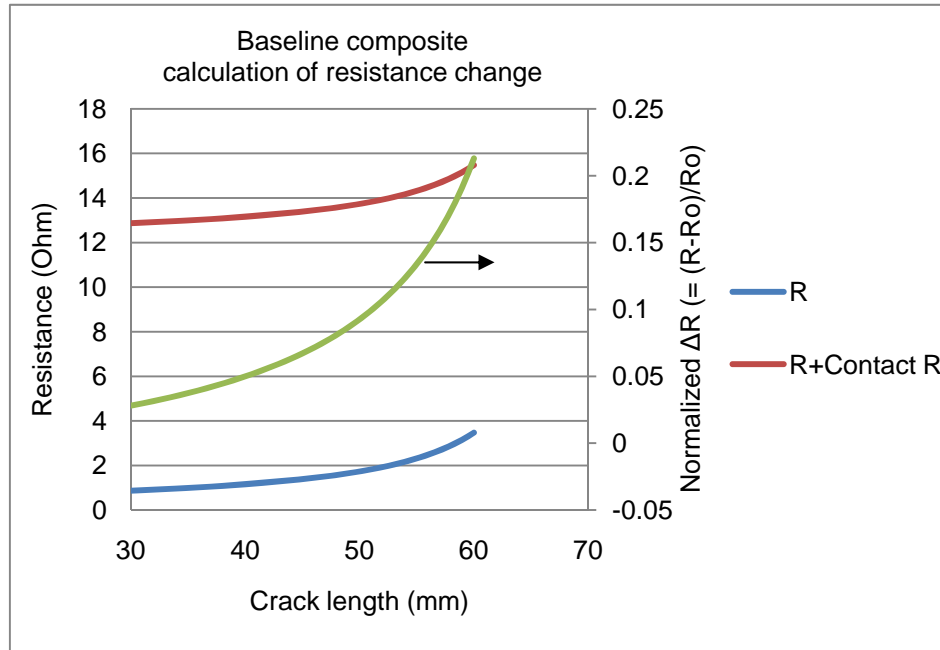
Figure 10. Estimated electrical resistance change during crack growth for the baseline composite.

Initial testing was performed on the baseline composite with no CNTs. Figure 11(a) is a plot of the load applied and the measured resistance change versus time. As the crack propagates, indicated by sudden drops in load, the electrical resistance increases. Using the data collected on a video camera allows the resistance to be correlated with the crack length. Figure 11(b) show the measured electrical resistance change increasing with the crack length for the baseline composite.
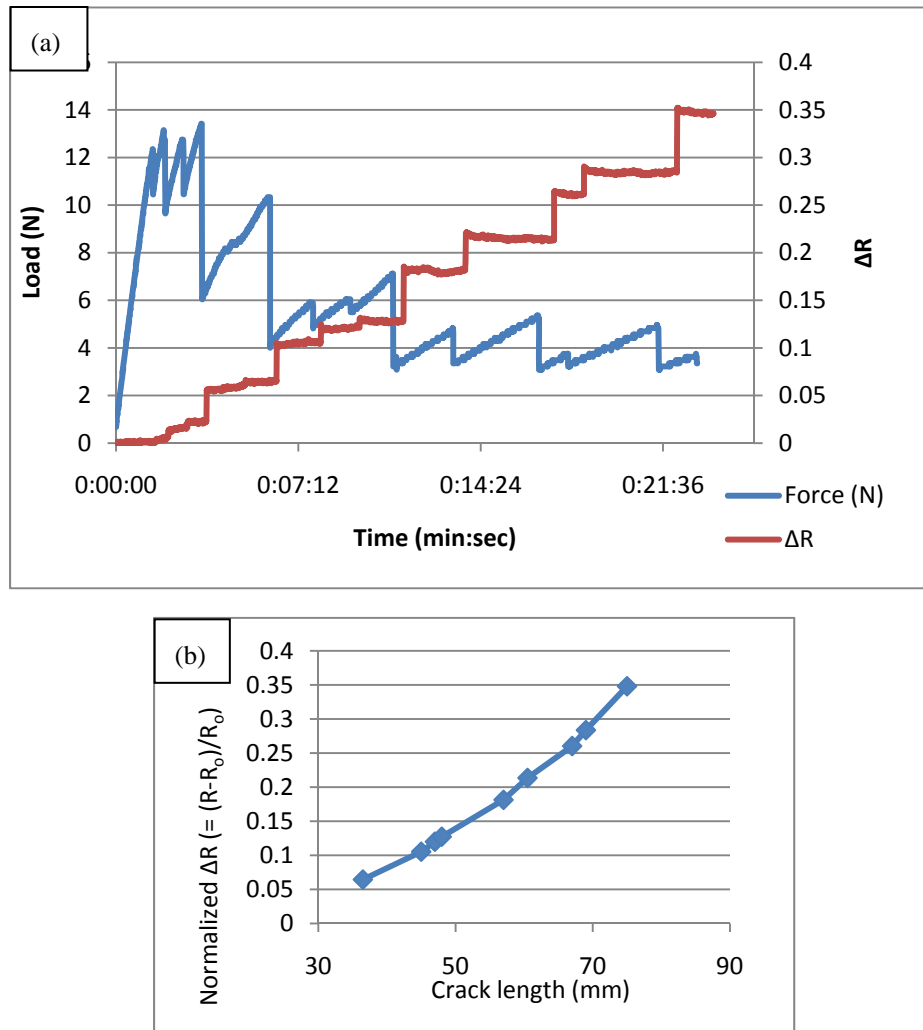
Figure 11. Baseline composite: (a) applied load and resistance change;
(b) resistance change vs. crack length.

In the next test series, one-sided CNT/CF plies were placed with the CNTs facing the pre-crack as illustrated in Figure 8. The results are compared with those of the two baseline composite specimens in Figure 12.

In the present case, the addition of CNTs appears to have rather minimal effect: the rate of resistance change in the CNT loaded composite does not appear much different from those of the baseline composite specimens. This is not surprising because the presence of CNTs in the mid plane alone does not ignificantly affect the overall through-the-thickness resistance of the composite.
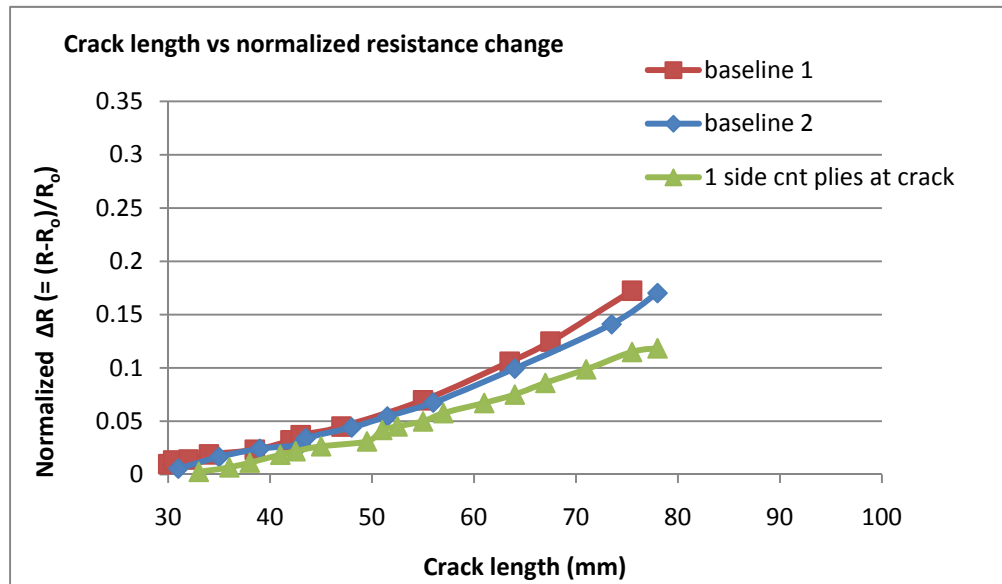
Figure 12. Single-sided CNT composite and baseline composite: resistance change during DCB test.

The next composite configuration used 2-sided CNT/CF plies throughout the full thickness of the composite, as shown in Figure 8. Figure 13 shows a higher resistance change in the presence of CNTs. The 2-sided CNT/CF composite shows a total resistance change of over 30%. The composite had an initial resistance of 0.53 Ohms which is much lower that the corresponding value of 8.04

Ohms for the baseline composite. Thus the presence of a crack, which hampers current flow, has more noticeable effect on the measured resistance.

Crack length vs normalized resistance change
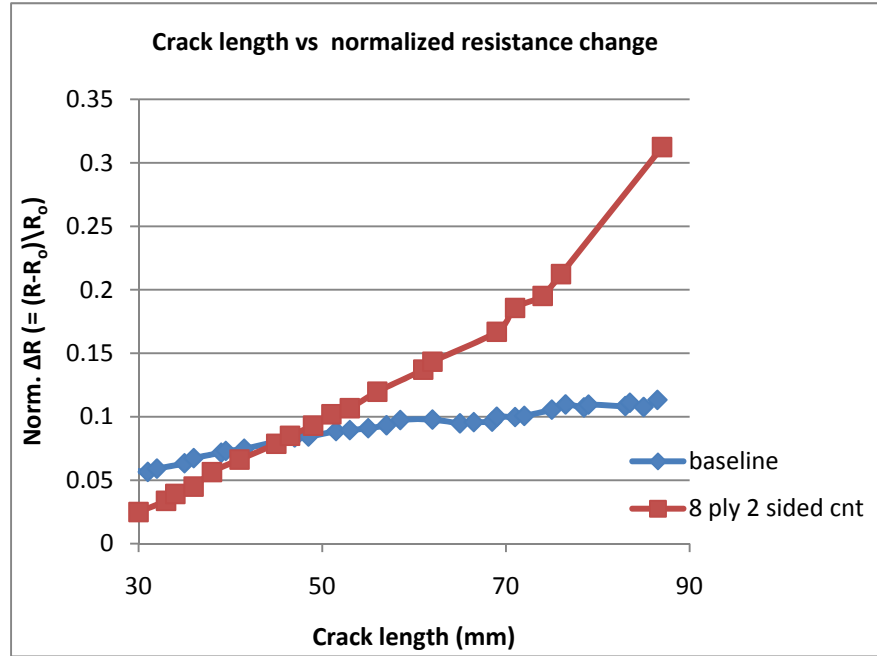
Figure 13. Two-sided CNT/CF composite vs. baseline composite.

The last set of tests employed one two-sided CNT/CF ply placed respectively at the top and bottom surfaces of the composite, Figure 8. Further, these composite samples and the corresponding baseline composite were not polished prior to the application of the conducting paint and wire electrodes. The initial resistance between electrodes was measured at 10.17 Ohms for the baseline composite, and 1.14 and 1.19 Ohms for the first and second CNT composite samples, respectively. This could partially be the result of CNTs in the surface layers lowering the contact resistance. Figure 14 shows a high level of resistance change, say 30%, for the composite samples with surface-mounted 2-sided CNT/CF plies.

(a) Resistance, Load vs Time: CNT/CF sample #1

(b) Resistance, Load vs Time: CNT/CF sample #2

(c) Crack length vs normalized resistance change
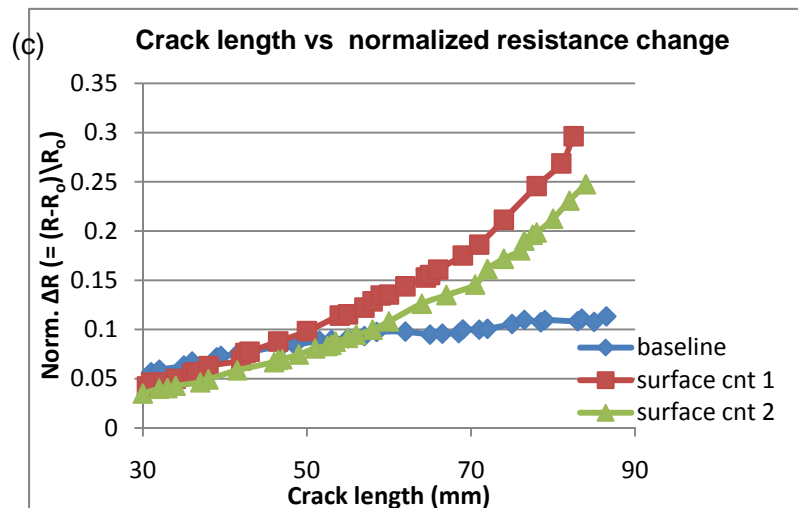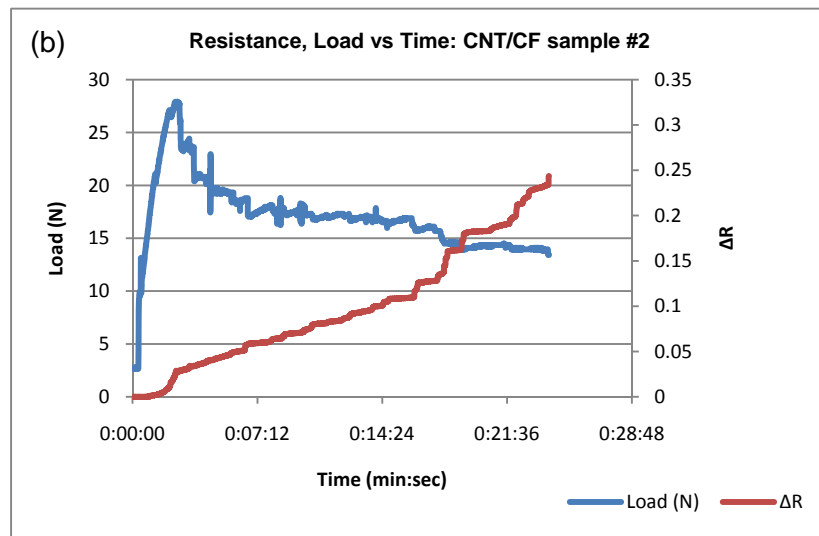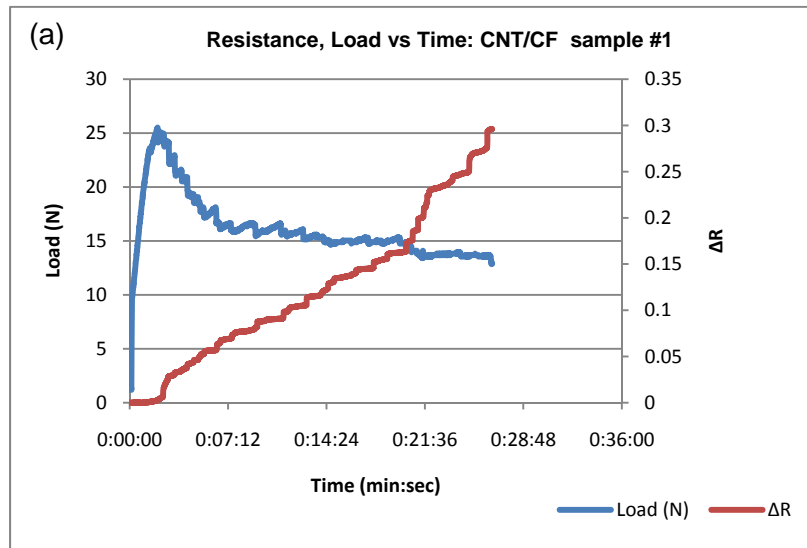
Figure 14. Composite with surface-mounted 2-sided CNT/CF plies:

(a) sample 1; (2) sample 2; (3) resistance change.

In order to investigate the effect of surface-mounted CNT-CF plies on the contact resistance, further tests were conducted on both types of composites: the baseline and the surface-mounted. Each composite sample unpolished was prepared with four 3-mm wide coatings of conducting paint placed at 10-mm intervals along the top surface, a wire was soldered to each electrode.   Figure 15 shows the electrode placement on a typical sample. Resistance was measured between the first electrode, denoted electrode 1, and each of the remaining four electrodes, denoted 3 through 4.
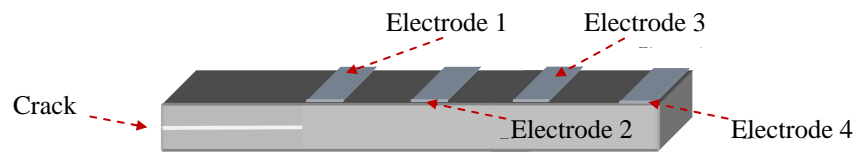
Figure 15. Electrode placement for contact resistance on a sample.

Figure 16 shows the resulting measured resistance versus distance between electrodes. For each sample, the measured resistance increases with the distance, as expected, and the presence of CNTs in the surface plies significantly decreases the contact resistance.
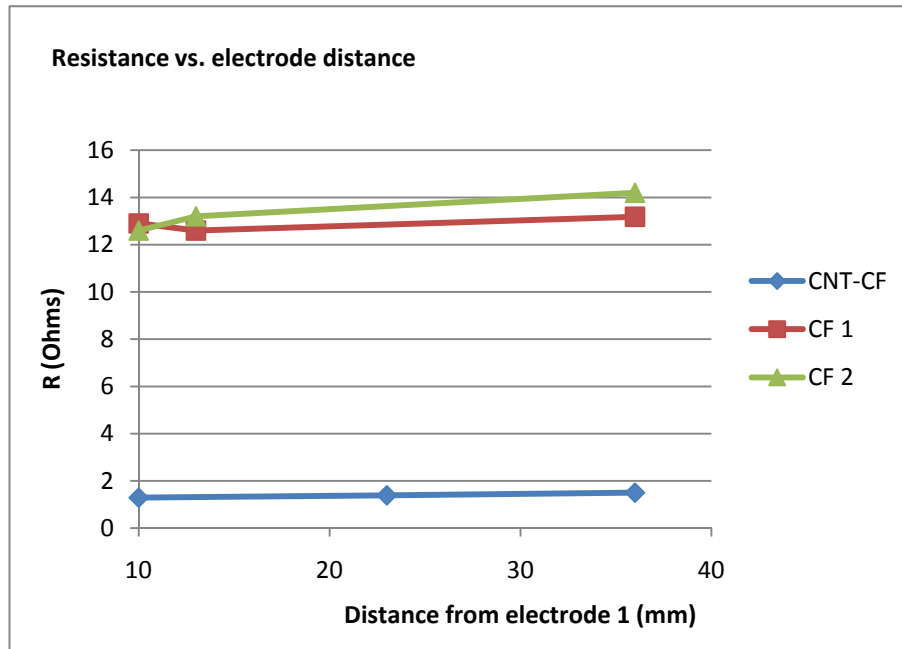
Figure 16. Contact resistance comparison: Resistance vs. electrode distance on top surface

1.3.4 Conclusions

The effectiveness of CNTs grown on carbon fiber surfaces to improve electrical conductivity and interlaminar facture toughness has been studied using a variety of hierarchical composites. Their role in the detection of interlaminar crack growth using electrical resistance change has also been investigated in the present research.

As expected, the CNTs increase the out-of-plane electrical conductivity substantially; however, they barely improve the in-plane conductivity. Also, CNTs in the surface layers reduces the contact resistance.

CNTs grown on carbon fiber surfaces can be quite effective in increasing the composite interlaminar fracture toughness as long as the bonding between CNTs and CFs is good. If the bonding is weak, however, the effectiveness diminishes as the fracture occurs at the CF-matrix interface.

17

Electrical resistance change can be used to monitor interlaminar crack growth. Its sensitivity can be increased by using CNTs throughout the volume or in the surface layers.

1.4 Personnel supported

1) H. Thomas Hahn: Principal investigator, Professor (UCLA).

2) Hansang Kim: Co-investigator, Assistant researcher (UCLA).

3) Eliah Novin: Co-investigator, Graduate student (UCLA).

1.5 Publications

1. Hansang Kim, Eliah Novin, H. Thomas Hahn, Eugene Oh, Gun-Hong Lee, "Processing and characterization of hierarchical carbon fiber composites," in preparation.

2. **Hansang Kim, Eliah Novin, H. Thomas Hahn, Eugene Oh, Gun-Hong Lee, "Enhanced crack detection sensitivity by using hierarchical carbon fiber composites," in preparation.**

Appendix A

A-1. Final report from KPI, Professor Gun-Hong Lee (POSTECH) (pp. 21 - 38)
A-2. Final report from co-KPI, Professor Sang-Gee Lee(Ewha Womans University) (pp. 39 - 52)

A-1. Final report from KPI, Professor Gun-Hong Lee (POSTECH)

Research Title: Hierarchical Carbon Fiber Composites Task I: Adhesion improvement between the carbon nanotube forest and the carbon fibers.
Research Institute: Department of Chemical Engineering, POSTECH
Principal Investigator: Professor Kun-Hong Lee
Co-Investigator: Eugene Oh, Seungho Cho, Nam Hyo Kim

1.1. Objective

The aim of the Task I in the third-year is the improvement of the adhesion between carbon nanotube (CNT) forest and carbon fibers (CFs). This CNT/CF hierarchical structure was achieved in the send year, but the CNTs were loosed bound to the CFs.

1.2. Status of Effort

The mechanical strength of hierarchical CNT-CFs composite laminates strongly depends on the adhesion between the CNTs and the CFs at the interface. To improve the adhesion between the CNT forest and CFs, SiO_2 and Al_2O_3 layers were sequentially deposited on the CFs before growing CNT forest. A thermal chemical vapor deposition (CVD) method was established to form a vertically-aligned CNT forest on the CF fabric. The degree of adhesion was qualitatively assessed using the Scotch-tape test.

1.3 Research accomplishments

1.3.1. Synthesis of the adhesion-improved CNT forest on CFs

To improve the adhesion between CNT forests and CFs, the SiO_2 layer of 20 nm thickness and the Al_2O_3 layer of 10 nm thickness were sequentially deposited on the CFs. Deposition of iron as a catalyst was followed as shown in Fig. 1. Since the SiO_2 and the Al_2O_3 layers are similar oxide layers, the adhesion between them is guaranteed.
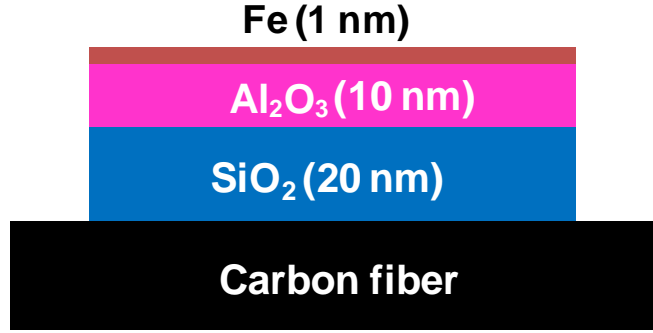
Fig. 1. Schematic diagram of deposition of the thin films on the CF.

Synthesis of CNT forest was investigated by thermal CVD method which is amenable for large-scale synthesis. Fig. 2 (a)-(d) show the adhesion-improved CNT forest grown on the surface of CFs. The length of the CNT forest is 350 μm in Fig. 1(a).
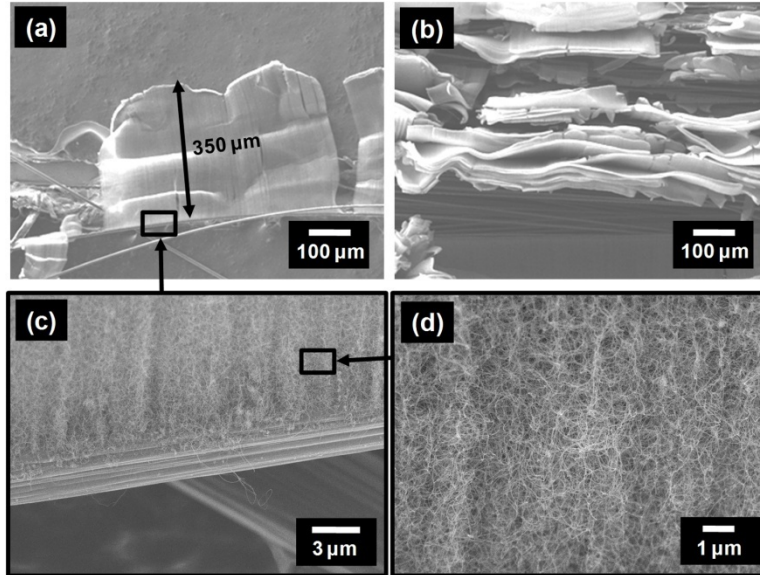
Fig. 2. Adhesion-improved CNT forests on the CFs. (a) side and (b) top view of high-density CNT forests. (c) and (d) show an enlarged SEM images taken from the area marked by a square in (a) and (c), respectively.

Fig. 3(a) and (b) show transmission electron microscopy (TEM) images of the adhesion-improved CNTs on the CF. CNTs grew from Fe nanoparticles which were embedded between the

Al_2O_3 and the carbon layer. It is believed that the adhesion of CNTs on Al_2O_3 layer is good. The CNTs are covered by the Pt nanoparticles in Fig. 3. These Pt nanoparticles were introduced in the process of preparing the TEM specimen for masking the ion beam. In addition, CNTs and buffer layers were slightly damaged by the ion beam.
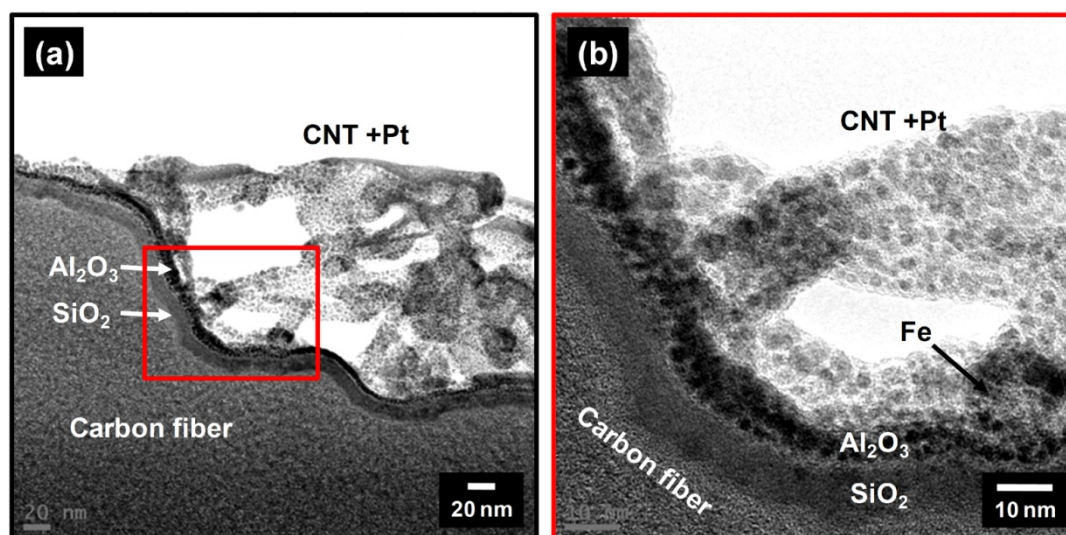
Fig. 3. (a) and (b) TEM images of the CNTs on CF. (b) shows an enlarged TEM image taken from the area marked by square in (a).

We used EELS technique to confirm the buffer layers and the CNTs. Fig. 4 (b)-(g) show EELS mapping images for Fe, Pt, C, O, Si, and Al, respectively. Fig. 4(a) is the TEM image corresponding to the EELS mapping images in Fig. 4 (b)-(g). It can be concluded that the SiO_2 and the Al_2O_3 layer were successfully deposited between the CNTs and the CFs.
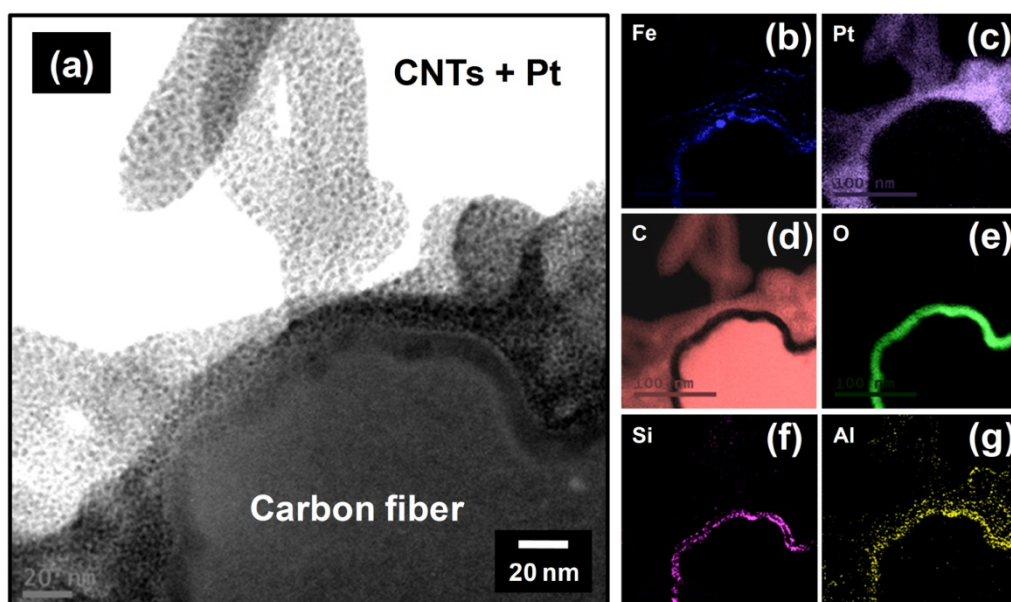
Fig. 4. (a) TEM image of the Pt coated CNTs on the CF corresponding to EELS mapping images of (b) Fe, (c) Pt, (d) C, (e) O, (f) Si, and (g) Al elements.
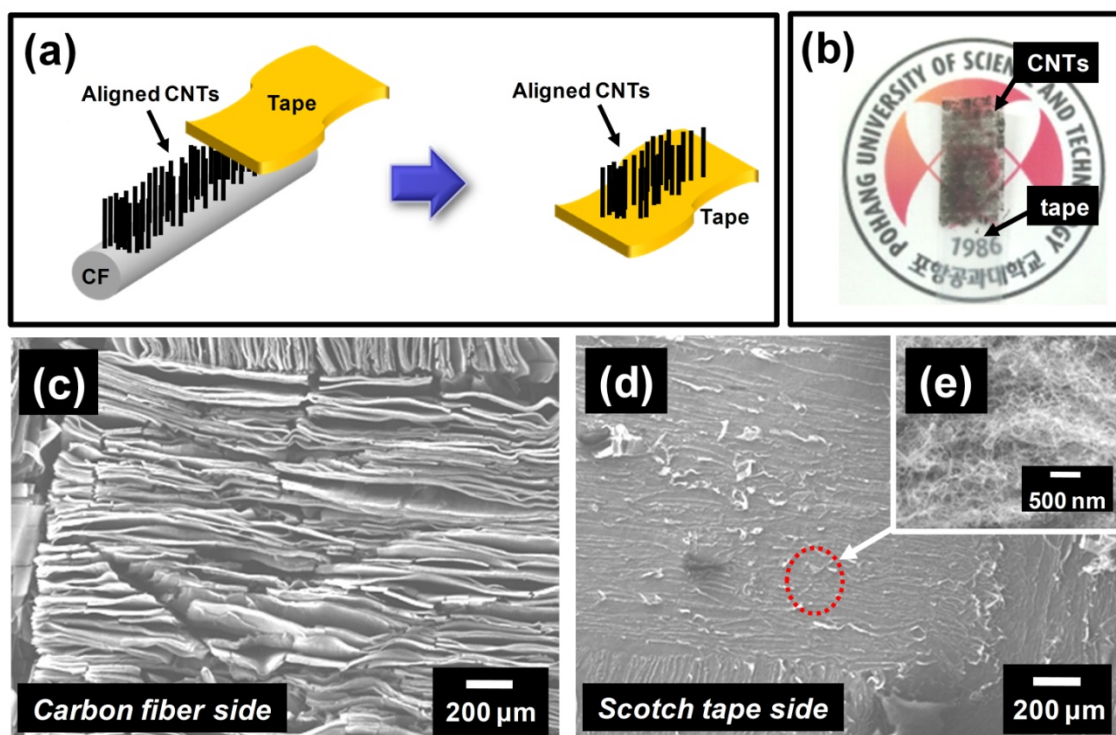
Fig. 5. (a) Schematic diagram of the Scotch tape test. (b) The tape used to test. The SEM images of (c) CF and (d) tape side after Scotch tape test. (e) An enlarged SEM image taken from the area marked by dotted circle in (d).

The strength of adhesion of the CNT forests on the CFs was qualitatively assessed using the Scotch-tape test (ASTM D3359) as shown in Fig. 5(a). A photograph of the tape used to Scotch tape test is shown in Fig. 5(b). Some CNTs were detached from the CFs and attached to the tape in Fig. 5(d) and (e). The majority of the CNT forests, however, still remained on the CFs as shown in Fig. 5(c). Among the scale of grade 0~5 (ASTM D3359), the adhesion-improved CNT forests has an excellent adhesion with a grade 5. As a result of tape test, we confirmed that the adhesion between CNT forests and CFs was dramatically improved.

We also confirm the adhesion of CNT forests by ultrasonication as shown in Fig. 6. An ultrasound was introduced at the power of 80 W (frequency: 47 KHz) for 5 min using ultrasound bath. Ethanol was used as a solvent. It is obvious that the CNTs are tightly bound on the CFs even after the ultrasonication.

- Solvent: ethanol
- Sonication time: 5 min
- Power: 80 W
- Frequency: 47 KHz
- Capacity: 1.9 L

Apply ultrasound
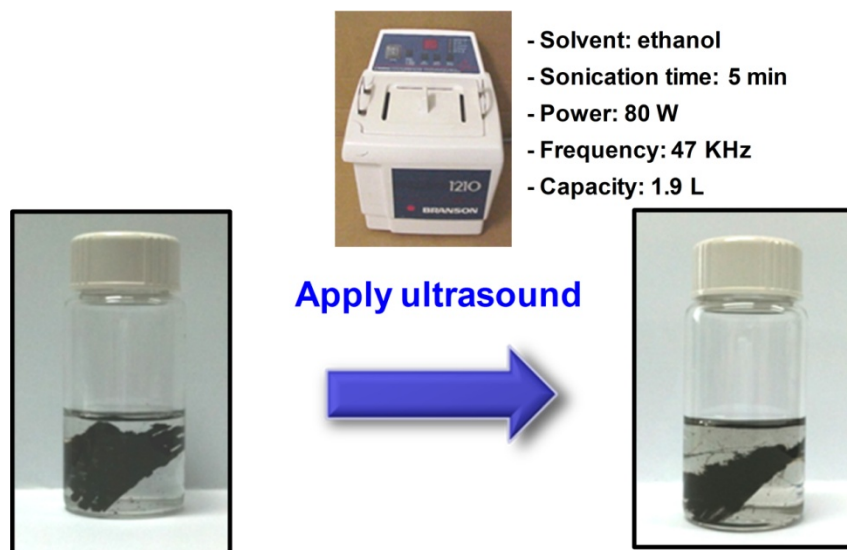
Fig. 6. Adhesion test using ultrasonic bath.

In summary, we synthesized the high-density CNT forest on CFs in the 2nd year, but the

CNT forests had poor adhesion to CFs. We synthesized the adhesion-improved CNT forests on CFs in the 3rd year. We assessed the adhesion between CNT forests and CFs using the Scotch-tape test (ASTM D3359) and the ultrasonication test as shown in Fig. 7. The specimen, adhesion-improved CNT forests grown on CFs, was supplied to Prof. Hahn (UCLA) for composite fabrication.
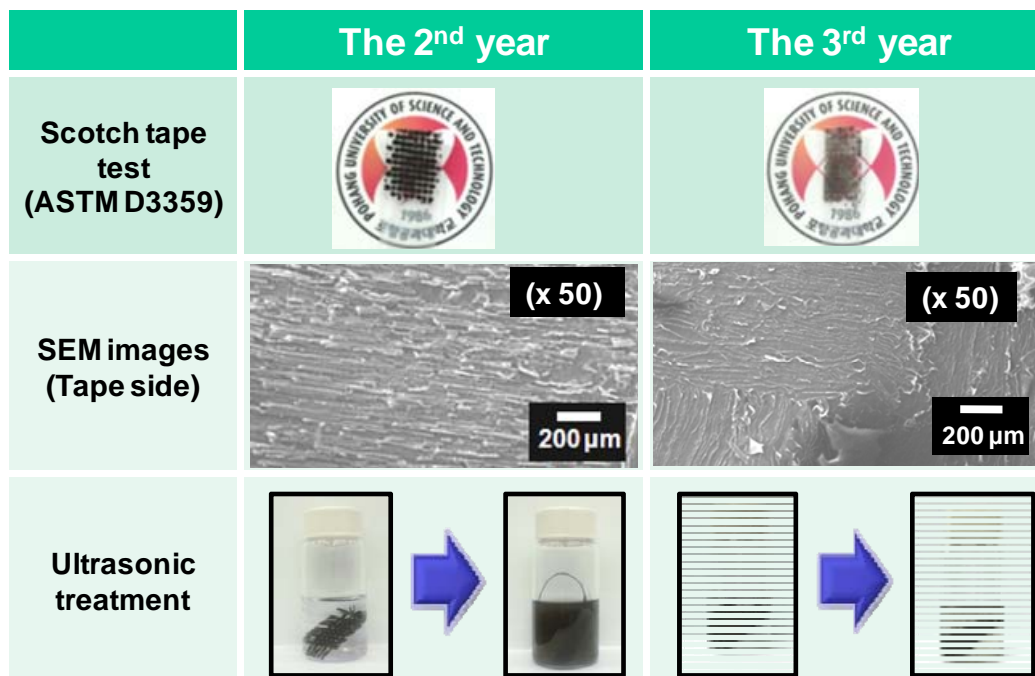
Fig. 7. Results of adhesion test in the 2nd and 3rd year

1.4 Personnel supported

1) Kun-Hong Lee: Principal investigator, Professor (POSTECH).

2) Eugene Oh: Co-investigator, Ph. D. candidate (POSTECH).

3) Seungho Cho: Co-investigator, Ph. D. candidate (POSTECH).

4) Nam Hyo Kim: Co-investigator, Ph. D. candidate (POSTECH).

1.5 Publications

1. Seungho Cho, Ji-Wook Jang, Seung-Ho Jung, Bo Ram Lee, Eugene Oh and Kun-Hong Lee, "Precursor Effects of Citric Acid and Citrates on ZnO Crystal Formation", Langmuir, 25, 3825-3831 (2009).

2. Seungho Cho, Dae-Seob Shim, Seung-Ho Jung, Eugene Oh, Bo Ram Lee, and Kun-Hong Lee, "Fabrication of ZnO nanoneedle arrays by direct microwave irradiation ", Materials Letters, 63, 739-741 (2009).

3. Eun-Ha Kim, Da-Hye Park, So-Ye Park, Kun-Hong Lee, Hyung Seok Kim, and Chan Gyung Park, "Synthesis of amorphous Si nanowires from solid Si sources using microwave irradiation", Thin Solid Film, 517, 6629-6634 (2009).

1.6 Presentation

1. Kun-Hong Lee, "Microwave synthesis of nanomaterials", The 3rd Workshop on Nano/Micro Integrated and Complex Systems, Gimhae, Korea (2009, 1/29-30).

2. Kun-Hong Lee, "Hierachical carbon fiber composites ", The 8th US-Korea workshop on nanostructured materials , Seoul, Korea (2009, 5/19-20).

3. Eugene Oh and Kun-Hong Lee, "Growth of carbon nanotube forest on the carbon fiber ", The spring meeting of the Korean Carbon Society , Incheon, Korea (2009, 5/7-8).

4. Eugene Oh, Jae-Geun Lee, and Kun-Hong Lee, "Synthesis of SiC nanowires by direct microwave irradiation", NDNC2010, Suzhou, China (2010, 5/16-20).

5. Eugene Oh, Jae-Geun Lee, and Kun-Hong Lee, "Synthesis of SiC nanowires by direct microwave irradiation", KIChE 2010, Daegu, Korea (2010, 4/21-23).

6. Eugene Oh, Jae-Geun Lee, and Kun-Hong Lee, "Selective synthesis of SiC and SiOx nanowires by direct microwave irradiation", Korea Carbon Society Spiring meeting,

Seoul, Korea (2010, 5/27).

Appendix A

Contents

Fig. A-1. SEM image of a bare Carbon Fiber (CF).

Fig. A-2. Results of the 2nd year. SEM images of high-density CNT forest on CFs by CVD.

Al (10 nm) and Ti (5 nm) thin films as buffer layers were deposited on CFs.
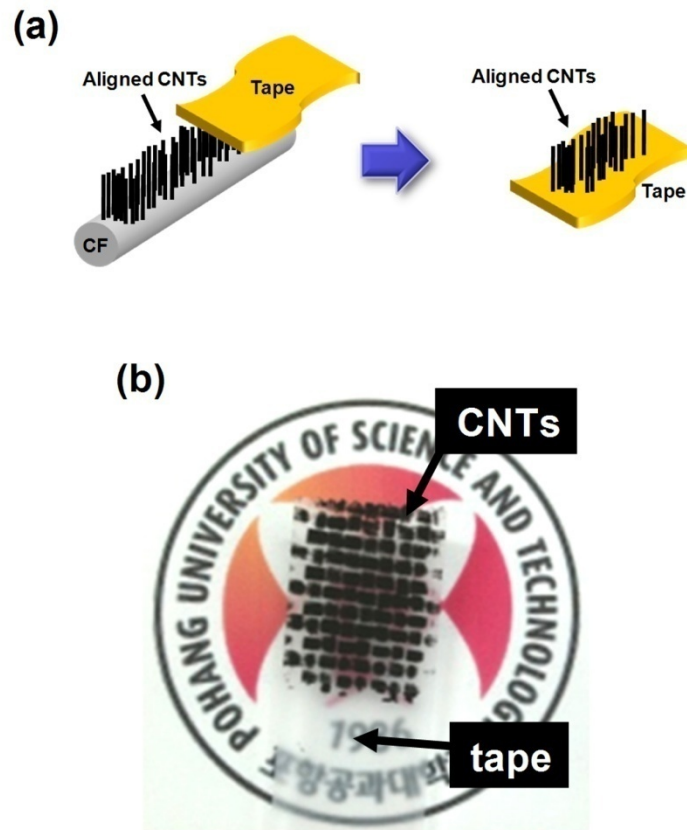
Fig. A-3. (a) Schematic diagram of scotch tape test. (b) A photograph of the tape used to Scotch tape test of CNT forests in Fig. A-2. Most CNTs were detached from the CFs. Among the scale of grade 0~5 (ASTM D3359), the adhesion-improved CNT forests has a poor adhesion with a grade 0 or 1.
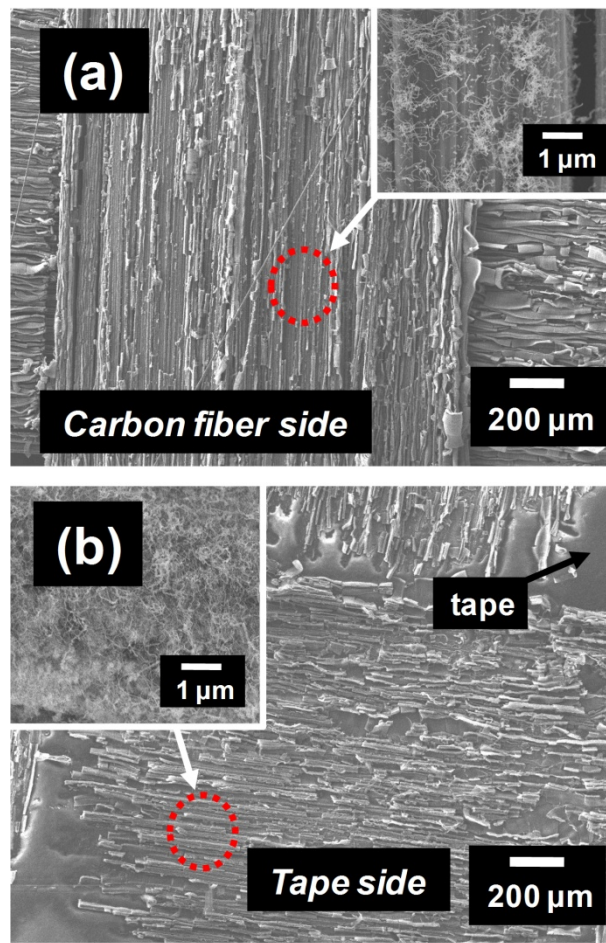
Fig. A-4. The SEM images of (a) CF and (b) tape side after Scotch tape test of CNT forests in Fig. A-2.

Apply ultrasound
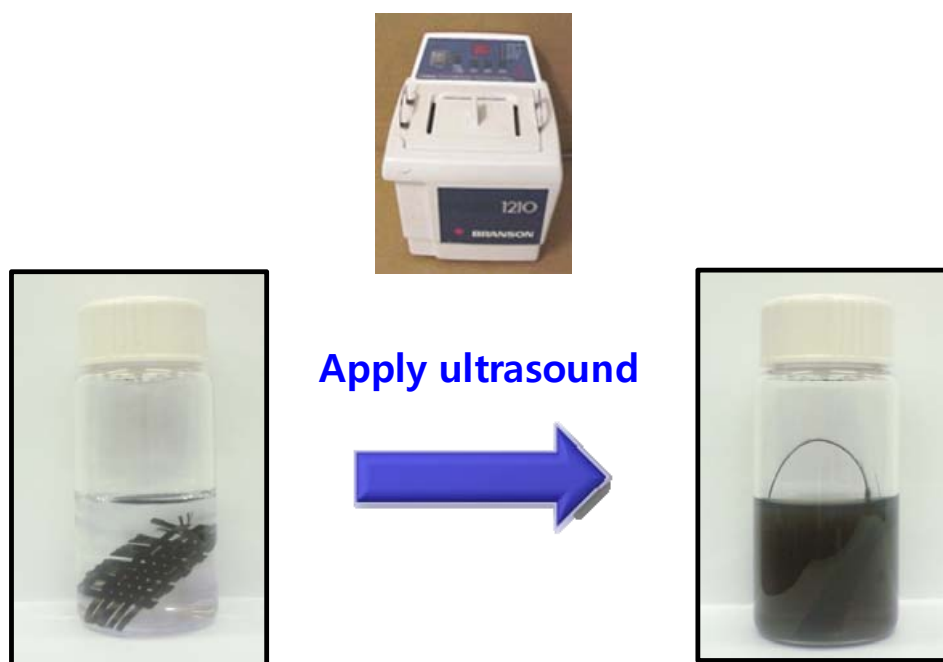
Fig. A-5. Adhesion test of CNT forests in Fig. A-2 using ultrasonic bath.

An ultrasound was introduced at the power of 80 W (frequency: 47 KHz) for 5 min using ultrasound

bath. Ethanol was used as solvent.
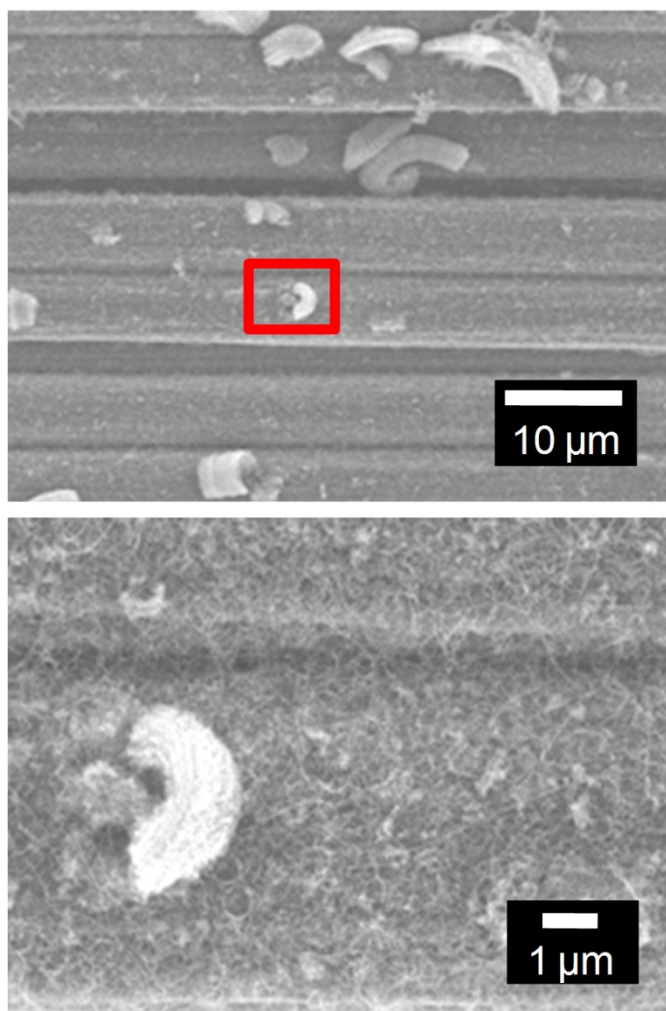
Fig. A-6. Control experiment 1. (without SiO₂ layer)

SEM images of CNT forests grown on CFs without SiO$_2$ layer between Al$_2$O$_3$ and CFs. The packing density of CNTs was very poor. We may need a SiO$_2$ buffer layer.
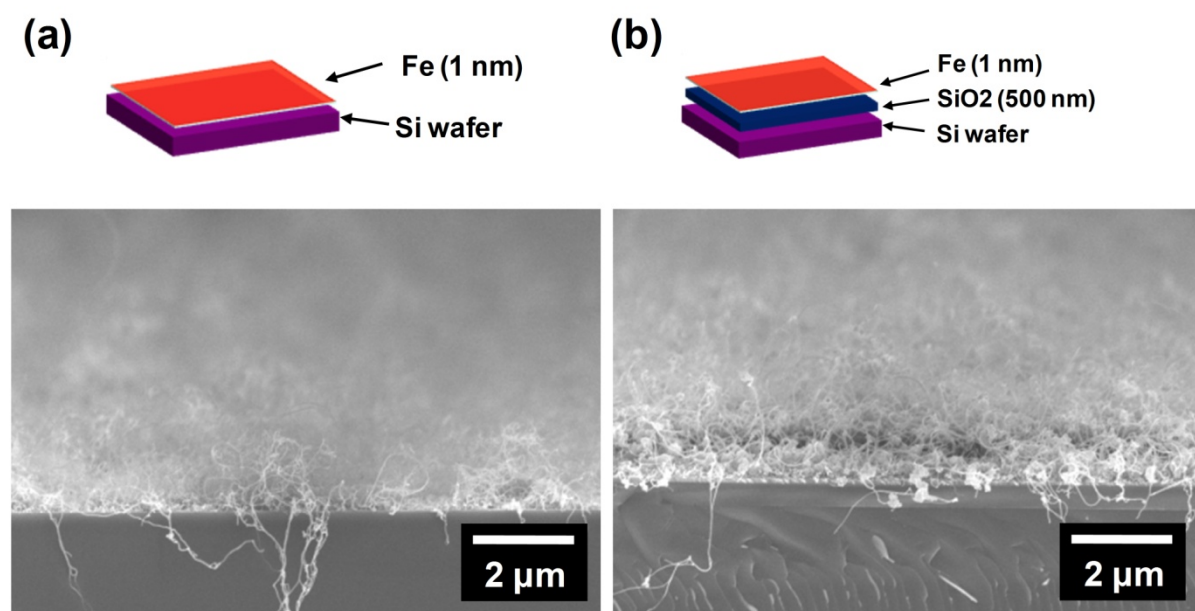
Fig. A-7. Control experiment 2. (without Al$_2$O$_3$ layer)

SEM images of CNTs grown on a Si wafer without Al$_2$O$_3$ layer. (a) Fe was coated on a Si wafer. (b) SiO$_2$ and Fe were deposited on a Si wafer. We were unable to grow high-density CNT forest on the Si wafer with SiO$_2$ alone.

1. Heat treatment

CNTs

C-C bond
formation
by heat treatment

CFs

- Thermal furnace (Lindberg)
- Temperature: 1100~1300 $^\circ$C
- Gas: Ar (500 sccm)
- Heat treatment time: 1 hr

1100 $^\circ$C
300 nm
5 µm

1200 $^\circ$C
300 nm
5 µm

1300 $^\circ$C
1 µm
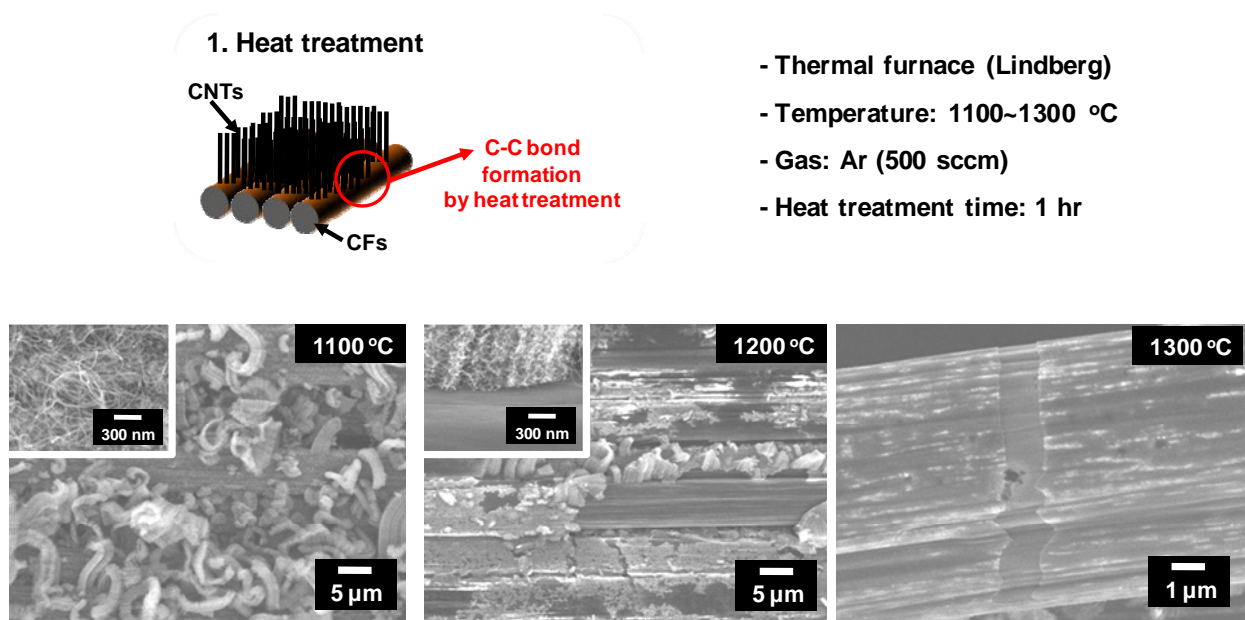
Fig. A-8. Heat treatment of CNT forests on CFs specimens at high temperature.

We expect that the C-C bonds are formed through heat treatment of CNT forest/CFs specimens. Higher temperature enhanced detachment of the CNTs from the CFs. C-C bonds were not formed between the CNTs and the CFs.

2. Ti buffer layer

Fe & Ti thin-films

CFs

[S. Srividya et al.
Appl. Surf. Sci. 256 (2010) 3563.]

- Thermal furnace (A-TEC system)
- Fe (1nm)/ Ti (10 nm) on CFs
- Temperature: 750 ℃
- Catalyst reduction: Ar (1500)/ H_2(1500 sccm) for 3 min
- Growth: Ar (1500)/ H_2(1500)/ C_2H_2 (30 sccm) for 30 min

300 nm

1 μm
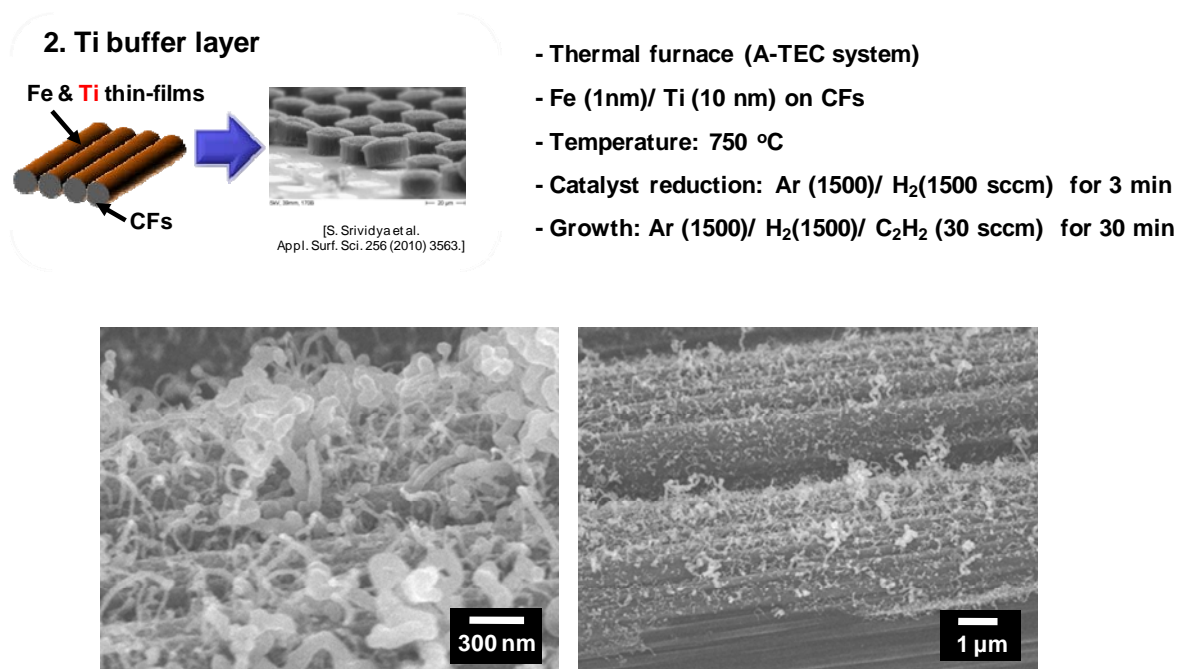
Fig. A-9. Ti buffer layer on CFs.

CNTs grown on the Ti layer were not aligned and had a low-density. The rough surfaces of CFs may impede the formation of the thin Ti adhesion layer.
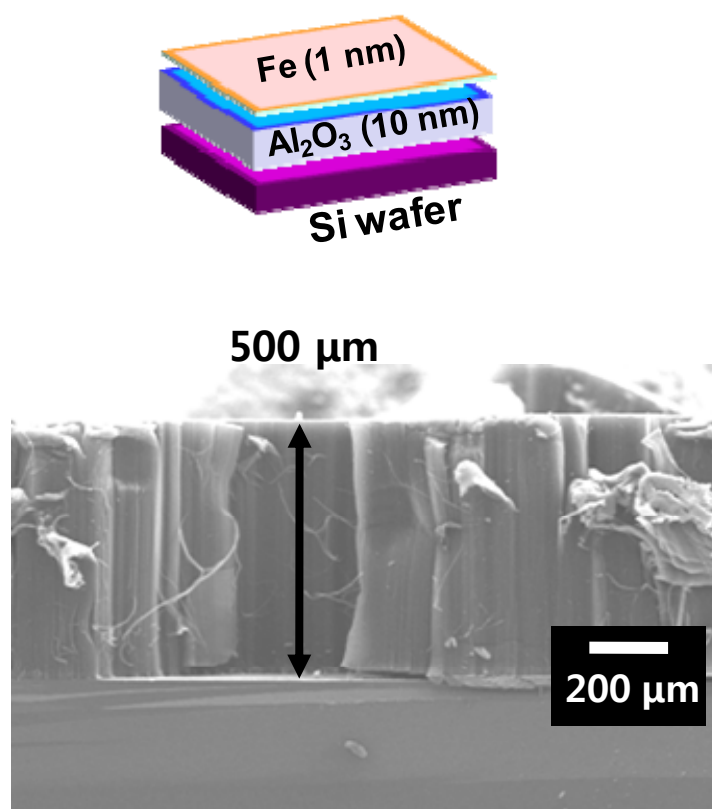
Fig. A-10. SEM image of adhesion-improved CNT forest grown on Si wafer.
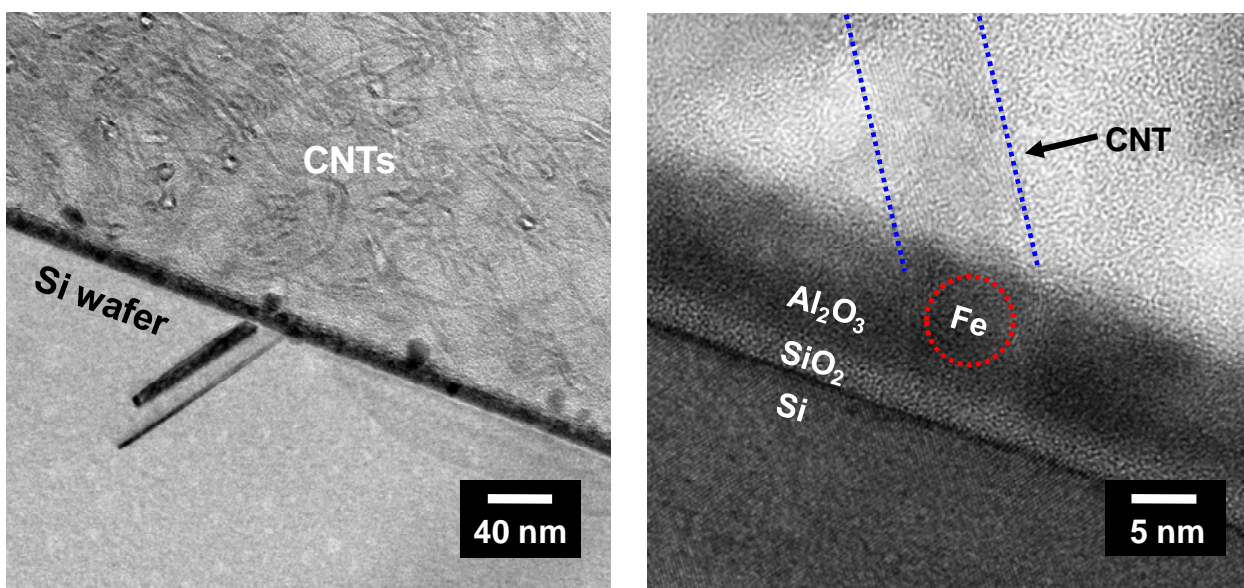
Fig. A-11. TEM images of adhesion-improved CNT forest grown on Si wafer.

The Fe catalyst particles were embedded inside the Al_2O_3 layer. Thin SiO_2 layer was observed between the Si wafer and the Al_2O_3 layer. The adhesion of the SiO_2 and the Al_2O_3 is good. [J. Mater. Chem., 2002, 12, 2559]
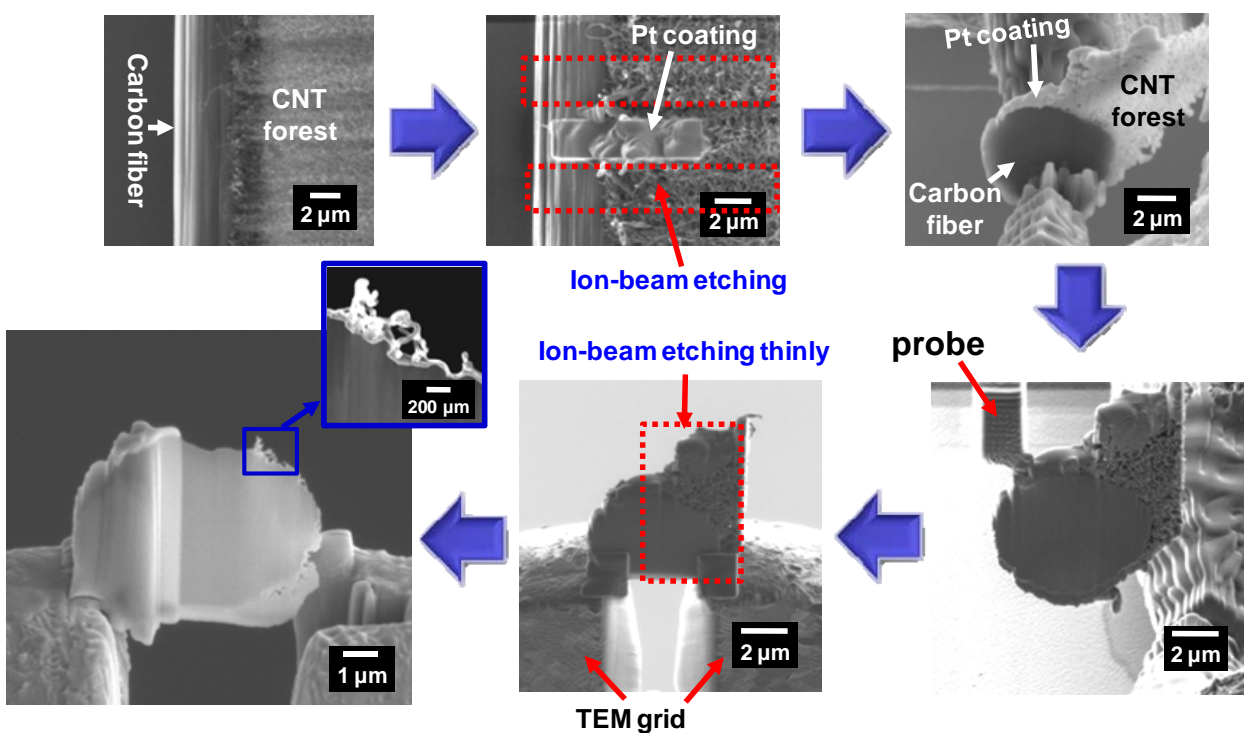
Fig. A-12. Focused ion beam was used for the sample preparation

Research Title: Functionalization of Carbon nanomaterials with Ionic liquids

Research Institute: Department of Chemistry and Nano Science, Ewha Womans University

Principal Investigator: Professor Sang-gi Lee

Co-Investigator: Yu Sung Chun, Ju Yeon Shin, Cho-Long Park

1.1. Objective

The aim of the research project is preparation of covalently functionalization of carbon nanotubes with ionic liquid moiety having polymerizable nobonene, epoxy, and amine functional groups, which can be utilized for the development of hierarchical carbon fiber composites in Task III. The objective of the research in the third-year is application of the ionic liquid-functionalization technique to other carbon nanomaterials such as nanodiamonds to solve the intrinsic nanodiamond aggregation problem for their applications.

1.2. Status of Effort

Functionalization methods for Nanodiamond with ionic liquids have been established and the behaviors of surface modified nanodiamond are investigated.

1.3 Research accomplishments

1.3.1. Synthesis of the ionic liquid-Nanodiamond composites

We have developed functionalization methods for ionic liquid-Nanodiamond having imidazole moiety. The pristine nanodiamond (100mg) were oxidized by mixture solution of H_2SO_4 and HNO_3 (60ml, 3/1, 45ml/15ml). The suspension was sonicated at 40℃ for 3h. The reaction mixture was poured into distilled water (1 L), and stirred for 10 h at room

37

temperature. After filtration by using polycarbonate membrane filter (Pore size 0.2 μm), the filter-cake was washed with distilled water several times, and dried at 80 ℃ for 12 h to provide carboxylic acid-functionalized nanodiamond particles (ND-COOH) (94 mg). A solution of ND-COOH (85 mg) in $SOCl_2$ (30 mL) was refluxed under nitrogen atmosphere for 48 h. Excess $SOCl_2$ was distilled off under reduced pressure to give the acid chloride-functionalized nanodiamond particles (ND-COCl), which used directly for next reaction.

A mixture of ND-COCl prepared above and 3-aminopropylimidazole (25 mL) was stirred at 130℃ for 48 h under nitrogen atmosphere. The mixture was diluted with anhydrous THF, and filtered through polycarbonate membrane (0.2 μm, Milipore). To remove non-covalently attached aminopropylimidazole, the filter-cake was stirred with 1N HCl solution, and then neutralized with saturated Na_2CO_3 solution and successively washed with H_2O, THF and acetone, and finally dried at 80℃ for 12 h to afford imidazole functionalized ND-imidazole (77 mg). A mixture of ND-imidazole (70 mg) and 1-bromobutane (30 mL) was stirred at 80℃ for 48 h under nitrogen atmosphere, and filtered, after cooling to room temperature, through polycarbonate membrane (pore size: 0.2 μm, Milipore). The filter-cake was washed with THF several times to remove excess of 1-bromobutane, and dried at 80℃ for 12 h to afford n-Butylimidazolium bromide-functionalized nanodiamond(IL-f-ND-2)(66mg).
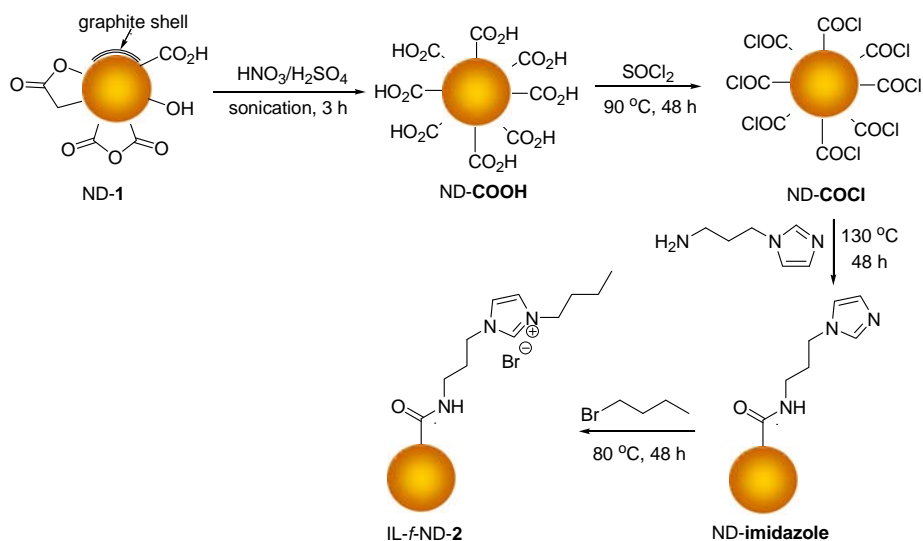
Fig. 8. Synthesis route of imidazolium bromide-functionalized IL-f-ND-2.

The resulting surface structure has extensively been studied by different techniques such as FT-IR, NMR spectroscopy, XPS, and Elemental analysis. FT-IR result indicated well fuctionalized-ND result (Figure 2). ND-COOH compounds have a strong peak at around 1629 cm^{-1} indicating the C=O steretching vibration band of the carbonyl group of ND-COOH. The carboxylic acid group of ND-COOH was converted acid chloride, which was subsequently reacted with (3-aminopropyl)imidazole. In the IR spectrum of ND-imidazole, the C=O band of the carboxylic acid group at 1629 cm^{-1} in ND-COOH was shifted to 1709 cm^{-1}, indicating the formation of the amide bond.
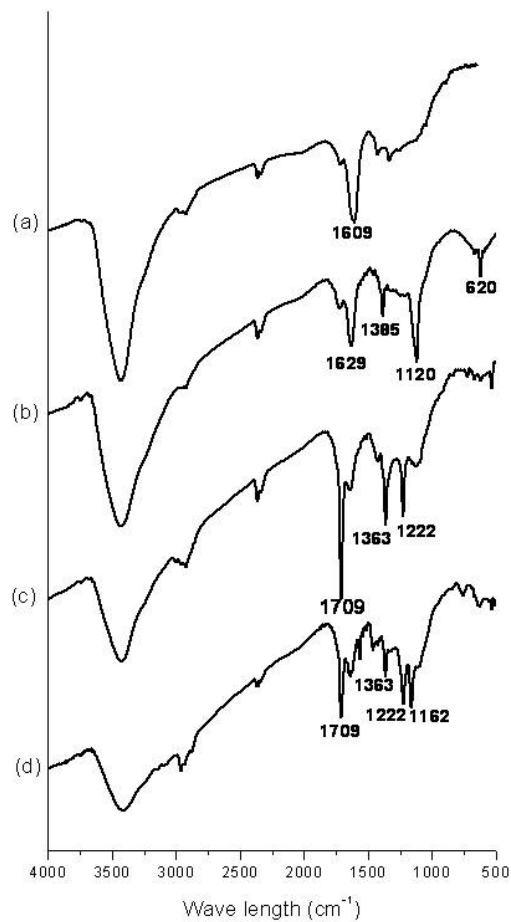
Fig. 9. FT-IR spectra of (a) detonation NDs, (b) ND-COOH, (c) ND-imidazole, (d) IL-f-ND-2

The IL-*f*-ND-**2** is partially soluble in D_2O allowing 1H NMR analysis because of the hydrophilic nature of the imidazolium bromide, (Figure 3). The characteristic imidazolium proton at 8.0 and 7.4 ppms as well as methylene and methyl protons signals clearly indicated formation of imidazolium bromide.

Fig. 10. 1H NMR spectrum of IL-f-ND-2

The XPS analysis of **IL-*f*-ND-2** further confirmed the formation of imidazolium bromide salt, which was indicated that bromide anion (Br3d, 65 eV) and elemenal analysis indicated that 0.550 mmol/g of imidazolium moiety was incorporated onto the ND surfaces.
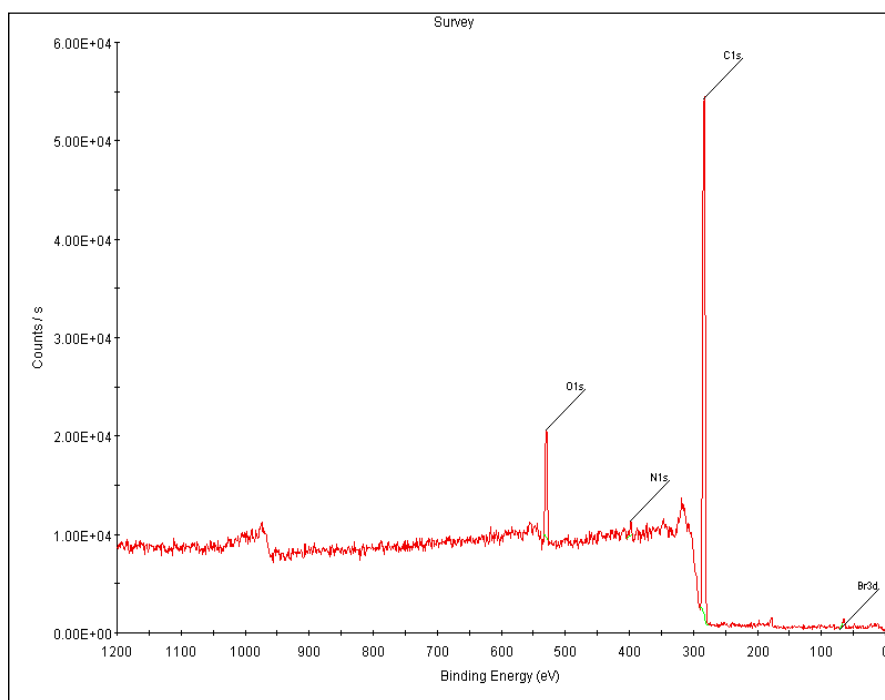
Name	Start	Peak	End	Height	FWHM	Area (P)	Area	At. %	SF
	BE	BE	BE	Counts	eV	CPS.eV	(N)		
Br3d	71.55	65.03	60.65	227.95	0.39	718.68	0.01	0.43	2.84
C1s	290.25	283.45	278.2	13073.41	3.98	52945.23	1.22	90.61	1
N1s	403.9	395.96	390	374.75	0	2112.21	0.03	2.03	1.8
O1s	536.35	529.84	523.5	3017.51	3.35	11532.04	0.09	6.93	2.93

Fig. 11. Wide range scan XPS data of IL-f-ND-2.

1.3.2. Gelation of Detonation Nanodiamonds

It has been found that the ND-1 formed a gel with a variety of ionic liquids (a–d in Figure 5A). For example, when 10 wt% of ND-1 was mixed thoroughly with [bmim][PF$_6$] for 5 min in an agate mortar and a pestle, all ionic liquid was trapped in ND-1 particles, affording gel, and no phase separation occurred after 1 min

centrifugation at 1200 rpm (a in Figure. 5A). However, in organic solvents such as MeOH and DMSO, the ND-**1** gels are fall-downed during centrifugation. Interestingly, yellowish ionic liquid solution was separated from 10 wt% of the imidazolium-functionalized IL-*f*-ND-**2** in [bmim][PF$_6$] after 1 min centrifugation (g in Figure 5A) implying that the IL-*f*-ND-**2** could easily be dispersed in ionic liquids. Due to the negligible volatility of ILs, the ionic ND-1 gels formed with [bmim][PF$_6$] were easy to process into any shape. Hence, by extrusion through a needle, it is possible to fabricate a cablelike material (Figure 5B) that is not easily torn apart and easy to handle.

First, to investigate the gelation of ND-**1** particles with ionic liquids, the 1.25~5 wt% of ND-**1** particles with ionic liquids were ground for 15 min in an agate mortar and a pestle. During this time the suspension turned viscous, affording a gel. Centrifugation at 13000 rpm for 3 h, the gel and ionic liquid phases were clearly separated from each other. However, under this condition, it does not take a lot of fine ND particles to gel, and showed pony-tail gel as shown in following photos. A suspension of ND-**1** (5 mg) in [bmim][NTf$_2$] (Figure 6. 100 mg, 200 mg, 300 mg, 400 mg, and 500 mg, from left to right) was mixed in an agate mortar with a pestle for 15 min, and centrifuged at 13000 rpm for 3 h. For other ionic liquids, 100mg, 200 mg, and 300 mg of ionic liquid, were used (from left to right).

However, The ND-**1** particles (2, 5, 7, and 10 wt%) in [bmim][PF$_6$] were ground for 5 min, and the resulting gel was centrifuged at 1200 rpm for 1 min, in which only the 10 wt% concentration of ND-**1** can trap all ionic liquid. A

43

suspension of 2 wt%, 5wt%, 7wt%, and 10wt% of ND-**1** (from left) in [bmim][PF$_6$] was mixed in an agate mortar with a pestle for 5 min, and centrifuged at 1200 rpm for 1 min.

Transmission electron microscopy (TEM) imaging of the ND gel formed with different ionic liquids revealed ionic liquid-coated ND islands consisting of ND particles with an average size of 10 nm (Fig. 8). This suggests that the formation of ND gels with ILs may be related to the characteristic polar surface groups of detonation ND-**1** such as hydroxyl or carboxylic acid functions,[10] which may have ionic interactions with the polar ionic liquid.
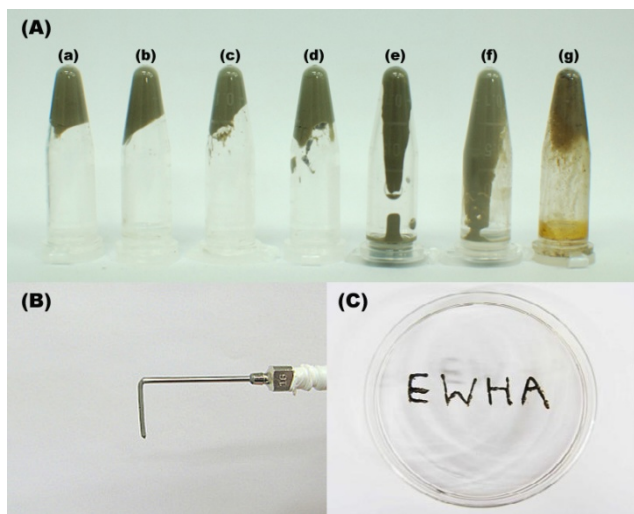
Fig. 12. Photographs of the ND-1 gels A) Photographs of the gels formed from 10 wt% of ND-1 in (a) [bmim][PF$_6$], (b) [bmim][NTf$_2$], (c) [bmim][SbF$_6$], (d) [bmim][BF$_4$], (e) MeOH, and (d) DSMO, and IL-*f*-ND-2 in [bmim][PF$_6$] (B) Extrusion of the ND-1 gel with [bmim][PF$_6$] from a needle, (C) letters written with the ND-1 gel.

[bmim][NTf$_2$]	[bmim][SbF$_6$]
[BMIM][PF$_6$]	[BMIM][BF$_4$]
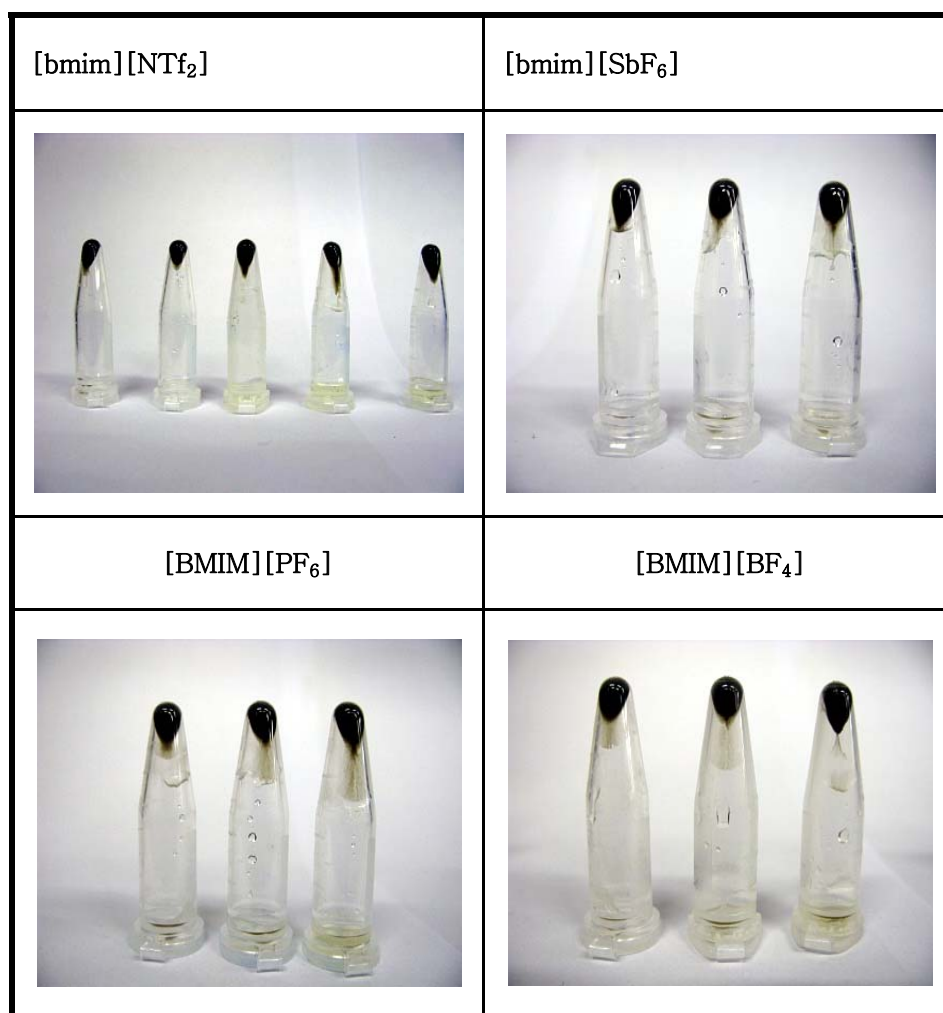
Fig. 6. Photographs of the ND-1 gels formed with different ionic liquids after centrifugation at high speed (13000 rmp) for 3 h.

Fig. 7. Photographs of the ND-1 gels formed with [bmim][PF$_6$]
after centrifugation at low speed (1200 rmp) for 1 min.
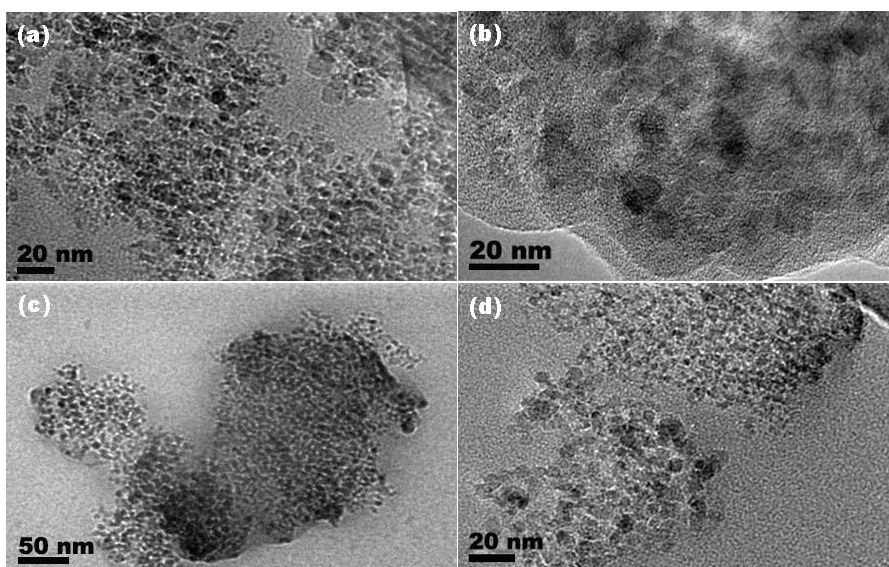
Fig. 8. TEM images of ND-1 gel with (a) [bmim][PF$_6$], (b) [bmim][NTf$_2$],
(c) [bmim][SbF$_6$], (d) [bmim][BF$_4$].

1.3.3. Solution behaviors of ND-1 and IL-*f*-ND-2 in different ionic liquids

The ND particles are not free from each other, but are glued together
possibly due to secondary ordering of the ionic liquids via interionic interactions.

Accordingly, the ND-**1** is well suspended in ionic liquids to form a homogeneous yellowish ND-**1** solution appenently (Fig. 9A). After being left to stand at room temperature for 24 h, only the ND-**1** particles in the most hydrophobic ionic liquid [bmim][NTf$_2$] precipitated (Figure 9B(b)). Similar solution behaviors were also observed with the imidazolium bromide-functionalized IL-*f*-ND-**2** in ionic liquids (Figure 9C). Therefore, the imidazolium-functionalized IL-*f*-ND-**2** were also well suspended in all ILs, where precipitation was again observed after 24 h in [bmim][NTf$_2$] (Fig. 9D (c)). However, the settling forces between ND-particles are still high enough to overcome the Brownian motion in ionic liquid, and thus, most of the ND particles were precipitated after 3 days.
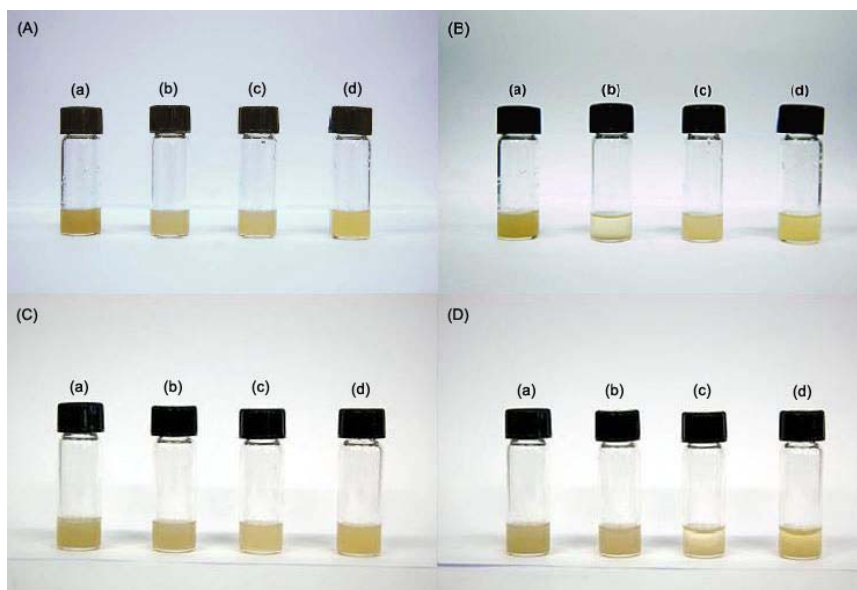
Fig. 9. Photos for the solution of ND-**1** and IL-*f*-ND-**2** in different ionic liquids

1.3.4. Size distribution of Nanodiamonds

The dynamic diameters of ND-**1** and imidazolium bromidefunctionalized IL-

f-ND-**2** were examined by dynamic light scattering (DLS) method (Figure. 10).
When we used DLS, 3~4 drops of solution, which was prepared by mixing of ND-**1**
or IL-*f*-ND-**2** (1.0 mg) with an ionic liquid (1.0 mL) was diluted with ionic liquid
(2.0 mL), and measured by DLS using laser irradiation.

As shown in Figure 10a, the ND-**1** in the ILs showed a smaller size of
dynamic diameters than the particles in water. In particular, the dynamic diameter
of ND-**1** in [bmim][PF$_6$] was smaller than in the other ionic liquids: 27 nm in
[bmim][PF$_6$], 49 nm in [bmim][BF$_4$], 57 nm in [bmim][SbF$_6$], and 105 nm in
[bmim][NTf$_2$]. In contrast, the hydrodynamic diameter of ND-**1** in water appeared
as a multimodal size-distribution with approximately 7 mm. Interestingly, the
imidazolium bromide-functionalized IL-*f*-ND-**2** showed an almost uniform diameter
with 5 nm in a relatively hydrophilic ionic liquid, [bmim][BF$_4$] (Fig. 13b, red line).
The size of IL-*f*-ND-**2** in a hydrophobic ionic liquid, [bmim][NTf$_2$], was smaller
(11 nm) than in [bmim][PF$_6$] (30 nm) and [bmim][SbF$_6$] (71 nm). The
hydrodynamic diameter of IL-*f*-ND-**2** in water was also smaller than that observed
with ND-**1**, which resulted in a mean diameter of 1 mm.

TEM analysis of the IL-*f*-ND-**2** dispersed [bmim][BF$_4$] showed smaller
IL-*f*-ND-**2** islands (Fig. 11a) compared to the ND-**1** islands formed in water (Fig.
11b). The IL-*f*-ND-**2** particles can be spin-coated onto a silicon wafer as indicated
by the AFM measurements (Fig. 11c). These suggest that surface functionalization
with imidazolium salts has a positive influence on the dispersion of nanodiamonds
in imidazolium-based ionic liquids.
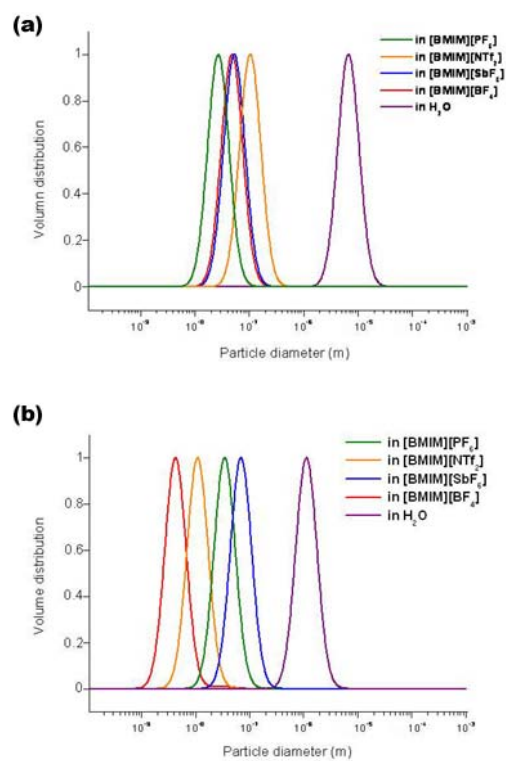
Fig. 10. Size distribution of Nanodiamond
(a) detonation ND-1 and (b) IL-*f*-ND-2 in ionic liquids and water.
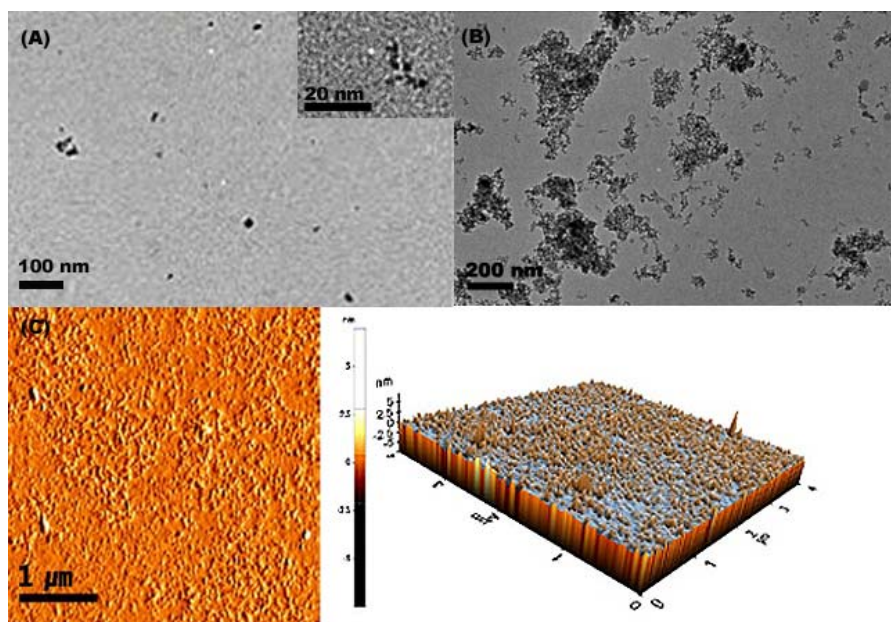
Fig. 11. TEM images of imidazolim bromide-functionalized IL-*f*-ND-2 in (a) [bmim][BF₄],

(b) in water, and (c) AFM image of spin-coated IL-*f*-ND-2 on a silicon wafer.

.

In summary, we investigated the synthesized surface functionalized IL−*f*−ND. We have covalently functionalized the Nanodiamonds (ND) with imidazolium bromide, gelated with ionic liquids, and investigated the effect on the solution behaviors of functionalized NDs. These features of nanodiamonds in ionic liquids suggest a variety of new possibilities for soft composite materials made from nanodiamonds. Further studies on the utilization of ionic gels to enhance the potentials of nanodiamonds are currently underway.

1.4 Personnel supported

1) Sang-gi Lee: Principal investigator, Professor (Ewha Womans University).

2) Yu Sung Chun: Co-investigator, Ph. D.(Ewha Womans University).

3) Ju Yeon Shin: Co-investigator, Ph. D. candidate (Ewha Womans University).

4) Cho-Long Park: Co-investigator, master's degree(Ewha Womans University).

1.5 Publications

1. Cho-Long Park, Ah Young Jee, Minyung Lee, Sang-gi Lee, "Gelation, Functionalization and solution behaviors of nanodiamonds with ionic liquids", Chemical communications, 5576-5578 (2009).

2. Ji Woong Lee, Ju Yeon Shin, Yu Sung Chun, Hyeong Bin Jang, Choong Eui Song, and Sang-gi Lee, "Toward understanding the origin of positive effects of ionic liquids on catalysis: Formation of more reactive catalysts and stabilization of reactive intermediates

and transition states in ionic liquids" Accounts of Chemical Research, 985-994 (2010)

1.6 Presentation

1. Ju Yeon Shin, Cho-Long Park and Sang-gi Lee, "Preparation of ionic Nanomaterials and Their application in Catalyst immobilization", International Symposium on Catalysis and Fine chemicals. Seoul, Korea (2009, 12/13-17)

2. Cho-Long Park, Ah Young Jee, Minyung Lee and Sang-gi Lee, "Gelation, Functionalization and solution behaviors of Nano diamonds with ionic liquids", The 3rd International Student Conference on Advanced Science and Technology, Seoul, Korea (2009, 12/11-12)

3. Cho-Long Park, Ah Young Jee, Minyung Lee and Sang-gi Lee, "Ionic Nanodiamond : Surface Functionalization of Nanodiamond with ionic liquids", The 103th spring meeting of the Korean chemical society, Seoul, Korea(2009, 4/16-17)

4. Cho-Long Park and Sang-gi Lee, "Ionic Nanodiamond : Surface Functionalization of Nanodiamond with ionic liquids" [Oral presentation] Organic chemistry 4 universities united workshop, Yangpyung, Korea (2009, 1/8-9)

Chapter 6

Title: **SiGe Alloy Nanowire Photonics**

Final Report

PI:
Korean PI: Prof. Moon-Ho Jo, Department of Materials Science and Engineering, POSTECH,
San 31, Hyoja-Dong, Nam-Gu, Pohang, Kyungbuk, 790-784, Korea
US PI: Prof. Hongkun Park, Department of Chemistry and Chemical Biology, Harvard University,
12 Oxford Street, Cambridge, MA 02138, USA

1. Objectives

   This research program is motivated by the clear demand for the development of photonic devices based on silicon that is the most prevailing material in modern electronics, particularly for the development of efficient light-emitters. The ultimate goal of this research is to develop prototype photonic/optoelectronic devices based on group IV semiconductor nanowires by providing a fundamental understanding of charge transport and photon emission/absorption from $Si_{1-x}Ge_x$ nanowires and their heterostructures.
   The joint research program of this international collaboration among three institutions includes:
- To synthesize optically active $Si_{1-x}Ge_x$ alloy nanowires and their quantum heterostructures (POSTECH)
- To characterize crystal and electronic structures of $Si_{1-x}Ge_x$ nanowire heterostructures (Seoul National University)
- To investigate the interplay between electron charge transport and photon emission processes in individual $Si_{1-x}Ge_x$ nanowire heterostructres. (POSTECH & Harvard University)

2. Status of effort

- Uniqueness:
- Energy tunable Si photonic elements by Si:Ge alloying and size-effects from nanowire geometries
- Electrically driven group IV semiconductor plasmonic elements exploiting one-dimensional structures

- Approaches:
- Controlled growth of group IV semiconductor nanowires and their heterostructures
- Spatially and spectrally resolved optoelectronic/plasmonic measurements on individual nanowires

- Progress in Phase I:
- Group IV semiconductor nanowires (Growth and Photonics): (3 Nano Letters, 2 Advanced Materials, 2 Applied Physics Letters)
- QD-Nanowire plasmonics: 1 Joint paper (1 Nature Physics)
- II-VII semiconductor nanowire optoelectronics: 1 Publication (1 Nano Letters)

- Perspectives for Phase II:
- Integrated Nano Optoplasmonics based on Group IV semiconductor nanowire heterostructures

3. Abstract

- We exploited energy band-gap engineering in one-dimensional $Si_{1-x}Ge_x$ alloy nanocrystals, where the electron-hole pairs can be electrically generated and the tunable emission energy range by Si:Ge alloying is appropriate in the industrially relevant range. Specifically we fabricated the optoelectronic device with an individual nanowire, operating at the fiber optic communication range by investigating electrically driven light-emission from $Si_{1-x}Ge_x$ alloy nanowires (*Applied Physics Letters* **92**, 263111 (2008)).

• We demonstrated highly efficient photoresponsivity of Ge NWs, arising from inherent size-effects of internal gain in one-dimensional semiconductor media, using a scanning optical probe technique. It is revealed that the highest internal gain of ~103 from the thinnest Ge NWs is attributed from strong photo-gating effects by the surface-trapped minority electrons and efficient carrier transport the hole drift. The photo detection efficiency can be measured in terms of the internal gain and the response time, both of which are related to the carrier life time, and in general there is a trade-off between gain and speed.

• In collaboration with the US PI, optoplasmonic circuits were also realized in which plasmons should be generated, manipulated, and detected on chip via near-field coupling without involving far-field radiation. The operation of such optoplasmonic circuits is challenging because it requires frequency conversion of electrical signals between conventional low frequency electronics and high (optical) frequency charge excitations. This near coupling is an essential prerequisite for realizing a truly nanoscale, integrated quantum plasmonic circuit (*Nature Phys.* **5**, 475 (2009)).

• A novel approach to develop prototype photonic/optoelectronic devices based on semiconductor nanowires in this research suggests implications in a wide variety of novel photonic applications, such as nanoscaled optical signal processing, sensing and imaging devices. In particular, this emerging concept of all-electrical manipulation of photons at the nanometer scale in this work is expected to provide a basal link between conventional optical communication components and nanoelectronic ones for data transmission and processing, thus its relevance to both optical and microelectronic technology are not exhaustively limited.

4. Personnel Supported

Name	Affiliation	Position (Status)	Starting Date	Participating Ratio (%)
	Department	Final Degree	Completion Date	
Korean Laboratories				
Moon-Ho Jo	POSTECH	Assistant Professor	20070301	20 %
	MSE	Ph.D	20100228	
Miyoung Kim	SNU	Assistant Professor	20070301	20 %
	MSE	Ph.D	20100228	
Jee-Eun Yang	POSTECH	Doctoral Course	20070301	20 %
	MSE	M.S.	20100228	
Jong-Myeong Jeon	SNU	Doctoral Course	20070301	20 %
	MSE	M.S.	20100228	
Cheol-Joo Kim	POSTECH	Doctoral Course	20070301	20 %
	MSE	M.S.	20100228	
Hyun-Seung Lee	POSTECH	Doctoral Course	20070301	30 %
	MSE	M.S.	20100228	
Dong An Kim	POSTECH	Master Course	20090301	10 %

	MSE	B.S.	20100228	
Sunyoung Yoo	POSTECH	Master Course	20090301	10 %
	MSE	B.S.	20100228	
US Laboratory				
Hongkun Park	Harvard U	Professor	20070301	20 %
	Chemistry/Physics	Ph.D	20100228	
Abram Falk	Harvard U	Doctoral Course	20070301	20 %
	Chemistry/Physics	B.S.	20100228	

5. Publications

1) "Near-field electrical detection of optical plasmons and signle-plasmon sources", Abram L. Falk, Frank H. L. Koppens, Chun Yu, Kibum Kang, Nathalie de Leon Snapp, Alexey V. Akimov, Moon-Ho Jo, Mikhail D. Lukin, and Hongkun Park, *Nature Physics 5, 475* (2009).

2) "Atomic structure of conducting nanofilaments in TiO2 resistive switching memory", Deok-Hwang Kwon, Kyung Min Kim, Jae Hyuck Jang, Jong-Myeong Jeon, Min Hwan Lee, Gun Hwan Kim, Xiang-Shu L, Gyeong-Su Park, Bora Lee, Seungwu Han, Miyoung Kim & Cheol Seong Hwang, *Nature Nanotechnology* 5, 148 (2010)

3) "Directionally integrated VLS nanowire growth by the local temperature gradient", Geunhee Lee, Yun Sung Woo, Jee-Eun Yang, Donghun Lee, Cheol-Joo Kim and Moon-Ho Jo, *Angewandte Chemie Int Ed.*, 48, 7366 (2009).

4) "Vertically aligned Si intra-nanowire p-n diodes by large-area epitaxial growth", Cheol-Joo Kim, Donghun Lee, Hyun-Seung Lee, Geunhee Lee, Gil-Sung Kim and Moon-Ho Jo, *Applied Physics Letters*. 94, 173105 (2009).

5) (Invited Review Paper) "Unconventional roles of metal catalysts in chemical-vapor syntheses of single-crystalline nanowires", Kibum Kang, Cheol-Joo Kim and Moon-Ho Jo, In press, *Journal of Applied Physics* (2009).

6) (Invited Review Article) "Massive integration of inorganic nanowire-based structures on solid substrates for device applications", Kwang Heo, Cheol-Joo Kim, Moon-Ho Jo and Seunghun Hong, *Journal of Materials Chemistry*, 19, 901 (2009).

7) "Large-Scale Assembly of Silicon Nanowire-based Integrated Devices using Conventional Microfabrication Facilities", Kwang Heo, Eunhee Cho, Jee-Eun Yang, Hee-Chul Han, Minbaek Lee, Byung Yang Lee, Moon-Sook Lee, Moon-Ho Jo, Heon-Jin Choi and Seunghun Hong, *Nano Letters*, 8 4523 (2008).

8) "Electricallly driven light emission from individual CdSe nanowires" Y. J. Doh, K. N. Maher, L. Ouyang, C. L. Yu, H. Park, and J. Park, *Nano Letters* 8, 4552 (2008).

9) "Self-organized growth of Ge nanowires from Ni-Cu bulk alloys", Kibum Kang, Gil Ho Gu, Dong An Kim, Chan Gyung Park and Moon-Ho Jo, *Chemistry of Materials*, 20 (21) 6577 (2008).

10) "Low-Temperature Deterministic Growth of Ge Nanowires Using Cu Solid-Catalysts", Kibum Kang, Dong An Kim, Hyun-Seung Lee, Cheol-Joo Kim, Jee-Eun Yang and Moon-Ho Jo, *Advanced Materials* 20 4684 (2008).

11) "Axially graded heteroepitaxy and Raman spectroscopic characterizations of Si1-xGex nanowires", Jee-Eun Yang, Won-Hwa Park, Cheol-Joo Kim, Zee Hwan Kim, and Moon-Ho Jo, *Applied Physics Letters* 92, 263111 (2008).

12) "The Role of NiO Overlayers on Spontaneous Growth of NiSix Nanowires from Ni Seed Layers", Kibum Kang, Sungkyu Kim, Cheol-Joo Kim, and Moon-Ho Jo, *Nano Letters* 8 431 (2008).

13) "Low-Temperature Deterministic Growth of Ge Nanowires Using Cu Solid-Catalysts", Kibum Kang, Dong An Kim, Hyun-Seung Lee, Cheol-Joo Kim, Jee-Eun Yang and Moon-Ho Jo, *Advanced Materials* 20 4684 (2008).

14) "Fabrication of $Si_{1-x}Ge_x$ alloy nanowire field-effect transistors", Cheol-Joo Kim, Won-Hwa Park, Jee-Eun Yang, Hyun-Seung Lee, Sunglyul Maeng, Zee Hwan Kim, Hyun M. Jang and Moon-Ho Jo, *Applied Physics Letters* 91, 033104 (2007).

Representative Publications:

6. Interactions
(a) Participation/presentations at meetings, conferences, seminars, etc.

Korean PI:
1) "Vectorially integrated VLS nanowire growth in the local temperature gradient", Geunhee Lee, The 6th International Conference on Advanced Materials and Devices (December 9~11, 2009, Jeju, Korea)
2) "Internal Gain in Ge Nanowire Field-Effect Transistors with Axially Modulated Charge Trap Density", Hyun-Seung Lee, 2009 Materials Research Society Fall Meeting (Nov 30 - Dec 4 2009, Boston, USA)
3) "Vertical Si intra-nanowire p-n diodes by large-area epitaxial growth", Cheol-Joo Kim, 2009 Materials Research Society Fall Meeting (Nov 30 - Dec 4 2009, Boston, USA)

4) "Broadband photovoltaic effects in axially composition-graded Si1-xGex nanowires", Cheol-Joo Kim, 2009 Materials Research Society Fall Meeting (Nov 30 - Dec 4 2009, Boston, USA)

5) The 3rd AEARU Advanced Materials Science Workshop at POSTECH, Korea (Nov. 11-13, 2009)

6) Group IV Semiconductor Nanowire Optoelectronics, Cheol-Joo Kim, (Oct 6 2009, The 216th Electrochemical Society Meeting - Vienna, Austria)

7) Moon-Ho Jo The 11th NRS Co-organizer, Nano Korea 2009 & The 11th Nanowire Research Society Meeting (Aug 27 -29 2009, KINTEX, Korea)

8) "Si:Ge Alloy Nanowire Optoelectronics", Cheol-Joo Kim, AWAD 2009 (2009 Asia-Pacific Workshop on Fundamentals and Applications of Advanced Semiconductor Devices, Busan, Korea, June 24-26),

9) "SiGe Nanowire Photonics", Moon-Ho Jo, Joint Symposium of the 8th US-Korea workshop on Nanostructures Materials & the 6th US-Korea Workshop on Nanoelectronics, (19-20 May 2009, Seoul)

10) "Si Nanowire Optoelectronics", Moon-Ho Jo, The 6th Korea-US Nano Forum (LA, 4/28-30, 2009)

11)"Low-Temperature Deterministic Growth of Ge Nanowires Using Cu Solid Catalysts", Kibum Kang, 2009 Materials Research Society (MRS) Spring Meeting (San Francisco, 4/21-4/25, 2009)

12) "Vertically-Aligned, p-i-n Core-Shell Si Nanowires by Large-Area Epitaxy for Photovoltaic Applications", Geunhee Lee, 2009 Materials Research Society (MRS) Spring Meeting (San Francisco, 4/21-4/25, 2009)

13) "Group IV Nanowire Optoelectronics", Moon-Ho Jo (Symposium VIII: Emerging Semiconductor Technologies, Shanhai, China March 17-19, 2009)

14) "Group IV Semiconductor Optoelectronics", Moon-Ho Jo, (International Symposium on Surface and Nano Science 2009, Jan. 27-30, 2009, Shizukuishi, Japan)

15) "A Brief Technological Perspective of Bottom-up Nanowires for Industrial Applications", Moon-Ho Jo, Nano Korea 2008 and The 9th Nanowire Research Society Meeting, (KINTEX, Korea Aug 29 2008)

16) "Electrical Detection of Surface Plasmons in the Near Field", Abram L. Falk, 2008 Gordon conference Plasmonics, Optics At The Nanoscale (U.S.A, Jul 27 - Aug 1 2008)

17) "Growth and optical characterizations of Si:Ge alloy nanowires for photonic applications", Jee-Eun Yang, NMDC 2008 (Kyoto, Japan, Oct 21 2008)

18) "Low temperature deterministic growth of Ge nanowires using solid Cu catalysts", Kibum Kang, NMDC 2008 (Kyoto, Japan, Oct 22 2008)

19) "Self-organized Growth of Ge Nanowires from NiCu Bulk Alloys", Kibum Kang, The 9th Asia-Pacific Microscopy Conference (Jeju, Korea, Nov 06 2008)

20) "Unconventional roles of catalysts in chemical-vapor syntheses of single-crystalline nanowires", Moon-Ho Jo, ICPS-2008 (Rio De Janeiro, Brazil, Jul 27 - Aug 1 2008)

21) "Growth and optical characterizations of Si:Ge alloy nanowires for photonic applications", Cheol-Joo Kim, ICPS-2008 (Rio De Janeiro, Brazil, Jul 27 - Aug 1 2008)

22) "Bottom-up semiconductor nanowires: materials syntheses and device developments", Moon-Ho Jo, IEEE EDS/MTT-S/SSCS (Taegu, Korea, May 14 2008)

23) "SiGe Nanowire Photonics", Moon-Ho Jo (Nanomaterial for Defense Conference (US Department of Defence) & 7th The US-Korea Workshop on Nanostructured Materials & 5th US-Korea Workshop on nanoelectronics, (Arlington, U.S.A, Apr 24 - 25 2008))

24) "Axial Modulation Doped Si Nanowire Field-Effect Transistors", Cheol-Joo Kim, 2008 Materials Research Society (MRS) Spring Meeting, (San Francisco, U.S.A, Mar 27 2008)

25) "Axially Composition-Modulated Si1-xGex Nanowires and Their Scanning Raman Scattering Imaging", Jee-Eun Yang, 2008 Materials Research Society (MRS) Spring Meeting, (San Francisco, U.S.A, Mar 27 2008)

US PI:
- "Optoplasmonic engineering of light-matter interactions," Physical Chemistry Seminar, University of California, Berkeley, CA, March 2010
- "Optoplasmonic engineering of light-matter interactions," Center for Ultracold Atoms Seminar, Massachusetts Institute of Technology, Cambridge, MA, December 2009

- "Capturing light with plasmonic circuits," Canadian Institute for Advanced Research Nanoelectronics Program, Quebec City, Canada, November 2009
- "Optoplasmonic engineering of light-matter interactions," Institute of Physics Seminar, Chinese Academy of Sciences, Beijing, China, October 2009
- "Nanostructure-based optoelectronics and plasmonics," Conference on Lasers and Electro-Optics and the International Quantum Electronics Conference, Baltimore, MD, June 2009
- "Capturing light quanta with plasmonic nanowires," US-Korea Workshops on Nanomaterials & Nanoelectronics, Seoul, Korea, May 2009
- "Capturing light and poking neurons," Micro/Nano Seminar Series, Massachusetts Institute of Technology, Cambridge, MA April 2009
- "Capturing light," Chemistry Seminar, University of Wisconsin, Madison, WI, October 2008
- "Capturing light and poking cells using nanowires," Institutional Seminar, KIST, Seoul, Korea, October 2008
- "Capturing light," Max Planck Society-Korea Joint Symposium, POSTECH, Pohang, Korea, October 2008
- "Detection of single plasmons," Gordon Research Conference, Tilton, NH, July 2008
- "Nanostructure-based optoelectronics, plasmonics, and bio-electronic interfacing," French-American Young Engineering Scientists Symposium, Washington, DC, July 2008
- "Capturing light: fundamental investigations of optoelectronic and plasmonic devices," Materials and Structures for Energy Workshop, Harvard University, Cambridge, MA, May 2008
- "Single-nanostructure electronics, optoelectronics, and plasmonics," ACS National Meeting, New Orleans, LA, April 2008
- "Nanostructured Materials," Subpanel Co-Chair, ACS National Meeting, New Orleans, LA, April 2008
- "Single-nanostructure electronics, optoelectronics, and plasmonics," Chemical Biology Seminar, Cornell University, Ithaca, NY, April 2008
- "Single-nanostructure electronics, optoelectronics, and plasmonics," Materials Science and Engineering Colloquium, Stanford University, Stanford, CA, February 2008
- "Single-nanostructure electronics, optoelectronics, and plasmonics," ULTRA Program Workshop, Jeju, Korea, December 2007
- "Electronics, optoelectronics, and plasmonics based on individual nanostructures," Chemical Physics Seminar, California Institute of Technology, Pasadena, CA, October, 2007
- "Chemically grown nanostructures for optoelectronic applications: synthesis, characterization, and incorporation into device test beds," Keynote Presentation, SPIE Optics East Nanomaterials Synthesis, Interfacing, and Integrating in Devices, Circuits, and Systems II, Boston, MA, September 2007
- "Optoelectronic properties of chemical nanostructures," Joint Symposium of 6th US-Korea Workshop on Nanostructured Materials & 4th US-Korea Workshop on Nanoelectronics, Seoul, Korea, June 2007
- "Single-nanostructure electronics, optoelectronics, and plasmonics," Physics and Astronomy Department, University of California, Riverside, Riverside, CA, May 2007

Collaborative Team Efforts and Researcher Exchange:

- Year 2007

1) Program kick-off meeting: June 4-5 2007, Seoul Korea by both KPI and USPI
2) The 1st Research training of a graduate student (Cheol-Joo Kim from KPI) at the USPI Lab: Jul 19-27 2007
: Collaboratively developed and bench-marked individual nanowire optoelectronic measurement set-ups:
3) The 1st Team Meeting: Jul 19-21 2007, Harvard University, US
4) US researcher (Dr Myung-Han Yoon from USPI) visit to KPI's Lab: Nov 13 2007
5) The 2nd Team Meeting: Dec 4-7 2007, Seoul, Korea
6) The 2nd Research training of a graduate student (Hyun-Seung Lee from KPI) at the USPI Lab: May - Jul 2008

- Year 2008

1) Review Meeting (Apr 24-25 2007, Arlington, US) by both KPI and USPI

2) The 3rd Team Meeting (Aug 07-08 2008, Seoul, Korea) by both KPI and USPI

4) The 4th Team Meeting (Nov 08-09 2008, Pohang, Korea) by both KPI and USPI

5) The 3rd Research training of a graduate student (Hyun-Seung Lee from KPI) at the USPI Lab: Jun 06 - Sep 07 2008; Collaboratively characterized photoconductivity of Si1-xGex nanowire devices

- Year 2009

1) A joint publication came out: "Near-field electrical detection of optical plasmons and signle-plasmon sources", Nature Physics, 5, 475 (2009).

2) The 2nd Year Review Meeting (Hanyang Univ., Seoul Korea) with both PIs' participation

3) The 5th Team Meeting at KPI's Lab: May 28. 2009

4) The 6th Team Meeting (Seoul Korea): Nov. 15. 2009

5) The 4th Research training of graduate students (Cheol-Joo Kim and Hyun-Seung Lee from KPI) at the USPI Lab: Dec. 1-2. 2009

(b) Describe cases where knowledge resulting from your effort is used, or will be used, in a technology application. (Not all research projects will have such cases, but please list any that have occurred.)

- None.

7. Inventions

(a) List discoveries, inventions, or patent disclosures. (If none, report None.).

- None.

(b) Complete the attached **"DD Form 882, Report of Inventions and Subcontractors."**

- None.

8. Honors/Awards

1) Best Research Award of 2009 (National Research Foundation of Korea)

2) Best Research Award of 2007 (Korean Research Foundation)

9. Archival Documentation

- None.

10. Software and/or Hardware

- None.

Final Report

Self-Assembled Liquid Crystalline Gels:
From nanostructure to function

Julia A. Kornfield
jak@cheme.caltech.edu
California Institute of Technology
Chemical Engineering Department
Mail Code 210-41
1200 E. California Boulevard
Pasadena, CA 91125, USA
(626) 395-4138

Objectives:

Motivation to Discover Nanostructure of Self-Assembled LC Block Copolymers:
Exquisite control of the material properties of liquid crystalline gels and liquid crystal
interfaces can be achieved by adjustment of the molecular parameters of block
copolymers that couple a side-group liquid crystalline polymer with a random coil
polymer. The choice of coil domain and its length dictate the conditions under which the
end-blocks will associate in a given LC host, producing micelles or vescicles. Using
electron microscopy and neutron scattering, our objective is to characterize and control
these aggregate structures, which provide exceptionally uniform, single-phase gels.
Technologically, deeper understanding of these new self-assembled LC gels can be used
to increase the switching speed and sensitivity of the material. SGLCP-coil block
copolymers are also interfacially active and the NBIT collaboration is the first study of
this area of physics and materials science. Specifically, our objective is to illustrate the
important phenomena associated with self-assembly of SGLCP-coil diblocks at LC-air
and LC-water interfaces.

Status of Effort:

Collaborative research between KNU and Caltech on new materials formed from block
copolymers and small molecule liquid crystals (LC) during our AFOSR-MOST
collaboration has included work at Caltech on:

- A bottom-up approach to studying side-group liquid crystal block copolymer
  behavior by first analyzing the structure and conformations of dilute solutions of
  side-group liquid crystalline (SGLCP) homopolymers with different modes of
  attachment ("end-on" and "side-on," to guide the design of future block
  copolymers for different applications.
- Exploration of the self-assembly of coil-LC diblock copolymers in small molecule
  LC solvent.
- Begun a long-reaching project with an end goal of rationally designing smart
  materials that are stimuli-responsive at LC interfaces.

These results and their relationship to our overarching goals are described below (see
Archival Documentation).

Abstract:

Polymers that include a side-group liquid crystalline polymer (SGLCP) domain are
examined in solution, dissolved in a small molecule liquid crystal (LC), and at interfaces,
particularly LC-water interfaces. Systematic changes in the molecular structure revealed
the physics of self-assembly from the bottom up: first, homopolymer SGLCPs were used
to establish the effects of chain length and LC order on chain dimensions in solution; then,
diblocks of a random coil polymer and an SGLCP ("coil-SGLCP diblocks") were used to
understand self-assembly in LC solution; and, finally, responsive coil-SGLCP diblock
copolymers were used to understand reconfiguration of the polymer monolayer at an LC-
water interface in response to stimuli in the aqueous phase. To control the molecular
structure of the polymers, two complementary synthetic approaches were used: polymer
analogous synthesis (Caltech) and Radical Addition Fragmentation chain Transfer

(RAFT) polymerization (Kyungpook University). When dissolved in an LC, coil-SGLCP diblocks show a surprisingly strong tendency to form vescicles (rather than micelles). At water-LC interfaces, coil-SGLCP diblocks were shown to mediate responsive changes in the orientation of the LC as a whole, providing an easily detected response to changing conditions. The interfacial switching follows from the known behavior of the responsive coil domain (such as pH induced expansion/collapse of polyacrylic acid, PAA). Proof-of-principle measurements showed that protein binding by the coil domain can be transduced into LC reorientation, inspiring the design of water soluble domains with highly specific interactions (e.g., RNA aptamers).

Personnel Supported:

Julia A. Kornfield (PI), Zuleikha Kurji (Graduate Student), Paul Pirogovsky (Graduate Student)

Publications:

Work from our AFOSR-MOST collaboration has been published in the following publications:

Scruggs, Neal R; Verduzco, Rafael; Uhrig, David; Khan, Waliullah; Park, Soo-Young; Lal, Jyotsana; Kornfield, Julia A. MACROMOLECULES (2009), 42, "Self-Assembly of Coil/Liquid-Crystalline Diblock Copolymers in a Liquid Crystal Solvent."

Lee, Dong-Yul; Seo, Jung-Min; Khan, Waliullah; Kornfield, Julia A; Kurji, Zuleikha. SOFT MATTER (2010), 6, "pH-Responsive Aqueous/LC Interfaces Using SGLCP-*b*-Polyacrylic Acid Block Copolymers."

Interactions:

Invited talks:
Julia A. Kornfield:
- 2008 SPIE Liquid Crystals Conference XII: "Nematic gels via self-assembly of block copolymers."
- 2009 Hougen Symposium on Frontiers of Liquid Crystals: "Self Assembly of Coil-LCP Block Copolymers in Nematic LCs and at LC-Air Interfaces."
- May 2009 - Seoul National University, "Molecular Aspects of Flow-Induced Crystallization of Polymers"
- May 2009 - Kyungprook National University, "Molecular Aspects of Flow-Induced Crystallization of Polymers"
- 2009 Gordon Conference, Liquid Crystals: "Block Copolymer Assembly in and on Liquid Crystals."
- 2009 Invited talk, University of Colorado, Boulder: "Ordering Behavior of Dilute Liquid Crystal Polymer Solutions."

Student Attended Conferences:
- 2008 International Liquid Crystal Conference XXII: <u>Zuleikha Kurji</u>, Neal R, Scruggs, and Julia Kornfield: "Characterizing the Effect of Spacer Length on Side-Group Liquid Crystal Polymers."
- 2008 SPIE Liquid Crystals Conference XII – August 2-6, San Diego, CA
- 2008 International Materials Research Society Conference: <u>Zuleikha Kurji</u>, Neal R, Scruggs, and Julia Kornfield: "Characterizing the Effect of Spacer Length on Side-Group Liquid Crystal Polymers."
- US-Japan POLYMAT 2008 Summit, (*Presented by the ACS Division of Polymer Chemistry, Inc. and the Society of Polymer Science, Japan)*. <u>Zuleikha Kurji</u>, Neal R, Scruggs, and Julia Kornfield: "Characterizing the Effect of Spacer Length on Side-Group Liquid Crystal Polymers."
- 2009 Hougen Symposium on Frontiers of Liquid Crystals, <u>Zuleikha Kurji</u>, Neal R, Scruggs, and Julia Kornfield "Characterizing the Effect of Spacer Length on Side-Group Liquid Crystal Polymers."
- APS March Meeting 2010. <u>Rohan Hule</u>, Zuleikha Kurji, Paul Pirogovsky, Julia A. Kornfield. "Self-Assembly of Side Group Liquid Crystalline Block Copolymers in a Nematic Solvent."
- APS March Meeting 2010. <u>Paul Pirogovsky</u>, Zuleikha Kurji, Rohan Hule Julia A. Kornfield Anisotropic Conformation of a Side-Group Liquid Crystalline Polymer in an Isotropic Small Molecule LC Solvent."

Inventions:

None (Caltech)

Honors/Awards during the Period of the NBIT Project:

One Hundred Chemical Engineers of the Modern Era, AIChE Centennial Award   2008
National Science Foundation Special Creativity Extension   2008
Fellow, American Association for the Advancement of Science   2007

Archival Documentation:

Introduction

Side-group liquid crystal polymers (SGLCPs) are flexible-chain polymers that are functionalized with liquid crystalline (LC) side-groups. They exhibit unique properties that arise from the coupling of the orientational order inherent in the LC side group to the flexible backbone of the polymer.[12] In contrast to random coil polymers in good solvents, SGLCPs adopt an *<u>anisotropic</u>* conformation upon dissolution in a small-molecule LC because the side-group LC moieties couple locally to the director of the nematic solvent, leading to a synergistic ordering effect. Block copolymers with an SGLCP midblock and LC-phobic endblocks spontaneously form gels under conditions

that cause the end-blocks to reject the solvent; this gelation is reversible, opening new opportunities for processing the materials[3]. In contrast to *in-situ* polymerized networks, these physical gels are homogeneous systems, consequently the gels have exceptional clarity and sharp responses to stimuli such as temperature or electric field—overcoming two of the major deficiencies of prior LC elastomers and gels. Our collaboration addressed the need for structure-property relationships that connect the <u>molecular structures</u> of the polymer and LC solvent with the <u>nanostructure</u> that they spontaneously form, and between the nanostructure and <u>macroscopic properties</u>.

To this end, we begun our examination with SGLCP homopolymers, followed by detailed studies of the polystyrene-SGLCP diblock copolymers both in the bulk and at LC interfaces. Small angle neutron scattering, SANS, revealed two new and exciting phenomena in SGLCP homopolymers: long range order and a possible "pre-transitional effect." Our SANS studies on dilute solutions of coil-SGLCP diblock copolymers yielded informative results that we expect to publish upon completing our analyses, in the near future. Further analysis of these diblock copolymer solutions at LC interfaces is the beginning of a project that has proven to be important to both the Kornfield and Park groups' long term goals: the rational design of smart-LC materials.

SGLCP Homopolymers

To gain physical understanding of the self-assembly processes of coil-SLCP polymers in LC solution, we used a bottom-up approach: we not only studied coil-SGLCP diblock copolymers themselves, we also studied the structure and conformation of the SGLCP homopolymers in LC solvent to isolate the orientational behavior of the SGLCP blocks alone. We're able to further segregate the effects of the backbone from the LC side-groups using two families of SGLCPs with profoundly different orientational coupling between their liquid crystal mesogens and their polymer backbones. The first type of SGLCP, the "end-on" SGLCP (Figure 1a) adopts a mildly oblate conformation while the "side-on" SGLCP (Figure 1b) adopts a strongly prolate conformation[4]. By utilizing polymer analogous chemistry, we were able to produce end-on and side-on polymers with identical degrees of polymerization, allowing for rigorous comparison between the two families of orientations.
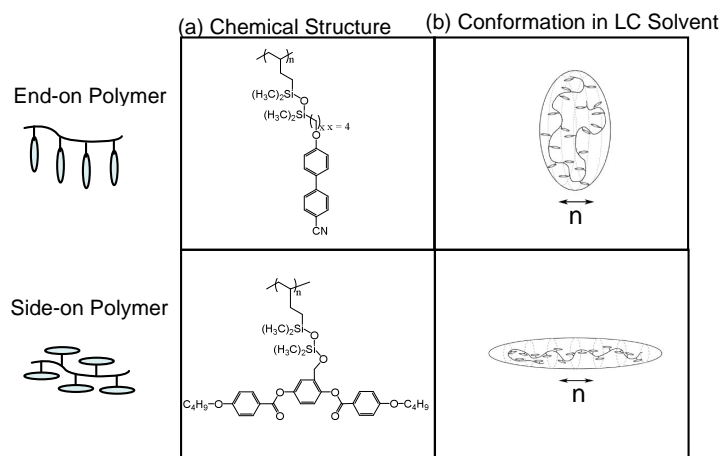
Figure 1. Our homopolymers have liquid crystalline side groups either terminally attached, or "end-on" (top) and laterally attached, or "side-on" SGLCP blocks (bottom). (a) The chemical structure of our polymers is shown here. (b) When dissolved in LC solvent, both types of polymer adopt anisotropic conformations.

The majority of our studies, both of homopolymer conformation and diblock nanostructures, uses small angle neutron scattering (SANS) which is ideal for studying the conformational behavior of polymers as well as the orientational behavior of SGLCPs. In particular, SANS is essential because the director fluctuations of the small molecule solvent prevents the use of light scattering and the lack of contrast between the polymer and the solvent precludes the use of SAXS, two common tools to investigate polymers. Our SANS studies revealed two exciting phenomena in dilute solutions of SGLCP homopolymers. First we saw an unprecedented type of chain-chain interaction mediated by the LC solvent, and, second, we noticed the persistence of nematic order inside the pervaded volume of the side-on SGLCPs *past* the nematic-isotropic transition temperature (T_{ni}).

Even Homopolymers Assemble In Long Range Structures.

Our previous SANS studies of our homopolymer solutions (at 5wt% polymer in small molecule LC) in an aligned nematic phase show 2D SANS patterns characteristic of oblate ($R_{\parallel}/R_{\perp} \approx 1.6$) ellipsoidal conformation for the end-on SGLCP (Figure 2a, top) and prolate($R_{\parallel}/R_{\perp} \approx 4.5$) for the side-on homopolymers (Figure 2a, bottom)[5]. The dimensions deduced from these patterns showed that the coils were overlapping, which motivated our recent experiments at still lower concentrations, to determine the

dimensions of the individual coils. The 2D SANS patterns obtained at 1wt% polymer and confirmed by 0.5wt% polymer experiments, yielded a surprising new feature: an intense streak oriented along the director which is very strong at low q (Figure 2b).
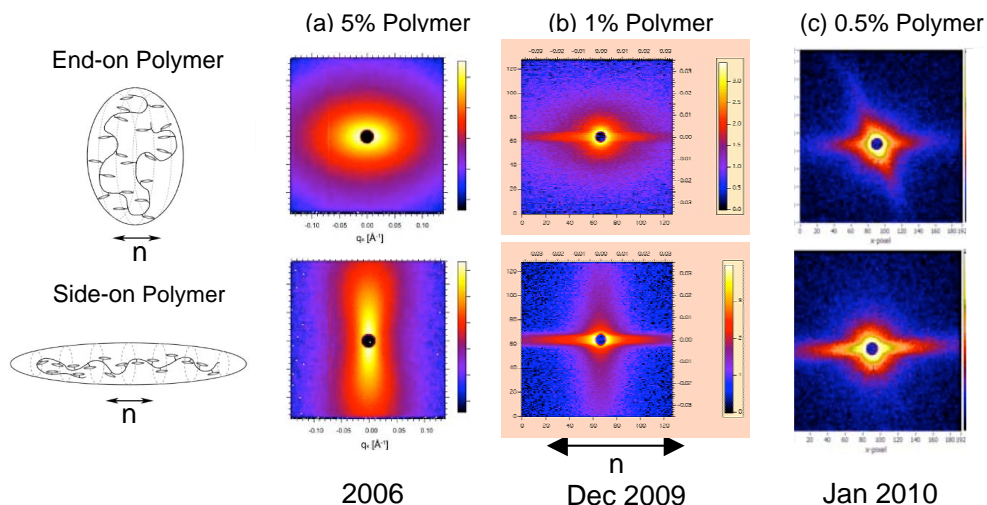
Figure 2. 2-D SANS patterns at low q for (a) 5% by weight of the end-on and side-on homopolymers in the nematic phase, (b) 1% by weight, or below the overlap concentration, of the end-on and side-on homopolymers in the nematic phase and (c) 0.5% by weight, well below the overlap concentration. The patterns are of from longest detector distances (13m, 11m and 18m) available for NG5 (at NCNR), NG3 (at NCNR), CG2 (at ORNL) respectively.

A high intensity, low q (large size scale) streak suggests a long-range interaction that biases the pair-pair distribution of the chains; however, the long range interactions now familiar for colloidal particles in a small molecule nematic cannot describe the observed orientation of the streak (in colloids, particles tend to form lines along the director, which would in turn result in a streak perpendicular to the director in the 2-D SANS patterns). Instead, we believe this streak is the result of fluctuation mediated Casimir-like attraction of the (individual polymer chains) perpendicular to the director. The SGLCPs do not disturb the orientation of the director; rather, they perturb the fluctuations of the director[6]. This explains the orientations of the streak as well as why it retains this orientation for both oblate and prolate SGLCPs. If Casimir-like interactions are indeed responsible, then small changes in concentration will strongly affect the "streak," (since these interactions are expected to fall off as the sixth power of the interchain distance). Indeed, at 0.5wt% and 0.25wt% polymer (Figure 3b and c), the streak, at least qualitatively, appears to decrease in intensity. To our knowledge this effect

has never been reported before and we are currently working to quantify this phenomenon.
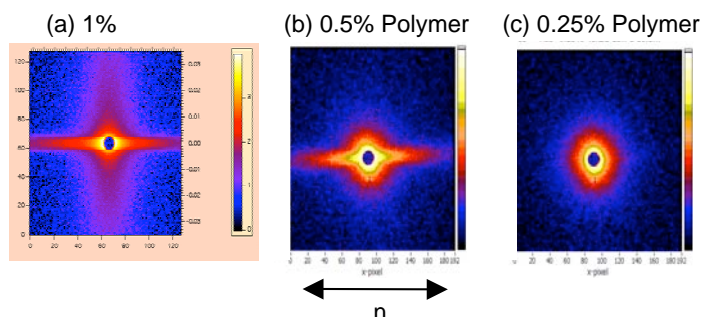
Figure 3. 2-D SANS patterns at low q for (a) 1%, (b)0.5% and (c)0.25% by weight of the side-on homopolymer in the nematic phase show the "streak" decreases with concentration. (The patterns are of from longest detector distances (11m and 19m) available for NG3 (at NCNR), CG2 (at ORNL) respectively.)

Side-on Homopolymer Shows Unexpected Response upon Increasing Temperature.

In general, upon heating polymer solutions above the nematic-isotropic transition temperature (T_{ni}), we expected that the polymers would also become isotropic. However, when 1% polymer samples were heated to temperatures above, but close to of the LC solvent, another surprise emerged: as the solvent becomes isotropic, the 2D SANS patterns *generally* become isotropic but *anisotropy persisted above the Tni* (Tni +2, Figure 4) for the side-on homopolymer in the mid and high q regimes. Additional experiments indicated that the magnetic field does not induce the effect; it breaks symmetry – making it possible to observe the effect. We believe that the polymer may create an "internal nematic field" resulting in local ordering of the small molecule LC within/around the polymer, similar to the way certain boundary conditions can locally condense isotropic LC into the nematic phases above the bulk T_{ni} (capillary condensation).Again, to our knowledge *this* effect has not been reported and further probing of this unexpected finding with, for example, different molecular weights of this polymer can help us elucidate this phenomenon as well as it's potential usefulness as part of a stimulus-responsive polymer-LC system.
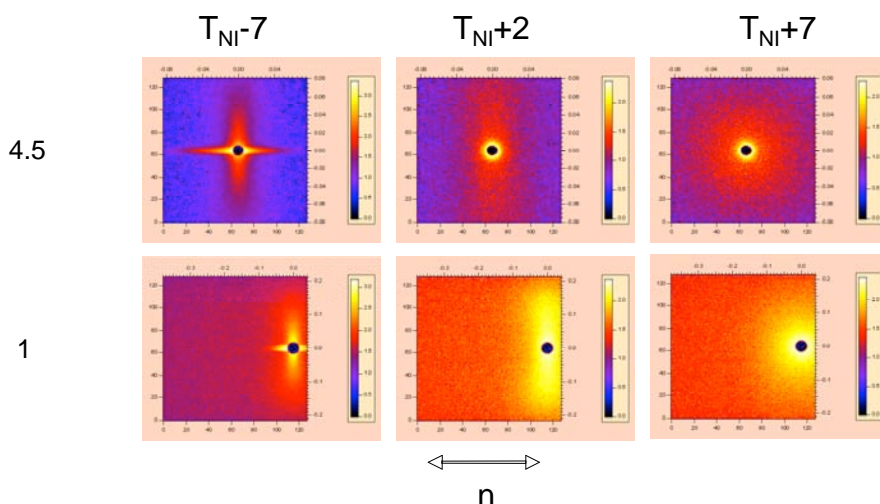
Figure 4. 2-D SANS patterns of the side-on homopolymer across the nematic-isotropic transition in the mid and high-a regimes. Data were obtained at 20 °C, 29 °C and 34 °C.($T_{NI} \sim$ 27 °C) at detector distances of 4m and 11m on NG3 (at NCNR),

Coil-SGLCP Diblock Copolymers

One of the main shared interests between the both the Kornfield and Park group is the self-assembly of liquid crystal diblock copolymers. Indeed, it is this interested that motivated this AFOSR-MOST collaboration. In the Kornfield group, we've addressed this interest by studying polystyrene-SGLCP block copolymers, where polystyrene, PS, is LC-phobic and will thus drive self assembly when dissolved in small molecule LC solvent, or at an LC interface. With the help of ORNL's Center for Nanophase Materials, who provided the polymer backbones, we synthesized a series of both end-on and side-on coil-SGLCP diblock copolymers (Figure 5). These polymers had near-constant SGLCP content, and while their polystyrene block varied across the series from less than that of the SGLCP to more than that of the SGLCP. Polystyrene is LC-phobic, so solutions of these diblocks in LC solvent spontaneously form complicated and interesting nanostructures.

n	m
400	1250
550	1050
800	1100
1150	900
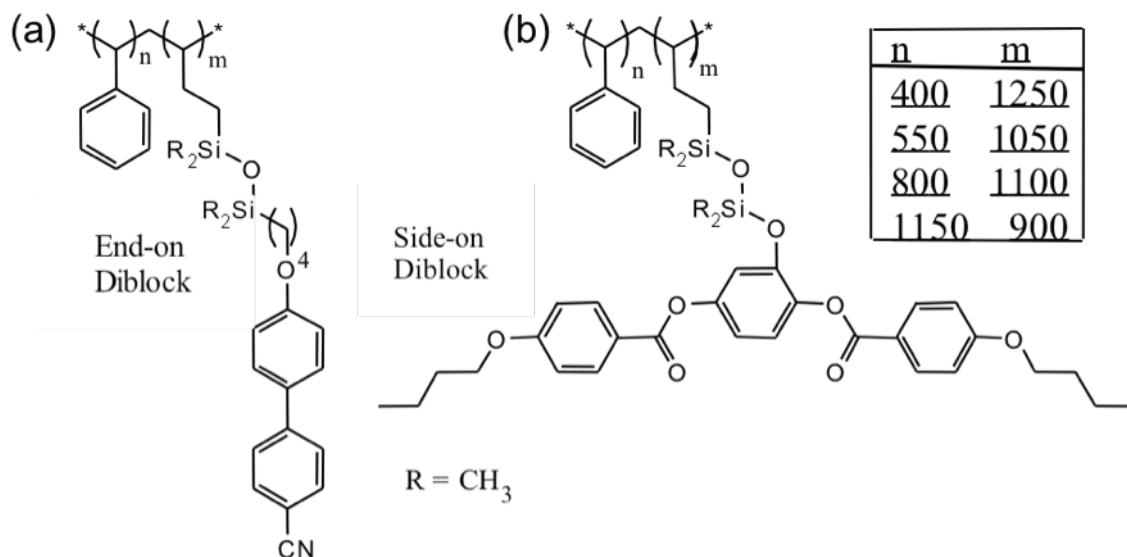
Figure 5. Our diblocks are made up of a polystyrene coil block and either (b) terminally attached, or "end-on" and (b) laterally attached, or "side-on" SGLCP blocks. The diblocks have approximately constant SGCLP content, *m*, while their polystyrene content, *n*, varies across the series from less than that of the SGLCP to more than that of the SGLCP[7].

Sector-averaged 1-D SANS data for dilute solutions of this series of coil-LC diblock in LC solvent shows the presence of a Guinier regime in the nematic phase (2D data shown below, Figure 6). The dimensions extracted from Guinier analyses agree well with direct, visual confirmation of these structures as seen via Transmission Electron Microscopy (TEM), Figure 7. (These measurements build on the initial TEM characterizations carried out both by students in the Park lab, and by a joint effort of both Caltech and Kyungpook students, in Year 1 of this grant).
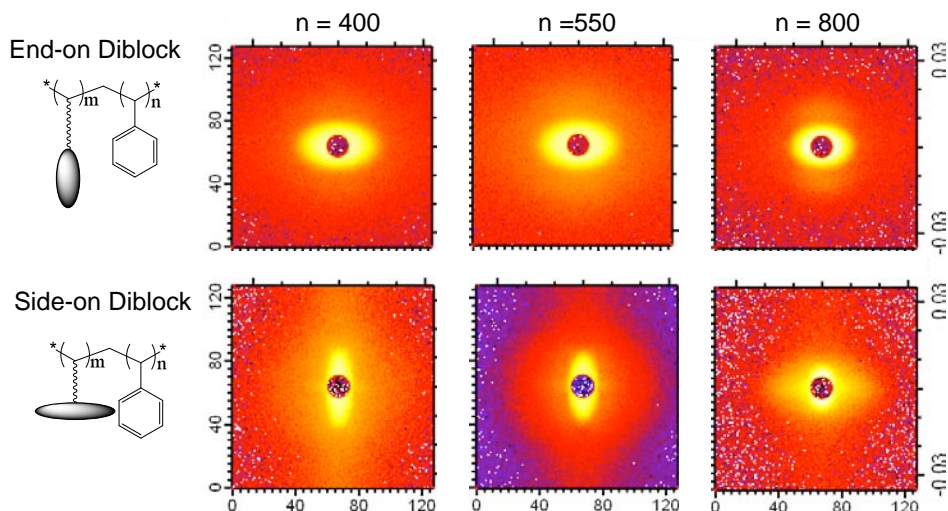
Figure 6. 2D SANS patterns at low q for end-on and side-on diblock copolymers with increasing polystyrene content. The sense of anisotropy is reversed from end-on to side-on, for the most part, with an interesting change between n=550 and n=800 for the side on diblock. Data was obtained at the largest detector distance (11m) available for NG3 (at NCNR),
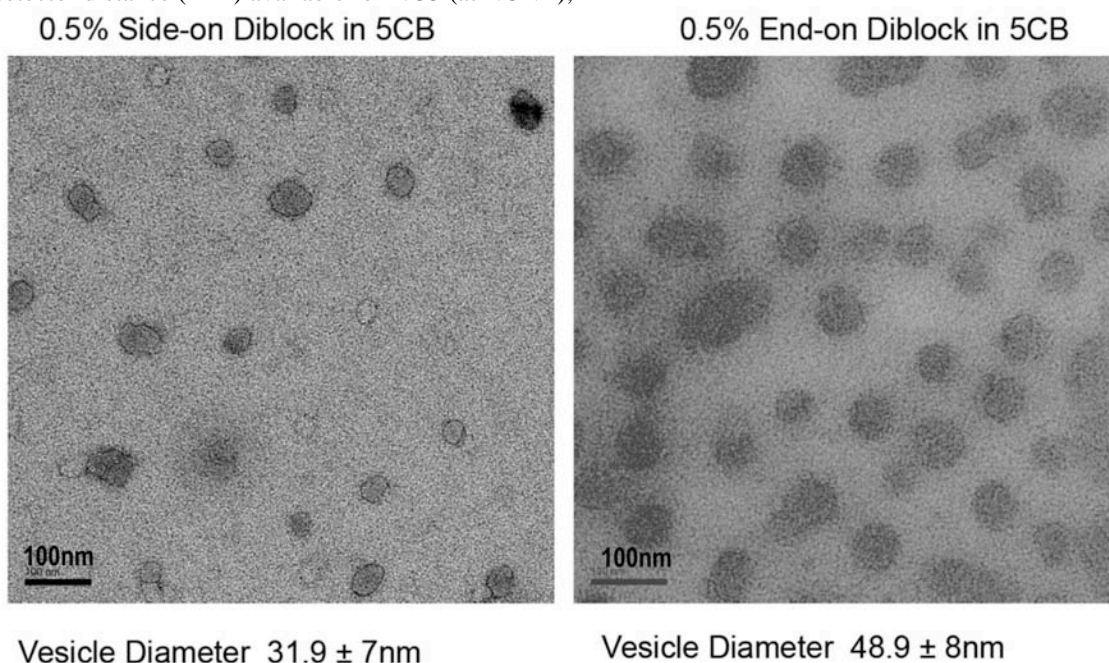
Figure 7. Unstained TEM micrographs of 0.5 wt% (left) side-on and (right) end-on PS-SGLCP (n = 1150, m = 900, for both cases) in 5CB. Solutions were cast on a carbon-coated Cu grid and dried under ambient conditions.

These techniques probing both the reciprocal and real space indicate larger structures than would be expected of typical block copolymers in selective solvents. For example, Lodge[7] and Register[8] found micelle diameters in the range of 10-20nm for polystyrene-*b*-polyisoprene diblocks of comparable molecular weights in selective

solvents, while the diameters seen in the micrographs of our SGLCP system are on the order of 30-100nm. Furthermore, the broader distribution of sizes seen in the TEM micrographs of the diblock copolymers is suggestive of possible vesicular structures.

Adding the PS block to the SGLCP block has many interesting and complex effects that we are able to tease out t because of our bottom-up approach: we've done detailed studies of the SGLCP homopolymer of similar molecular weights (see above), and thus can directly compare this work to our diblock work. When you compare the homopolymers to their PS-diblock analogs, one can see that the side-on diblock is much less anisotropic than it's corresponding homopolymer. Instead of an aspect ratio of 5:1, the side-on diblocks have aspect ratios of 1.5-2.5:1 (Figure 8, bottom). On the other hand the end-on diblocks have much more similar aspect ratios than their corresponding homopolymer (Figure 8, top), especially at low q (which corresponds to the larger dimensions).
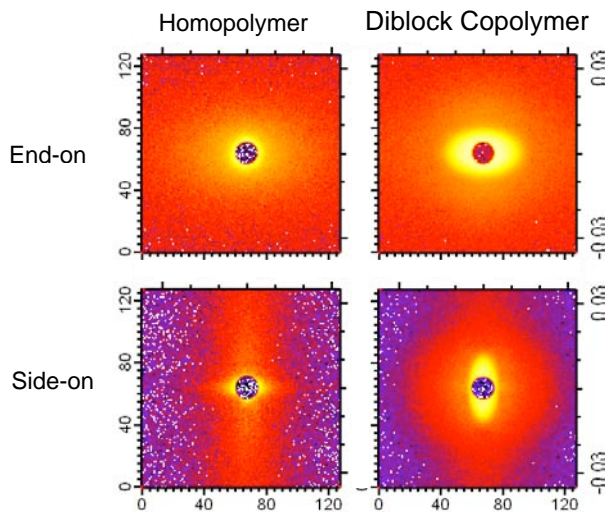
Figure 8. The end-on and side-on homopolymers as compared to their respective PS-diblock copolymers. The anisotropy of the side-on homopolymer is muted when it is involved in a diblock copolymer nanostructure. Data was obtained at the largest detector distance (11m) available for NG3 (at NCNR),

Another interesting feature is found in the side-on diblock: as the PS molecular weight increases, there appears to be a flip in the sense of orientation, at least qualitatively (Figure 6, bottom). When n goes from 550 to 800, the nanostructure they form seems to be oriented in the opposite direction. 2D SANS patterns for the diblock with higher molecular weight polystyrene would help confirm this apparent orientation switch.

Diblock copolymers at the Air-Liquid Crystal Interface

In addition to the studying these diblock copolymers' orientation and conformations in the bulk, both the Kornfield and the Park group are very interested in the diblocks' structure, conformation and orientation at solvent interfaces. Interactions at interfaces are of great interest in the development of chemical or biological sensors[9]. Liquid crystal ordering is sensitive to the microscopic structure at interfaces[10] and their ability to respond to changes in this environment makes liquid crystals ideal for sensors and actuators[11]. Abbott *et al.* have extensively studied the behavior at the liquid crystal-water interface, recently using surfactants to create emulsions and thus stabilized droplets of liquid crystal[12].

Analogous to surfactants, the non-liquid crystal blocks of our polymers can act as the agents driving the phase separation of the emulsions. These end-blocks can be tailored to the interface being studied, *i.e.* polystyrene for air, and polyphenylene vinylene, or polyacrylic acid for water. The self-assembly of the block copolymer at the interface may spontaneously create an anchoring condition, either parallel or perpendicular to the interface according to the molecular design (e.g. end-on vs. side-on).

Continuing our bottom-up strategy, the Kornfield group carried out experiments with our polystyrene-LC diblock copolymers at the air-LC interface -- studying polymers whose structure and conformation we have studied in detail (see above) at an interface appropriate for said polymers. We saw this as an ideal first step to the more complicated, though more industrially relevant, synthesis and investigation of stimuli-responsive blocks at the LC-water interface. These studies will guide us to our eventual goal of rationally designing smart materials using appropriate diblock copolymers. Our PS-SGLCP experiments were carried out by mounting films of dilute (0.5%) diblock copolymer solutions on copper TEM grids mounted on a metal or nylon washer (thus having an air-LC interface both above and below the film). After thermal equilibration, we found that pure 5CB (small molecule LC solvent) and 0.5% solutions of side-on diblock copolymer solutions both tended to orient almost exclusively homeotropically (see Figure 9(a)) while 0.5% end-on diblock copolymer solutions had a much higher percentage of homogenously aligned squares, though this polymer system also had homeotropically aligned squares (see Figure 9(b)).
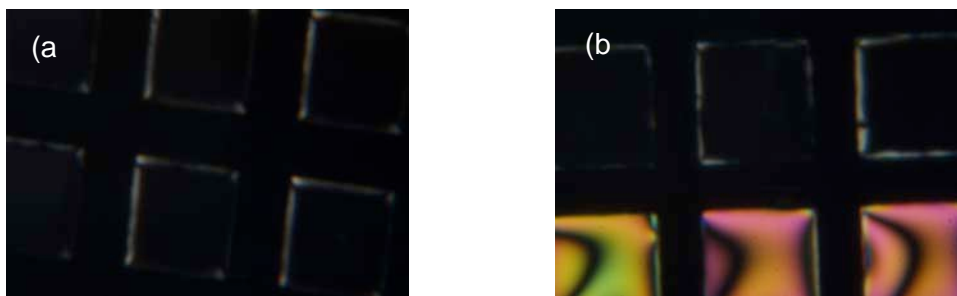
Figure 9. (a) 1% 50(121)ABPS-PBSiBB (side-on) in 5CB on a copper TEM grid, with air above and below the LC layers, (b) a) 1% 50(121)ABPS-PBSiCB4 (side-on) in 5CB on a copper TEM grid.

The difference in alignment of the two types of SGLCP can be explained by their structural differences. The side-on polymer's mesogens orient parallel to the backbone, while the end-on's mesogens tend to orient perpendicular to the backbone, so as the polystyrene segregates at the air-LC interface, the systems (if they can overcome the surface alignment favored by the LC solvent) will align homeotropically and homogenously, respectively (see Figure 10). The tendency for some homeotropic alignment in the end-on case can be explained by the behavior of 5CB at the interface: the most likely orientation of 5CB at the interface would be with its non-polar tail oriented towards the interface to minimize the surface energy. This would contribute to the systems likelihood of homeotropic alignment. Interestingly, this could lead to a frustration in orientation between the homogenous state preferred by the polymer and the homogenous state preferred by the LC solvent, a possible industrially-exploitable property.
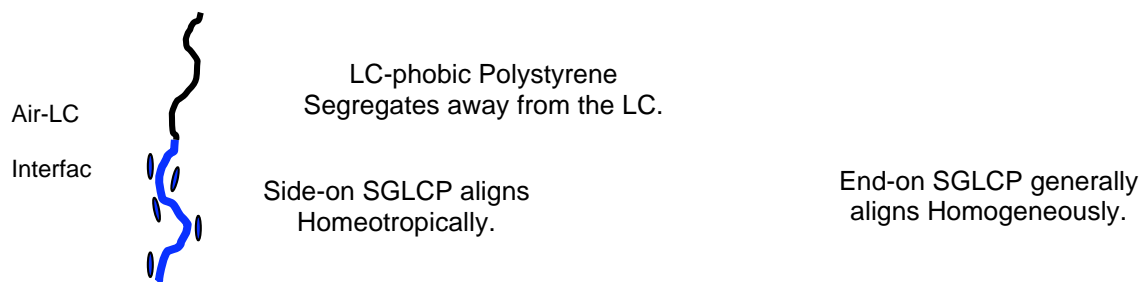
Figure 10. A schematic representation of the orientation of the two types of polymers at the air-LC interface.

Preliminary investigations into this system have shown that the presence of the polymer in the system is very important to maintaining alignment. Figure 10(a) shows that heating the system to above the Tni of 5CB and cooling again results in the system

returning to the exact alignment and even texture it had before the heating. However heating the system past the *polymer's* Tni results in a definite change in texture (see Figure 11(b)).
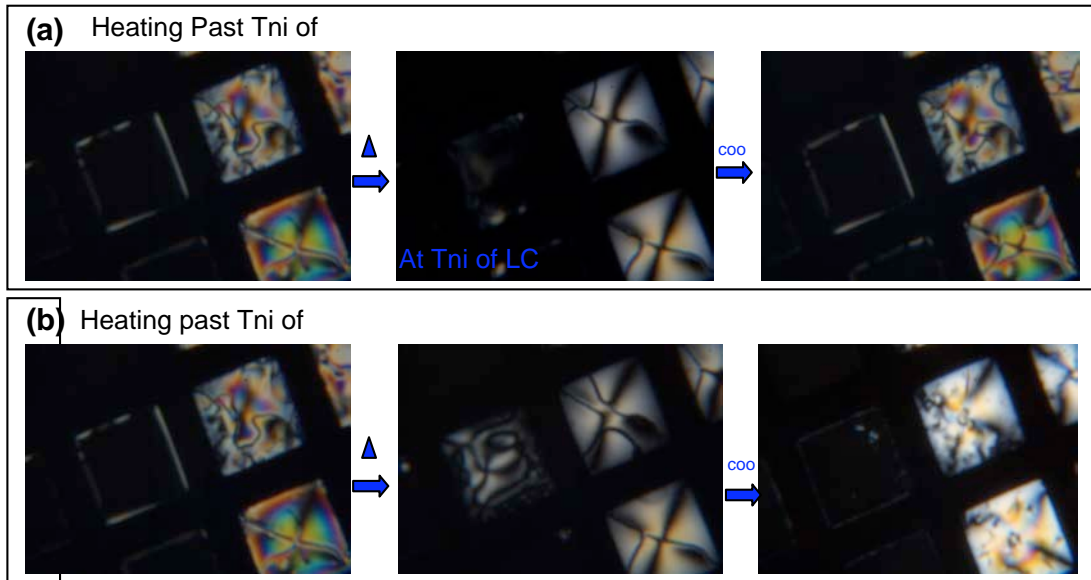
Figure 11.(a) Heating the system of past the Tni of the LC solvent returns it to the same alignment and texture as the initial equilibrated state. (b) Heating the system past the Tni of the polymer results in a change in alignment and texture.

One of the most interesting features of thy system to date is the appearance of apparent thermal bistability in the end-on polymer system (see Figure 12).Heating the system can result in a flip in alignment both from homeotropic to homogenous as well as the reverse. Bistability is a very desirable state in engineered devices, because instead of needing continuous energy to keep the sample in one phase or another, energy is only required to switch the LC system's alignment. Thus a device that takes advantage of this property can have very low power consumption. If this system in indeed bistable, it opens up many potential applications for this system beyond the sensor-detector regime. Our next step would be to confirm bistability by testing the film's response to magnetic or electric fields.
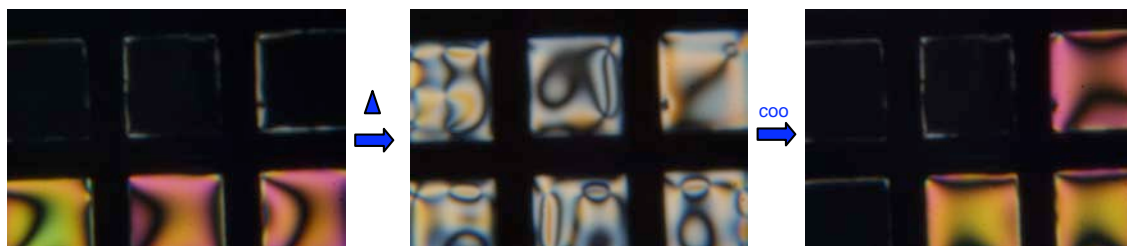
Figure 12. The end-on polymer system displays potential bistability. Upon heating and subsequent cooling the alignment of both homeotropic and homogenous cells can flip.

We plan to use the foundation that we have developed here, thanks to the AFORS_MOST program to design new liquid crystal nanostructures at the interface that function intelligently by environmental stimuli such as temperature, pH, or the presence of particular analytes. For example, we can replace the PS block with a stimulus-responsive block, similar to what our collaborators in the Park group have done and couple a liquid crystals' ability to amplify signals and display responses optically to responsive polymers sensitivity to stimuli.

The AFOSR-MOST Program.

The AFOSR-MOST has been a profoundly positive experience for all of us involved. In particular, the exchanges of Caltech team members to Korea have been extremely important. Caltech graduate student, Zuleikha Kurji, who spent greater than 2 weeks in Daegu with the Park lab, calls it "one of the highlights of my graduate career." As science becomes more international, and as countries in Asia continue to grow as leaders in the scientific community, we're grateful to have made a connection to the continent. Perhaps most importantly, this program has sparked a fruitful scientific collaboration that we expect to continue for years to come.

[1] M. D. Kempe, J. A. Kornfield, and J. Lal, Macromolecules **37**, 8730 (2004).
[2] M. D. Kempe *et al.*, Nat. Mater. **3**, 177 (2004).
[3] *Ibid,* 177.
[4] *Ibid,* 177.
[5] *Ibid,* 177.
[6] Bartolo, D.; Long, D.; Fournier, J. B. *Europhysics Letters* **2000**, *49*, 729-734.
[7] Lodge, T.P, Hamley, K.J, Pudil, B. Alahapperuma, V, *Macromolecules,* **2003**, *36¸* 816.
[8] Lai, C. Russel, W.B, Register, R.A, *Macromolecules* **2002,** *35,* 841.

[9] J.S. Park, C.H, Jang, M.L. Tingey, A.M. Lowe, N.L. Abbott, J. or Colloid and Interface Sciences **304** (2006).

[10] *Ibid.*

[11] M.I. Kingsinger, B. Sun, N.L.Abbott, D.M.Lynn, Advanced Materials **19** (2007).

[12] E.Tjipto, K.D. Cadwell, J.F.Quinn, A.P.R. Johnston, N.L. Abbott, F.Caruso, Nanoletters **6** (2006)

Chapter 8

Final Report

Extremely Low Noise Carbon Nanotubes for Peltier and Photo-Detector Device Applications

PI: Dr. Minhee Yun,   University of Pittsburgh

Dr. Moon J. Kim,   University of Texas at Dallas

Objectives

The objective of the three year CNT project was to investigate contact phenomena between CNT (metallic or semiconducting) and metal electrodes of varying work function and physical properties. Fundamental knowledge gained from this fundamental study was to be applied in fabrication and analysis of CNT-based photodetectors and Peltier coolers. To achieve both these goals, we proposed improved CNT growth procedures, improved and scalable fabrication (multiple metal type contacts per CNT), and analysis based on low temperature I-V measurements.

Status of effort

We have successfully implemented a moderately-scalable approach to fabricating hundreds of hetero-metal contacted carbon nanotube transistor/resistor devices on a one single tube to study contact-dependent properties of electric transport. Using this reproducible approach, the metal-contact work function dependence was quantitatively and explicitly determined (first time) by matching experimental data with derived theoretical models based on thermionic field emission principles. Schottky barrier measurements and low temperature I-V data was utilized to propose a new "Surface Inversion Channel" or SIC model to more accurately describe the energy band alignment at the metal-CNT interface. As part of the study, we also found significant impact on electron transport due to electron exposure (even in small doses). The effect of such exposure on metal and semiconductor CNT was quantitatively analyzed, and a model/theory proposed based on hopping transport at electron-induced trap centers in the CNT channel. Lastly, we utilized the scaled CNT device fabrication approach to examine the work function dependence on CNT Schottky diodes with hetero contacts. Using this model, we demonstrated and proposed an adaptable-diode design based on CNT with an n-type Schottky drain contact, and a p-type Schottky source contact.

Abstract

We have introduced a surface-inversion channel model based on low temperature and electrical measurements of a distinct single-walled semiconducting CNT contacted by Hf, Cr, Ti and Pd electrodes. Anomalous barrier heights and metal-contact dependent band-to-band tunneling phenomena were utilized to show that dependent upon contact work function and gate field, transport occurs either directly between the metal and CNT channel or indirectly via injection of carriers from the often ignored electrode covered CNT. This model is in stark contrast to other previous models which often definitevly stated (but not proved) that edge-transport was the dominant factor, and the metal-covered CNT region had little effect on transport properties. Next, incorporating experimental and analytical analysis, we demonstrated a relationship between the contact metal work function and electrical transport properties saturation current (Is_{at}) and differential conductance in ambient exposed carbon nanotubes (CNT). The observed exponentially increasing relationship of I_{sat} and σ_{sd} with metal-contact work function was explained by a theoretical model derived from thermionic field emission. Statistical analysis and spread of the data suggested that the conduction variability in same-CNT devices results from differences in local surface potential of the metal contact. Based on the theoretical model and methodology, an improved CNT-based gas sensing device layout was suggested in a recently submitted paper based on this topic, and a method to experimentally determine gas-induced work function changes in metals was also examined. Using the derived analytical relationship,

$$\ln\left(\sigma_{sd}\right) \propto \frac{1}{2}\ln\left(\Phi_{CNT} - \Phi_m\right) - \left(\frac{1}{E_0}\right)\left(\Phi_{CNT} - \Phi_m\right),$$ we proposed that a quantitative (concentration dependent) gas

sensing system could be fabricated by using multiple metal contacts to a single CNT. This work provides a simple model for fellow researchers to utilize in CNT-FET gas sensing. Lastly, a current rectification model for CNT Schottky diodes was derived and correlated to experimental data from Pd-Hf, Ti-Hf, Cr-Hf, Ti-Cr, and Pd-Au mixed metal devices fabricated on one single 6 mm-long CNT. Theory and experimental fitting suggest that the difference in work functions of the two contact-metals, and not a dominant Schottky contact, determines diode rectifying ability. Thus, we were able to plot the anisotropy of CNT Schottky diodes against the difference in contact work functions, and obtain a strongly correlated exponential relationship. Devices measured in vacuum after ambient measurement displayed markedly decreased IR, and significant increases in overall anisotropy. The analysis was then applied in demonstrating a reversible polarity diode, e.g. a device which permits current to pass in a single switchable direction dependent upon the applied gate potential. With further work, this concept could be utilized in highly-versatile adaptive logic circuit designs.

Personnel Supported:

1. **David Perello M.S.,** Electrical Engineering University of Pittsburgh. Student is currently working towards a PhD degree in ECE.

Publications:

1. David Perello, Seong Chu Lim, Seung Jin Chae, Innam Lee, Moon J Kim, Young Hee Lee, and Minhee Yun. "Thermionic field emission transport in carbon nanotube transistors" *Submitted ACS Nano,* Sept. 2010

2. David Perello, Seong Chu Lim, Seung Jin Chae, Innam Lee, Moon J Kim, Young Hee Lee, and Minhee Yun. " Current anisotropy of carbon nanotube diodes: Voltage and work function dependence" *Appl. Phys. Lett*. 96, 263107 (2010).

3. David Perello, Seong Chu Lim, Seung Jin Chae, Innam Lee, Moon J Kim, Young Hee Lee, and Minhee Yun, "Anomalous Schottky Barrier and Contact Band-to-Band Tunneling in Carbon Nanotube Transistors", *ACS Nano* 4 (6), 3103 (2010).

4. David J. Perello, Woo Jong Yu, Dong Jae Bae, Seung Jin Chae, M.J. Kim, Young Hee Lee, and Minhee Yun, "Analysis of hopping conduction in semiconducting and metallic carbon nanotube device", *Journal of Applied Physics*, 105, 124309 (2009)

5. S. C. Lim et al., "Contact resistance between metal and carbon nanotube interconnects: Effect of work function and wettability", *Appl. Phys. Lett*., 95(26), 264103-1~264103-3, Dec. 2009

6. F. Guneset al., "'Large-Area graphene-based flexible transparent conducting films", *NANO*, 4(2), 83-90, Aug. 2009

7. David Perello, Dong Jae Bae, Moon J. Kim, DongKyu Cha, Seung Yol Jeong, Bo Ram Kang, Woo Jong Yu, Young Hee Lee, and Minhee Yun, "Quantitative experimental analysis of Schottky barriers and Poole–Frenkel emission in carbon nanotube devices", *IEEE Transactions on Nanotechnology,* 8 (3), 355 (2009)

8. C. Biswas et al., "Strategy for High Concentration Nanodispersion of Single-Walled Carbon Nanotubes with Diameter Selectivity", *J. Phys. Chem. C.*, 113(23), 10044-10051(Apr. 2009)

9. Seung Yol Jeong, S. C. Lim, D. J. Bae, Y. H. Lee, H. J. Shin, S. M. Yoon, J. Y. Choi, O. H. Cha, M. S. Jeong, D. Perello, and M. Yun, "Photocurrent of CdSe nanocrystals on single walled carbon nanotube-field effect transistor, *Appl. Phys. Lett.,* 92(24), 243103-1~3, 2008

10. S. Y. Jeong et al., "Efficient Synthesis of Individual Single-Walled Carbon Nanotube by Water-Based Catalyst with Poly(vinylpyrrolidone)", *Journal of Nanoscience and nanotechnology*, 8(1), 329-334, (Jan. 2008)

11. David Perello, Moon J. Kim, DongKyu Cha, Gang Hee Han, Dong Jae Bae, Seung Yol Jeong, Young Hee Lee, and Minhee Yun, "Schottky barrier engineering in carbon nanotube with various metal electrodes", *IEEE Review on Advances in Micro, Nano, and Molecular Systems*, 2007

12. Seung Yol Jeong, David Perello, Sung Jin Kim, Jin Ho Jang, Bo Ram Kang, Woo Jong Yu, Dong Jae Bae, Minhee Yun, and Young Hee Lee, "Chirality-specific transport phenomena of isolated single-walled carbon nanotube", *Phys. Stat. Sol. (b)* 244, No. 11, 4204–4211 (2007)

Interactions:

(a) Conferences:

1. David Perello, Moon J. Kim, DongKyu Cha, Gang Hee Han, Dong Jae Bae, Seung Yol Jeong, Young Hee Lee, and Minhee Yun, "Schottky barrier engineering in carbon nanotube with various metal electrodes". *IEEE Nano Hong Kong 2007* (Speech).

2. Minhee Yun, Perello David, Moon J Kim, DongKyu Cha, Young Hee Lee, Dong Jae Bae, Seung Yol Jeong and Kang Hee Han, "Explicit Determination of Various Metal-dependent Contact Properties to Single-wall Carbon Nanotubes". *MRS Conference Boston December 2007* (Poster).

3. David Perello, Moon J Kim, SeongYeol Jeong, BoRam Kang, Dong Jae Bae, Young Hee Lee, and Minhee Yun, "CNT-FET Schottky Barrier Devices Fabricated by E-beam Lithography". *Microscopy and Microanalysis Albuquerque August 2008* (Invited Speech).

4. David Perello, Dong Jae Bae, Seung Yol Jeong, Bo Ram Kang, Woo Jong Yu, Young Hee Lee, Dong K. Cha, Moon J. Kim and Minhee Yun, "Investigation of Transport Properties of Schottky Carbon Nanotube FET Devices". *MRS Conference Boston 2008* (Poster).
5. David Perello; Woojong Yu; Dong Jae Bae; Seung Jin Chae; Moon J. Kim; Young Hee Lee; Minhee Yun. "Pool-Frenkel emission and hopping conduction in semiconducting carbon nanotube transistors" *SPIE San Diego August 2009* (Speech).
6. David Perello, Seong Chu Lim, Seung Jin Chae, Innam Lee, Woo Jong Yu, Young Hee Lee, and Minhee Yun. "Thermionic Field Emission in Carbon Nanotube Transistors and Proposal of Surface Inversion Channel Model". *MRS Conference Boston December 2010* (Speech).

(b) Describe cases where knowledge resulting from your effort is used, or will be used, in a technology application.

There are no direct applications we are knowledgeable of that resulted from this project.

Inventions:

No inventions or patents were filed as a result of this project.

Honors/Awards:

"Analysis of hopping conduction in semiconducting and metallic carbon nanotube devices," published in Journal of Applied Physics 105, 124309 (2009) was selected for publication in the July 6, 2009 issue of Virtual Journal of Nanoscale Science & Technology

Archival Documentation:

See the publication list

Software and/or Hardware (if they are specified in the contract as part of final deliverables):

No Software and/or Hardware to disclose as part of the project.

Final Report

HIGH-RESOLUTION, LARGE-AREA, NANO IMPRINT LITHOGRAPHY USING ELECTRON LATTICE IMAGES AND ELECTRON-EMITTING NANOPROBES

AFOSR Contract Number: FA4869-01-4048
AOARD Reference Number: AOARD-084048

AFOSR/AOARD Program Manager: Lt Col John Seo

Period of Performance: 2007-2010

Submission Date: October 7, 2010

US-PI = Prof. Sungho Jin, UC San Diego, La Jolla CA 92093-0411, USA.
(Tel) 858-534-4903, (e-mail) jin@ucsd.edu

Korea PI = Prof. Ki-Bum Kim, Seoul National University

Abstract and Status of effort

The ultimate objectives of this joint research project (Seoul National University – UC San Diego) is to develop large area nano imprint lithography techniques for applications such as ultra-high-density, patterned magnetic recording media with at least 1 terabit/in^2 recording density, about 5 times higher than the current hard disk memory in the market. Such a high recording density requires a patterned media with the recorded magnetic island bit size of ~12.5 nm in diameter. In order to obtain such a small islands, both electron lattice imaging and field emitting nanoprobe arrays have been investigated.

Nano-patterning of Si substrate and patterned island formation with a bit density as high as 1.6 1 terabit/in^2 which is capable of high magnetic recording density has been accomplished by using e-beam lithography associated with nano-imprinting. The bit size is on the order of 10 nm in diameter, and a spacing of similar dimension. A relatively large area of 2 mm x 2 mm area nano-imprint mould has been demonstrated. Magnetic switching behavior of patterned bit islands of (CoPd)n perpendicular anisotropy magnets has been investigated. A technique for planarization of topographically undesirable magnetic island arrays has also been developed to allow the read/write head to fly on the hard disk media surface.

The concept of multiprobe AFM lithography --- an alternative approach of nanomanufacturing using distributed AFM lithography probe tips that use local nanoscale field emission has also been demonstrated. A massively parallel probe array of 100 million periodically spaced tips has been produced for future multi-probe AFM lithography studies.

Results and Discussion

The aim of this research project is to design and fabricate large area nano imprint lithography techniques for applications such as ultra-high-density, patterned magnetic recording media with at least 1 terabit/in^2 recording density, about 5 times higher than the current hard disk memory in the market. Such a high recording density requires a patterned media with the recorded magnetic island bit size of ~12.5 nm in diameter. In order to obtain such a small islands, both electron lattice imaging and field emitting nanoprobe arrays have been investigated.

The project requires R&D in both nanostamp fabrication and nano-imprint processes. An additional task of designing and fabricating multi-probe AFM lithography techniques and massively parallel probe arrays has also been undertaken with considerable progress made during the project period.

With regard to the nanoimprint fabrication aspects, initial experiments were carried out to begin to establish nano-imprint processes. Using UV-curable elastomer (PDMS) resist as the basis, silicon nanostamps were imprinted onto the resist which was spin coated on a transparent substrate (flat glass or quartz) and UV light was illuminated

from underneath to cure the resist during the stamping. The procedure is schematically illustrated in Fig. 1.
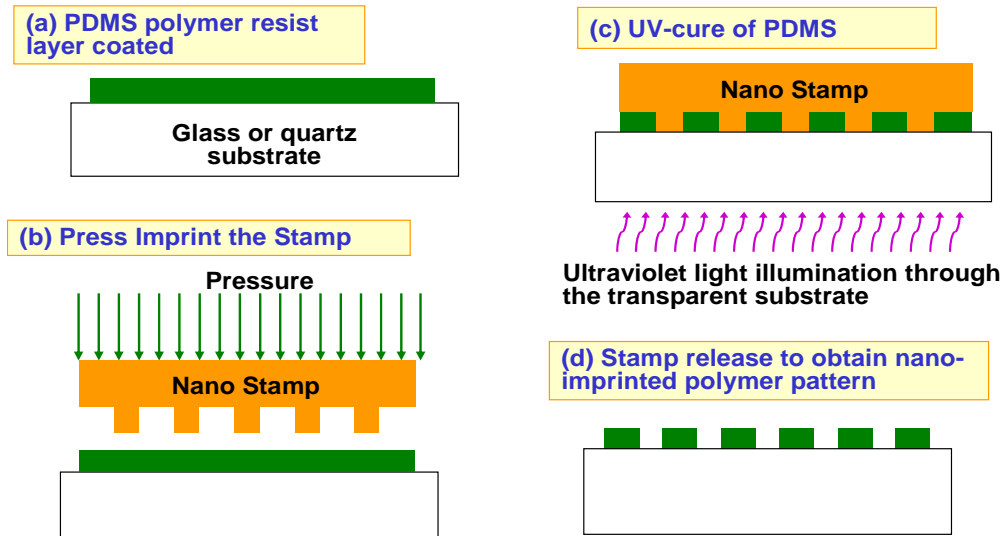
Fig. 1. Schematic illustration of the nano-imprint patterning technique.

Shown in Fig. 2(a) and (b) are SEM micrographs of circular hole patterns fabricated by the nano-imprint process, with 200 nm diameter and 40 nm diameter patterns of the UV-curable PDMS resist.
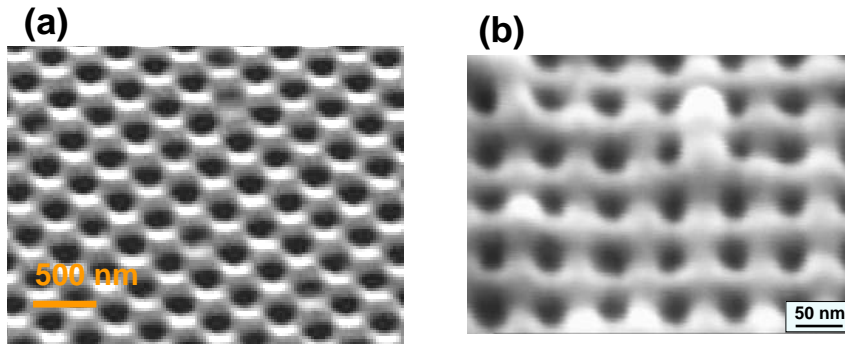
Fig. 2. Circular hole patterns by nano-imprint lithography. (a) 200 nm diameter and (b) 40 nm diameter patterns of the UV-curable PDMS resist.

In addition to fabrication of nano-array patterned structure and imprint stamps that the SNU-UCSD joint R&D team is pursuing, there are some other major issues that need to be resolved for successful fabrication of viable, sub-20 nm magnetic recording media --- (1) One issue is the problem of magnetic switching field distribution (SFD)

among various writable bits. (2) The second issue is the difficulty of read/write head (slider) flyability on patterned media disk due to the surface roufhness induced aerodynamic dragging. (3) The third issue, more relevant for Field Emission Projection E-beam Lithography type nanofabrication is the difficulty of fabricating an extremely sharp tips on probe cantilevers. (4) The fourth issue is the difficulty of measuring the magnetic properties of small (sub-20 nm size) magnetic bit islands, especially for the laboratory samples with relatively small, patterned land of a few hundred micrometer size. These issues were investigated during the course of this project as described below.

(1) **Magnetic switching field distribution**

In the technical field of patterned magnetic media (also called "Bit Patterned Media"), one of the current issues is the problem of magnetic switching field distribution (SFD). To operate the magnetic hard disk drive memory, the recorded bits need to be switched between "1" vs "0" (which is typically obtained by changing of magnetization directions through north pole - south pole switching. The desired magnetic field for switching of recorded bits in future high-density hard disk drive is typically ~5 – 10 KOe. Recent literatures report a substantial undesirable variation of the magnetic switching field when the size of the magnetic nano islands is reduced to below ~ 50 nm.

The switching field distribution is sometimes more than 30% from the median coercive force value, which is unacceptable from the hard disk memory application point of view. Various possible causes were discussed --- dimensional variations after lithographic patterning, islands sizes variations, islands edge effects, local compositional variation of Co and Pd at interfaces, distribution of intrinsic magnetic anisotropy, grain orientation and sizes or grain boundary variations.

Understanding of why such a switching field variation occurs in nanoscale dimensions, and how to prevent such a phenomenon are of paramount issue that has to be resolved for developing the ultra-high-density magnetic recording media so that the switching of bit information is carried out in a reproducible manner. While some of the recent literature report that the distribution of intrinsic magnetic anisotropy might be the cause for the switching field variation, there are additional possibilities for the cause of the SFD (switching field distribution) that have not been addressed. One of these possibilities include the fact that the shape of nano-magnet islands fabricated by e-beam lithography is not always uniform. Depending on the shape of the substrate Si pillars (vertical, positively tapered, or negatively tapered) as illustrated in Fig. 3, there can be some sidewall deposition of magnetic recording media, which can contribute to the observed SFD.

As magnetic layer deposition on top of protruding pillars tends to have some corner and sidewall deposition, this may cause different magnetic properties and switching fields, and may cause SFD in the magnetic islands. To investigate if removal of such sidewall deposition reduces the SFD problem, we modified the RIE parameters to intentionally alter the shape of the sidewall in Si nanopillars and introduced negative tapered Si column geometry as illustrated in Fig. 3. The figure shows ~30-50 nm diameter Si islands having the three different sidewall configurations, fabricated by e-beam lithography utilizing various RIE conditions.
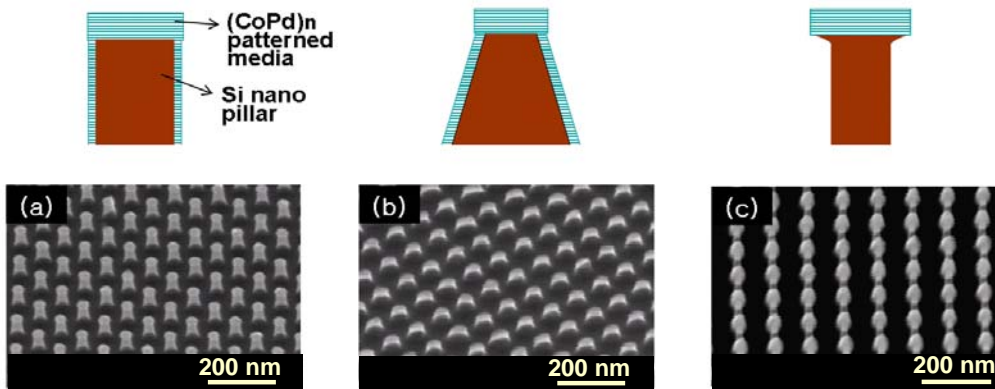
Fig. 3. Control of Si pillar sidewall configurations.

Based on reproducible Si nano-island array preparation, we have successfully fabricated patterned magnetic recording media as described in Fig. 4. About ~30 nm diameter Si pillar array was fabricated by E-beam lithography patterning as the basis to deposit magnetic material. High coercive force magnetic layer of multilayered magnet of (CoPd)n [n=8] with strong perpendicular magnetic anisotropy was deposited on the top surface of Si pillars. The structured multilayer nanomagnets consist of other adhesion layer and anisotropy-inducing layer by utilizing the geometry of Ta 3 nm\Pd 3 nm\[Co 0.3 nm\Pd 0.8 nm]$_8$. The coercivity was Hc ~4 KOe. (If FePt (L1o phase) is deposited, Hc of ~15KOe expected.)
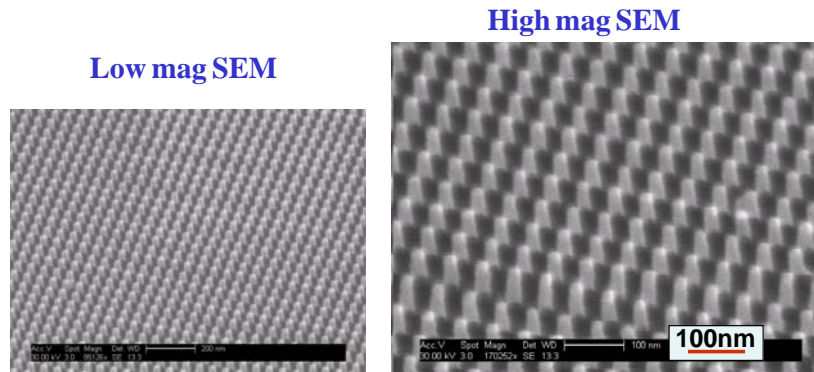
Fig. 4. Patterned magnetic recording media fabricated. The [CoPd]n islands with n=8 (~30 nm regime) were sputter deposited on Si nano pillars.

Comparative magnetic properties of patterned media islads with different sidewall configuration were evaluated using Micro MOKE measurements. As shown in Fig. 5 for the second quadrant M-H loop, the measurement data clearly indicates that the magnetic coercivity of [CoPd]n islands (~30 nm regime) on Si nano pillars with vertical sidewall has less variation in coercivity of ~15.3% in the switching field distribution (SFD) than that with positive side wall (~20.3%). Therefore it has been shown that the slanted geometry of the patterned media magnetic islands is less desirable than a vertical wall geometry. The magnetic measurement for the negative slope geometry sample will be carried out to see if a further reduced SFD can be obtained.
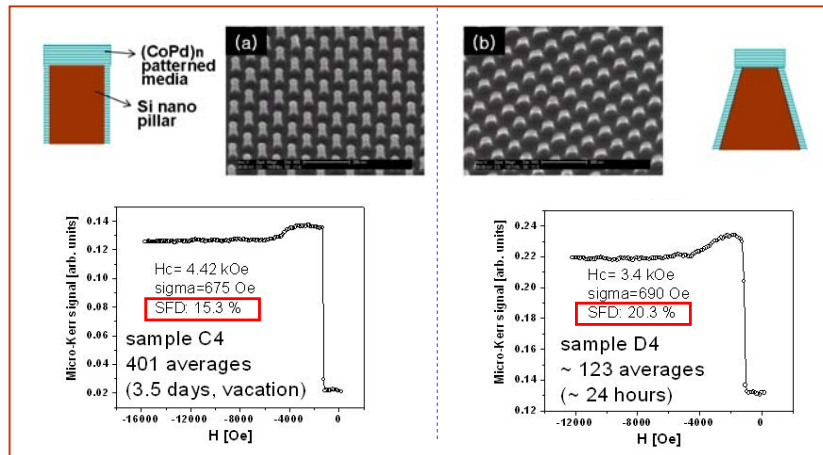
Fig. 5. Micro MOKE measurements of M-H loop for the patterned magnetic recording media, with the structured multilayer magnet of Ta 3 nm\Pd 3 nm\[Co 0.3 nm\Pd 0.8 nm]$_8$ sputter deposited on Si nano pillars.

For study of magnetic island size-dependence of magnetic switching field, distributed magnetic island sizes are sometimes desirable. The question that arises is then how one might be able to make the nano-islands with an intentional distribution of magnetic nano-island sizes. In this study, break-up and spheroidization of thin film layer has been utilized as described below.

As the sample preparation by e-beam lithography is slow and costly, distributed nano island dots with various sizes with a large coverage area (several millimeter area) have been fabricated by sputter deposition of Ni metal film (~3 nm thickness) on Si, followed by annealing heat treatment to break-up and ball up the film into a distributed particle sizes which can serve as etch mask for underlying Si substrate. The Si pattern so obtained is then used as the basis on which a magnetic recording media material of (CoPd)n multilayer. This process is schematically illustrated in Fig. 6.

Fabrication for distributed magnetic islands
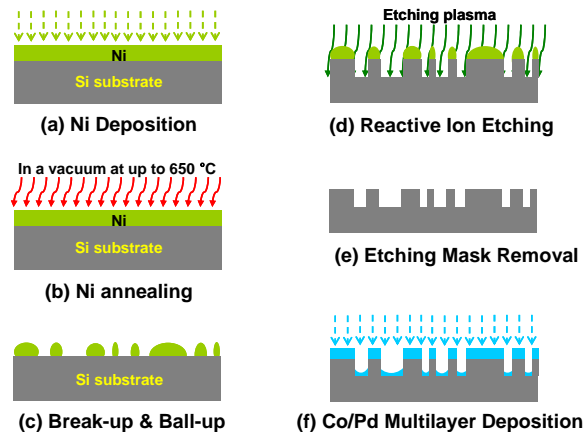
Fig. 6. Fabrication process to obtain magnetic island sizes using balled-up Ni islands as etch mask.

The morphology and size distribution of the Ni islands on Si surface are given in Fig. 7 and Fig. 8. When the thickness of the initial Ni film is increased, the average diameter and the distribution range of island sizes also increase as indicated in Fig. 9.

Ni island size distribution (Ni 3 nm thick layer)
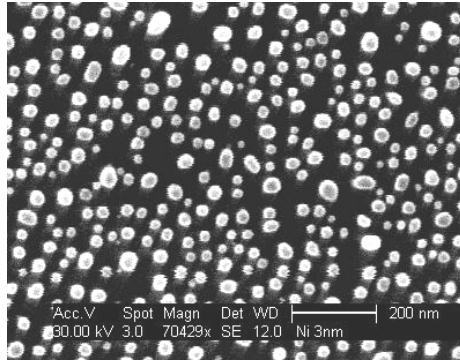
Fig. 7. Distributed size of Ni etch mask islands on Si substrate.
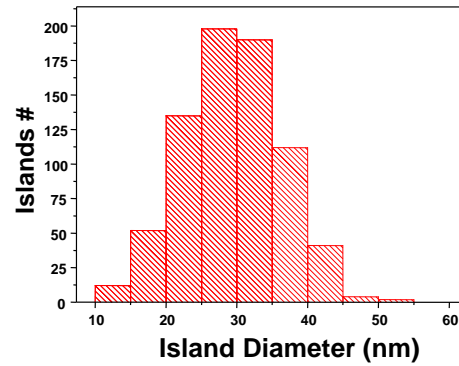
Fig. 8. Ni island particle size distribution.

The nanopatterning of Si underneath the Ni mask islands was carried out by RIE etching of Si. The resultant microstructure is shown in Fig. 10. Vertically aligned Si nanowires (pillars) with distributed diameters are obtained. The Ni islands are etched away by dilute acid, and then high-coercivity magnetic recording media, $(CoPd)_8$ multilayer was deposited with Ta and Pd seed layers for control of vertical texture and magnetic anisotropy (Ta 3nm/Pd 4nm/ [Co 0.2 nm/ Pd 0.8 nm)]$_8$. The magnetic material on top of the Si pillars is closer to the recording head and thus predominantly dictates the recording behavior as the media material deposited in the valley will be far away to contribute significantly to the signals picked up by read head.

Fig. 9. Ni island diameter and distribution as a function of the initial Ni coating thickness.
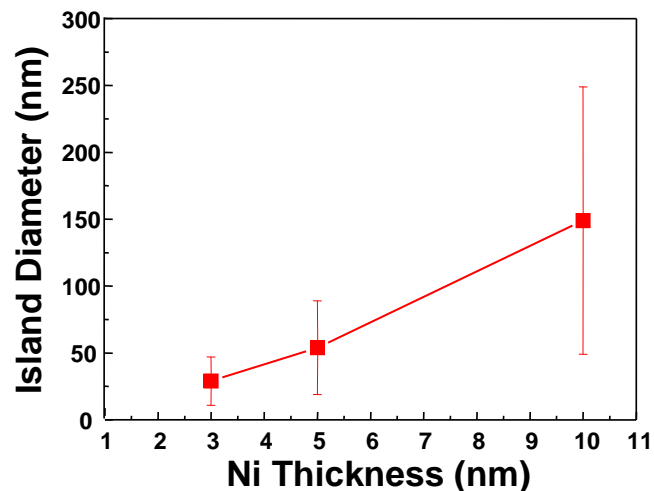
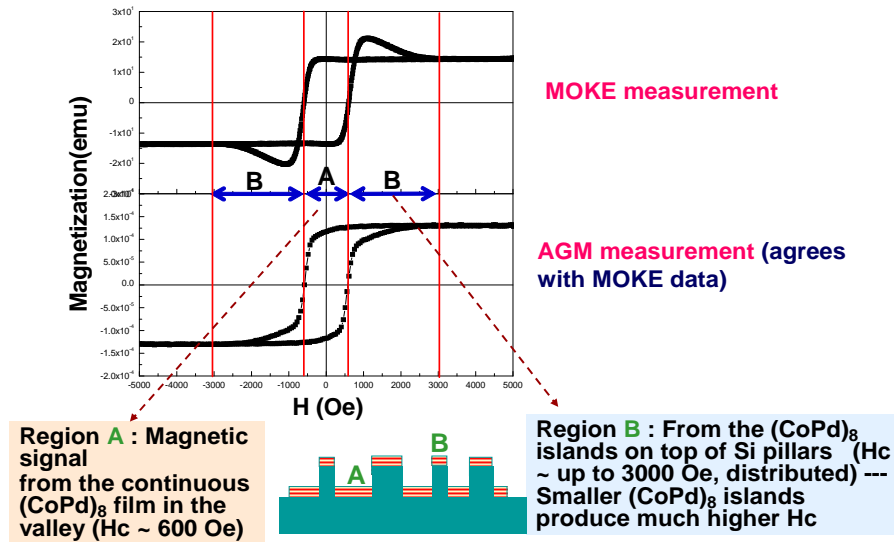The M-H magnetization loops were measured by MOKE (magneto-optical Kerr effect) and AGM (alternating gradient magnetometer) techniques and the data are shown in Fig. 11. Magneto-optical Kerr effect measurement of magnetic M-H loop for the magnetic recording media $(CoPd)_8$ multilayer on Si pillar arrays fabricated using Ni islands as the etch mask. The MOKE measurements agree well with the AGM data, and show that the "Region A" from the continuous $(CoPd)_8$ film in the valley location contributes to the lower switching field, which is corelated to the lower coercive force $(H_c \sim 600$ Oe) due to the disrupted multilayer texture alignment while the "Region B" from the $(CoPd)_8$ islands on top of Si pillars contributes to the much higher coercive force $(H_c \sim$ up to 3000 Oe, distributed).

The processing specifics of Ni island ball-up approach will be altered to obtain various distributions of the magnetic switching fields to gain insight on the effect of nanostructure geometry on the magnetic switching behavior. The required R&D toward ultra-high-density hard disk memory involve not only the reduction of magnetic island size but various materials and island shape parameters including texture formation, interface seed layer control (such as Pd, Ta type material layers), and the selection/modification of magnetic recording material itself (e.g., $L1_0$ phase vs $(CoPd)_n$ multilayer structure), and coercivity mechanisms. The advantage of this processing approach is that a relatively large sample area can be obtained (e.g., 1 cm^2) so that the difficulty of trying to measure extremely small magnetic M-H loop signals below the resolution of SQUID magnetometer in e-beam fabricated, small are (e.g., 100 x 100 μm area) can be bypassed. Materials parameters and processing specifics (for example, vertical texturing and anisotropy, coercivity control, etc.) can be optimized with these easily-measurable samples until the e-beam or nano-imprinted samples with desired geometry and large area can be fabricated to allow studies of magnetic switching and memory characteristics.
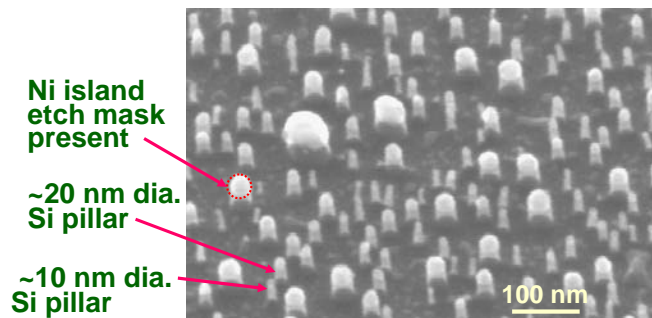
Fig. 10. SEM micrograph showing the Si pillars fabricated by RIE etching using Ni islands as the etch mask.

Magnetic properties *[3 nm Ni film + ball-up + RIE patterning + (CoPd)₈ deposition]*

MOKE measurement

AGM measurement **(agrees with MOKE data)**

Region **A** : Magnetic signal from the continuous (CoPd)₈ film in the valley (Hc ~ 600 Oe)

Region **B** : From the (CoPd)₈ islands on top of Si pillars (Hc ~ up to 3000 Oe, distributed) --- Smaller (CoPd)₈ islands produce much higher Hc

Fig. 11. Magneto-optical Kerr effect measurement of magnetic M-H loop for the magnetic recording media (CoPd)₈ multilayer on Si pillar arrays fabricated using Ni islands as the etch mask.

 (2) Read/Write head (slider) flyability on patterned media

When the magnetic material is deposited onto the lithographically pre-patterned substrate, the magnetic material in the trenches can introduce undesirable noise during Read/Write test, and also creates undesirable magnetic interactions between the magnetic materials deposited in the trench vs the island top. In order to minimize such deleterious effect, the height of the pillars must be tall enough. However, the read/write head can not smoothly fly over the patterned media if the depth of the trenches is too large, as we have observed with some of our island-patterned media as we attempted head flying experiments using standard Read/Write recording head for Co-Cr-Pt-SiO2 media. (For such a head flying experiments, randomly patterned nano-magnet structuresamples that we fabricated at UCSD with 5-50 nm diameter magnetic islands was used, since a large-area, hard disk size preparation was necessary, and since a disk-size periodic patterning with e-beam lithography would be too costly, e.g., many millions of dollars, at the moment).

To solve such a problem of recording head not being able to fly due to the drag of the trenches, we developed a technique of filling the trenches with a nonmagnetic material to planarize and make the hard disk surface as smooth as possible. We used the hydrogen silsesquioxane (HSQ) material to fill and planarize the trenches on a recording media disk because HSQ is easy to spin coating and the mechanical properties and thickness of the resultant SiO2 can be controlled for optimal read/write recording head flyability by changing the baking temperature after spin coating and plasma treatment. HSQ was spun over the patterned media to fill the grooves and re-etched slightly by

reactive ion etch (RIE) to remove the overfilled part. As shown in Fig. 12, the SEM micrographs and AFM surface profiling data for trench depth measurements indicate that the planarized patterned media exhibit a much smoother surface than the as-made patterned media surface.
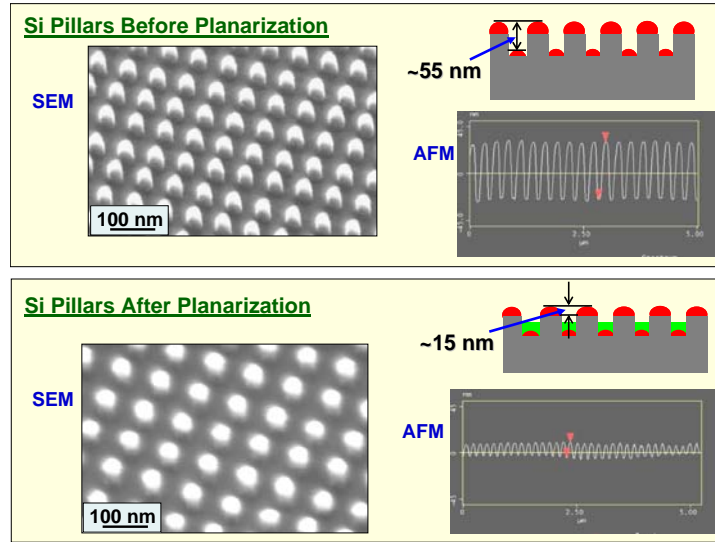
Fig. 12. (a) Comparative SEM microstructure of as-fabricated vs planarized nano-island patterned media using HSQ filling and back etching. (b) AFM profile of the patterned media sample surface before vs after planarization.

For some of the samples, intentional over-etch by RIE was used to artificially control the surface roughness (trench depth) for comparison purpose. The flyabilities of these planarized patterned media surface with various trench depths were measured and compared with that of the unplanarized patterned media as shown in Fig. 13. We used a slider which was designed to fly at a flying height of 11 nm at a velocity of 22 m/s. The slider didn't show any flyability on the as-patterned [Co-Pd]n disk with 40 nm bit height, while planarized disk allowed the head flying. Fig. 13(b) shows fluctuation of a slider on the planarized patterned media disk of which the depth of recess is ~0 nm. The fluctuation of a slider on this disk is almost the same as that of the unpatterned smooth media shown in Fig. 13(a). In this case, the standard deviation of flying fluctuation of a slider on the disk was 0.1 nm, while the standard deviation on the smooth disk was 0.09 nm. It shows very stable flying condition. As the final depth of recess is increased as 10 and 20 nm shown in Fig.13 (c) and Fig.13(d), increased dragging interaction between the head and disk was observed. The standard deviation of flying fluctuation of a slider on those disks was 0.18 and 0.52, respectively. From this flyability test, we have demonstrated that the flaybility of a patterned media slider (read/write head) can be greatly improved with planarization.

(3) Fabricating extremely sharp tips on probe cantilevers

For FEPEL type lithography, extremely sharp field emitter tips, desirably less thatn 10 nm tip diameter, is desirable. Fabrication of such a tip on small cantilever is not
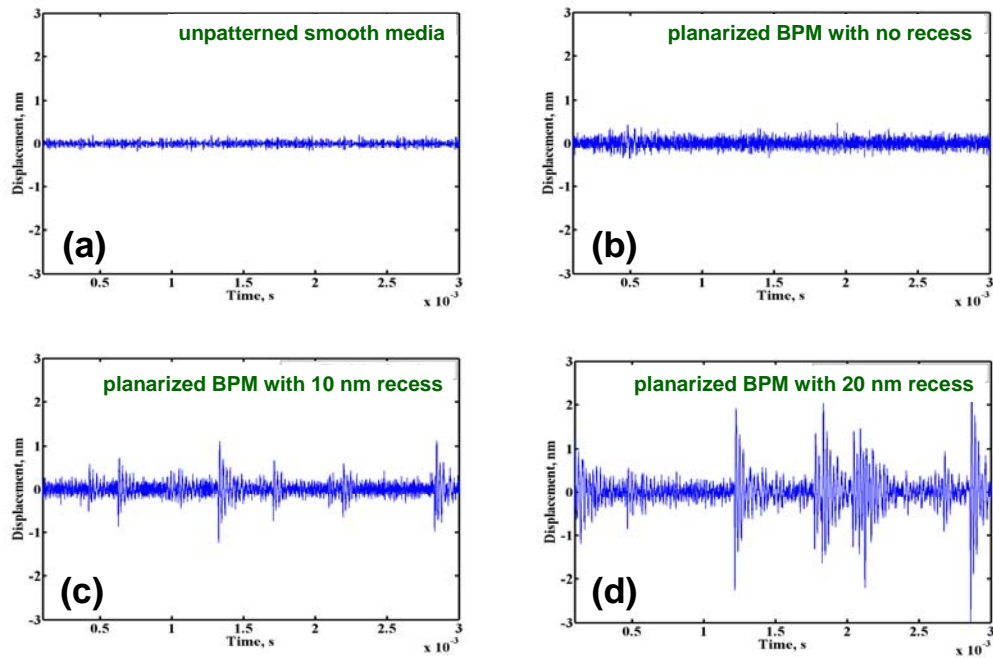
Fig. 13. Comparative measured fluctuation of flying read/write head slider, (a) unpatterned smooth media, (b) planarized patterned media with no recess, (c) planarized patterned media back etch to intentionally create an average 10nm recess, and (d) planarized patterned media with induced 20 nm recess.

always easy. We utilized electric-field-guided CVD growth of carbon nanotubes on Si cantilever to produce such a sharp tip. Shown in Fig. 14 is an example of tip geometry control by using the DC plasma electric field during the CVD growth to intentionally sputter and gradually reduce the CNT catalyst nanoparticles (Ni particles in this case) so that the nanotube diameter is also gradually reduced leading to extremely sharp tip configuration.
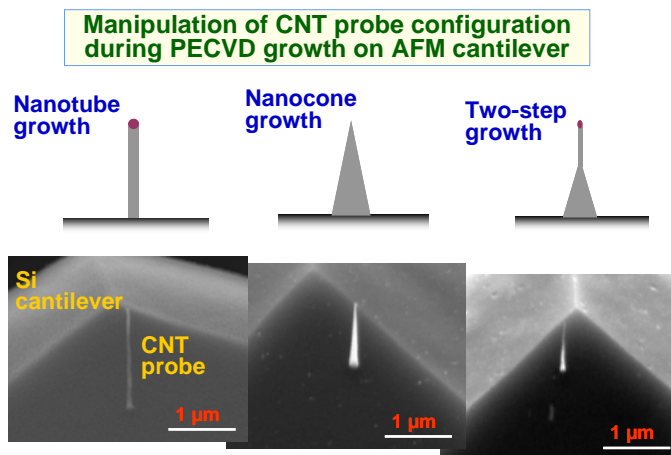
Fig. 14. Control of Carbon nanotube tip geometry on Si cantiler during CVD growth.

Pedestal-configured AFM or MFM probes using carbon nanocone (fabricated in the Jin Lab at UCSD)
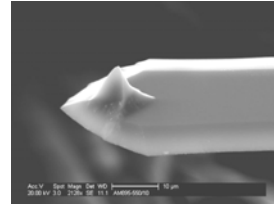
Fig. 15. SEM micrographs for the CNT probe made at UCSD, exhibiting sharp tip configuration grown on truncated AFM probe base.

Higher mag SEM
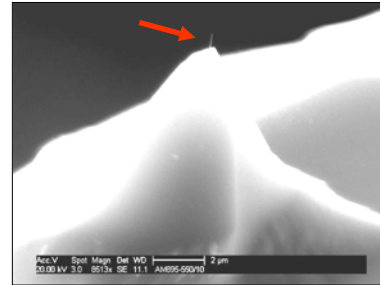
An alternative material for field emitter tip is the silicon tip, which is easier to fabricate utilizing nanofab processes. We have prepared an array of extremely sharp Si tips (with just a few to several nanometer diameter tips) as shown in Fig. 16(a) – (c). A precursor nano-pillar array of Fig. 17, e.g., fabricated by nano-imprinting and RIE or chemical etching, can be used as the basis for such nanotip array fabrication. These silicon nanotip arrays can be fabricated easily by a combination of nano-imprinting and advanced RIE processing. To impart a lower-work-function, relatively easily field emitting tips, the surface of these tips will be either metallized by coating with a thin, stable metal (or alloy, or compound), or carburized to form a conductive or semiconductive carbide layer.

(a)

(b)

(c) Higher mag SEM of probe tip geometry
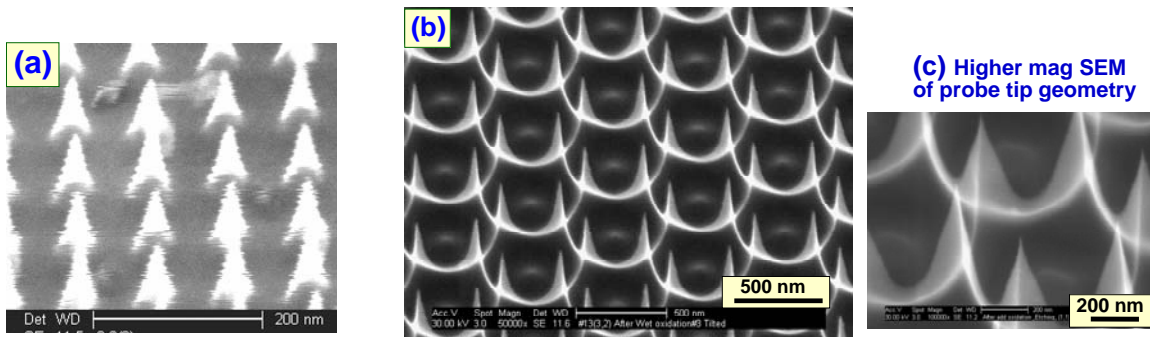
Fig. 16. SEM micrographs for Si nanotip array with very sharp tips for FEPEL probe arrays.
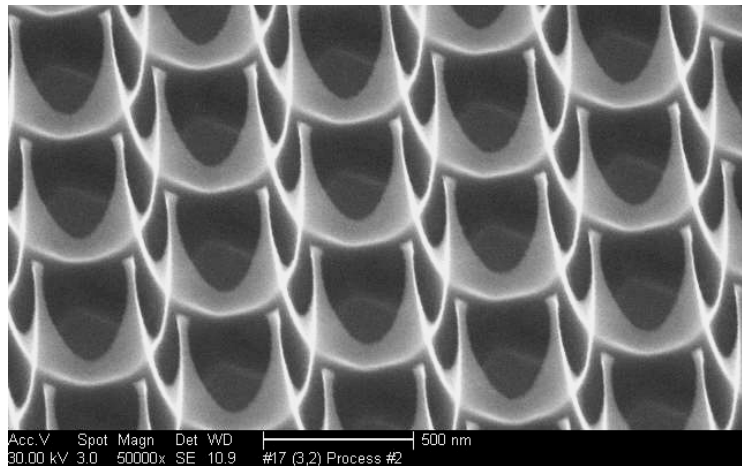
Fig. 17. SEM micrograph for Si pillar arrays in a large area (~0.5 x 0.5 cm area) containing a periodically arranged, ~35 nm diameter tips.

Using advanced e-beam lithography processes, an array of ~10 nm diameter, periodic pillars have successfully been obtained, as shown in Fig. 18. This is equivanent to 1.6 Terabit/in^2, higher than the target bit density of 1.0 Terabit/in^2. The diameter of each island can further be RIE etched to exhibit much sharper tip configuration. Magnetic recording media of (CoPd)n multilayer has been deposited on these high-density islands.
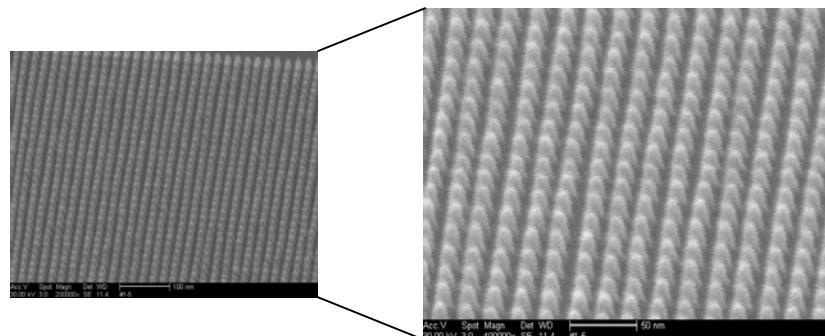
Si nano pillar array with 1.6 TB/in^2 density

• Sub. 20 nm pitch island array obtained (~10 nm diameter Si islands).
• Need further improvements in e-beam lithography for higher density and uniformity

Fig. 18. Periodic ~10 nm dia. Si pillar array by E-beam lithography

(4) Sub-20 nm resolution MFM for Magnetic measurement of nanomagnets

For R&D progress of nanopatterning and preparation of nanomagnets, an evaluation of small area arrays of nanomagnets, such as typical e-beam lotho fabricated

area of 10 x 10 or 100 x 100 μm samples is essential. However, the magnetic signals from such areas are very small, many orders of magnitude smaller than the typical resolution of SQUID machines.Therefore a development and optimization of MFM (magnetic force microscopy) probes for more accurate evaluation patterned media magnetic islands can be very useful. The patterned media magnetic materials, due to their small size, planar distribution and low volume fraction, are well beyond the available SQUID measurement resolution, and there is no other viable techniques except some home-made microMOKE (magneto Optical Kerr Effect) analysis apparatus available only in handful research institutes in the world. When the patterned media island size becomes ~10 nm regime, even the microMOKE will exhibit insufficient sensitivity to measure the M-H loop of these magnetic islands. Currently available MFM probe barely allow measurement of 40 nm magnetic islands.

Therefore, there is an urgent need to develop a new magnetic measurement technology. With the expertise at UC San Diego in fabricating ultra-sharp AFM probes using carbon nanotubes (see the SEM micrographs below), we are also planning to devote substantial amount of time and effort to develop new, ultra-sensitive magnetic measurement technology based on ~10 nm MFM probes and operational techniques. Such a new magnetic MFM probes will enable the study of magnetic switching properties by allowing M-H loop measurements on sub-20 nm island size patterned media, desirably to allow M-H loop characterization of individual islands.

Shown in Fig. 19 is a schematic illustration of a CNT cantilever tip for MFM tip application, made by sputter coating of high-coercivity Fe-Pt magnetic film. The CNT based MFM tips exhibits much enhanced resolution of Co-Cr-Pt-SiO2 recording media on MFM measurements as shown in Fig. 19.
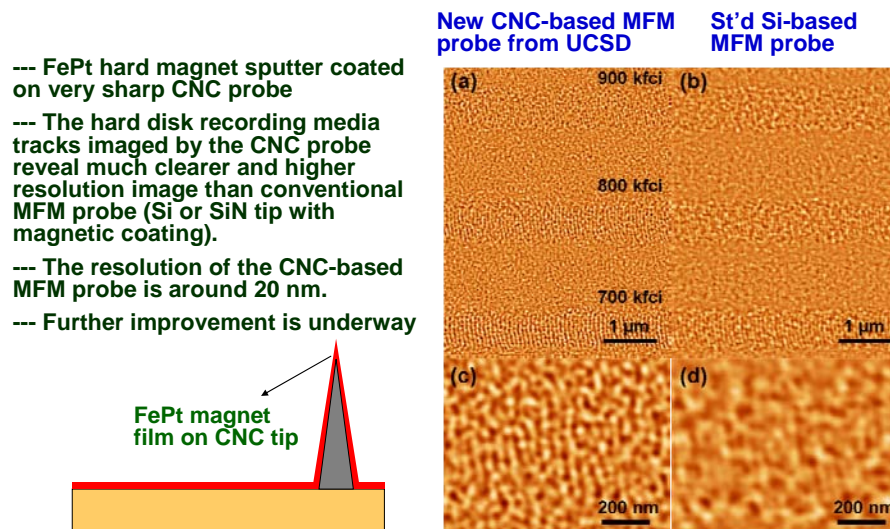
Fig. 19. FePt-coated Carbon Nanocone probes for improved MFM (magnetic force microscopy) imaging.

Currently a new MFM probes tips with sub 10 nm tips are being developed, Fig. 20, for eventual high-resolution MFM measurements of a single magnetic island. Here the high-coercive force, Fe-Pt or Co-Pd type L1o phase nanoparticles are directly used as CNT growth catalyst, the size of which can be gradually reduced during CVD growth by sputter etch process toward ideal size regime.
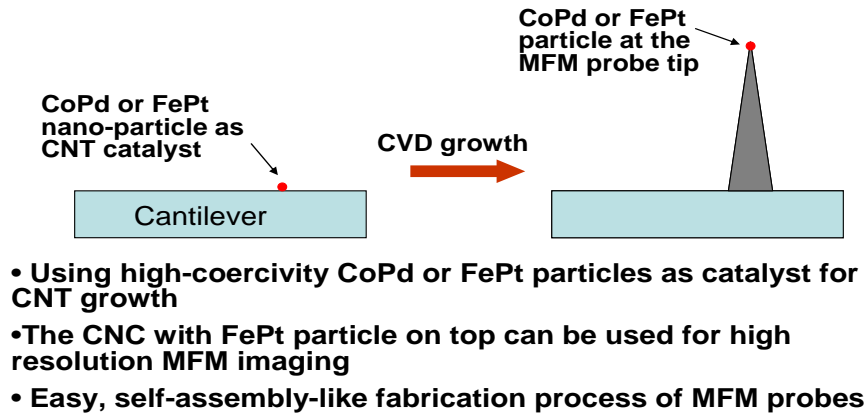

CoPd or FePt particle at the MFM probe tip

CoPd or FePt nano-particle as CNT catalyst

CVD growth

Cantilever

• **Using high-coercivity CoPd or FePt particles as catalyst for CNT growth**

•**The CNC with FePt particle on top can be used for high resolution MFM imaging**

• **Easy, self-assembly-like fabrication process of MFM probes**

Fig. 20. Direct fabrication of high-resolution MFM tips with high coercivity L1o particles positioned at the MFM probe tip.

Shown in Figs. 21 and 22 are such probe tips made of CNT with ~12 nm diameter Co-Pd alloy (L1o phase) nanoparticles, and 10 – 15 nm diameter magnetic Ni nanoparticle at the tip of CNT.

Co-Pd alloy magnet sphere at the CNT tip (Radius of curvature =~12 nm, diameter=~25 nm)

12 nm dia Co-51%Pd alloy magnet sphere at the CNT tip
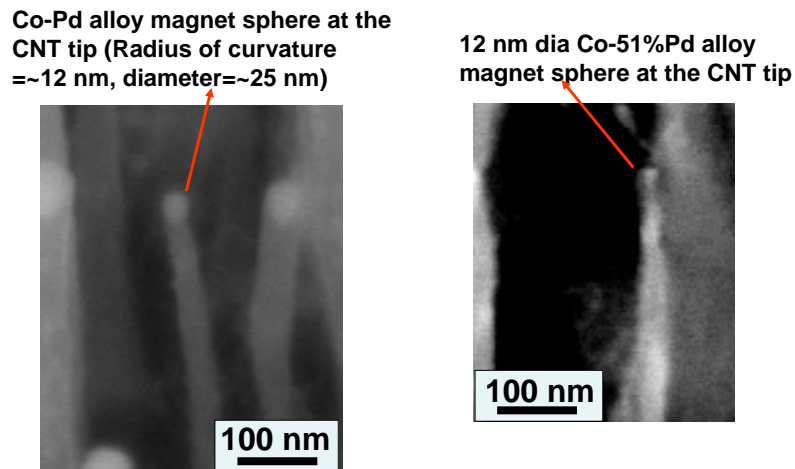
Fig. 21 Carbon nanotube tip with ~12 nm Co-Pd alloy nanoparticle at the apex of the CNT.

100 nm

100 nm

15 nm radius (30 nm dia) Ni island at the CNT tip

~10 nm radius (20 nm dia) Ni sphere at the CNT tip

200 nm

200 nm
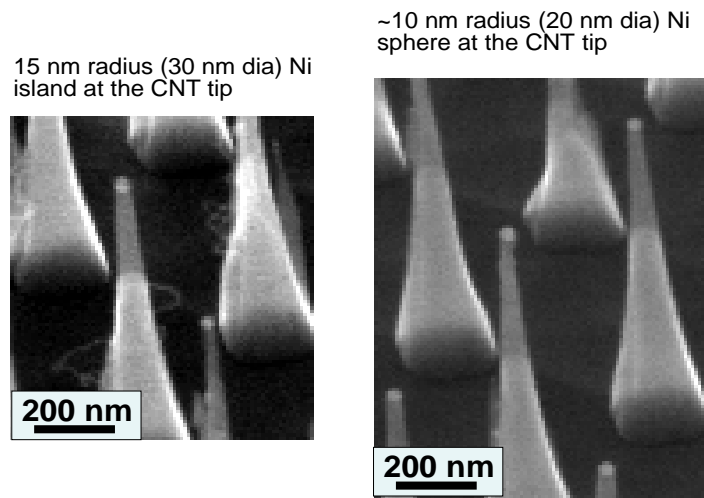
Fig. 22. Carbon nanotube tip with (a) ~15 nm diameter magnetic nanoparticle (Ni) at the tip, and (b) ~10 nm diameter Ni nanoparticle (Ni) at the tip in an array configuration.

(5) Massively Parallel Probe Lithography Toward 10 Terabit/in2 Density Nanofabrication

High-throughput nanofabrication is essential for successful tech transfer of nano materials/device innovations to viable manufacturing levels. Significant advances in the field of nano materials and devices have been made, but, the progress toward large scale integration into useful electronic devices and systems has been rather slow, due to the lack of industrially viable nanofab techniques. New viable solutions are needed to resolve two major bottleneck needs in nano manufacturing, i.e., i) precise placement of nanomaterials/devices in high enough densities, and ii) convenient los-cost high-throughput fabrications.

An alternative approach that has been investigated in this project for such future high-throughput nanomanufacturing is to prepare a multi-tip AFM or STM probes which simultaneously enable massively parallel electron field emission to occur and expose the resist for rapid nanopatterning. Multi-beam based e-beam lithography has been attempted, e.g., SCALPEL projection lithography, however, the complexity and high cost of such systems did not allow successful implementation of the two-dimensional e-beam lithography technique. AFM probe arrays have also utilized for parallel writing (e.g., MILLIPEDE System), however, the operation of tens of thousands of parallel cantilevers makes such a system too complicated and difficult to allow reliable and low cost operation of nanopatterning.

In this project, we take an entirely different approach of employing massively parallel tips (e.g., 100 million of them) all placed on a single AFM probe cantilever for easy operation of parallel writing. The design, development and fabrication of multi-tip arrayed AFM probe was pursued for demonstration of multi-tip probe fabrication and

principle of high-throughput AFM lithography patterning. Either localized field emission from the probe tips for parallel electron exposure of a resist layer, or localized induced oxidation of substrate surface by applied voltage can be utilized.
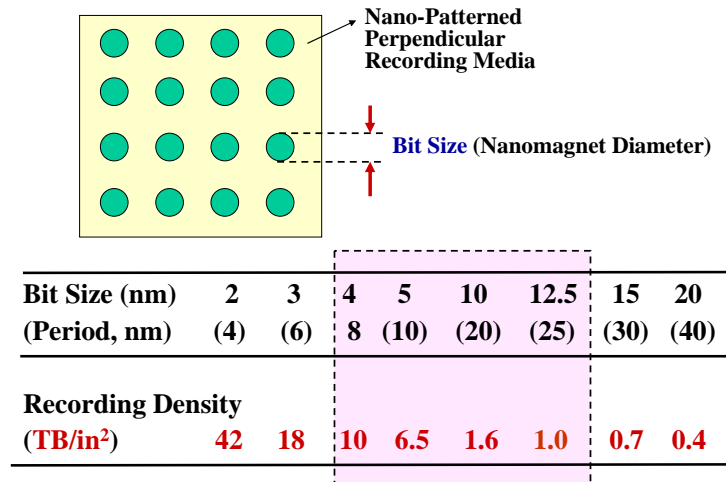
Upper Limit Magnetic Recording Density vs Bit Size

Nano-Patterned
Perpendicular
Recording Media

Bit Size (Nanomagnet Diameter)

Bit Size (nm)	2	3	4	5	10	12.5	15	20
(Period, nm)	(4)	(6)	8	(10)	(20)	(25)	(30)	(40)
Recording Density (TB/in^2)	42	18	10	6.5	1.6	1.0	0.7	0.4

Fig. 23. Schematic description of the required nanopatterning dimensions to achieve certain areal bit memory density.

Shown in Fig. 23 is a schematic description of the required nanopatterning dimensions to achieve certain areal bit density, for example, for ultra-high-density magnetic hard disk memory media. To achieve an ultra-high-density bit array of $1 - 10$ terabit/square inch (TB/in^2) memory density so that the current hard disk memory density can be increased by a factor of 5 - 50, the individual bit size will have to be ~$4 - 12.5$ nm diameter. Using advanced e-beam lithography, 10 nm island arrays (equivalent to 1.6 TB/in^2) have been successfully demonstrated. However, nanomanufacturing requires highthroughput operations, and a multi-tip probe systems is one of the viable candidate lithography techniques.

Fig. 24. High-density (1 TB/in^2) AFM lithography by a sharp carbon nanotube probe tip.
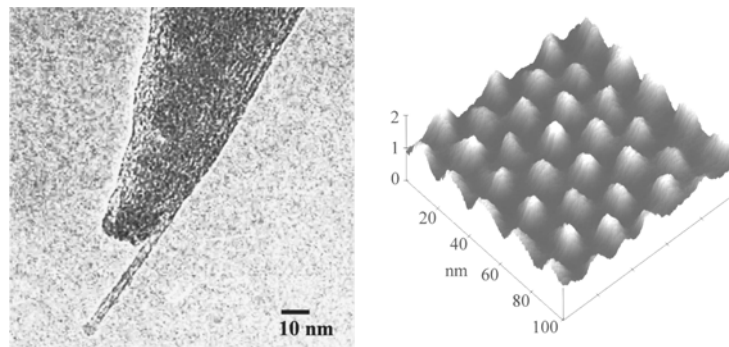
Single probe CNT for "1 Terabit-per-square-inch" AFM Lithography
--- E.B Cooper (C.F. Quate's group), APL 75, 3566 (1999)
--- Ti film oxidized pattern with 8 nm bits, 1 nm TiO2 height (on single-crystal Al2O3 (sapphire))

3.3 TB/in² bit density written

Single probe (heated) AFM tip on Gd-Sb-Te film for "3.3 Terabit/in²" AFM Lithography
--- Hamann, et al, Nat. Mater. 5, 383 (2006).
--- Gd-Sb-Te phase change alloy film -- Amorphous-crystalline phase change by laser heated AFM probe tip.
--- 10 Terabits/in² may not be far away if millions of tips are utilized.

Fig. 25. Bit density of 3.3 TB/in² demonstrated by laser beam heated AFM probe tip.

High-density AFM lithography has been demonstrated using a sharp probe tip such as a singlewall carbon nanotube probe tip. Quate's group has demonstrated 1 TB/in² AFM writing as shown in Fig. 24. Even higher bit density of 3.3 TB/in² has been demonstrated, again with a single tip AFM which was laser heated for nano-localized heat-induced nanopatterning on Gd-Sb-Te film, as described in Fig. 25.

For room temperature operation of electron-emitting AFM tips, field emission from periodically arranged, multiple carbon nanotubes (CNTs) have been evaluated. Such a CNT field emission tip array fabricated in the Jin lab is shown in Fig. 26. The field emission-I-V curves obtained (on the right side of Fig. 26) indicate that an overall high current density of ~1.7A/cm² can be obtained for an emitter array with 2 μm CNT spacing (25 million emitters), for the given applied voltage and 3.3 μm gap. Much higher current density is expected for 2-10 nm gap (for AFM mounted emitter arrays), which can be operated without vacuum because of little collision of electron beam with air molecules at such a small gap distance. The operating voltage can also be very small at 2-10 nm gap.
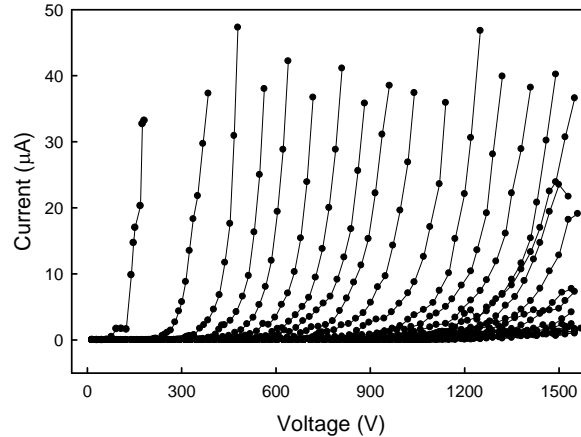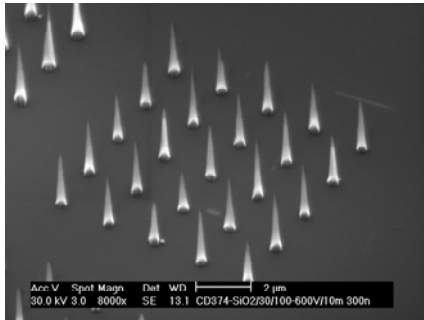
Field emission I-V curves at various distances in steps of 3.3 µm between anode probe and patterned CNT array

Fig. 26. Periodically arranged, multiple CNTs and field emission I-V curves at various cathode-anode gaps.

A field emission I-V curve from a single carbon nanotube (MWNT) was also evaluated using a ~20 nm diameter MWNT. An emission current of ~1 µA was measured at 500 V applied voltage as shown in Fig. 27. This value is in rough agreement with reported values in the literatrure by other investigators. This single CNT probe tip current is much higher than is actually needed for most e-beam exposures on known resist materials (requiring only ~200 pA - 200 nA current level). Even more field concentration (and emission current concentration) is anticipated for sharp 1-4 nm diameter tips that we plan to utilize for massively parallel multi-tip AFM probe field emitters at a closer range of 2-5 nm writing gap.

(a) Decreasing probe height
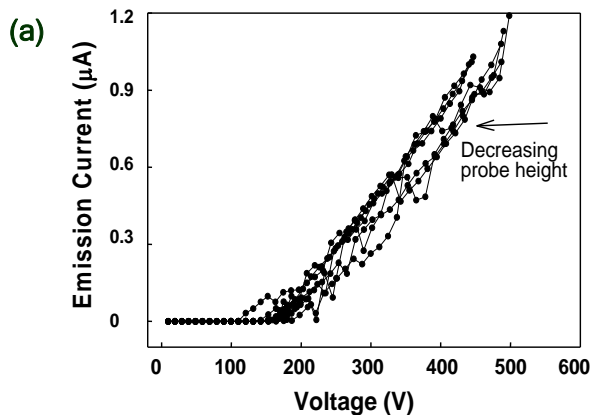
(b) Single CNT cathode (MWNT) attached at the tungsten wire tip
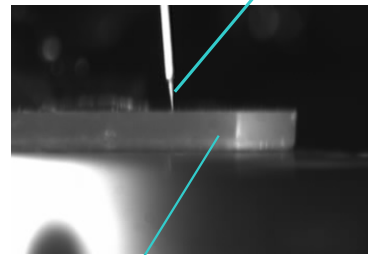
Anode (Cu-coated quartz)

. Field emission I-V curve from a single carbon nanotube (MWNT) field emitter.

Once the desired field emitter array is fabricated, either CNT arrays or Si tip arrays, desirably coated with a low work function (ϕ) surface on a single AFM cantilever, a parallel write operation such as illustrated in Fig. 28 can be performed. We have fabricated a nano emitter arrays of 10^8 (100 million) extremely sharp (~3-5 nm) Si tips with a very thin coating of tungsten, or lower TaC or LaB_6 in 0.6 x 0.6 cm^2 area. These field emitter arrays can be placed either on AFM cantilever or simple horizontal cantilever mounted on a x-y-z nanomanipulator base. An essential requirement is that all writer tips have to be of identical height to ensure identical and reproducible field emission or surface oxidation operations.

Shown in Fig. 29 is an SEM micrograph depicting an AFM cantilever with a CNT tip, which is produced in the Jin lab at UCSD. On a triangular Si pedestal, a single CNT tip was grown using CVD deposition technique. The next step is to fabricate multi-tip arrays on the pedestal surface. We have successfully fabricated multi tip or multi-pillar structures as described in Figs. 30 – 32. Once these multi tip writer is fabricated, many nano devices can be manufactured simultaneously as illustrated in Fig. 23. With 100 million tips operating simultaneously, the nanopatterned devices can be fabricated with a relatively small number of lateral movement and field emission exposures. For example,
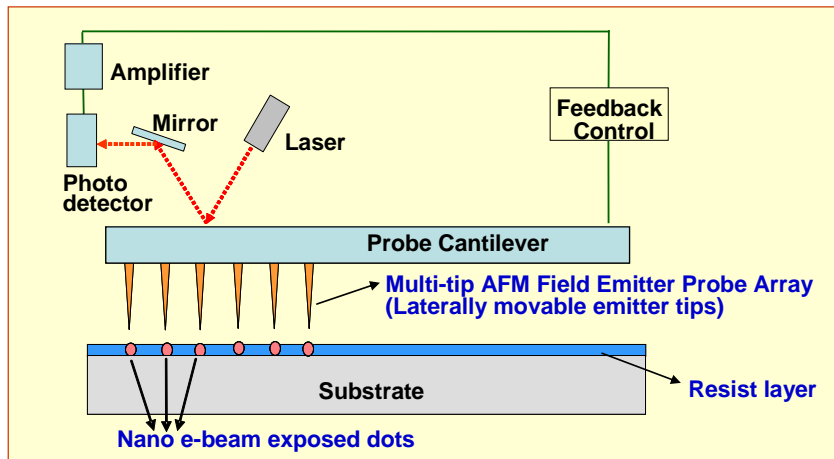
Fig. 28. Multi-tip AFM lithography using a single AFM cantilever containing many parallel tips with identical height.

with 200 nm spacing between the neighboring tips, 10 times horizontal and 10 times vertical movement for repeat exposures will be sufficient to pattern the whole 0.6 x 0.6 cm area in a very short time to fabricate 100 million devices (Fig. 33).

Pedestal-configured AFM or MFM probes using carbon nanocone (fabricated in the Jin Lab at UCSD)

(a)

(b)

(c)
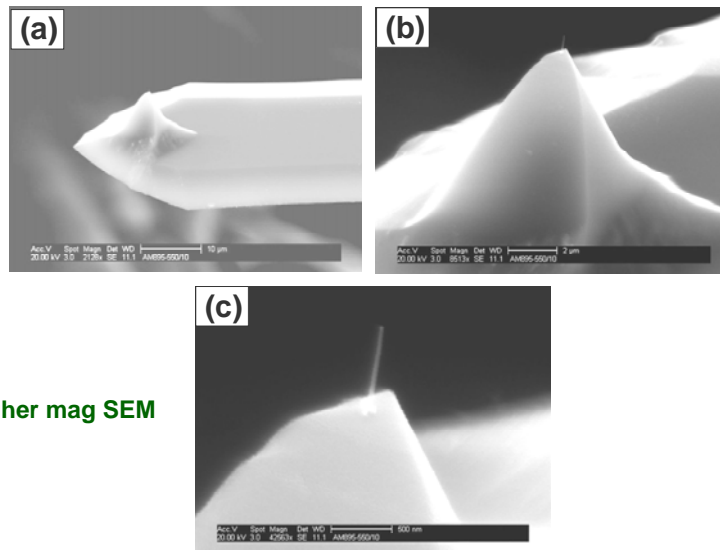
Higher mag SEM

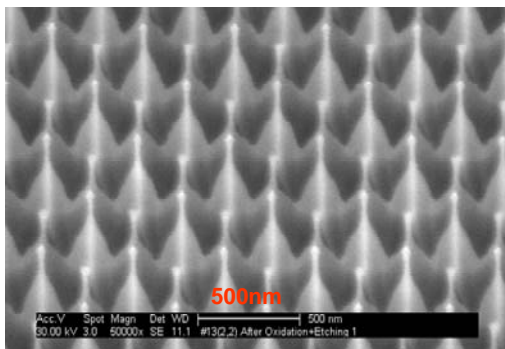Fig. 29. SEM micrograph of an AFM cantilever with a CNT tip.

500nm

Fig. 30. SEM micrograph showing 100 million, identical height Si pillar arrays (~30 nm tip diameter) obtained by controlled patterned etching using nano-imprint lithography and RIE/chemical etching.
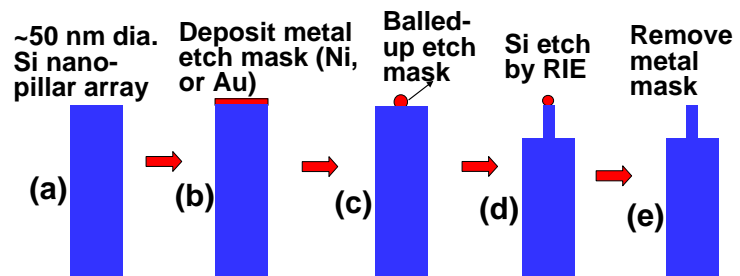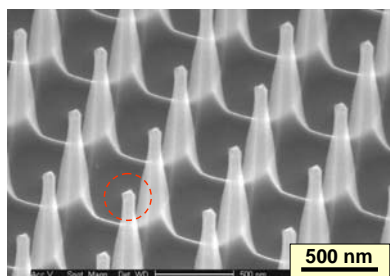

500 nm

~50 nm dia. Si nano-pillar array

Deposit metal etch mask (Ni, or Au)

Balled-up etch mask

Si etch by RIE

Remove metal mask

(a) (b) (c) (d) (e)

Fig. 31. (Left) Periodic Si pillar array with 50x50 nm square (or circular) top surface (100 million pillars with identical height have been fabricated, on a 6 x 6 mm area, which will be utilized as a basis for fabrication of 5 nm diameter Si probe at each pillar top using balled-up metal mask and RIE as illustrated in the schematics (Right).
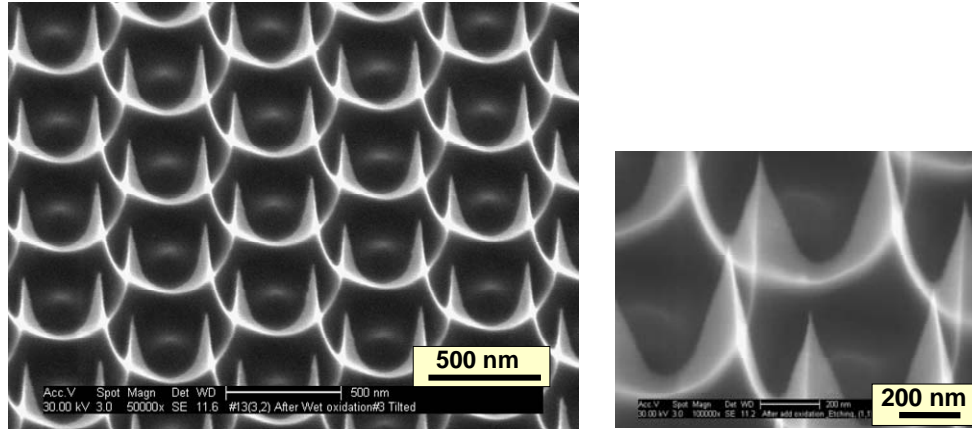
Fig. 32. Massively parallel Si tips fabricated with identical heights. (100 million identical tips). The right side image represents a higher SEM micrograph.
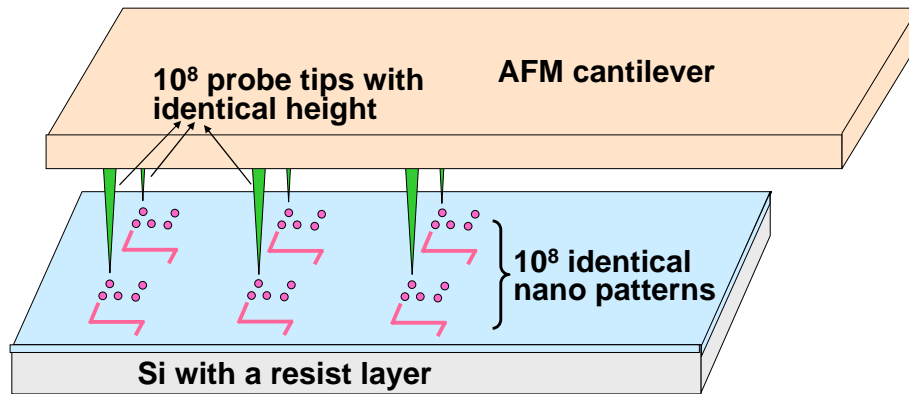

Fig. 33. Multi-tip AFM nano manufacturing of many devices simultaneously (100 million identical devices fabricated at the same time) by lateral movement of AFM lithography cantilever, e.g., for nanomanufactuiring of nano transistor arrays, Qbit array, memory element arrays (magnetic memory, phase change memory), etc.

As the AFM cantilevers are typically operating at a slanted angle of ~12 degrees, there could be an issue of how to ensure all 100 million tips touch down on the substrate simultanesouly with identical gaps. To resolve this issue, we have successfully fabricated

❑ **The bending of the cantilevers after the plasma processing has been studied as a function of NH3/H2 flow ratio**

❑ **Adjusting hydrogen/ammonia gas ratio in CNT growth and manipulating the surface stress conditions**
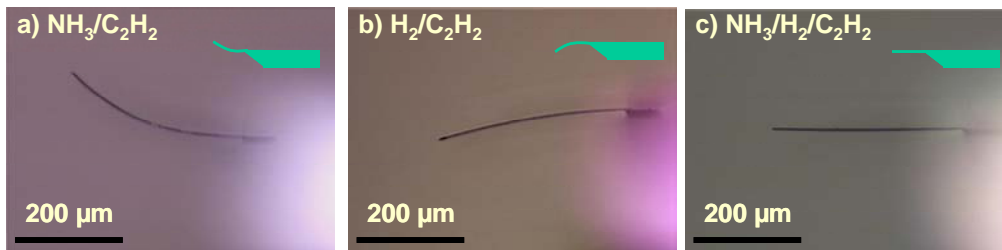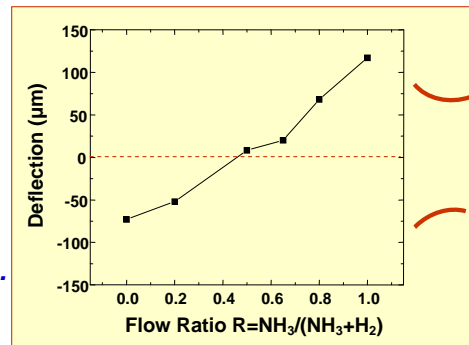
(I.-C. Chen et al., *Nano Lett. 7, 3035 (2007).*

a) NH_3/C_2H_2 200 μm

b) H_2/C_2H_2 200 μm

c) $NH_3/H_2/C_2H_2$ 200 μm

Fig. 34. Control of thin Si cantilever curvature using exposure to a different gas mixture.

thinner cantilever structures (~1/1000 elastic stiffness of standard AFM probe cantilever) without cantilever bending or curvature (Fig. 34). Such a lowered modulus allows an operation of the Si cantilever so that all the tips come down and maintain identical gap distance for identical field emission exposure of the resist layer. This is schematically illustrated in Fig. 35.

(a) **Multi-tip AFM probe array (100 million tips)** — **Compliant AFM cantilever** — **Spacer (rigid or compliant)** — **Si substrate**

(b) **Magnetic layer for gradient field attraction and flattening** — **Compliant AFM cantilever** — **Si substrate** — H   H
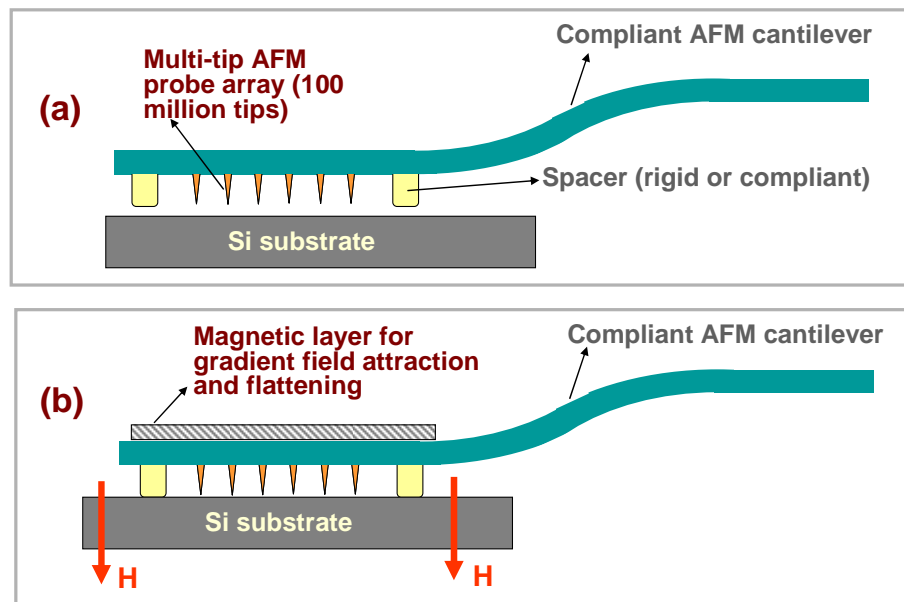
Fig. 35. Thin, lower modulus cantilever to enable identical gap distance when the AFM probe cantilever touches down on to the substrate to be nanopatterned.
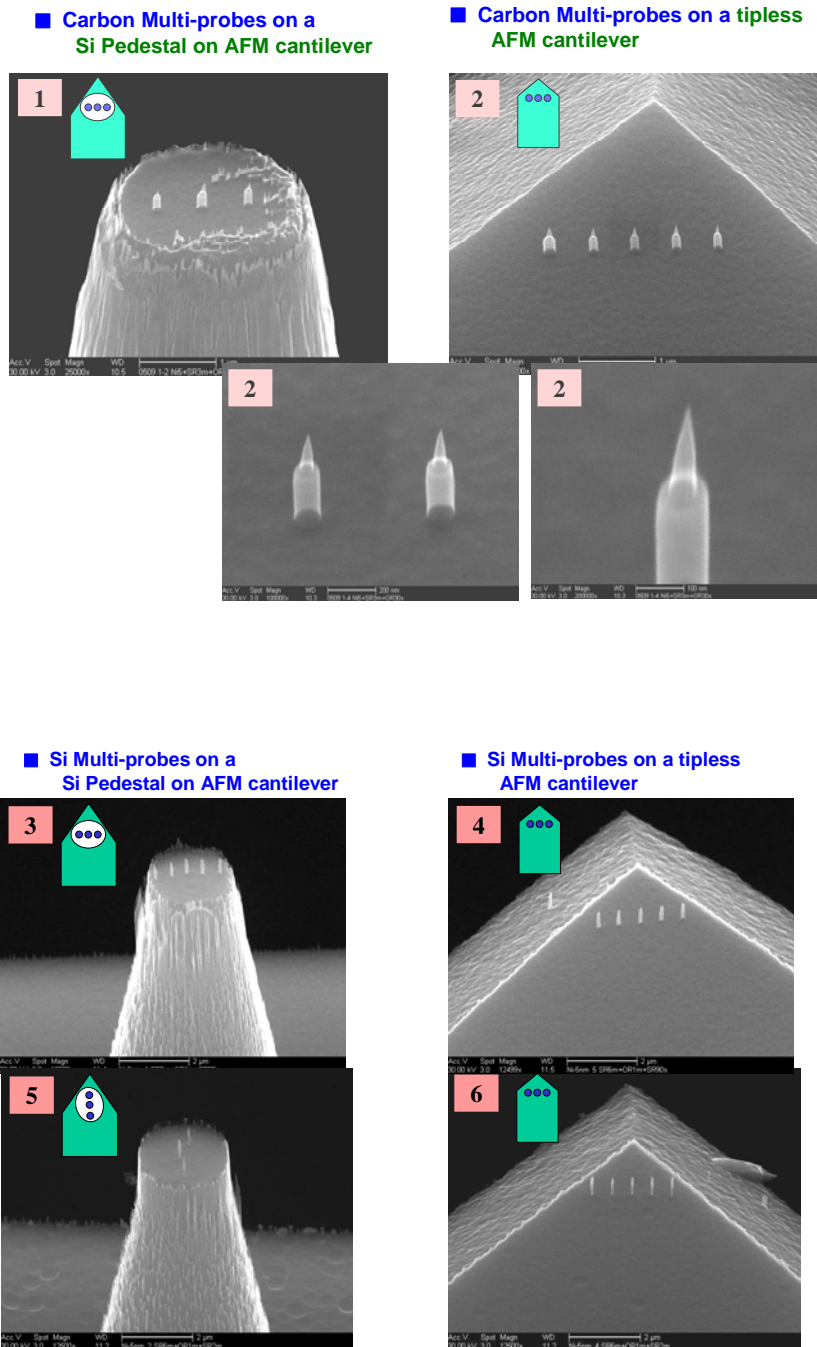
■ Carbon Multi-probes on a Si Pedestal on AFM cantilever

■ Carbon Multi-probes on a tipless AFM cantilever

■ Si Multi-probes on a Si Pedestal on AFM cantilever

■ Si Multi-probes on a tipless AFM cantilever

Fig. 36. Fabricated multi-tip carbon emitters on a Si pedal, positioned on Si cantilevers. Probe #1 and #2 are carbon tips while the Probe # 3-6 are made of Si tips.

Some preliminary AFM lithography experiments were conducted, in collaboration with Prof. Haiwon Lee's group at Hanyang University, using multi-tip AFM probes

fabricated from carbon or Si. The principles of AFM lithography are illustrated in Fig. 37. The probe tips used are made of Si as shown in SEM micrographs of Fig. 38.
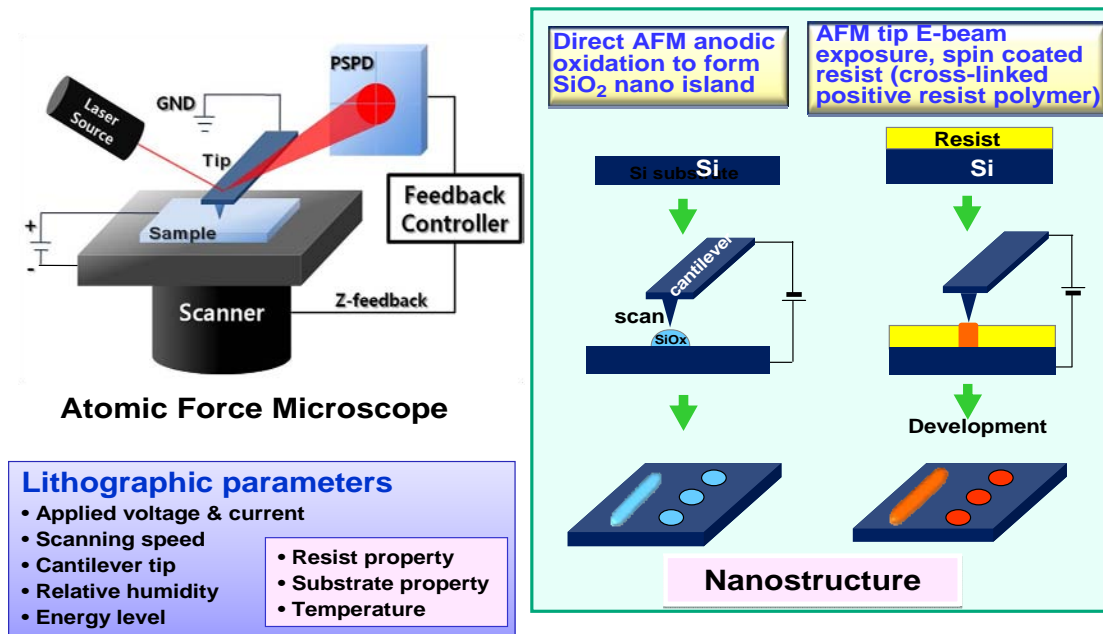
Fig. 37. Schematic illustration of the principles of AFM lithography.
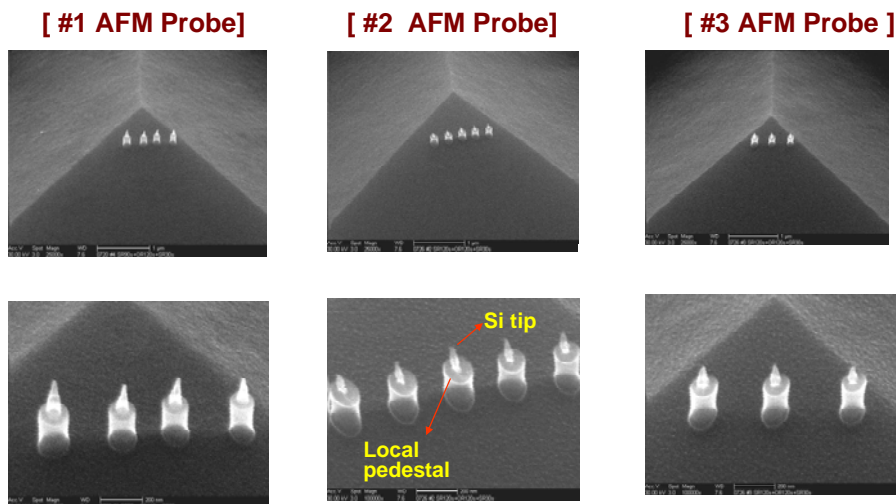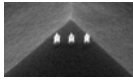

Fig. 38. Three multi-tip AFM probes made for AFM nano lithography experiments.

Dot Array Patterns by Multi-tips E-beam Exposure Lithography (using Spin-coated+Baked Positive Resist)
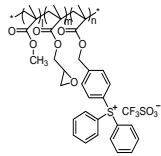
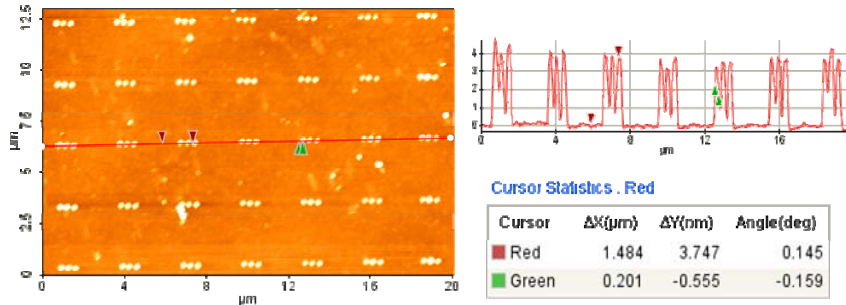**Ambient condition : humidity 63 %, temp. 28 ºC**
Lithographic condition: XE-100(Park Systems Inc.) contact mode,
Pulse sample bias: - 25 V, 200 kHz, 2.5 μsec, litho. time 2 sec, Cantilever force: 5 ~35nN

28 : 54 : 18

PAG ratio	Solution concentration	Resist Spin speed	Thickness (nm)	Soft bake	Development (D.I.W. & IPA)
Ter-polymer	2 wt. %	3000 rpm / 40 sec	26	100 ℃ / 1 min	2 min

Cursor Statistics . Red

Cursor	ΔX(μm)	ΔY(nm)	Angle(deg)
Red	1.484	3.747	0.145
Green	0.201	-0.555	-0.159

Dot arrayed patterns
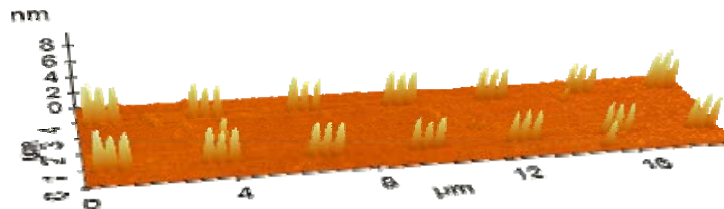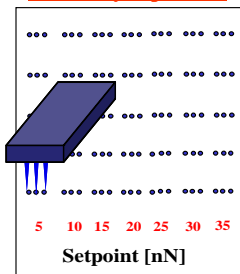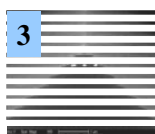
Setpoint [nN]   5 10 15 20 25 30 35

Fig. 39. Multi-tip AFM lithography demonstration using the probe #3 of Fig. 38. Clear nanoisland patterning is shown, with additional repeat patterning on lateral movement of the AFM probe.

Using the multi-tip AFM probe made at UCSD (for example, using the probe #3 in Fig. 38) on a single cantilever, AFM lithography write experiments have been conducted on resist-coated Si substrate wafers. Some preliminary success was obtained using these multi-tip probes as indicated in Figs. 39-41. Either island arrays or line arrays were obtained depending on the mode of AFM lithography utilized.

For nanopatterning of probe tip arrays and other arrangements, an ability to perform a high-resolution electron beam lithography is important, especially for large area patterning. Shown in Fig. 42 are SEM micrographs of e-beam litho patterned Si pillar arrays with two exemplary nanopatterning dimensions, achieved by HSQ polymer exposure and pattern transfer to underlying Si substrate. For nano-imprinting mould

Contact mode Lithography for line pattern generation

Ambient condition : humidity 63 %, temp. 28 ºC
Lithographic condition: XE-100(Park Systems Inc.) contact mode,
Pulse sample bias: - 25 V, 200 kHz, 2.5 µsec, litho. time 2 sec, setpoint: 10 nN

Line patterns

Line Profile, Red

Curser Statistics : Red

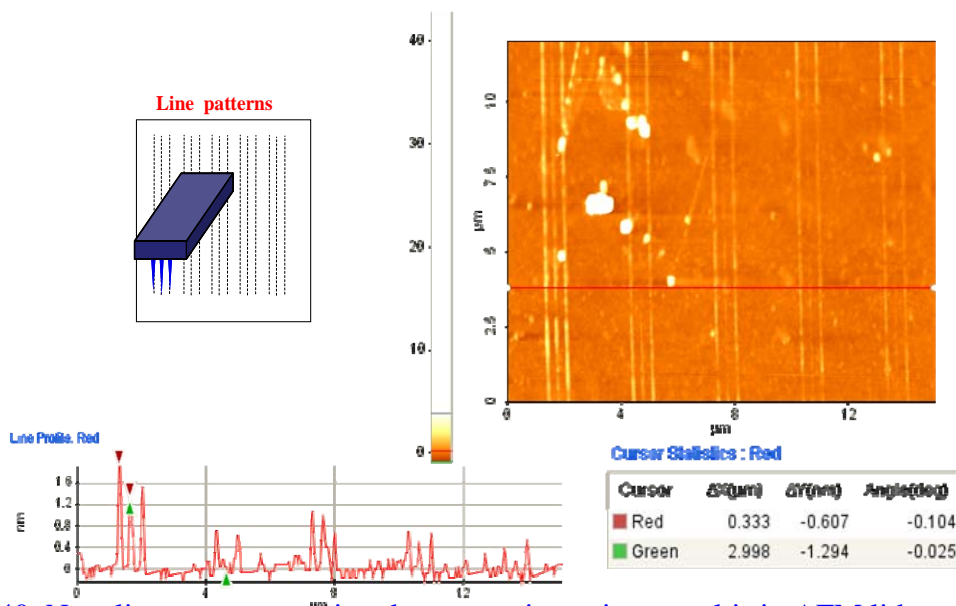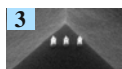| Cursor	∆X(µm)	∆Y(nm)	Angle(deg)
■ Red	0.333	-0.607	-0.104
■ Green	2.998	-1.294	-0.025

Fig. 40. Nanoline array patterning demonstration using a multi-tip AFM lithography lateral continuous movement of the probe #3 of Fig. 38. Clear nanoisland patterning is shown, with additional repeat patterning on lateral movement of the AFM probe.

3 **Repeat Scan Dot Array Patterns by Multi-tips Lithography**
(for fixed cantilever force)

090729 tip number 3

❖ Ambient condition : humidity 63 %, temp. 28ºC
❖Lithographic condition: XE-100(Park Systems Inc.); contact mode, resist-coated Si substrate
❖Cont. bias: - 21 V, setpoint: 10 nN

PAG ratio	Concentration	Spin speed	Thickness (nm)	Soft bake	Development (3D.I.W. & 7 IPA)
36 % PAG co polymer	3 wt. %	5000 rpm / 30 sec	30	100 ℃ / 1 min	2 min

Dot Array Lithography

Negative Resist

Si
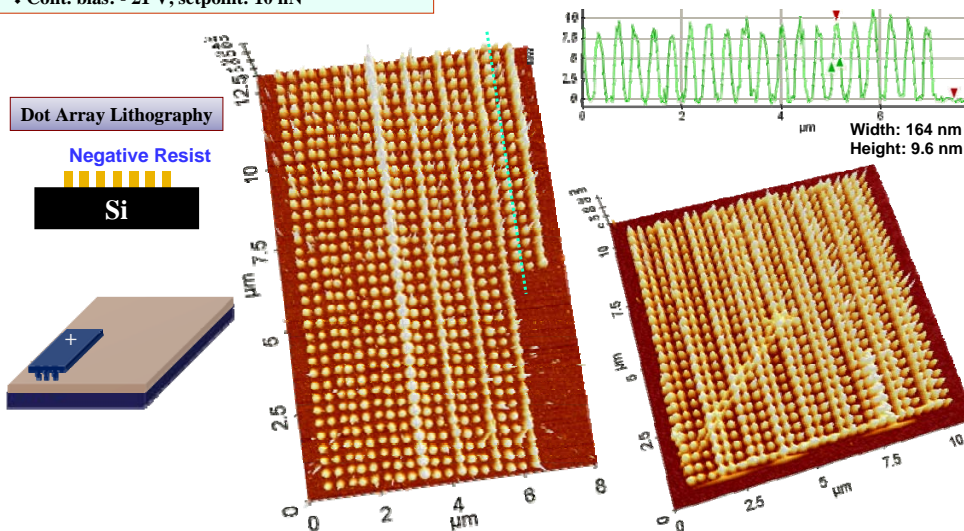
Width: 164 nm
Height: 9.6 nm

Fig. 41. Additional lateral movement of multi-tip AFM lithography tip for nanoislands array synthesis demonstration using the probe #3 of Fig. 38.

fabrication and other fabrication of nano arrays or nanoprobes, a larger area patterning was attempted. A successful nanopatterning of periodic nanopillars of ~10 nm diameter and ~10 nm spacing was achieved over 2 x 2 mm area as shown in Fig. 43. This area coverage is significantly larger than typical e-beam lithography of tens (or at most hundreds or micrometers). Stiching of millimeter size areas by successive nano-imprinting can be useful for obtaining even larger nanopattern size. Shown in Fig. 44 is an example stepwise nano-imprinting of neighboring areas to enlarge the imprinted area aiming at follow-up pattern transfer to produce yet larger nano-imprint moulds.

Fig. 42. SEM images showing topographical features of bit patterned media. (a) 30 nm diameter bit array(~0.18 Terabit/in2 density), (b) 10 nm diameter bit array (1.6 Terabit/in2 density).

(a) 30nm dia x 60nm height

1.6 Terabit/in2 density

(b) 10nm dia x 20nm height

100 nm

50 nm
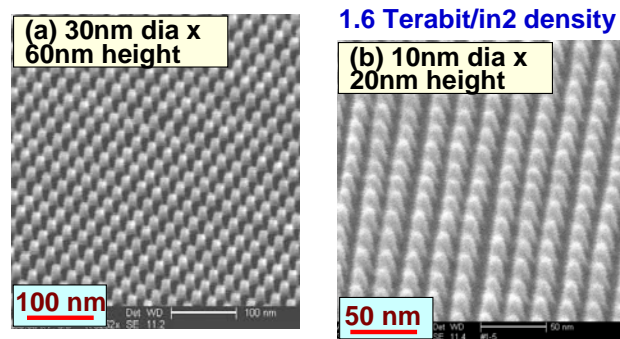
"Nano-imprint stamp" fabricated --- *Long range order of uniform array over 2 mm × 2 mm area with 1.6 TB/in2 density(10 nm Si island, 20 nm pitch)* – *To be used as nano-imprint stamp for magnetic recording media fabrication.*

2 mm

Blown up image

10 μm
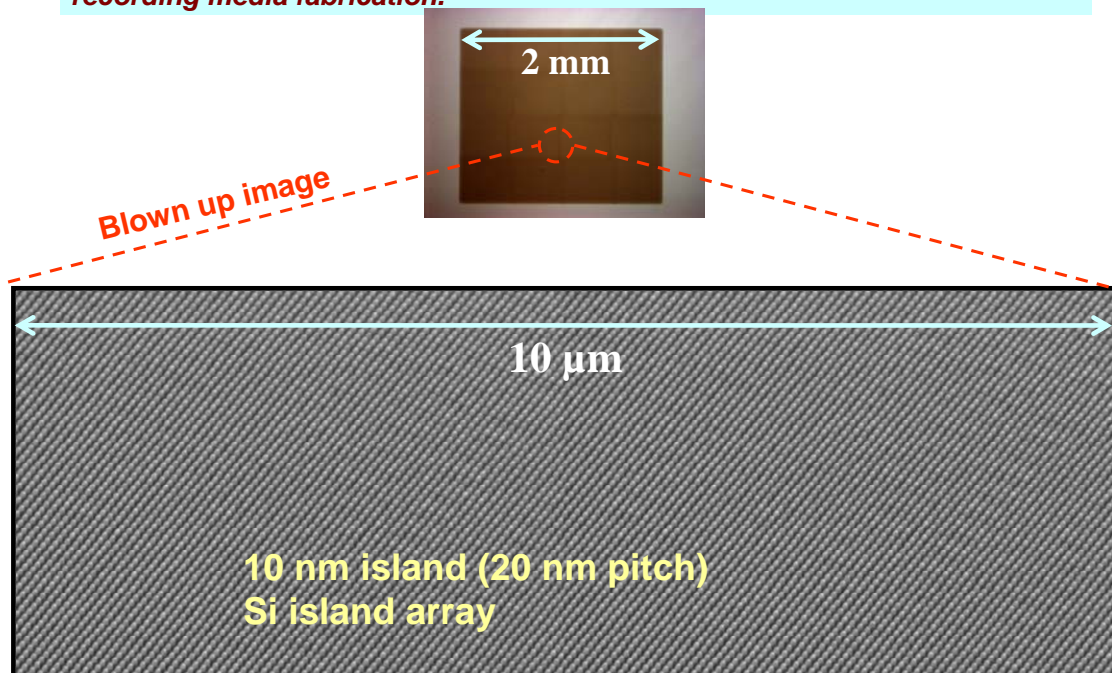
10 nm island (20 nm pitch) Si island array

Fig. 43. Long-range ordered Si pillar array with 1.6 terabits/in2 density (~10 nm diameter and 10 nm spacing).
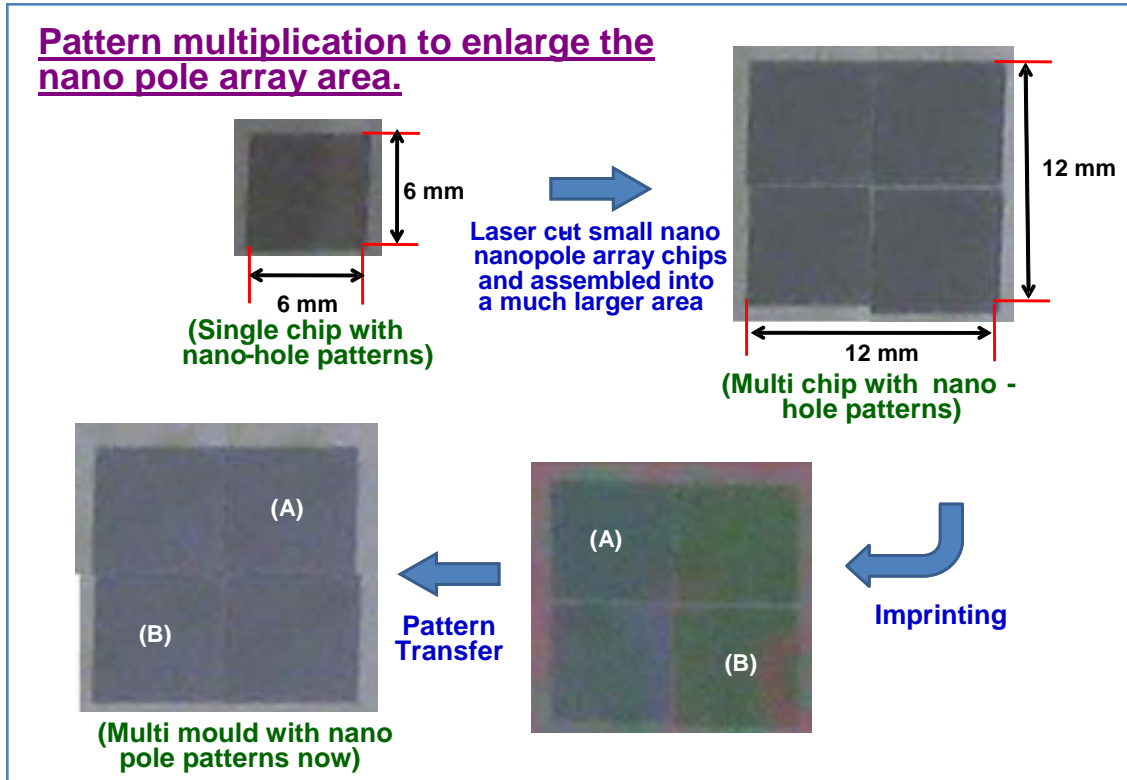

Fig. 44. Nano-imprint mould size (area) enlargement by assembling smaller area chips with a negative (hole) pattern, which is then used for nano-imprinting onto a PMMA layer to produce a positive (pillar) array pattern followed by pattern transfer to the Si substrate underneath to generate a new, pillar geometry, larger-area nano pole arrays. As a demonstration, four square pieces of 0.6 x 0.6 cm sized nano-stamps of hole arrayed Si (DUV patterned, 150 -300 nm hole diameter) were assembled, imprinted onto PMMA, followed by DUV etching to create a new nano pole array having a positive (pillar array) pattern with a larger area (1.2x1.2 cm size).

For magnetic recording media, the patterned magnetic bit storage islands need to arranged, not in linear fashion, but in a circular arrangement because of the disk drive rotational movement. We therefore conducted experiments on nano-island patterning to achieve such a circular geometry as illustrated in Fig. 45 and shown in Fig. 46. A CAD (computer-aided-design) operation was utilized to generate such patterns.

Circularly patterned Si imprint moulds
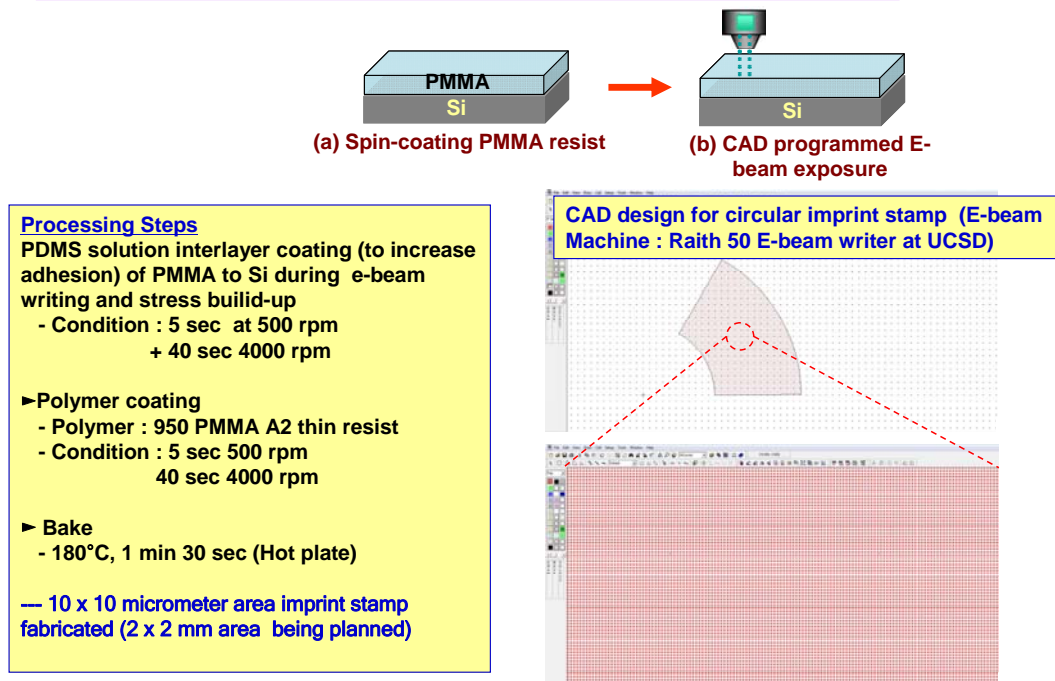(Necessary for magnetic hard disk memory)

PMMA
Si

Si

(a) Spin-coating PMMA resist

(b) CAD programmed E-beam exposure

Processing Steps
PDMS solution interlayer coating (to increase adhesion) of PMMA to Si during e-beam writing and stress builid-up
** - Condition : 5 sec at 500 rpm**
**   + 40 sec 4000 rpm**

►Polymer coating
** - Polymer : 950 PMMA A2 thin resist**
** - Condition : 5 sec 500 rpm**
**   40 sec 4000 rpm**

► Bake
** - 180°C, 1 min 30 sec (Hot plate)**

--- 10 x 10 micrometer area imprint stamp fabricated (2 x 2 mm area being planned)

CAD design for circular imprint stamp (E-beam Machine : Raith 50 E-beam writer at UCSD)

Fig. 45. E-beam lithography patterning exposure for circularly arranged dots.

SEM image of circular pattern (curved) nano-island array
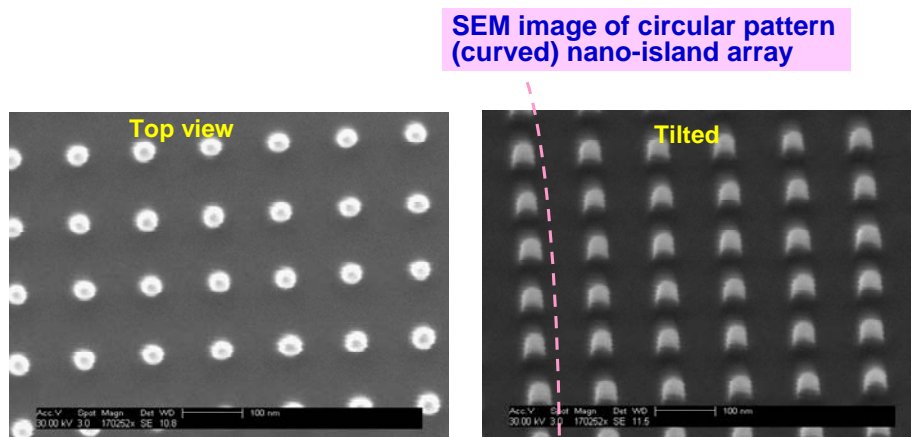

Top view

Tilted

Fig. 46. Circularly arranged Si nanoisland array. The dotted curve traces the curved geometry.

In magnetic disk drive memory utilizing patterned magnetic media, the magnetic islands need to be separated with minimal magnetic material in between spaces to minimize magnetic signal interference. Also, the topographical configuration should be planar on the surface so as to allow the read/write head slider to fly. This desired configuration is schematically illustrated in Fig. 47.
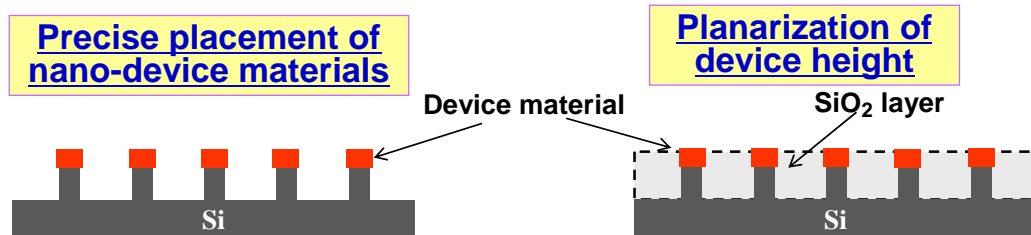

Fig. 47. Desired configuration of magnetic nano-island bits in patterned media hard disk drive media. (Left): Selective precise positioning of the magnetic islands in patterned media. (Right) Planarization of in-between spaces to enable read/write head flying on patterned media in magnetic hard disk drives.

As a demonstration of principle to illustrate that such a structure can be realized, we fabricated a ~100 nm diameter periodic array of Si nano pillars using nano imprint lithography (NIL). Each of the samples contained ~100 million Si nanopillars over a relatively large area of 0.6 cm x 0.6 cm. The processing sequence utilized is illustrated in Fig. 48. The oblique angle SEM image of the bit patterned media consisting of high-coercivity magnetic multilayer stacks of [Ta 3 nm\Pd 3 nm\[Co 0.3 nm\Pd 0.8 nm]$_8$] deposited on top of Si islands as well as in the valleys (trenches) is shown in Fig. 49(a). The patterned Si islands have a dimension of ~100 nm diameter, ~ 100 nm height and a periodicity of 400 nm. It is notable that the Si island nanofeature dimension is undesirably altered during the magnetic multilayer deposition, with the magnetic materials deposited in the trench, on the top, as well as on the sidewall of the pillars. Also shown in Fig. 49(b) is the SEM image of the Fig. 49(a) nanopillar structure subjected to an additional process of geometrical planarization using HSQ (hydrogen silsesquioxane) spin coating, back etch and conversion of the trench HSQ into SiO$_2$ by annealing. The trenches are completely filled by HSQ. The planarization process has reduced the bit height from ~ 100 nm to ~ flat, 15 nm layer. Only the magnetic bit islands are exposed. In order to restrict the presence of magnetic materials only on the pillar top, not in the unwanted places such as sidewall and valley, the samples were pre-covered by PMMA (poly-methylmethacrylate) using spin coating before magnetic layer deposition so as to exclude the magnetic materials on these unwanted locations. After spin coating, the superfluous PMMA is back-etched by RIE to reveal the top of the Si islands. The required RIE time depends on the thickness of PMMA, the height of the Si pillars, and
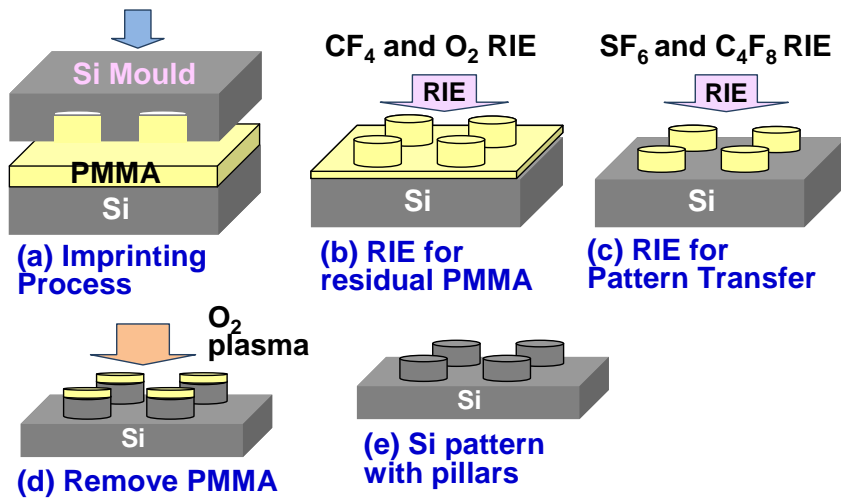
Fig. 48. Schematic illustration of the fabrication processes for bit patterned media (BPM) using trench-filling process.
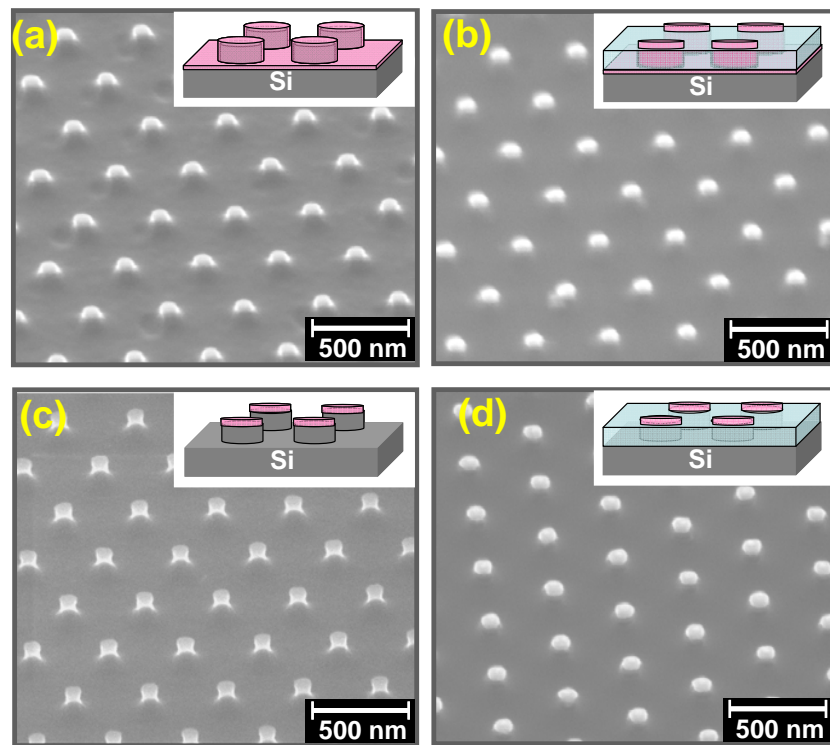

Fig. 49. SEM images showing topographical features of bit patterned media. (a) magnetic media deposited without trench filling, (b) the structure of (a) + additional geometry planarization, (c) magnetic media deposited with trench filling for isolated magnetic islands, and (d) the structure of (c) + additional geometry planarization. The insets show the schematic description of the BPM nanostructures.

the etching rate. A SEM image of a BPM with the magnetic recording media material restricted to the Si pillar top area via the trench-filling process is shown in Fig. 49(c). It is apparent that the trench filled nanostructure controls the location of magnetic material in a well-defined manner and prevents the unwanted deposition of magnetic material outside the pillar tip region.
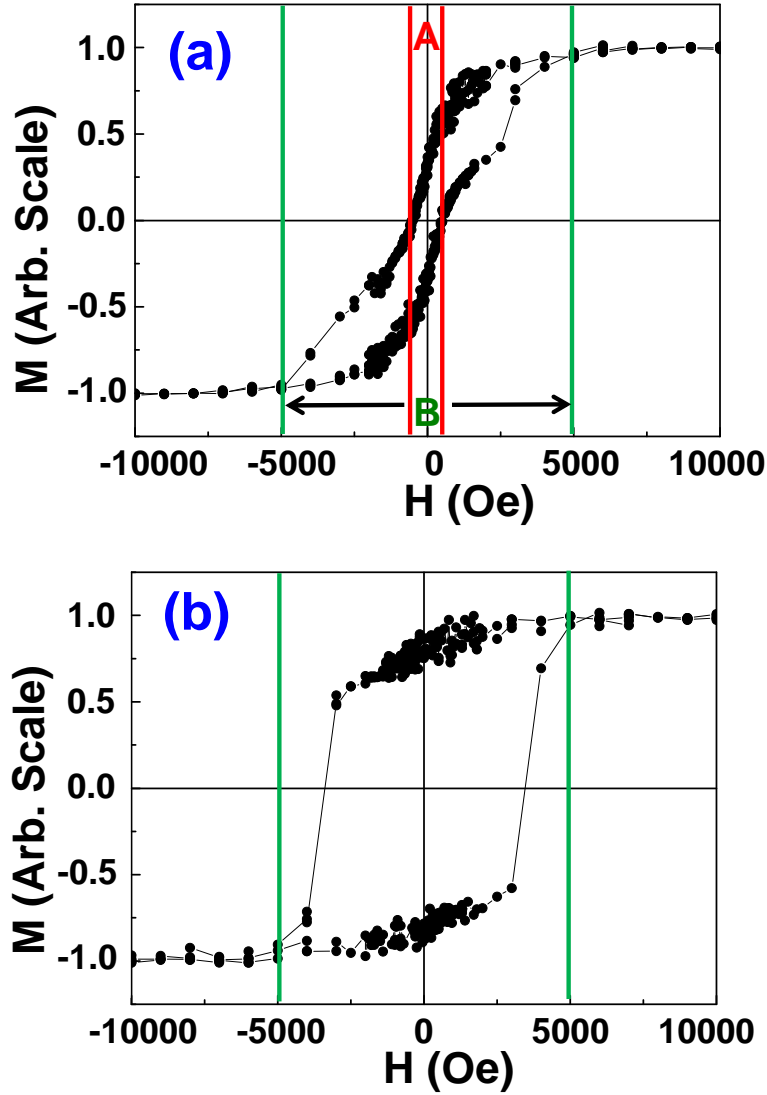

Fig. 50. M-H loop of bit patterned media by SQUID measurements for (a) BPM with unremoved magnetic materials in the trenches, (b) BPM with trench filling process for isolated magnetic islands.

To evaluate how such nanostructural manipulations influence the magnetic behavior of BPM media, the magnetic properties of BPM were measured and analyzed. Figure 50(a) shows the M-H magnetization loop of the patterned media measured by SQUID (superconducting quantum interference device), without the trench filling process. This M-H loop appears to have two distinctly different regions. The Region A (marked in Fig. 50(a)) represents the magnetic signal from the relatively continuous CoPd multilayer film in the valley, which exhibits a low coercivity of only about 600 Oe as anticipated for non-nanosize Co-Pd layer materials. The Region B, on the other hand, shows the magnetic signal from the ~100 nm diameter size-confined CoPd multilayer islands on top of the Si pillars, which exhibits a much higher coercivity of about 5000 Oe. It is known that the smaller CoPd multilayer islands produce much higher coercivity. The M-H loop clearly shows that not only was the magnetic multi layer present on top of pillars, but on sidewall and valley. Shown in Fig. 50(b) is the M-H loop measured from BPM with magnetic material confined to the Si pillar top only, accomplished by using the trench-filling process. Contrary to the M-H loop of Fig. 50(a) for the BPM without filling process, Fig. 50(b) exhibits a much better defined M-H loop indicative of a more uniform material, namely only the pillar top island magnetic material.
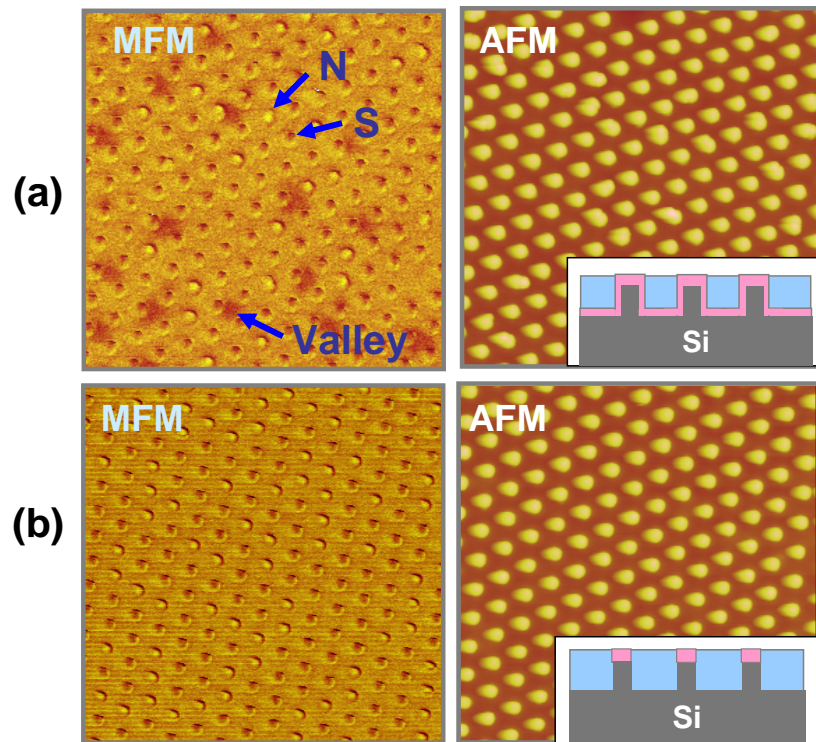

Fig. 51. MFM data (left) and AFM data (right) of BPM (a) without trench filling process vs. (b) with trench filling process.

Shown in Fig. 51(a) are typical magnetic force microscopy (MFM) & atomic force microscopy (AFM) images of the BPM without the valley (trench) filling process. The schematics in the insets illustrate the cross-sectional geometry of the magnetic recording media in relation to the substrate and the HSQ filler material. The AFM data, Fig. 51(a) (rightside image, representing ~5 µm square area) indicates a relatively uniform pillar array. The MFM image (leftside image) shows a somewhat smaller island images, which is possibly related to the larger measurement distance between MFM probe tip and magnetic multilayer surface as compared to the AFM imaging. The light phase vs dark phase represent opposite magnetization direction in the MFM imaging. It is seen that the valley regions also show some response to the MFM imaging (darker and blurry contrast regions) indicating the presence of magnetic materials in the valley. In the BPM processed with the trench-filling step (thus having the magnetic material only on the island top), the MFM image of Fig. 51(b) leftside is much more uniform than the case of Fig. 51(a) MFM imaging, and Fig. 51(b)exhibits no dark contrast regions from the valley seen in Fig. 51(a).

Higher resolution MFM image of the BPM with the filling process (magnetic material only on the pillar top), Fig. 52, indicates further details of the domain structure. Because of the somewhat larger island diameter of ~ 100 nm, the magnetic island is not a single domain in this particular case, and a two-domain structure is therefore observed. It is anticipated that single domain structure in a periodic arrangement will be obtained if the island diameter is reduced to ~50 nm or smaller, which is one of our current research topics.
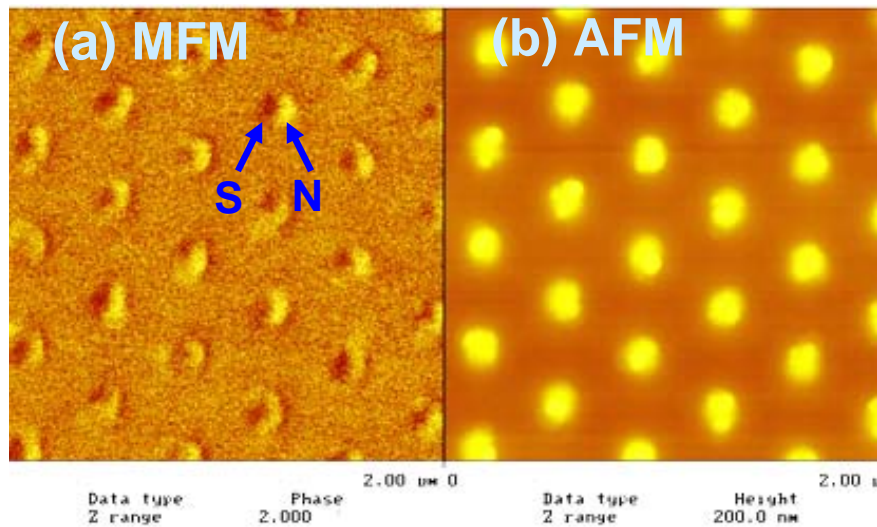

Fig. 52. Higher resolution images of (a) MFM and (b) AFM for the BPM with trench filled nanostructure.

Summary

Over the 3 year project period, substantial R&D progress has been obtained, with the main accomplishments listed below.

1. Magnetic memory bit density as high as 1.6 TB/in^2 (with the magnetic nanoisland size of 10 nm and 10 nm spacing) has been accomplished by using advanced e-beam lithography processing. Nano-imprint mould with relatively large coverage area of 2 mm x 2 mm has been fabricated, and the principle of stiching smaller size moulds to produce larger-area moulds has been demonstrated.

2. It is shown that the magnetic nanoisland switching field distribution can be reduced by eliminating or decreasing the slanted wall of Si nanoisland structures for magnetic bit deposition.

3. Advances in MFM tip fabrication for measurement of small magnetic signals and magnetic sensing have been made. The eventual goal is to develop magnetic sensor with M-H loop measurements with a sensitivity/resolution of ~6 orders of magnitude higher than the typical SQUID magnetometer.

4. Fabrication of huge number of CNT or Si nanotip field emission array has been demonstrated, with as many as 100 million identical-height tips demonstrated using Si pattern transfer with nanoimprint patterning and chemical/RIE etching steps.

5. Multi-tip AFM probes have been successfully fabricated, and multi-nanoislands or nanolines patterning has been demonstrated. Additional research is in progress toward 100 million tip AFM lithography (or nanomanipulator system lithography) toward high throughput nanomanufacturing.

UCSD Personnel Participated in the NBIT Research (2007 – 2010)

-- Research Scientist: Dr. & Prof. Leon Chen
-- Postdoctoral researcher: Edward Chulmin Choi
-- Graduate student: Michael Oh, Mariana Loya, Kunbae Noh

Publications (supported by NBIT Program)

1.. Jung-Sub Wi, Hyo-Sung Lee, Kipil Lim, Sung-Wook Nam, Hyun-Mi Kim, Soo-Yeon Park, Jae Jong Lee, Chris Daehoon Hong, Sungho Jin, and Ki-Bum Kim, "Fabrication of Silicon Nanopillar Teradot Arrays by Electron-Beam Patterning for Nanoimprint Molds", *Small 4(12)*, 2118 (2008).

2. Kunbae Noh, Karla S. Brammer, Hyunsu Kim, Se-Yeon Jung, Tae-Yeon Seong, and Sungho Jin, "Highly Self-assembled Nanotubular Aluminum Oxide by Hard Anodization", *J. Mater. Res*. (in press, December 2010).

3. J.Y. Kim, K. Noh, C. Choi, K.S. Brammer, M. Loya, L.H.Chen and S. Jin, "Optically Transparent Glass with Vertically Aligned Surface Al2O3 having Superhydrophobic Characteristics", *NANO: Brief Reports and Reviews*, Vol. 5(2), 89–95. [DOI: 10.1142/S1793292010001962]. (in press, 2010)

4. Kunbae Noh, Chulmin Choi, Jin-Yeol Kim, Young Oh, Karla S. Brammer, Mariana Loya, and Sungho Jin, "Long-Range Ordered Anodic Alumina Nanotubes by Nanoimprint-Assisted Aluminum Surface Engineering", **J. Vac. Sci. Tech. B28(6),** (DOI: 10.1116/1.3498759) [in Press, November 2010].

Interactions:

 (a) Conference Presentations
1. Sungho Jin and Kibum Kim, "High-Resolution, Large-Area Nano-imprint Lithography using Crystalline Lattice Imaging and Electron-Emitting Nanoprobes --- Part II", Joint Symposium of the 5th US-Korea Workshop on Nanoelectronics, and the 7th US-Korea Workshop on Nanostructured Materials and Nanomanufacturing, 24-25 April 2008, Arlington, Virginia, USA. (INVITED).

 2. Sungho Jin and Kibum Kim, "High-Resolution, Large-Area Nano-imprint Lithography using Crystalline Lattice Imaging and Electron-Emitting Nanoprobes --- Part II", Joint Symposium of the 6th US-Korea Workshop on Nanoelectronics, and the 8th US-Korea Workshop on Nanostructured Materials and Nanomanufacturing, Hanyang Univ., Seoul, Korea, 19-20 May 2009. (INVITED).

3. Sungho Jin, "Massively Parallel Probe Lithography Toward 10 Terabit/in^2 Density Nanofabrication, Special Workshop on Tera-Level Nano Devices (TND), November 2-3, 2009, Seoul Korea. (Invited Talk)

4. Sungho Jin, "New Materials Structures for Advanced Nanomanufacturing", Nano Korea Conference August 28-20, 2010, the 5th International Symposium on Nanoscale Mechatronics & Manufacturing (ISNMM), Seoul Korea (Overseas Invited Talk)

 5. Leon Chen and Sungho Jin, and Kibum Kim, "High-Resolution, Large-Area, Nano Imprint Lithography using Electro Lattice Image & Electron-emitting Nanoprobes (Part

2 of 2) – Massively Parallel Probe Lithography Toward Ultra-High-Density", Joint Symposium of the 9th US-Korea Workshop on Nanostructured Materials and Nanomanufacturing and the 7th US-Korea Workshop on Nanoelectronics 11-12 August 2010, Seattle, WA. (INVITED).

6. "Geometry-Controlled Carbon Nanotubes and Related Structures", <u>Sungho Jin</u>, 2007 TMS Annual Meeting, February 25 - March 1, 2007, Orlando, Florida (INVITED).

7. "Fabrication and Magnetic Behavior of Nano-Patterned Magnetic Media", <u>Sungho Jin</u>, MRS Fall Meeting, Boston, November 26 - 30, 2007 (INVITED).

8. "Nanoprobes and Applications Based on Carbon Nanotubes", <u>Sungho Jin</u>, 2008 TMS Annual Meeting, March 9-13, 2008, New Orleans, Louisiana (INVITED).

9. "Recent Industrial Applications of solid State Phase Transformation", <u>Sungho Jin</u>, 2008 TMS Annual Meeting, March 9-13, 2008, New Orleans, Louisiana (KETNOTE LECTURE).

10. "Growth and Manipulation of Carbon Nanotubes toward Desirable Geometry and Properties", <u>Sungho Jin</u>, MRS (Materials Research Society) Fall Meeting, Boston, December 1-5, 2008 (INVITED).

11. "Formation and Manipulation of Nanotubes, Nanowires and Nanopores for Desirable Geometry and Properties", <u>Sungho Jin</u>, TMS'09 Annual Meeting, Feb. 15-19, 2009, San Francisco (INVITED).

(b) Potential Use of Knowledge from This Project
    The outcome of this research can be useful for high-density magnetic hard disk memory applications as well as many other nanofabrications and nanomanufacturing of nanostructures and nano-device arrays.

Inventions: none filed.

Honors/Awards:
1.. John Bardeen Award from TMS (The Metals, Minerals and Materials Society), 2007 for outstanding contributions to the electronic materials. (2007).

2.. Inaugural MRS Fellow (2008).

3.. Albert-Sauveur Achievement Award, ASM International for pioneering research for discovery of new materials and phenomena in the fields of electronic, magnetic and superconducting materials. (2009).

Chapter 10

Title: Distributed Detection of Attacks/Intrusions and Prevention of Resource-Starvation Attacks in Mobile Ad Hoc Networks
Final Report

Principal Investigator: Kang G. Shin
Department of Electrical Engineering and Computer Science
The University of Michigan
Ann Arbor, MI 48109-2121

Research Objectives

Mobile ad-hoc networks (MANETs) face unique problems that are not present in infrastructure-based wireless networks. Our research objective is to address the problems of detecting malicious/ compromised nodes using monitoring and preventing resource-starvation attacks in MANETs.

Status of effort

1) Efficient deployment of IDS

For the detection of malicious/compromised nodes in MANETs, we have developed methods for selecting "monitor" nodes by considering the characteristics of MANETs. To minimize the monitoring overhead, we proposed a *Distributed Energy Efficient Cluster Formation* (DEECF) scheme that reduces the number of monitor nodes and stand-alone nodes. We have conducted extensive experiments to demonstrate the energy efficiency of DEECF in comparison with other clustering schemes.

To detect and prevent the sleep-deprivation attack in MANETs, we proposed a scheme based on the discrete cosine transform and the coefficient of each frequency domain. We have shown the reality of various sleep-deprivation attacks including slow-and-steady attacks. A slow-and-steady attack prevents a node from moving into sleep-mode using low-rate steady packet transmissions and has not been considered elsewhere, despite its importance. We use the discrete cosine transform to detect the sleep-deprivation attack. We also developed a new detection tool to evaluate the effectiveness of our detection scheme.

Considering limited battery energy, computation, and communication capacities of MANET nodes, we have also developed a light-weight, locally-collaborative intrusion detection method for MANETs. We target both existing and unknown attacks, passive and active attacks, from both inside and external attackers as well. To prevent these attacks, we have proposed a mobile-agent-based intrusion detection scheme. So far, we have defined the functions of a mobile agent (MA) and have demonstrated the effectiveness of our MA-based detection scheme.

2) Fortification of MANETs

We have identified the selfish behavior of mesh routers and proposed a scheme for the detection of selfish routers in a wireless mesh networks. First, we defined the selfish behavior of a router and then proposed a way of detecting the selfish router's packet dropping by analyzing the type of damage it caused. The proposed method is based on sending a probe message between two nodes that are two hops away. The probe message is a normal encrypted message so as to evade its detection by a selfish node. If the selfish node can identify a probe

message, it can evade the detection via probe messages. The return path of the probe message is the same as that from the sender to the target. When the res rate of responding to the probe messages is low, we extend the probing to identify the selfish node.

To prevent link-spoofing attacks, we proposed a modified OLSR protocol that transmits a hello message to two-hop neighbor nodes with relay by one-hop neighbors. The proposal of transmitting hello message up to two-hop neighbors with the help of one-hop neighbors can prevent various types of link-poofing attacks, but it requires changes in the OLSR protocol. We proposed and implemented a required change in the hello message and the protocol. Also, we have specified things for attack detection and also for tolerance of the errors caused by attacks. We have analyzed all the behaviors resulting from the extended delivery of hello messages. Our performance evaluation has shown the proposed OLSR protocol to be more efficient and securer than existing secure OLSR protocols.

Abstract

A Mobile Ad Hoc Network (MANET) self-configures the wireless connection of mobile devices. Each device in a MANET moves in any direction and independently of others, and hence will dynamically change its connectivity to other devices. MANETs can be very effective for various applications, such as future combat systems, search-and-rescue in the event of a disaster, vehicle-to-vehicle communication and coordination, etc. However, for the successful realization and deployment of MANETs in the field, we must resolve several important research issues, such as network node discovery and connectivity, intrusion detection and countermeasures, efficient node resource (especially energy) management, etc. This joint Korea-US research project focuses on how to secure the MANET-usage environment. Thus far, we have made two main research contributions: (i) the efficient deployment of Intrusion Detection System (IDS) in MANETs, and (ii) fortification of MANET connections or systems.

Personnel Supported: Katharine Chang

Publications

- Katharine Chang and Kang G. Shin, ``Distributed authentication of program integrity verification in wireless sensor networks,'' *ACM Trans. on Information and System Security*, vol. 11, no. 3, pp. 14:1--34, March 2008.

- Katharine Chang and Kang G. Shin, ``Application-Layer Intrusion Detection in MANETs,'' *43rd Hawaii International Conference on Systems Science* (HICSS-43), Jan. 2010.

- Abhijit Bose, Xin Hu, Kang G. Shin, and Taejoon Park, ``Behavioral detection of malware on mobile handsets,'' *ACM MobiSys 2008*, pp.~225--238, Breckenridge, CO, June 2008.

- Hahnsang Kim, Joshua Smith, and Kang G. Shin, ``On detecting energy-greedy anomalies,'' *ACM MobiSys 2008*, pp. 239-252, Breckenridge, CO, June 2008.

Interactions

Presented talks on this project at Annual NBIT PI Workshops, AFOSR Annual PI meetings for the Information Assurance Program, Pohang University of Science and Technology, ACM/USENIX MobiSys 2008, US-Korea Conference 2008, MSR Asia, and Seoul National University.

Inventions: None

Honors/Awards: None

Archival Documentation: Four pdf files are attached

Software and/or Hardware: None